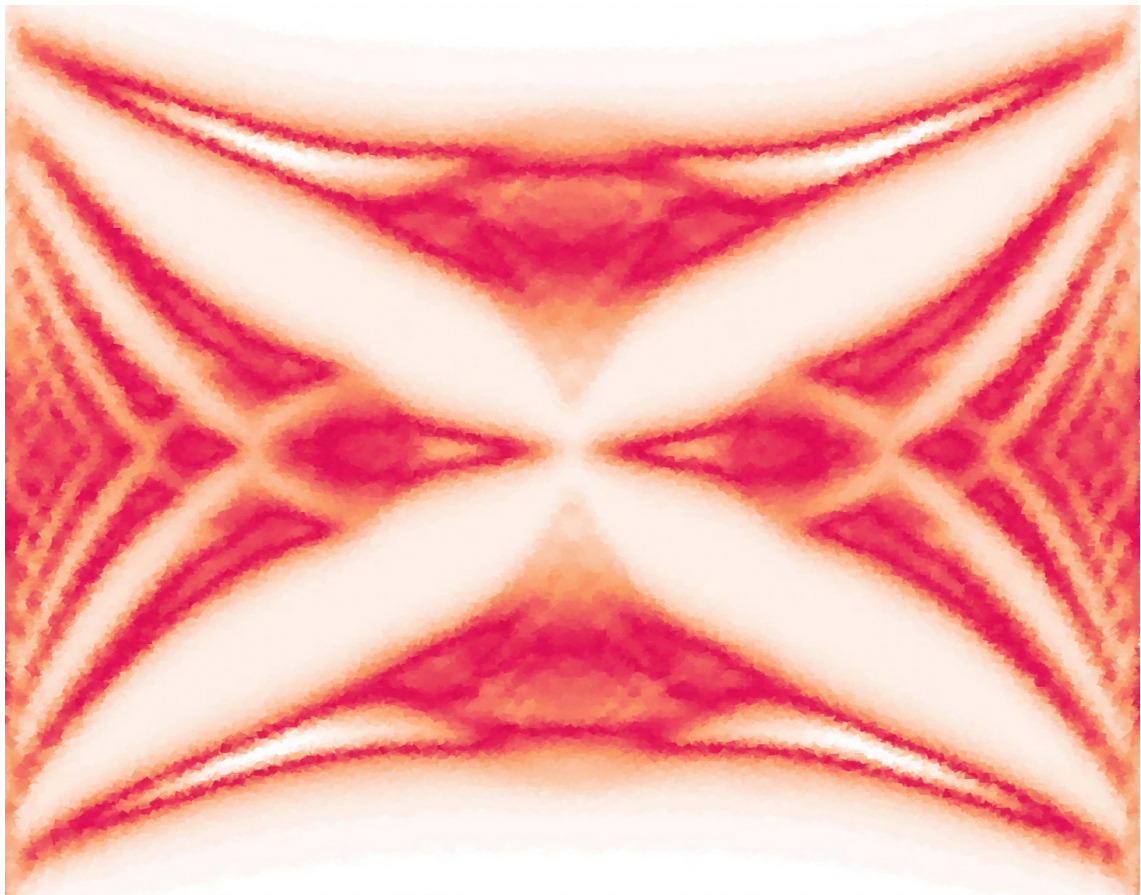

Artificial Gauge Fields in Photonics and Mechanical Systems

Grazia Salerno



Ph.D. thesis submitted to the Dipartimento di Fisica
Università degli studi di Trento

Artificial Gauge Fields in Photonics and Mechanical Systems

Grazia Salerno



A dissertation submitted to the
Dipartimento di Fisica
Università degli Studi di Trento

In fulfilment of the requirements for the Degree of
Philosophiæ Doctor in Physics

Under the Supervision of
Dr. Iacopo Carusotto

Dottorato di Ricerca XXVIII Ciclo
April 19th, 2016

Supervisor:

Dr. Iacopo Carusotto

Members of the committee:

Prof. Fabrice Mortessagne - Université Nice-Sophia Antipolis

Prof. Mikael Rechtsman - Pennsylvania State University

Prof. Sandro Stringari - Università di Trento

Acknowledgements.



No woman is wise enough by herself, paraphrasing Plauto.

It is hence more than a pleasure to acknowledge everyone who helped and encouraged me during my Ph.D. and in particular during the realization of this thesis.

It has been a privilege for me to be a member of the INO-CNR BEC Center of Trento. From the bottom of my heart, I would like to thank my supervisor Iacopo Carusotto, for he guided me through these years with enthusiasm, expertise, competence and patience. I am very grateful for his remarkable advice, his physical insights as well as for the freedom he gave me, allowing me to learn and grow without pressure, but rather having a lot of fun.

I am also very grateful for the opportunities I had to participate in conferences and workshops, to know and be taught from the finest scientists of the field, who also motivated me throughout my path.

I am particularly thankful to Prof. Fabrice Mortessagne for the possibility to have a taste of the work in his lab at the CNRS-LPMC in Nice. Many thanks to him but also to Mathieu Bellec, Ulrich Kuhl and Julian Böhm for the useful and constructive discussions, and for having shared their expertises in the lab. They all made my stay in Nice delightful and simply unforgettable.

I want to acknowledge Prof. Nicola Pugno for stimulating discussions, and his support from the Department of Civil, Environmental and Mechanical Engineering of Trento, together with Ludovic Taxis and Giuseppe Vettori, in the realization of a mechanical benzene. I also appreciate Alice Berardo for the outstanding team-work we had in and outside the lab.

I owe a very huge thanks to Tomoki Ozawa and Hannah Price who have been more than just collaborators. No words will ever express properly the enormous gratitude I have towards them, not only for the suggestions and the many helpful scientific discussions, but also for the friendship, the fun and the moral support.

I am grateful to the permanent members of the BEC group for having established such a lovely, rich, international, sparkling and stimulating scientific environment. I thank Prof. Franco Dalfovo for the opportunity of being a tutor for his General Physics I course, together with Prof. Stefano Giorgini, Prof. Lev Pitaevskii and Prof. Sandro Stringari, because their expertise and outstanding knowledge are a constant source of inspiration. I extend my gratitude to the other brilliant INO-CNR researchers: Gabriele Ferrari, Chiara Menotti, Giacomo Lamporesi and Alessio Recati. From each of them I have learnt a lot.

I acknowledge the former as well as the current members of the BEC crew, who I was glad to meet and discuss with. Thanks to Marta Abad, Nicola Bartolo, Tom Bienaimé, Russell Bisset, Giacomo Colzi, Marco Di Liberto, Simone Donadello, Eleonora Fava, Stefano Finazzi, Yan-Hua Hou, Pierre-Élie Larré, Natalia Matveeva, Carmelo Mordini, David Papoular, Chunlei Qu, Riccardo Rota, Alberto Sartori, Simone Serafini, Marek Tylutki, Li Yun and Peng Zou. I deeply thank Giulia De Rosi for her lovely cheering «*Dai, gnocca!*» boosted me up during the writing of this thesis and for the friendship, together with José Lebreuilly, Giovanni Martone and Luis Peña Ardila. I extend my acknowledgements to the short-visit students of the BEC Center and to the Ph.D. students of the University of Trento, with whom I shared many enjoyable moments, in particular Andrei Berceanu, Roberta Giusteri, Mathieu Isoard, Giovanna Pintori and Mary Tringali. And also to the many others friends and colleagues that I met during these years.

I want to express my gratitude to Giuseppe Froner for the technical support as well as to the administrative personnel, for the exquisite work and immense help and support with bureaucracy. Thanks to Rachele Zanchetta, Flavia Zanon (ERC), Lucia Appoloni, Micaela Paoli, Marina Zuanelli (Ph.D. School), and in particular to Beatrice Ricci (INO-CNR).

A special thanks goes to my dear friend and colleague Ilaria Carleo, for distracting me from time to time and for all the fun we had together. Even from far away, her presence and deep friendship are important to me, for we share a common path.

Last but not least, I am indebted towards my love and my family, for all the encouragements, the solace, the happiness and the faithful trust in me. This thesis is for you.


| | |
|--|-----------|
| Introduction. | 1 |
| 1 Real magnetic field on a lattice: the Harper-Hofstadter model. | 5 |
| 1.1 The tight-binding model. | 5 |
| 1.2 The tight-binding model of a particle in a magnetic field. | 6 |
| 1.2.1 The magnetic translation operator. | 7 |
| 1.2.2 The Harper equation. | 8 |
| 1.3 The Hofstadter butterfly. | 9 |
| 1.4 Topological properties of the energy bands. | 10 |
| 1.5 The integer quantum Hall effect and the Chern number. | 12 |
| 1.5.1 The TKNN formula. | 13 |
| 1.5.2 The Diophantine equation. | 13 |
| 1.5.3 Chern number of the Harper-Hofstadter bands. | 14 |
| 1.5.4 The bulk-edge correspondence. | 15 |
| 2 Artificial fields in artificial systems. | 17 |
| 2.1 Artificial systems. | 18 |
| 2.2 The minimal coupling. | 19 |
| 2.2.1 Rotation. | 19 |
| 2.2.2 Strain. | 20 |
| 2.3 The Peierls phase. | 20 |
| 2.3.1 Using internal degrees of freedom. | 20 |
| 2.3.2 Floquet-based systems. | 21 |
| 2.3.3 Geometrical implementation. | 22 |
| 3 The Peierls phase for coupled pendula. | 25 |
| 3.1 Temporal modulation of classical harmonic oscillators. | 25 |
| 3.2 The rotating-wave approximation. | 27 |
| 3.2.1 Connection to the tight-binding model. | 27 |
| 3.3 Analytical equations of motion within the rotating-wave approximation. | 28 |
| 3.3.1 Monochromatic driving. | 30 |
| 3.3.2 First-order correction beyond the rotating-wave approximation. | 30 |
| 3.4 Results of the driven-dissipative numerical simulations. | 31 |
| 3.4.1 The coupling phase. | 33 |
| 4 The Harper-Hofstadter model in a classical mechanical system. | 35 |
| 4.1 The model. | 35 |
| 4.1.1 The temporal and spatial modulation. | 36 |
| 4.1.2 Analytical derivation of the Harper-Hofstadter effective equation of motion. | 38 |
| 4.2 Results of the numerical simulations. | 40 |
| 4.2.1 The response spectrum. | 40 |
| 4.2.2 Topological edge states. | 41 |

| | | |
|----------|--|------------|
| 4.2.3 | Bulk wave functions. | 43 |
| 4.2.4 | The Hofstadter butterfly. | 44 |
| 4.2.5 | The quantum Hall effect and the Chern number. | 45 |
| 5 | The Harper-Hofstadter model in a classical mechanical system: beyond the rotating-wave approximation. | 47 |
| 5.1 | A reformulation of the model. | 47 |
| 5.1.1 | The mapping at a period. | 48 |
| 5.2 | The instability. | 49 |
| 5.2.1 | The Krein signature. | 49 |
| 5.2.2 | The parametric instability. | 51 |
| 5.3 | The band-gap closing and the topological transition. | 52 |
| 6 | The honeycomb lattice. | 55 |
| 6.1 | Band structure of the honeycomb lattice. | 55 |
| 6.1.1 | Expansion around the K point: Dirac-like Hamiltonian. | 58 |
| 6.2 | Gauge field in honeycomb lattices. | 59 |
| 6.2.1 | Motion of Dirac points for a homogeneous uni-axial strain. | 60 |
| 6.3 | The edge states. | 61 |
| 6.4 | The next-nearest-neighbour coupling. | 62 |
| 6.5 | Artificial graphene. | 63 |
| 7 | Artificial magnetic field and pseudo-Landau levels in a strained honeycomb lattice. | 65 |
| 7.1 | The strained honeycomb lattice. | 66 |
| 7.1.1 | Analytical derivation of the Landau levels in a uni-axially strained honeycomb lattice. | 67 |
| 7.1.2 | Comparison with numerical results from exact diagonalization. | 69 |
| 7.2 | Steady state in a coherently driven-dissipative lattice. | 70 |
| 7.2.1 | The perfect honeycomb lattice. | 71 |
| 7.2.2 | The strained honeycomb lattice. | 72 |
| 7.3 | Experimental remarks. | 74 |
| 8 | Spin-orbit coupling in a honeycomb lattice. | 77 |
| 8.1 | L-T splitting in classical mechanics. | 77 |
| 8.2 | Modes of honeycomb lattices with L-T splitting. | 78 |
| 8.2.1 | The circular polarization basis. | 81 |
| 8.3 | A mechanical model of the benzene molecule with L-T splitting. | 82 |
| 8.3.1 | Experimental data. | 85 |
| | Conclusions and outlooks. | 89 |
| | Appendices | 91 |
| | A Solution of the Harper Equation. | 93 |
| | B Derivation of the effective dynamics: two sites. | 95 |
| | C Derivation of the Bloch-Siegert shift. | 97 |
| | D Derivation of the effective dynamics: the lattice. | 99 |
| | E Fourier decomposition of the equations of motion. | 103 |
| | F Calculation of edge states of the honeycomb lattice. | 105 |
| | G Overlap between Landau levels due to a coherent external pump. | 107 |
| | Bibliography. | 108 |

Introduction.

«Begin at the beginning,» the King said, gravely,
«and go on till you come to the end; then stop.»

Lewis Carroll – *Alice in Wonderland*

ne of the most fundamental interactions in physics is that between elementary particles and gauge fields. The most renowned example of these is probably the coupling between the electromagnetic field and charged particles, described through the scalar and vector potentials. While some of the effects of electromagnetism are familiar even to non-physicists, many of the most surprising phenomena arising from gauge fields are only understood through quantum mechanical concepts. For example, when a free electron is immersed in a uniform magnetic field, its quantum-mechanical energy splits into equally-spaced Landau levels. Such energy quantization vanishes in any classical calculation and it provides a nice explanation of the integer quantum Hall effect, that is the exact quantization of the transverse Hall conductance of a two-dimensional electron gas at a very low temperature and in a strong magnetic field. If instead we consider an electron moving on a crystal lattice immersed in a extremely high magnetic field, the interplay between the Bloch bands and the Landau levels results in a beautiful fractal self-recursive energy spectrum. Moreover, the energy bands of this system, described by the Harper-Hofstadter model, can be connected by robust one-way propagating states which are localised on the physical edge of the system and which are also directly related to the integer quantum Hall effect.

Another important effect related to gauge fields is the coupling between the electron's spin and its own momentum, where the coupling results from the Dirac equation of relativistic quantum mechanics. In this case, the gauge field is said to be non-Abelian, because its components do not commute with each other due to their momentum-dependence. This spin-orbit coupling is well-known in atomic and molecular physics because it explains the atomic fine-structure, but it is also present in condensed matter systems, leading to interesting phenomena such as the quantum spin Hall effect or Majorana fermions.

Recent technological advances in quantum simulators have proven that synthetic materials are very well suited to study and implement almost any type of condensed matter model, thanks to the high level of control and the ability to tune almost at will the system parameters. However, since many of these synthetic systems are characterized by neutral particles that do not naturally couple to real gauge fields, there is the need for the implementation of artificial gauge fields to simulate interesting electromagnetic phenomena such as the ones introduced above. In fact, the aforementioned Harper-Hofstadter model requires magnetic fields that are too huge to be experimentally produced in a laboratory, hence the possibility to simulate an artificial magnetic field allows for the observation of effects that are otherwise impossible to achieve with conventional solid-state materials.

One among the many motivations for the implementation of artificial gauge fields in artificial materials, is the realization of topological insulators, which were first found in real condensed matter systems. These are bulk insulating materials that carry a certain number of edge states which are topologically protected against small perturbations of the system. One example of such

a topological insulator is the quantum Hall effect introduced above. Topological insulators are then very interesting both from the point of view of fundamental physics and concrete applications.

While there have been many works studying topological physics with quantum artificial systems, such as ultracold atoms in optical lattices or polaritons in semiconductor microcavities, very little attention was dedicated to the interplay of topology and the purely classical world. As a matter of fact, only in the last couple of years has there been an explosion of interest towards the realization of a classical acoustic topological insulator, which is just beginning as a rich, brand-new field of research. For instance, in the mechanical meta-material context there can be floppy modes localized on the edges, which are insensitive to local perturbations and which can be viewed as having a topological origin. In these directions, pioneering efforts to encode a non-trivial topology in the dynamical matrix or into the Hamiltonian of a system have proven that the hallmarks of a topological insulator are not the prerogative of quantum mechanics, but can be also observed with a classical system governed by Newton's equations. The first part of this thesis is therefore based on our studies dedicated to the implementation of a classical analogue of the integer quantum Hall system, by realizing the Harper-Hofstadter model for classical coupled harmonic oscillators.

The achievement of an artificial gauge field allows also for the deeper study of fascinating magnetic effects such as, for example, Landau levels. One among the many remarkable properties of graphene, a two-dimensional carbon allotrope, is that its low-energy excitations are described by a Dirac equation for massless fermions. In graphene, an inhomogeneous strain introduced, for example, as an elastic deformation of the honeycomb lattice, is equivalent to an artificial pseudo-magnetic field: in this case the energy spectrum of the Dirac electrons shows the formation of relativistic pseudo-Landau levels. Artificial graphene materials offer a tunable implementation of the strain through a spatial modulation of the tight-binding couplings or through a physical deformation of the lattice. In particular, with photonic graphene the formation of Landau levels stemming from a strain-induced magnetic field has been proven. However, the observation of the spatial wavefunction associated to these levels was not possible, due to limitation of the specific set-up used in the experiment. The second part of the thesis is therefore focussed on the honeycomb lattice geometry and our theoretical proposal for a configuration based on an intrinsically driven-dissipative system in which to probe the physics of the Landau levels, and especially the spatial structure of their wavefunctions. We have also focussed our attention to the effect of a spin-orbit coupling on a pristine honeycomb lattice. More specifically, we have experimentally realised a mechanical system of coupled pendula to investigate some of the aforementioned effects. As a first step, we studied the eigenmodes of a mechanical benzene molecule in the presence of a spin-orbit coupling. The mechanical benzene is composed of six pendula connected in pairs by six springs. The springs are pre-tensioned and they split the coupling along the longitudinal and transverse direction of the two connected masses. As the motion along the longitudinal (L) and transverse (T) directions acts as a pseudo-spin, this L-T splitting can be described as a spin-orbit coupling.

The detailed outline of the thesis is the following.

Chapter 1. The Harper-Hofstadter model, that is a tight-binding model of condensed matter describing an electron on a lattice in the presence of a strong magnetic field, can be considered as the archetypal lattice model of a quantum Hall system. We justify this statement by reviewing the main properties of the model, illustrating the existence of topological edge states between energy bands and their relationship with the Chern invariant, a non-trivial topological integer that characterises the bands.

Chapter 2. We review some of the most relevant methods used for the implementation of an artificial gauge field in various artificial systems, mainly focussing on ultracold atoms, photonics and classical systems. We clarify the differences between the various methods in connection with the specifications of each system and we review the different topological models that have been realized in the literature.

Chapter 3. We make use of the concepts introduced in the previous chapters to design a scheme that realizes an artificial gauge field for coupled classical harmonic oscillators. We start by theoretically studying the dynamics of two coupled pendula subject to a periodic temporal modulation of their natural frequency, to show that Newton's equations of motion, in a certain regime within the rotating wave approximation, can have the same form as the

Heisenberg equations of motion written for a quantum tight-binding Hamiltonian. Applying Floquet theory, we derive the effective Hamiltonian and we show dynamical localization and dynamical isolation effects together with the occurrence of non-trivial coupling Peierls phase between the classical oscillators. The Chapter is based on the publication [Salerno and Carusotto \[2014\]](#).

Chapter 4. We extend the scheme of the previous Chapter by considering frequency-modulated coupled classical harmonic oscillators on a two-dimensional square lattice to realize a classical analogue of the Harper-Hofstadter model. We show that when the natural frequencies of such oscillators are suitably modulated in time and under the same regime as the previous chapter, the energy bands are arranged in the self-similar structure of the Hofstadter butterfly. Between the bands, we find topologically-protected one-way propagating edge states and we also point out that the non-trivial topological Chern invariant of the quantum Hall effect can be estimated from the shift of the oscillation amplitudes. The findings of this Chapter were published in [Salerno et al. \[2016\]](#).

Chapter 5. In the system introduced in the previous Chapter, we explore a region of parameters beyond the rotating wave approximation, where the quantum analogy with the classical oscillators is weaker. We investigate the appearance of complex energy modes that signals a parametric instability of the system and we also find a distortion of the Hofstadter bands, yet the topological effects remain. For parameters that are further away from the rotating wave approximation, a closing of the Hofstadter band gaps is accompanied by a disappearance of topological edge states, and the system becomes topologically trivial. The results of this Chapter were included in [Salerno et al. \[2016\]](#).

Chapter 6. We explore another method, namely strain in honeycomb photonic lattices, to implement an artificial gauge field and study magnetic effects. In this chapter, we start by reviewing in a concise manner the properties of honeycomb lattices in general, as well as in the presence of a homogeneous strain, implemented as different hopping amplitudes of the tight-binding model along the lattice directions. Such a homogeneous strain is described as a pseudo-artificial vector potential.

Chapter 7. In the presence of a suitable spatially-dependent strain, a pseudo-artificial magnetic field appears and the low-energy eigenmodes have the form of relativistic Landau levels. We study the driven-dissipative steady-state of a coherently driven photon field in a honeycomb lattice. We show how the main properties of the pseudo-Landau levels can be extracted by observing the peaks in the absorption spectrum of the system and the corresponding spatial intensity distribution. We also give quantitative predictions for realistic lattices based on photonic or microwave technologies. The main results of this Chapter were published in [Salerno et al. \[2015\]](#).


Chapter 8. We study spin-orbit coupling in a mechanical system of masses and springs, induced by pre-tensioned springs that split the longitudinal and transverse couplings in a honeycomb geometry. We theoretically derive the eigenmodes of the single hexagonal plaquette, that is a benzene molecule, as well as the ones of the extended system. We also present the experimental results of a simple mechanical benzene composed of six pendula connected with pre-tensioned springs, to verify that the eigenfrequencies of this system are well described by our theory in the presence of spin-orbit coupling.

Chapter 1

Real magnetic field on a lattice: the Harper-Hofstadter model.

You might well wonder whether such an intricate structure would ever show up in an experiment. Frankly, I would be the most surprised person in the world if *Gplot* came out of any experiment. The physicality of *Gplot* lies in the fact that it points the way to the proper mathematical treatment of less idealized problems of this sort. In other words, *Gplot* is purely a contribution to theoretical physics, not a hint to experimentalists as to what to expect to see!

Douglas R. Hofstadter – *Gödel, Escher, Bach.*

he Harper-Hofstadter model describes the behaviour of a Bloch electron immersed in a strong magnetic field on a lattice, and it was studied for the first time by Harper [1955] and then by Hofstadter [1976]. This is a very interesting problem of condensed-matter physics, combining two simple and fundamental physical situations that are both understood starting from quantum mechanical principles: an electron in a perfect crystal, and an electron in a homogeneous magnetic field. In the first case, we know that the energy of the electrons moving in a periodic potential splits into the Bloch bands. In the second case, the energy of an electron moving in a magnetic field is quantized into highly degenerate Landau levels. In both situations, the motion of the electron has a characteristic length: the lattice spacing and the magnetic length. We shall also see that the ratio of the two lengths is, surprisingly, the key parameter of the combined problem, as it holds information about the distribution of allowed electron energies. The resulting energy bands are arranged in a self-recursive structure, called by Hofstadter himself “Gplot”, but now commonly known as the “Hofstadter butterfly”.

In this Chapter we will also review the topological properties of the Harper-Hofstadter model, showing that a topological invariant, the Chern number, is associated to the eigenstates forming the energy bands. We will also discuss how this Chern invariant is related to the quantized Hall conductance and the topological edge states, legitimizing the idea that the Harper-Hofstadter is one of the archetypical lattice models of a quantum Hall system.

1.1 The tight-binding model.

We first consider a particle of mass m moving in a lattice potential V_{lattice} . The Hamiltonian,

written in the second quantization formalism, is the following:

$$\hat{\mathcal{H}} = \int \hat{\psi}^\dagger(\vec{r}) \left(-\frac{\hbar^2}{2m} \nabla^2 + V_{\text{lattice}} \right) \hat{\psi}(\vec{r}) d\vec{r}. \quad (1.1)$$

We know from solid-state physics textbooks, such as [Aschroft and Mermin \[1976\]](#) or [Marder \[2010\]](#), that the energies of such a Hamiltonian are organized in a band structure, and the eigenstates are the Bloch wavefunctions: $\psi_{\nu, \vec{k}}(\vec{r}) = e^{i\vec{k} \cdot \vec{r}} u_{\nu, \vec{k}}(\vec{r})$, where \vec{k} is the quasi-momentum, ν is the index of the energy band and the function $u_{\nu, \vec{k}}(\vec{r})$ is periodic with the same periodicity of the lattice. We consider the case where only the lowest band is populated and drop, for the moment, the band index ν . Such an approximation is valid in the case of a deep potential when the particle is tightly bound to the region of the minimum of the potential. Since the particle is confined to move around the lattice sites, the wavefunction can be expressed in the basis of the Wannier functions, that are strongly localised on the sites. These functions are defined from the Bloch functions as:

$$\mathcal{W}(\vec{r}, \vec{R}) \equiv \frac{1}{V} \int_{\vec{k} \in BZ} e^{-i\vec{k} \cdot \vec{R}} \psi_{\vec{k}}(\vec{r}) d\vec{k}, \quad (1.2)$$

where V is the area of the Brillouin zone, \vec{R} is the Bravais vector, and the integral is done over all quasi-momenta in the Brillouin zone $k_x, k_y \in [-\pi/a, \pi/a]$, where the lattice spacing is a .

As a consequence of Bloch's theorem, the Wannier functions depend on the position of the particle \vec{r} and the position of the lattice site \vec{R} only through their difference: $\mathcal{W}(\vec{r}, \vec{R}) = \mathcal{W}(\vec{r} - \vec{R})$. The field operators in the Hamiltonian Eq. (1.1) are then defined as:

$$\hat{\psi}(\vec{r}) \equiv \sum_{\vec{R}} \mathcal{W}(\vec{r} - \vec{R}) \hat{a}_{\vec{R}}, \quad \hat{\psi}^\dagger(\vec{r}) \equiv \sum_{\vec{R}} \mathcal{W}^*(\vec{r} - \vec{R}) \hat{a}_{\vec{R}}^\dagger, \quad (1.3)$$

where $\hat{a}_{\vec{R}}$ and $\hat{a}_{\vec{R}}^\dagger$ are the annihilation and creation operators of a particle in the Wannier state at the lattice position \vec{R} , whose wavefunction is $\mathcal{W}(\vec{r} - \vec{R})$. Substituting the definition of the field operators Eq. (1.3) in the Hamiltonian Eq. (1.1), we have:

$$\hat{\mathcal{H}}_{\text{TB}} = \sum_{\vec{R}, \vec{R}'} -J(\vec{R} - \vec{R}') \hat{a}_{\vec{R}}^\dagger \hat{a}_{\vec{R}'}. \quad (1.4)$$

The quantity $J(\vec{R} - \vec{R}')$ is the matrix element:

$$J(\vec{R} - \vec{R}') \equiv \int \mathcal{W}^*(\vec{r} - \vec{R}) \left(-\frac{\hbar^2}{2m} \nabla^2 + V_{\text{lattice}} \right) \mathcal{W}(\vec{r} - \vec{R}') d\vec{r}. \quad (1.5)$$

Since the overlap of the Wannier functions between distant sites is very small, the sum in the tight-binding Hamiltonian Eq. (1.4) can usually be restricted to the nearest-neighbour sites only.

1.2 The tight-binding model of a particle in a magnetic field.

We now consider the square lattice potential V_{lattice} in the $x-y$ plane penetrated by a magnetic field that is oriented in the positive vertical direction: $\vec{B} = B\vec{z}$. In the Hamiltonian of a particle of mass m and charge e , we consider the minimal coupling with the magnetic vector potential \vec{A} by substituting $-i\hbar\vec{\nabla} \rightarrow -i\hbar\vec{\nabla} - e\vec{A}$. The vector potential, written in the Landau gauge, is $\vec{A} = -By\vec{x}$ and it is such that $\vec{\nabla} \cdot \vec{A} = 0$ and $\vec{\nabla} \times \vec{A} = \vec{B}$. The Hamiltonian in Eq. (1.1) will now read:

$$\hat{\mathcal{H}} = \int \hat{\psi}^\dagger(\vec{r}) \left(-\frac{1}{2m} (-i\hbar\vec{\nabla} - e\vec{A})^2 + V_{\text{lattice}} \right) \hat{\psi}(\vec{r}) d\vec{r}. \quad (1.6)$$

This new magnetic potential term introduces some complications with respect to the derivation of the previous section, that was based on Bloch's theorem expanded in Wannier functions. In fact, Bloch's theorem holds for any Hamiltonian that is spatially periodic and Eq. (1.6) is no longer translationally invariant due to the presence of the magnetic vector potential that depends linearly on the coordinates. However, we can still define new translation operators that commute with this Hamiltonian and that differ from the usual translation operators only by a phase factor, as shown by [Zak \[1964a\]](#), [Zak \[1964b\]](#).

1.2.1 The magnetic translation operator.

We now shall find a suitable translation operator that commutes with the magnetic Hamiltonian in Eq. (1.6). We start by noticing that the magnetic vector potential satisfies the following relation:

$$\vec{A}(\vec{r} + \vec{a}) = \vec{A}(\vec{r}) + \vec{\nabla}f(\vec{r}),$$

having defined $\vec{\nabla}f(\vec{r}) \equiv \vec{A}(\vec{r} + \vec{a}) - \vec{A}(\vec{r}) = \Delta\vec{A}$, so that the previous relation stems from the identity. Since the vector potential in the Landau gauge is linearly dependent on the position, the difference $\Delta\vec{A} = -B\vec{a}$ is independent of \vec{r} , and we can write the gradient as $\vec{\nabla}f(\vec{r}) = \vec{\nabla}(\Delta\vec{A} \cdot \vec{r})$. We now apply a gauge transformation to the vector potential, such that $\vec{A} \rightarrow \vec{A} - \vec{\nabla}f(\vec{r})$ such that in this new gauge the vector potential is invariant under translation by a lattice vector. From standard quantum mechanics textbooks, such as Sakurai [1994], we know that the wavefunction in this new gauge is transformed according to:

$$\psi(\vec{r}) \rightarrow e^{ie f(\vec{r})/\hbar} \psi(\vec{r}) \quad (1.7)$$

where we could also write $f(\vec{r}) = \int \vec{\nabla}f(\vec{r}) \cdot d\vec{r}$. This state is the magnetic-translated state, therefore we can define the *magnetic translation operator* as:

$$\hat{T}_{\vec{a}}^M = e^{ie/\hbar \int \vec{A} \cdot d\vec{r}'} \hat{T}_{\vec{a}} \quad (1.8)$$

where $\hat{T}_{\vec{a}}$ is the usual translation operator: $\hat{T}_{\vec{a}} \varphi(\vec{r}) = \varphi(\vec{r} + \vec{a})$. In general, two magnetic translation operators do not commute with each other:

$$\hat{T}_{\vec{a}_1}^M \hat{T}_{\vec{a}_2}^M = \hat{T}_{\vec{a}_2}^M \hat{T}_{\vec{a}_1}^M e^{ie/\hbar \int_{\vec{a}_1}^{\vec{a}_2} \vec{A} \cdot d\vec{r}'}$$

The phase factor that appears when commuting two magnetic translations is the *dynamical phase* of Aharonov and Bohm [1959] that the electron gains on the path defined along the lattice vectors \vec{a}_1 and \vec{a}_2 . When such a path is a closed loop, for example, defined around the unit cell, the two magnetic translations do commute with each other. In this case we have that the phase factor is:

$$\frac{e}{\hbar} \oint \vec{A} \cdot d\vec{r} = 2\pi \frac{eBa^2}{h} \equiv 2\pi \frac{\Phi}{\Phi_0} = 2\pi\theta \quad (1.9)$$

where $\Phi_0 \equiv e/h$ is the flux quantum and $\Phi \equiv Ba^2 = \theta\Phi_0$ is the magnetic flux enclosed in the unit cell. The parameter θ tells us how many flux quantum are in the magnetic flux Φ that is generated by the magnetic field B . For this reason, in the following of the thesis, we will simply refer to θ as being the ‘‘magnetic flux’’. It is quite remarkable that θ can be also expressed as the ratio of two characteristic length scales of the problem, as in Dalibard [2015]:

$$2\pi\theta = \frac{a^2}{\ell_B^2}, \quad (1.10)$$

where $\ell_B = \sqrt{\hbar/|eB|}$ is the magnetic length and a the unit length of the lattice.

Another important consequence of the magnetic translation operator, is that a modified *magnetic unit cell* is introduced. In fact, for the Landau gauge that we have chosen, the translation operator along the x direction is unaffected, while the one along y is modified by a phase factor $e^{-i2\pi\theta R_y/a}$ that depends on the position R_y . This means that, for a rational magnetic flux $\theta = p/q$, the periodicity along the y direction is restored after q lattice sites, therefore a magnetic unit cell is enlarged with respect to the pristine unit cell, as can be seen in Fig. 1.1. Different shapes of the magnetic unit cell can be taken, although the number of plaquettes enclosed in the cell must always be q . From this modified magnetic unit cell we can also define the *magnetic Brillouin zone*, that extends for $k_x \in [-\pi/a, \pi/a]$ and $k_y \in [-\pi/(qa), \pi/(qa)]$.

By using the translated state in Eq. (1.7), the tight-binding Hamiltonian in magnetic field becomes:

$$\hat{\mathcal{H}}_{\text{MTB}} = \sum_{\vec{R}, \vec{R}'} -J(\vec{R} - \vec{R}') e^{ie/\hbar \int_{\vec{R}'}^{\vec{R}} \vec{A} \cdot d\vec{r}'} \hat{a}_{\vec{R}}^\dagger \hat{a}_{\vec{R}'}. \quad (1.11)$$

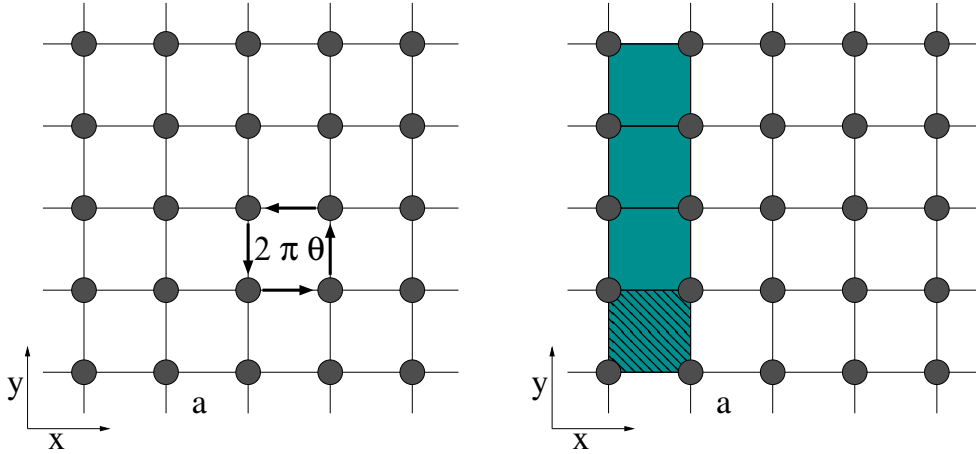


Figure 1.1: A sketch of a square lattice with lattice unit vector a immersed in a uniform perpendicular magnetic field. On the left, the phase acquired in a closed loop around a unit cell of the lattice. On the right, the original unit cell versus the magnetic unit cell in real space. The magnetic unit cell is shaded in green and is enlarged with respect to the original unit cell that is highlighted by black lines. The magnetic unit cell depends on the magnetic flux and the gauge that is chosen for the vector potential. For $\theta = 1/4$ in the Landau gauge $\vec{A} = -By\vec{x}$, this cell contains $q = 4$ lattice vectors and covers an area of four pristine unit cells $4a^2$ along the y direction.

The presence of the vector potential \vec{A} modifies the tight-binding Hamiltonian by only adding a *Peierls phase* factor to the hopping term Wannier [1962]. In the Landau gauge the Hamiltonian in Eq. (1.11) becomes:

$$\hat{\mathcal{H}} = -J \sum_{\vec{R}} \left(e^{-i2\pi\theta R_y/a} \hat{a}_{\vec{R}+\vec{x}a}^\dagger \hat{a}_{\vec{R}} + \hat{a}_{\vec{R}+\vec{y}a}^\dagger \hat{a}_{\vec{R}} + \text{H. c.} \right) \quad (1.12)$$

where we have considered the nearest neighbour approximation and so coupled a lattice point in position \vec{R} to the nearest points that are only one unit cell away $\vec{R} + \vec{x}a$ along x and $\vec{R} + \vec{y}a$ along y . This is the Harper-Hofstadter Hamiltonian.

1.2.2 The Harper equation.

We now calculate the energy dispersion of the Harper-Hofstadter model. It is convenient to write the time-independent Schrödinger equation starting from the Hamiltonian in Eq. (1.12). We have that:

$$E\psi(R_x, R_y) = -J \left(e^{-i2\pi\theta R_y/a} \psi(R_x + a, R_y) + e^{i2\pi\theta R_y/a} \psi(R_x - a, R_y) + \psi(R_x, R_y + a) + \psi(R_x, R_y - a) \right). \quad (1.13)$$

Since the coefficients in the above equation only involve R_y , there is still translational invariance along x . We can assume a plane wave behaviour and expand as:

$$\psi(R_x, R_y) = g(R_y) e^{iR_x k_x}$$

We can define new coordinates in units of the quantities of the lattice (the spacing a and the tunnelling J) as:

$$i = \frac{R_x}{a}, \quad j = \frac{R_y}{a}, \quad \kappa = ak_x, \quad \varepsilon = \frac{E}{J}. \quad (1.14)$$

With simple calculations, Eq. (1.13) becomes the Harper equation:

$$-\varepsilon g(j) = g(j+1) + g(j-1) + 2 \cos(2\pi\theta j - \kappa) g(j), \quad (1.15)$$

that was studied for the first time by Harper [1955].

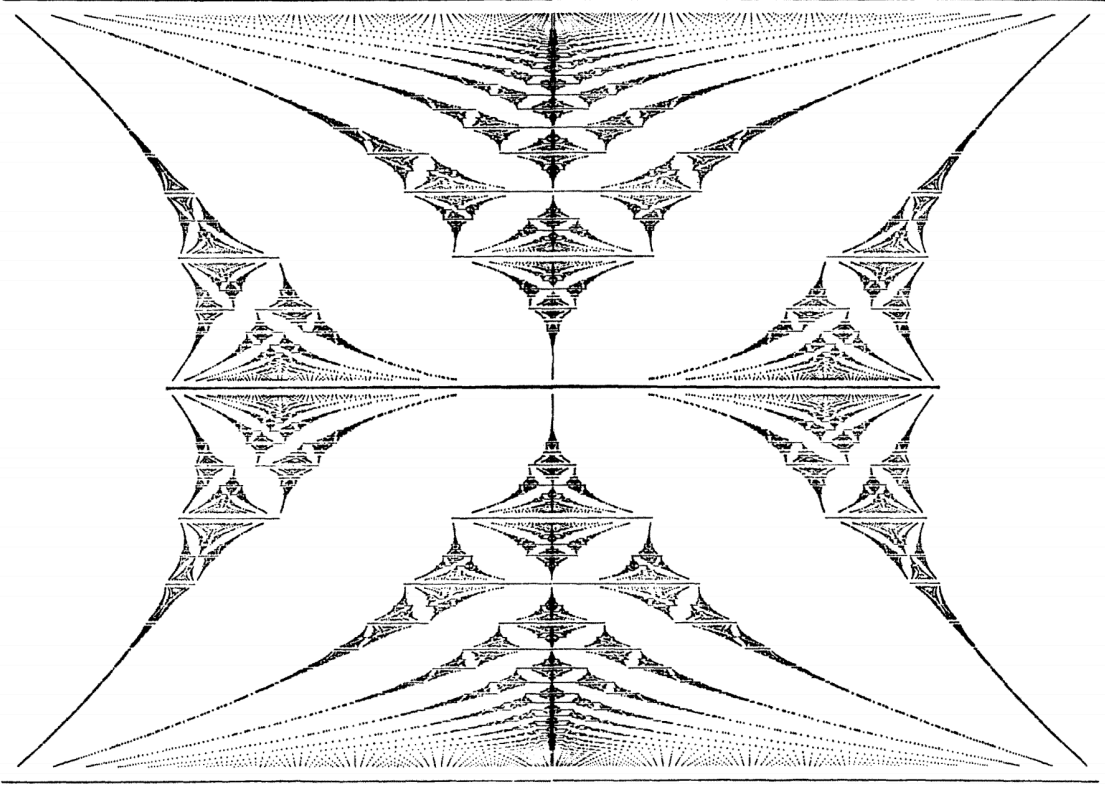


Figure 1.2: “*Gplot: a recursive graph*” from Hofstadter [1976]. Energy bands for the Bloch electron in a uniform magnetic field. The magnetic flux θ runs vertically from 0 to 1, while energy runs horizontally from -4ε to 4ε . The horizontal line segments are bands of allowed energies. As it resembles a butterfly, this graph is now known as the “Hofstadter butterfly”. Copyright © 1976, American Physical Society.

1.3 The Hofstadter butterfly.

One of the most surprising properties of the Harper equation in Eq. (1.15) is evident when the magnetic flux is a rational number:

$$\theta = p/q$$

with p and q being co-prime integers. In this special case, investigated by Hofstadter [1976], Bloch’s theorem implies that the energy levels split into exactly q bands, because the potential term in the Eq. (1.15) is periodic with period q . To calculate these energy bands, it is convenient to write Harper’s equation in the iterative-matrix form:

$$\begin{pmatrix} g(q+1) \\ g(q) \end{pmatrix} = \prod_{m=1}^q \begin{pmatrix} \varepsilon - 2 \cos(2\pi m\theta - \kappa) & -1 \\ 1 & 0 \end{pmatrix} \begin{pmatrix} g(1) \\ g(0) \end{pmatrix} = Q(\varepsilon, \kappa) \begin{pmatrix} g(1) \\ g(0) \end{pmatrix}. \quad (1.16)$$

It can be shown that the product matrix Q is such that:

$$\left| \text{Tr}[Q(\varepsilon, \frac{\pi}{2q})] \right| \leq 4. \quad (1.17)$$

If ε satisfies Eq. (1.17), then this ε is an allowed eigenvalue. A full derivation of this result is given in the Appendix A.

The energy spectrum predicted by Eq. (1.17) as a function of the magnetic flux θ has a recursive and self-similar structure, which is shown in Fig. 1.2. The magnetic flux θ runs vertically from 0 to 1, while energy runs horizontally from -4ε to 4ε . For rational values of the flux $\theta = p/q$, it is easy to identify q horizontal line segments, that represent the bands of allowed energies. This result is peculiar because it implies that changing the flux from $\theta = 0.5$ to $\theta = 0.500001$ changes

the number of bands from 2 to 1000000. Besides, there is no guarantee that the magnetic flux θ is always a rational number. Upon these two arguments, the result in Eq. (1.17) seems unreasonable: an arbitrarily small variation on the strength of the magnetic field (hence the flux) should not influence the physical observable. Nevertheless, the result is correct. In Hofstadter [1976], we read:

“For any θ , as θ' approaches θ , then all points of spectrum(θ) are approached by points belonging to spectrum(θ'); furthermore, only the points of spectrum(θ) are so approached. [...] vertical motion along the graph is continuous.”

This means that the whole physics of the system can be recovered from the rational cases, even for the irrational θ , by indefinitely approaching this irrational value with a rational value of the magnetic flux. However, the butterfly resulting from a real experiment will be “blurred”, because of the unavoidable uncertainty on the value of the magnetic field that will result into an uncertainty $\Delta\theta$ on the magnetic flux. Due to the continuity argument of Hofstadter, the behaviour of this blurred butterfly will be continuous for all magnetic field values. The entire graph is recovered in the limit $\Delta\theta \rightarrow 0$.

1.4 Topological properties of the energy bands.

The Hofstadter butterfly in Fig. 1.2 shows us the single-particle energy as a function of the magnetic flux through a very beautiful fractal self-similar structure. More insights on the specific energy dispersion in momentum space of the Harper-Hofstadter model and the topological properties of its eigenfunctions can be obtained by directly diagonalizing the Harper-Hofstadter Hamiltonian. Equation (1.12) in the tight-binding formalism is written as:

$$\hat{\mathcal{H}} = -J \sum_{i,j} \left[e^{-i2\pi\theta j} \hat{a}_{i+1,j}^\dagger \hat{a}_{i,j} + \hat{a}_{i,j+1}^\dagger \hat{a}_{i,j} + \text{H. c.} \right] \quad (1.18)$$

where i and j are the same as introduced in Eq. (1.14). We move to quasi-momentum space:

$$\hat{a}_{i,j} = \frac{a^2}{4\pi^2} \int_{-\frac{\pi}{a}}^{\frac{\pi}{a}} dk_x \int_{-\frac{\pi}{a}}^{\frac{\pi}{a}} dk_y e^{ik_x ai} e^{ik_y aj} \hat{a}_{k_x, k_y}. \quad (1.19)$$

Due to the presence of the magnetic flux, the quasi-momenta should belong to the magnetic Brillouin zone, as previously defined, instead of to the original Brillouin zone as in Eq. (1.19). To this end, the quasi-momentum along y goes to $k_y \rightarrow k_y - 2\pi\theta m$, where m is an integer that runs over $m = 0 \dots q-1$. Substituting into Eq. (1.18), we have that :

$$\hat{\mathcal{H}} = \frac{a^2}{4\pi^2} \int_{-\frac{\pi}{a}}^{\frac{\pi}{a}} \int_{-\frac{\pi}{qa}}^{\frac{\pi}{qa}} \hat{\mathcal{H}}(\vec{k}) dk_x dk_y,$$

where:

$$\begin{aligned} \hat{\mathcal{H}}(\vec{k}) = -J \sum_{m=0}^{q-1} \left[\cos(k_x a - 2\pi\theta m) \hat{a}_{k_x, k_y - 2\pi\theta m}^\dagger \hat{a}_{k_x, k_y - 2\pi\theta m} \right. \\ \left. + e^{ik_y a} \hat{a}_{k_x, k_y - 2\pi\theta(m+1)}^\dagger \hat{a}_{k_x, k_y - 2\pi\theta m} + e^{-ik_y a} \hat{a}_{k_x, k_y - 2\pi\theta(m-1)}^\dagger \hat{a}_{k_x, k_y - 2\pi\theta m} \right]. \end{aligned} \quad (1.20)$$

This Hamiltonian can be viewed as a tight-binding model in one dimension, where the sites are labelled by m . We can obtain the single-particle energies by expanding into single-particle states according to:

$$|\Psi(\vec{k})\rangle = \sum_{m=0}^{q-1} \varphi_m(\vec{k}) \hat{a}_{k_x, k_y - 2\pi\theta m}^\dagger |0\rangle \quad (1.21)$$

where $|0\rangle$ is the vacuum state and the expansion coefficients $\varphi_m(\vec{k})$ are such that $\varphi_m(\vec{k}) = \varphi_{m+q}(\vec{k})$, if the flux $\theta = p/q$. From the Schrödinger equation $\hat{\mathcal{H}}(\vec{k})|\Psi(\vec{k})\rangle = E(\vec{k})|\Psi(\vec{k})\rangle$, we find that the expansion coefficients satisfy the following expression:

$$\hat{\mathcal{H}}_k \begin{pmatrix} \varphi_0(\vec{k}) \\ \vdots \\ \varphi_{q-1}(\vec{k}) \end{pmatrix} = E(\vec{k}) \begin{pmatrix} \varphi_0(\vec{k}) \\ \vdots \\ \varphi_{q-1}(\vec{k}) \end{pmatrix}, \quad (1.22)$$

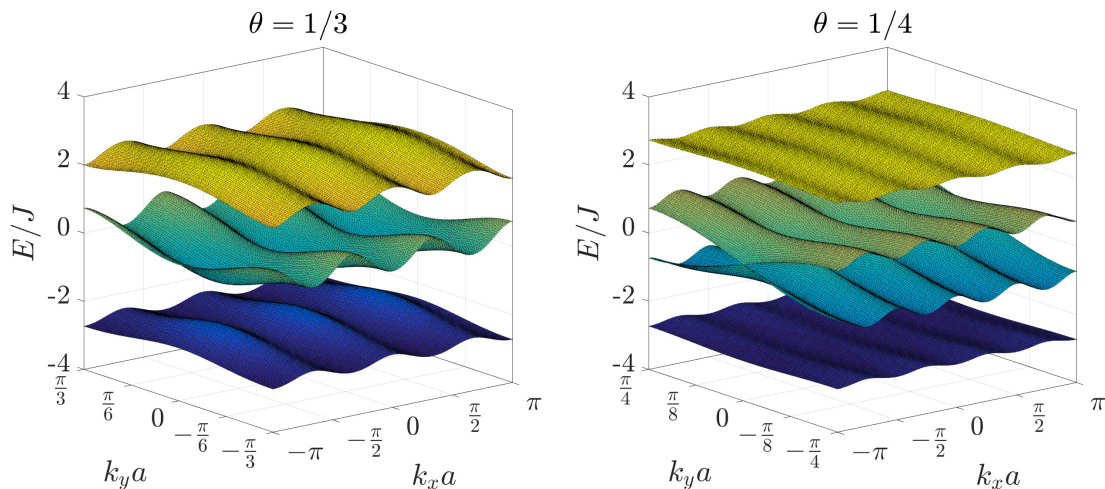


Figure 1.3: Bulk energy dispersion in units of J as a function of the quasi-momenta k_x and k_y in the magnetic Brillouin zone for two values of the magnetic flux θ . On the left for $\theta = 1/3$, we see that there are three energy bands. On the right for $\theta = 1/4$, there are four bands, but the two central ones are touching in Dirac points at zero energy.

where:

$$\hat{\mathcal{H}}_k = -J \begin{pmatrix} 2 \cos [k_x a] & e^{ik_y a} & 0 \dots & e^{-ik_y a} \\ e^{-ik_y a} & 2 \cos [k_x a - 2\pi\theta] & e^{ik_y a} & \dots 0 \\ \vdots & \vdots & \ddots & \vdots \\ e^{ik_y a} & 0 \dots & e^{-ik_y a} & 2 \cos [k_x a - 2\pi\theta(q-1)] \end{pmatrix}. \quad (1.23)$$

The eigenvalues of this q -by- q matrix are the energy bands shown in Fig. 1.3 for two values of θ in the magnetic Brillouin zone $k_x \in [-\frac{\pi}{a}, \frac{\pi}{a}]$ and $k_y \in [-\frac{\pi}{qa}, \frac{\pi}{qa}]$.

The eigenfunctions of the ν -th band $\hat{\mathcal{H}}_k u_\nu(\vec{k}) = E_\nu(\vec{k}) u_\nu(\vec{k})$, namely

$$u_\nu(\vec{k}) = \begin{pmatrix} \varphi_1^\nu(\vec{k}) \\ \vdots \\ \varphi_{q-1}^\nu(\vec{k}) \end{pmatrix}, \quad (1.24)$$

are associated with a geometrical quantity, that is the *Berry curvature*, defined as [Xiao et al., 2010]:

$$\vec{\Omega}_\nu(\vec{k}) \equiv \nabla_{\vec{k}} \times \langle u_\nu(\vec{k}) | i \nabla_{\vec{k}} | u_\nu(\vec{k}) \rangle. \quad (1.25)$$

The Berry curvature is an intrinsic geometrical property of the band that only depends on its wave function, and is a local gauge invariant quantity, see Xiao et al. [2010]. Equation (1.25) can be also written as $\vec{\Omega}_\nu(\vec{k}) \equiv \nabla_{\vec{k}} \times \vec{\mathcal{A}}_\nu(\vec{k})$, where

$$\vec{\mathcal{A}}_\nu(\vec{k}) \equiv \langle u_\nu(\vec{k}) | i \nabla_{\vec{k}} | u_\nu(\vec{k}) \rangle \quad (1.26)$$

defines the *Berry connection*, [Berry, 1984]. A physical interpretation of the Berry connection and curvature, is that they represent a magnetic vector potential and field in momentum space, as found by Berry [1984], and recently discussed also by Price et al. [2014].

By integrating the Berry connection on a path \mathcal{C} in the Brillouin zone, we obtain a geometrical phase called *Berry phase*, [Berry, 1984]. If \mathcal{C} is a closed path, the Berry phase is:

$$\gamma_\nu = \oint_{\mathcal{C}} \vec{\mathcal{A}}_\nu(\vec{k}) \cdot d\vec{k} \quad (1.27)$$

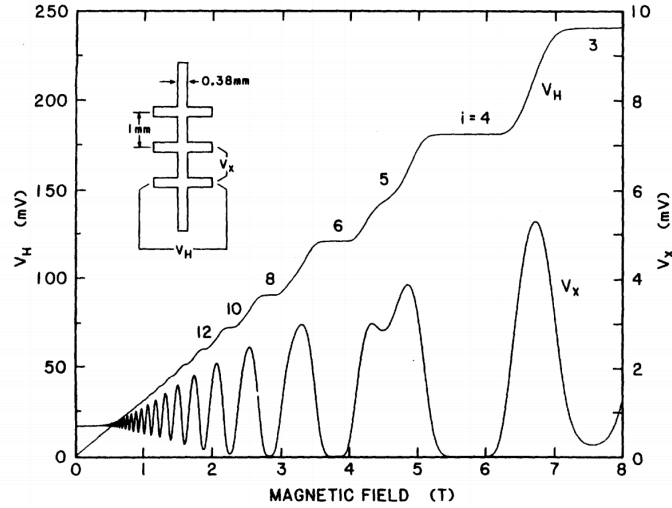


Figure 1.4: Figure from [Cage et al. \[1985\]](#), showing the series of plateaux in the (transverse) Hall voltage V_H as a function of the external magnetic field B . The $V_H = I/\sigma_{xy}$, where I is the current applied to the Hall device. Each plateau is highlighted with the integer i . The longitudinal voltage V_x is also showed. © 1985 IEEE.

and it is a gauge-invariant quantity. The physical interpretation of the Berry phase is that it represents a magnetic flux in momentum space. In fact, the Berry phase can also be written as:

$$\gamma_\nu = \int_{\mathcal{S}} \vec{\Omega}_\nu(\vec{k}) \cdot d\vec{S} \quad (1.28)$$

where we have used Stoke's theorem and \mathcal{S} is the surface enclosed by the contour \mathcal{C} . From the expression given in Eq. (1.28), it is clear that the Berry phase is similar to the Aharonov-Bohm phase [Aharonov and Bohm \[1959\]](#), with the Berry curvature playing the role of a magnetic field in momentum space.

The integral of the Berry curvature over the Brillouin zone is an integer, called the *Chern number*:

$$C_\nu = \frac{1}{2\pi} \int \vec{\Omega}_\nu(\vec{k}) \cdot \vec{z} dk_x dk_y. \quad (1.29)$$

This topological quantity has important physical consequences in the integer quantum Hall effect, as we shall see in the following.

1.5 The integer quantum Hall effect and the Chern number.

The exact quantization of the Hall conductance was experimentally discovered by [von Klitzing et al. \[1980\]](#). They considered a silicon-based device, cooled down to low temperatures, in which the electrons can move only in a two dimensional layer between a metal and a semiconductor. This system is immersed in a strong magnetic field along the z axis and subjected to a longitudinal electric field E_y , as in a usual Hall device.

In contrast to the classical Hall effect, as the strong magnetic field is varied, the transverse Hall current follows a linear relation $j_x = \frac{e^2}{h} i E_y$, where i is an integer and we shall see in the following that it is related to the Chern number. This means that the Hall conductance, defined as $\sigma_{xy} = j_x/E_y$, is quantized, *i.e.* it exhibits a series of plateaux at well-defined values:

$$\sigma_{xy} = \frac{e^2}{h} i. \quad (1.30)$$

The previous expression is for the integer quantum Hall effect.

In the following, we will show why the conductance must be quantized, first from the Kubo formula, and then through a simple argument based on the Diophantine equation and the Strěda

formula, for example see [Bernevig \[2013\]](#). The former approach is more general, while the latter is less rigorous but simpler and it can be specifically applied to the Harper-Hofstadter model to calculate the Chern invariant. However, the integer quantum Hall effect can also be derived from semi-classical arguments [Chang and Niu \[1996\]](#), by considering the effects of a magnetic field perturbation on the density, as also discussed by [Price et al. \[2016\]](#).

1.5.1 The TKNN formula.

The integer quantum Hall effect was explained by [Laughlin \[1981\]](#) as the consequence of gauge invariance, and then related to the topological Chern invariant of the energy bands by [Thouless et al. \[1982\]](#), [Niu et al. \[1985\]](#) through the so-called *TKNN formula*.

In solid-state experiments, the quantization of σ_{xy} is observed by applying a constant current to the sample and measuring the voltage difference in the transverse direction. Therefore, the conductivity can be calculated from the linear response of the two-dimensional gas on a lattice with magnetic field to an externally applied electric field. We assume that all energy bands below the Fermi energy E_F are filled and that the Fermi energy lies within a spectral gap. The Hall conductance is determined by the following:

$$\sigma_{xy} = \frac{ie^2}{2\pi h} \sum_{E_\nu < E_F} \int \left(\left\langle \frac{\partial u_\nu(\vec{k})}{\partial k_x} \middle| \frac{\partial u_\nu(\vec{k})}{\partial k_y} \right\rangle - \left\langle \frac{\partial u_\nu(\vec{k})}{\partial k_y} \middle| \frac{\partial u_\nu(\vec{k})}{\partial k_x} \right\rangle \right) dk_x dk_y, \quad (1.31)$$

where $u_\nu(\vec{k})$ is the eigenvector $\hat{\mathcal{H}}(\vec{k})u_\nu(\vec{k}) = E_\nu(\vec{k})u_\nu(\vec{k})$ associated to the ν -th band E_ν , *e.g.* the solution of Eq. (1.22). The sum runs over all occupied bands below the Fermi energy, while the integral is taken over the first Brillouin zone. Equation (1.31) was derived from the Kubo formula by [Thouless et al. \[1982\]](#). The quantity in the parenthesis is the Berry curvature of the ν -th band. Using Eq. (1.29), it is evident that the Hall conductance of a band insulator in Eq. (1.31) is quantized, as shown also by [Chang and Niu \[1996\]](#) and [Xiao et al. \[2010\]](#). More specifically, it is equal to the sum of all the Chern number associated to the occupied bands:

$$\sigma_{xy} = \frac{e^2}{h} \sum_{E_\nu < E_F} C_\nu. \quad (1.32)$$

An important property that one can derive from Eq. (1.32) is that the sum of the Chern number of all bands must be zero, since if all bands are occupied there are no conducting states available and the Hall conductance is zero.

1.5.2 The Diophantine equation.

Three positive integers r , p and q , where p and q are co-prime, always satisfy the following *Diophantine equation*:

$$pt_r + qs_r = r, \quad (1.33)$$

with unknowns t_r and s_r that depend on the value of r . A mathematical theorem states that this equation has a solution for $t_r, s_r \in \mathbb{Z}$ if and only if r is a multiple of the greatest-common-divisor of p and q . As these two are co-prime integers, the greatest-common-divisor of p and q is of course 1 and Eq. (1.33) has a unique solution if:

$$0 \leq r \leq q, \quad |t_r| \leq q/2. \quad (1.34)$$

We now show that an analytical computation of the Hall conductivity can be extracted from the fractal structure of the Harper-Hofstadter model using the Diophantine equation. In fact, dividing Eq. (1.33) by q , we get:

$$n_e \equiv \frac{r}{q} = \theta t_r + s_r. \quad (1.35)$$

The quantity n_e is the density of states below the r -th gap. It is reasonable to take such a quantity equal to the number of the occupied bands r , divided by the total number of bands q , although this argument is not rigorous. A simple argument due to [Strěda \[1982\]](#) shows that the Hall conductance can be written as:

$$\sigma_{xy} = -e \frac{\partial n_e}{\partial \Phi}. \quad (1.36)$$

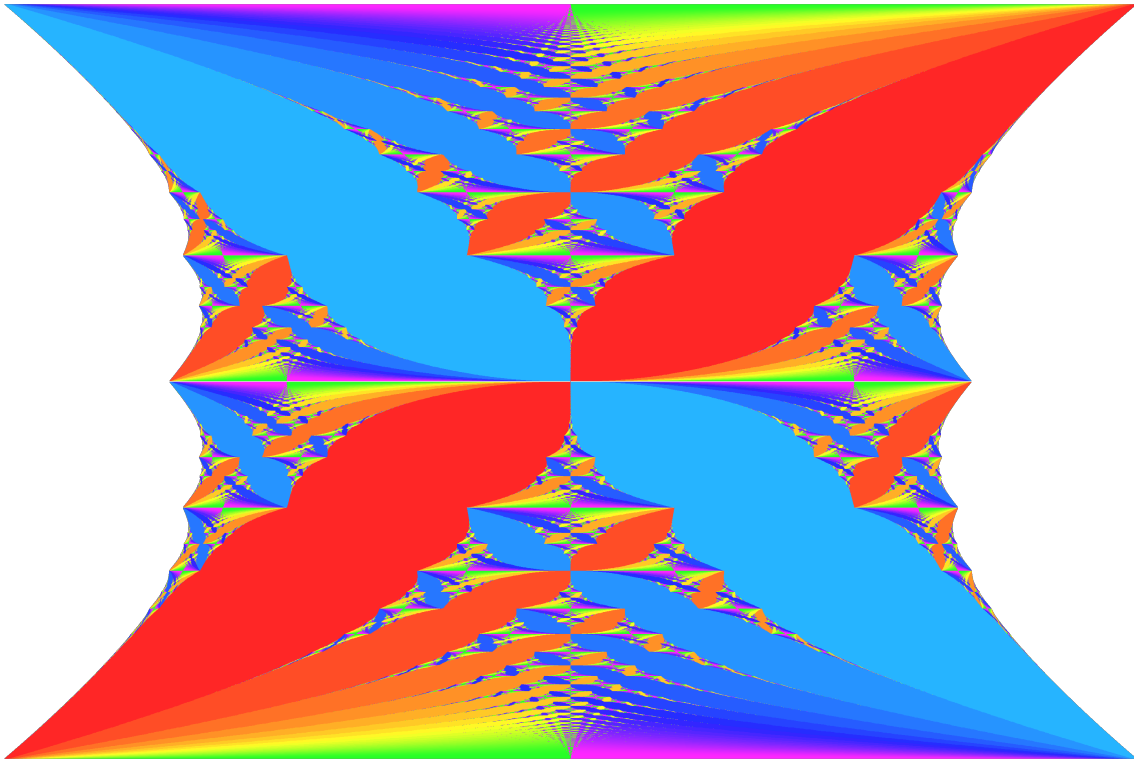


Figure 1.5: The coloured butterfly, from Avron [2003], shows energy gaps coloured according to the quantized values of the Hall conductance. The axes are the same as in Fig. 1.2. Warm colours indicate positive Chern numbers, and cool colours negative. Zero Hall conductance is left blank. Copyright © 2004, Springer Basel AG.

Inserting Eq. (1.35) into the Stréda formula, we get that the conductance is:

$$\sigma_{xy} = -e \frac{\partial}{\partial \Phi} (\theta t_r + s_r) = -\frac{e^2}{h} t_r, \quad (1.37)$$

having used that $\theta = \Phi/\Phi_0$ and $\Phi_0 = h/e$.

This result tells us that the Hall conductivity is:

$$\boxed{\sigma_{xy} = -\frac{e^2}{h} t_r}, \quad (1.38)$$

with $t_r \in \mathbb{Z}$ being a solution of the Diophantine equation. This expression is valid if we assume that the density n_e is a differentiable function of the magnetic flux. Also both s_r and t_r must be independent of the magnetic field, which is quite reasonable to assume, since they are integers and cannot depend on a quantity that can be infinitesimally tuned.

1.5.3 Chern number of the Harper-Hofstadter bands.

Comparing the conductance in Eq. (1.32) with the one obtained from the Stréda formula and the Diophantine argument in Eq. (1.38), we see that:

$$\boxed{t_r = -\sum_{\nu=1}^r C_\nu}. \quad (1.39)$$

This equation means that to each of the q bands of the Harper-Hofstadter model we can associate a topological invariant C_ν , such that Eq. (1.39) is a solution of the Diophantine equation (1.33). In

Fig. 1.5, we show each energy gaps of the Hofstadter butterfly coloured according to the quantized values of the Hall conductance, t_r . We shall now see how from these very simple arguments, the Hall conductance and the Chern number of all the Harper-Hofstadter bands can be easily obtained.

The same results can be also obtained numerically, following the method proposed by Fukui et al. [2005]. This method relies on the calculation of the Berry curvature from the eigenvectors of Eq. (1.22) on a grid in quasi-momentum space and summing over the discretized Brillouin zone to obtain the Chern number of the non-degenerate bands from Eq. (1.29).

Chern numbers for $\theta = 1/3$.

Consider, for example a flux of $\theta = 1/3$, which corresponds to $p = 1$ and $q = 3$. From the condition of existence of a unique solution to the Diophantine equation, we must have $r \leq 3$ and $|t_r| \leq 3/2$, that is $t_r = 0, \pm 1$ since $t_r \in \mathbb{Z}$. Consider the first gap $r = 1$. The solution to Eq. (1.33) is $t_r = 1, s_r = 0$, which from Eq. (1.39) implies that $C_1 = -1$. Now assume $r = 2$: the Diophantine equation is satisfied for $t_r = -1, s_r = 1$, and from Eq. (1.39) we have $C_1 + C_2 = 1$. Finally, for $r = 3$, we must have $t_r = 0, s_r = 1$, corresponding to $C_1 + C_2 + C_3 = 0$. From all these arguments, the Chern numbers of the single bands are straightforwardly obtained:

$$C_1 = -1, C_2 = 2, C_3 = -1.$$

Chern numbers for $\theta = 1/4$.

For a flux of $\theta = 1/4$, we must have $r \leq 4$ and $|t_r| \leq 2$. As for before, for the first gap $r = 1$ we obtain $s_r = 0$ and $t_r = 1$, leaving us with $C_1 = -1$. For $r = 2$, an interesting thing happens. In fact, a unique solution of the Diophantine equation does not exist, since $s_r = 0, t_r = 2$ and $s_r = 1, t_r = -2$ are both satisfying Eq. (1.33). This is because for even qs , the two middle bands are not really separated by a gap, as is visible also in Fig. 1.3. Instead the bands touch at a finite number of points in momentum space with a linear dispersion; consequently these points are called *Dirac points*. The finite number of degenerate points between bands is enough to invalidate the predictions from the Diophantine equation, which can therefore only predict the sum of the two Chern numbers of the two bands together. In fact, for $r = 3$, we have $C_1 + C_2 + C_3 = 1$, meaning that $C_2 + C_3 = 2$. Finally, as we know, the four Chern numbers add up to zero, leaving us with $C_4 = -1$. In the end we have:

$$C_1 = -1, C_2 + C_3 = 2, C_4 = -1.$$

1.5.4 The bulk-edge correspondence.

In the previous sections, we have obtained that the Hall conductance of a bulk insulator, with the Fermi energy in the band-gap between Hofstadter bands, is non-zero and quantized. It may seem to be an apparent contradiction, but it is easily explained from the energy dispersion of a finite system. In fact, even though the system is a bulk insulator, it has gap-less edge modes across the bulk gaps that carry a non-zero current from one edge to another. These states are contributing to the Hall conductance Bernevig [2013], and therefore their number in a given gap is equal to:

$$N_{\text{edge states}} = \left| \sum_{E_\nu < E_F} C_\nu \right|. \quad (1.40)$$

The chirality of these edge states is set instead by the sign of the sum of the Chern numbers of the occupied bands, where -1 means that a certain edge state is counter-clock wise circulating in a planar geometry, while $+1$ means that the edge state is clock wise circulating.

The presence of states in the band gap is evident in Fig. 1.6, where we plot the energy, in units of J , of a finite system with N_y sites along the y direction and infinite (periodic boundary conditions) along the x direction. The energy dispersion is represented as a function of the quasi-momentum along k_x for different values of the magnetic flux θ .

The left panel of Fig. 1.6 shows the energy spectrum for $\theta = 1/3$: we see that the three bands are connected by energy levels, highlighted in red. The wave functions associated to these states are localized on the two opposite edges of the system, and have opposite velocity, meaning that they are chiral. In fact, from Eq. (1.40) we have that the lowest gap has one edge state with

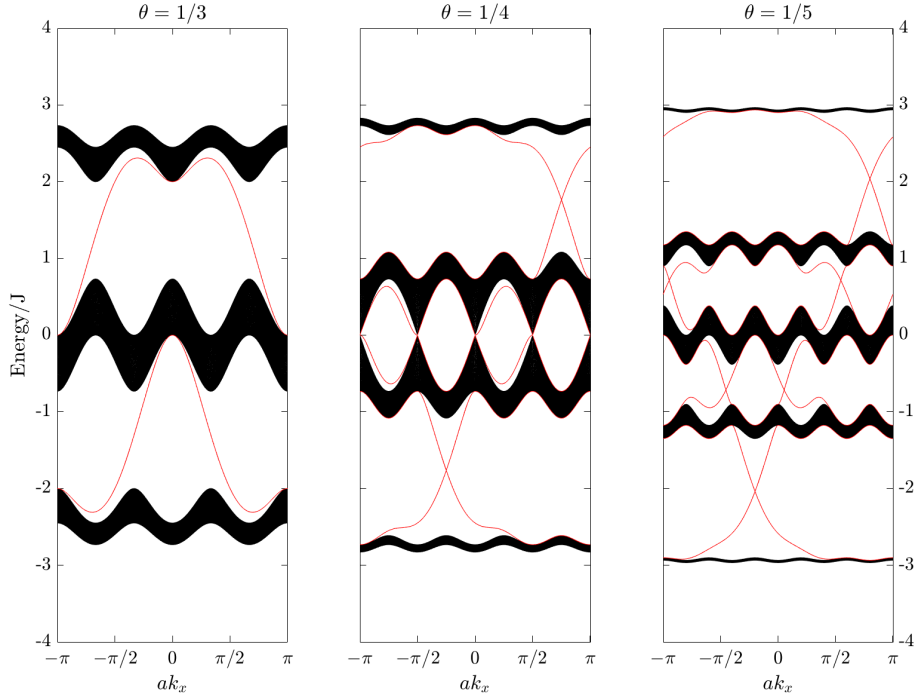


Figure 1.6: Energy dispersion, in units of J , as a function of the quasi-momentum along k_x for different values of the magnetic flux θ of a semi-infinite system, with N_y sites along the y direction. The energy levels corresponding to states localized on the edges of the system are highlighted in red. Panels from left to right: $\theta = 1/3, 1/4, 1/5$.

counter-clock-wise chirality -1 . The higher gap has again a single edge state but an opposite chirality $+1$.

Edge states are found also in the central panel, for $\theta = 1/4$; we also see that the two middle bands are touching at Dirac points, hence the gap is not defined, though localized edge states exist. Again, the lowest gap has one edge state with counter-clock-wise chirality -1 , while the higher gap has one edge state with clock-wise chirality $+1$.

The band dispersion for $\theta = 1/5$ is represented in the last panel of Fig. 1.6. From Eq. (1.40), it is easy to check that the numbers of edge states in the band gaps (lower to higher) are: 1, 2, 2, 1. This is exactly what we see from the numerical band dispersion. Additionally, the chiralities are negative for the edge states in the two lower gaps and positive for the remaining states.

These edge states are one-way propagating along the edge and are topologically protected from disorder, since there is no other state available for backscattering, an important fact that underlies the perfectly quantized transport of the quantum Hall effect. The chiral edge states that are found in the forbidden gaps between the bands of the Harper-Hofstadter model represent the smoking gun of a non-trivial topological system.

Having used the Harper-Hofstadter model as a concrete example to introduce the physics of the quantum Hall effect, we are now going to review some of the methods that are used in the literature to implement such topological systems also in artificial materials.

Chapter 2

Artificial fields in artificial systems.

There are more things in Heaven and Earth,
Horatio, than are dreamt of in your philosophy.

William Shakespeare – *Hamlet*.

Since topological concepts were first introduced by Thouless et al. [1982] to understand the behaviour of electrons in the integer quantum Hall effect, *topology* itself has become a powerful theme in condensed matter physics, applicable to a wide-range of different systems. These systems are generally called *topological insulators*, as reviewed by Hasan and Kane [2010], Qi and Zhang [2011] and Lu et al. [2014]. A topological insulator is characterized by electronic bulk bands separated by energy gaps in which gap-less states live. Such states are localized on the edge of the system and are topologically protected, *i.e.* they are robust against any perturbations that do not close the energy gaps. The presence of the edge states is also related to robust bulk physics, such as the precise quantisation of the Hall conductance introduced in the previous Chapter.

While the study of real materials is usually complicated, the essential physics of various topological phenomena can be captured through simple lattice models. We have seen in Chapter 1 one of the most famous of these models: the Harper-Hofstadter model. Not only does this model exhibit the quantum Hall effect thanks to its topological energy bands and unidirectionally-propagating edge states, but it has a rich fractal energy spectrum. However, the direct realization of such a model in real crystalline solids with a real magnetic field is almost impossible, since the magnetic field required for the generation of a flux per plaquette of the order of the flux quantum is out of reach with the current technology. For example, if one wanted to achieve a flux of $\theta = 1/10$ in some material which has typical lattice constant $a = 5\text{\AA}$, the required magnetic field is of the order of $B = 1600\text{ T}$, that is too high to be experimentally generated¹. Only with the help of solid-state superlattice devices, studies by Dean et al. [2013], Yu et al. [2014], Ponomarenko et al. [2013] have reported the realization of self-similar energy structures analogous to the Hofstadter butterfly.

Recent advances in *quantum simulators* have proven that artificial systems are well-suited to study a whole variety of condensed matter Hamiltonians and explore their physical properties over a much wider range of parameters than is possible in real materials, as reviewed in the *Nature Physics Insight* [2012] or by Carusotto and Ciuti [2013], Georgescu et al. [2014]. A quantum simulator is a quantum system that mimics a quantum model, as proposed by Feynman [1982], and can have huge advantages compared to a natural material. For example, many lattice geometries can be engineered with a high degree of experimental control. The lattice depth can be changed freely, and also the interaction strengths are precisely controllable. These synthetic materials also provide access to physical observables typically not attainable in solid-state experiments, and a very intriguing possibility is the implementation of novel effective Hamiltonians, that can be tailored through some suitable temporal modulations of the system. For all of the above reasons, artificial

¹The strongest pulsed magnetic field yet obtained in a laboratory is $B = 730\text{ T}$ Nakamura et al. [2012]

systems constitute promising candidates to gain deeper insights into the rich physics of topological materials.

However, many of these systems are based on neutral objects such as atoms, photons or even classical harmonic oscillators, meaning that the simple application of a magnetic field is not enough to observe neither magnetic nor topological effects. Hence there is the need for the realization of an “*artificial gauge field*” acting on neutral particles, as has now been made possible by important interdisciplinary developments, as reviewed for example in [Raghu and Haldane \[2008\]](#), [Dalibard et al. \[2011\]](#), [Goldman et al. \[2014, 2015a\]](#). The fundamental idea relies on making neutral objects behave like charged particles immersed in a real magnetic field.

It is important to notice, at this point, the relation between the real magnetic field and time reversal symmetry in electronic systems. In fact, the presence of a real magnetic field breaks explicitly time reversal symmetry, therefore if one wants to simulate an artificial field, the desired Hamiltonian must also break time reversal symmetry, *i.e* it must not commute with the time reversal operator, that is $\mathcal{T}t \rightarrow -t$. Besides, from the study of topological phases, [Schnyder et al. \[2008\]](#) showed that, in two-dimensional systems, time reversal symmetry breaking is needed for achieving a topological phase characterized by a \mathbb{Z} -invariant, such as the Chern number in the integer quantum Hall effect.

When the Hamiltonian is instead time reversal symmetric, we can obtain a topological phase characterized by a \mathbb{Z}_2 -invariant, provided there are no other symmetries, such as *particle-hole* symmetry or *chiral* symmetry. In the presence of a spin-orbit coupling, one example of such a topological phase is the *quantum spin Hall effect*, as first theorized by [Kane and Mele \[2005a,b\]](#). Such a quantum spin Hall system consists of two copies of an integer quantum Hall system, where if the spin-up electron has a clock-wise edge state, the spin-down one exhibits an anti-clock-wise edge state. This results in a quantized spin Hall conductance and a vanishing charge Hall conductance. The edge states participating to the spin Hall conductance are protected by the time reversal symmetry, therefore this effect appears in absence of a real magnetic field, that would destroy it. In fact, the edge states of the quantum spin Hall effect are not robust against a disorder which breaks the time reversal symmetry. However, the same spin Hall effect can be reproduced by creating an artificial magnetic field that has opposite sign for the two spin components, such that the net magnetic flux is zero and time reversal symmetry is preserved.

In the following, we shall review only some of the most relevant strategies employed for simulating an artificial gauge field and achieving topological effects in various artificial systems.

2.1 Artificial systems.

Ultracold atomic systems. Ultracold gases play a central role among quantum simulators, thanks particularly to the high level of flexibility and control of experimental parameters that is possible in these set-ups [Bloch et al. \[2008\]](#). Ultracold systems consist of dilute gases of atoms cooled to extremely low temperatures, where quantum effects can play a crucial role in describing the properties of the atoms themselves [Pitaevskii and Stringari \[2016\]](#). Usually, the neutral atoms are trapped in a harmonic potential and subjected to an additional periodic optical lattice potential; both of these potentials are created by interfering laser beams. The spacing, depth and geometry of an optical lattice can be freely tuned, and therefore a huge variety of lattice models can be easily implemented. For many atomic species, it is also possible to tune the interactions between atoms through Feshbach resonances. The properties of ultracold gases, such as their momentum distribution and quantum coherence, are typically obtained through the “time-of-flight” technique, which consists of imaging a gas after it is allowed to freely expand, once all trapping potentials are removed, see [Bloch et al. \[2008\]](#). Recent advances have also lead to the implementation of “quantum gas microscopes” which can access single-site and single-atom resolved density distributions of atoms in optical lattices [Sherson et al. \[2010\]](#), making the observations of these system possible also in-situ. Though the description of such systems is not the purpose of this thesis, it is useful to have a brief overview of the methods used in ultracold atoms for the realization of an artificial gauge field. For a more complete review, one could see [Dalibard et al. \[2011\]](#).

Photonic systems. Photonics are another excellent system for the simulation of a variety of topological lattice models. These systems are realised by manipulating photons in a wide-range of different scenarios, such as in free space, fibres, dielectrics, or cavities, with many interesting effects, as reviewed by [Carusotto and Ciuti \[2013\]](#). For some of these photonics systems, such as, for

example, arrays of evanescently-coupled waveguides, the system is described by a paraxial equation which has the same form as a Schrödinger equation except where the role of time is played by the propagating coordinate along the waveguide. For some other systems, instead, the evolution of the system is intrinsically driven-dissipative, allowing for a spectroscopic analysis. A great advantage of this spectroscopic technique is the immediate and direct imaging of the wave function, together with the excitation of any desired state by simply driving the system in a specific frequency band. In parallel with the advances in the ultracold community, there have also been studies in the photonics context focussed on the realization of artificial fields. The first works in this direction were by [Haldane and Raghunathan \[2008\]](#) and [Raghunathan and Haldane \[2008\]](#), who theoretically proposed a photonic crystal made from nonreciprocal (Faraday-effect) constituents that break time-reversal symmetry, showing that the crystal can act as a chiral waveguide. This was quickly experimentally realized by [Wang et al. \[2009\]](#) setting off the field of topological effects in photonics, that was further explored with many recent developments, as we shall see in the following.

Classical systems. Coupled classical harmonic oscillators, such as pendula connected by a spring or coupled RLC electrical circuits, are simple but fundamental objects in physics, familiar to everyone. For obvious reasons, they do not represent a quantum simulator, but during the preparation of this thesis, novel works have shown that the hallmarks of a topological insulator can be also found in purely classical systems. For example, recently [Kane and Lubensky \[2014\]](#), [Paulose et al. \[2015\]](#) showed that in mechanical meta-materials there can be topological soft modes, which are protected against local perturbations. This is because a non-trivial topology is encoded in the dynamical matrix or into the Hamiltonian of the system. Similar works have been done also by [Nash et al. \[2015\]](#), [Wang et al. \[2015a\]](#), in which the time-reversal symmetry is intrinsically broken by the use of coupled gyroscopes. In the following, we will discuss other classical systems with artificial gauge fields and topological properties that provide particularly relevant context to our own work.

2.2 The minimal coupling.

The minimal coupling is the appropriate method for taking into account the interaction between the electromagnetic gauge field with a charged particle in free space. It is implemented by modifying the momentum of a particle of charge e as:

$$\vec{p} \rightarrow \vec{p} - e\vec{A}, \quad (2.1)$$

where $\vec{B} = \vec{\nabla} \times \vec{A}$ as usual. The Peierls phase of the Harper-Hofstadter model, as we have seen in the previous chapter, is a consequence of the minimal coupling when the particle moves on a lattice.

One of the strategies used for simulating an artificial gauge field for neutral particles is therefore to engineer an Hamiltonian in which the minimal coupling in the form of Eq. (2.1) is present.

2.2.1 Rotation.

One of the first procedures to be proposed – thanks to its conceptual simplicity – for the generation of an artificial gauge field, is the exploitation of the formal analogy between the Coriolis force arising in a rotating frame at angular velocity $\vec{\Omega} = \Omega\vec{z}$ and the Lorentz force of magnetism. In fact, the Hamiltonian of a single particle in the rotating frame is [\[Dalibard, 2015\]](#):

$$\hat{\mathcal{H}} \rightarrow \frac{(\vec{p} - m\vec{\Omega} \times \vec{r})^2}{2m} + \frac{1}{2}m\omega^2 r^2 - \frac{1}{2}m\Omega^2 r^2, \quad (2.2)$$

where ω is the frequency of a harmonic trapping potential, which is usually present to trap ultracold atoms. The last term is the centrifugal force. The kinetic term in Eq. (2.2) has the same form as in Eq. (2.1) where the artificial gauge field is $e\vec{A} \equiv m\vec{\Omega} \times \vec{r}$.

[Madison et al. \[2000\]](#) and [Abo-Shaeer et al. \[2001\]](#) studied an ultracold gas confined in a 2D harmonic potential. The gas was put in rotation by stirring it with lasers or by rotating directly the harmonic trap. The creation of the artificial gauge field was confirmed by the formation

of quantized vortices in the rotating superfluid gas above a critical rotation frequency [Cooper, 2008]. These vortices ordered into an Abrikosov lattice and their number increased as the artificial magnetic field became larger, *i.e.* as the velocity of rotation increased. However, the presence of the centrifugal force modifies the trapping potential and limits the rate of rotation which in turn limits the maximum magnetic field that can be achieved. If the angular velocity exceeds the *centrifugal limit*, the gas is no longer confined and the atoms fly apart.

The rotation method was also very recently considered theoretically in a classical mechanical system of masses and springs arranged in a honeycomb lattice structure by Wang et al. [2015c] and Kariyado and Hatsugai [2015]. In both works the phonon dispersion showed chiral topologically protected edge states arising from the creation of an artificial magnetic field.

2.2.2 Strain.

The minimal coupling in the form as in Eq. (2.1) is usually implemented for a particle in free space. However, there are some lattice systems, such as, for example, the carbon allotrope known as graphene, in which the tight-binding Hamiltonian expanded around a highly symmetric point can be rewritten in the same form of a kinetic term for a free Dirac particle. For these lattice systems, the artificial gauge field is then implemented via a static modulation of some system parameters that results in a new Hamiltonian which has the form as in Eq. (2.1). If the time-reversal symmetry is not broken in these systems, the artificial gauge field is then known as an artificial *pseudo-gauge field*. For example, a beautiful result from the theory of electron motion in a honeycomb lattice is that the effect of a deformation of the material along the crystallographic axes can be described as an artificial pseudo-magnetic field. This effect was predicted by Kane and Mele [1997] for the elastic distortion as produced by mechanically straining a carbon nanotube. Remarkably, as we shall see further on in Chap. 6 and Chap. 7, the peculiar energy dispersion of graphene is such that the low-energy modes stemming from the pseudo-magnetic field are relativistic Landau levels.

Among the realizations with artificial systems, Rechtsman et al. [2013c] was the first to produce a pseudo-magnetic field in a strained photonic lattice, and to indirectly probe the existence of the Landau levels from the localized edge modes that reside in the energy-gaps. We have proposed in Salerno et al. [2015] an alternative photonic set-up for observing the Landau levels with intrinsically driven-dissipative photonic systems, and use spectroscopic techniques to characterize also their wave functions. A recent work by Tian et al. [2015] proposed, for ultracold atoms in a strained hexagonal optical lattice, the observation of Bloch oscillations and cyclotron motion resulting from the formation of Landau levels.

2.3 The Peierls phase.

The effect of a real magnetic field on a charged electron moving on a lattice, as we have also seen in Chapter 1 in the case of the Harper-Hofstadter model, is to modify the tight-binding tunnelling amplitude by adding a complex spatially-dependent phase, called the Peierls phase:

$$J_{1,2} \rightarrow J_{1,2} e^{ie/\hbar \int_{\vec{R}_1}^{\vec{R}_2} \vec{A} \cdot d\vec{r}}. \quad (2.3)$$

where 1 and 2 label two adjacent lattice sites. Vice versa, if a charged particle experiences a non-trivial phase when hopping on a lattice, then we can say it is subjected to a gauge field \vec{A} , such that Eq. (2.3) is valid, via the so called *Peierls substitution*. Regardless of the origin of such a phase, the particle will behave as it was charged and subjected to a gauge field. The route to the simulation of a magnetic lattice model with a neutral system, therefore, passes through the search of a mechanism alternative to a real gauge field to generate the suitable complex hopping phase.

2.3.1 Using internal degrees of freedom.

One of the first proposals to achieve an artificial magnetic field was theorized for neutral atoms in optical lattices by Jaksch and Zoller [2003]. They assumed that there were two distinct internal states of the atoms, trapped in alternating columns of the lattice, such that the tunnelling along one direction of the lattice was only possible with the help of laser beams, that are used to coherently transfer atoms from one internal state to the other. This is called *laser assisted tunnelling*, and the hopping amplitude in the Hamiltonian can acquire a Peierls phase that is freely set by these

laser beams. By appropriately adjusting the laser parameters, a non-trivial artificial magnetic flux can be generated across the plaquettes of the lattice. This proposal inspired the experimental realisation of [Aidelsburger et al. \[2011\]](#), who combined laser assisted tunnelling with a two-site superlattice to create a staggered flux, leading to the observation of the quantum cyclotron orbit of single atoms.

Two related experiments by [Mancini et al. \[2015\]](#) and [Stuhl et al. \[2015\]](#) used the laser assisted tunnelling to achieve a Peierls phase along a *synthetic dimension*, represented by the various spin states of the atoms, and implementing an artificial magnetic field that lead to the realization of a Hall system. By measuring the momentum of each spin state with the time of flight technique, they proved the existence of chiral edge states.

In photonics, a recent work by [Ozawa et al. \[2015\]](#) proposed a way to use this idea of the synthetic dimension to engineer gauge fields in integrated photonics set-ups of various dimensions. In fact, their scheme allows for the generation of a variety of topological phenomena, such as, for example, a topologically-robust optical isolator in a spatially one-dimensional ring-resonator chain and a driven-dissipative analogue of the four-dimensional quantum Hall effect in a spatially three-dimensional resonator lattice.

2.3.2 Floquet-based systems.

In these systems, we start by considering a periodic time-dependent Hamiltonian $\hat{\mathcal{H}}(t+T) = \hat{\mathcal{H}}(t)$ where $T = 2\pi/\omega$ is the period. From the Floquet theory of periodic systems [[Shirley, 1965](#), [Bukov et al., 2015](#)], it can be shown that $\hat{\mathcal{H}}(t)$ has a complete set of solutions to the time-dependent Schrödinger equation in the form:

$$|\psi_n(t)\rangle = e^{-i\varepsilon_n t/\hbar} |u_n(t)\rangle,$$

where the functions $|u_n(t)\rangle = |u_n(t+T)\rangle$ have the same periodicity as the Hamiltonian. Floquet theory can be viewed as Bloch's theory for time-periodic Hamiltonian. These new Floquet states $|u_n(t)\rangle$ are the eigenvectors of the Floquet operator $\hat{\mathcal{H}}(t) - i\hbar\partial_t$:

$$\left(\hat{\mathcal{H}}(t) - i\hbar\partial_t\right) |u_n(t)\rangle = \varepsilon_n |u_n(t)\rangle.$$

As in Bloch's theory where the quasi-momenta are defined in the Brillouin zone, the eigenvalues ε_n are the quasi-energies of the system and are periodically defined $\varepsilon_n = \varepsilon_n + m\hbar\omega$, up to an integer times of $\hbar\omega$. The Floquet basis can be used to solve the problem and map the time-dependent Hamiltonian onto an effective time-independent one.

Floquet theory can be used as an excellent tool for engineering new lattice models. In fact, if the original Hamiltonian has a *temporal modulation* of some system parameters that explicitly breaks time-reversal symmetry, then we can design an effective topological time-independent Hamiltonian, whose tunnelling amplitudes implement the Peierls phase.

For ultracold atoms, the periodic modulation of the optical lattice was already proven to rescale the tunnelling amplitude of the Bose-Hubbard model [Eckardt et al. \[2005\]](#), [Eckardt and Holthaus \[2007\]](#), [Eckardt et al. \[2009\]](#). By applying the aforementioned Floquet theory, the system in which the lattice potential is shaken, is effectively described, in the co-moving frame, by a new Hamiltonian with a renormalised hopping amplitude. Subsequent studies have shown that, by a suitable modulation of the lattice that breaks the time-reversal symmetry, the hopping element can be made complex: [Struck et al. \[2012\]](#) used the double harmonic shaking shown in [Fig. 2.1](#), to implement a Peierls phase for ultracold atoms.

An even more elaborate modulation is used in [Jotzu et al. \[2014\]](#) for the realization of the *Haldane model* by [Haldane \[1988\]](#) on a shaken honeycomb optical lattice for ultracold atoms, in which the next-nearest-neighbours coupling is complex (rather than the first-nearest one). Related works on shaking of a triangular optical lattice studied frustrated magnetism [[Sacha et al., 2012](#)], a non-abelian gauge field [[Hauke et al., 2012](#)] and implemented the Ising-XY model [[Struck et al., 2013](#)].

A proposal by [Kolovsky \[2011\]](#) introduced a periodic modulation of a tilted optical lattice for ultracold atoms, combining this with a laser assisted tunnelling to generate the required Peierls phase. The tilting of the lattice suppresses the tunnelling, while the modulation through the shaking of the lattice restores a complex hopping, whose phase depends on the phase of the shaking. However, a comment by [Creffield and Sols \[2013\]](#) showed that this proposal produces a field that

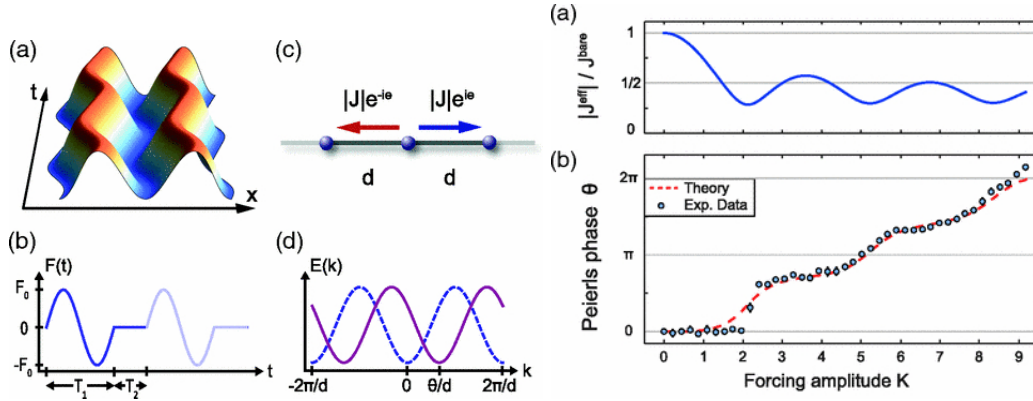


Figure 2.1: From [Struck et al. \[2012\]](#). On the left, periodic driving of the optical lattice for neutral gases, shown in (a). The forcing that shakes the lattice breaks time-reversal symmetry (b) and creates a Peierls phase (c), which also shifts the single particle dispersion relation (d) used to experimentally measure the Peierls phase. On the right, measured effective tunnelling, in absolute value (a) and phase (b), as a function of the amplitude of the modulation. Copyright © 2012 American Physical Society.

is constant only over a finite number of lattice cells. The idea was improved and extended to superlattices with resonant modulations by [Goldman et al. \[2015b\]](#). [Aidelsburger et al. \[2013\]](#) and [Miyake et al. \[2013\]](#) applied such a technique and both groups were able to experimentally realize the Harper-Hofstadter model with ultracold atoms in optical lattices.

In photonics, [Fang et al. \[2012\]](#) proposed a system of resonators in which the temporal modulation is applied to the coupling and the gauge field is controlled by the spatial distribution of the modulation phases. They discuss possible implementations with crystal resonators in the optical range or RLC resonators in the microwave range, to observe the chiral edge states.

[Rechtsman et al. \[2013b\]](#), instead, used a system made of coupled helical waveguides arranged in an hexagonal array, which is described by the paraxial equation that was mentioned above. In this system, the spatial coordinate for the light travelling along the waveguide – that is perpendicular to the two-dimensional hexagonal lattice – is equivalent to time for a particle in a lattice. Following this analogy, the shaking of the potential is implemented as an helical shaping of the waveguide profile, that is shown in the left part of Fig. 2.2. The helical shaping breaks explicitly time reversal symmetry, leading to the realization of a gauge field for photons. Since the temporal modulation is not fast compared to the other frequencies of the system, it is not possible to derive an effective Hamiltonian as was later done in [Jotzu et al. \[2014\]](#), though the system shares the same topology of the Haldane model. As a result, the system is a Floquet topological insulator, with topologically protected edge states living in the energy bulk gaps. The existence of these edge states was experimentally proven by sending light through the system and collecting the light emerging at the end of the waveguides. These results are reported in the right part of Fig. 2.2, clearly showing that light moves along the edge and does not scatter into the bulk.

As an extensive part of the work carried out in this thesis, in [Salerno and Carusotto \[2014\]](#) we used a temporal modulation to break time reversal symmetry and implement a Peierls phase for coupled pendula. By applying a gradient of frequencies of the pendula, in [Salerno et al. \[2016\]](#) we also achieved an artificial magnetic field and the topological Harper-Hofstadter model. Comprehensive details about our proposal are given in the following Chapters.

2.3.3 Geometrical implementation.

The desired coupling phase can be also be engineered into the system either with some clever hard-wiring of the connections, or by using some intermediate objects between the neighbouring sites that encode a Peierls phase that itself depends on some degrees of freedom of the system. In these types of systems, time-reversal symmetry is usually not broken and instead two copies of the quantum Hall effect are realized for two degrees of freedom, that act as “pseudo-spins”. The resulting chiral edge states are not protected against perturbations which flip the pseudo-spin, as is the case in the quantum spin Hall effect.

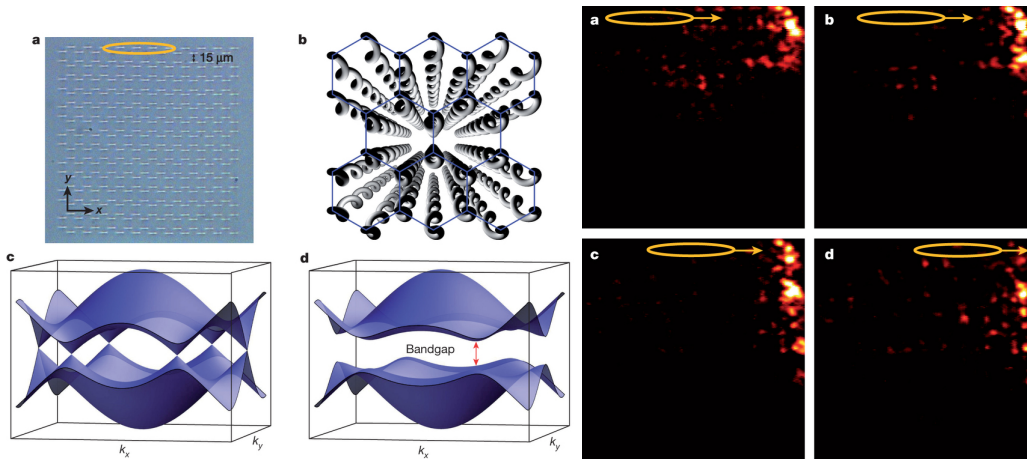


Figure 2.2: From [Rechtsman et al. \[2013b\]](#). On the left, geometry of the photonic lattice (a), and sketch of the helical waveguides in (b). For straight waveguides, the gapless band dispersion is shown in (c). For the helical waveguides, a gap is opened (d), supporting edge states. On the right, experimental evidence of the topological edge states living in the bulk energy gap. Light is sent in the system at the position highlighted by the yellow ellipse, which is moved progressively to the right (a-d), showing that the emerging beam moves accordingly along the edge and does not scatter into the bulk. Copyright © 2013, Nature Publishing Group.

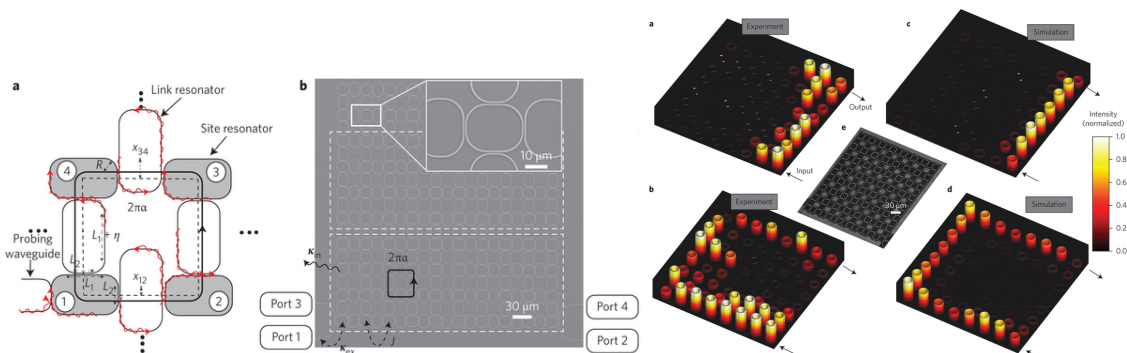


Figure 2.3: From [Hafezi et al. \[2013\]](#). On the left, in (a) sketch of the single plaquette, showing the link resonators (in white) between the site resonators (in grey). In (b), real image of the photonic lattice. On the right, chiral edge state propagation, as they result from the experiment (a-b) compared to the numerical simulations (c-d). Copyright © 2013, Nature Publishing Group.

A theoretical proposal by [Umucalilar and Carusotto \[2011\]](#) considered the implementation of a gauge field for photons in optical cavities, by exploiting the (circular) polarization of light, which acts as a pseudo-spin. The Peierls phase is then acquired by the photon as it passes through an active optical medium or a particular geometrical arrangement of the mirrors forming the optical cavities. Additionally, circularly birefringent layers are needed to protect the system from unwanted pseudo-spin flips.

A similar proposal and subsequent experiments in [Hafezi et al. \[2011, 2013\]](#), [Mittal et al. \[2014\]](#) realized a hopping Peierls phase for photons in ring resonator arrays. In this scheme, ring resonators (sites) are coupled through another off-resonant ring resonator (links), as seen in Fig. 2.3. Due to a resonance mismatch, the light is confined in the site rather than in the link, whose only purpose is to let the photon acquire a hopping phase that depends on the position of the links. The pseudo-spin is the clockwise or anti-clockwise circulation of the light in the rings. To avoid backscattering processes, directional couplers are used in the coupling regions, allowing for the experimental observation of chiral edge states, reproduced in the right part of Fig. 2.3.

Another example of a spin-dependent gauge field is realized experimentally in a system of classical coupled RLC circuits, by [Ningyuan et al. \[2015\]](#). In this system, the spin state is encoded in two equivalent inductors on each lattice site, and the coupling phase is provided by a latticework of wires and capacitors, realizing a net artificial magnetic flux that is opposite for the two pseudo-

spins. One of the beauties of this configuration is that, with a suitable wiring, it realizes a Möbius topological insulator, by exploiting the pseudo-spin flip at the edges to achieve a single chiral edge state. A related theoretical work by [Albert et al. \[2015\]](#), using classical coupled RLC circuits, generalizes the procedure of the intersite wiring to achieve an arbitrary hopping phase.

Similar ideas are also found in the classical mechanical context of the experiment by [Süsstrunk and Huber \[2015\]](#), where a clever arrangement of springs allowed for the realization of an artificial magnetic flux for coupled pendula. Also in this case, the pseudo-spins, realized by using two pendula on a single site, experience opposite artificial magnetic fields, thus the system is the classical analogue of a quantum spin Hall.

Chapter 3

The Peierls phase for coupled pendula.

Despite the huge interest for the simulation of topological phenomena with artificial quantum systems, the interplay of topology and the classical world is not yet well-understood and is only just beginning to open up a brand-new field of research. Our goal is to show that the features of a topological insulator are not the prerogative of quantum mechanics, but can be also observed with a classical system governed by Newton's equations.

In this Chapter we start by describing how the very simple and familiar physics of a pair of coupled classical harmonic oscillators can be related to the quantum mechanical world. We show that Newton's equations of motion, in a certain regime, can be put in the same form as Heisenberg's equations of motion written for a quantum tight-binding Hamiltonian, by replacing commutators with Poisson brackets. This analogy will then be exploited to introduce established concepts of quantum mechanics in the context of classical physics, such as the implementation of a non-trivial coupling phase between two classical harmonic oscillators, that constitutes the classical analogue of the Peierls phase acquired by a quantum particle hopping on a lattice immersed in a magnetic field. As we have seen, the generation of such a Peierls phase would allow us to achieve a magnetic lattice model, such as the Harper-Hofstadter model of Chap. 1, in a classical mechanical context.

The key element that we have implemented in our theory, is time reversal symmetry breaking through a temporal modulation of the system parameters, as introduced briefly for other systems in Chap. 2. The Floquet method, in fact, is a powerful and flexible method for engineering a particular Hamiltonian starting from the system at one's disposal and to induce non-trivial dynamical effects. In the following, we will define a *temporal modulation* of the natural frequencies of the coupled classical harmonic oscillators and study the effective dynamics of the system. We anticipate a *dynamical decoupling* effect, where exchange of energy between the pendula is suppressed. This phenomenon is analogous to the coherent destruction of tunnelling of a quantum particle in a double-well potential, [Großmann et al., 1991, Grifoni and Hänggi, 1998, Lignier et al., 2007, Kayanuma and Saito, 2008, Zenesini et al., 2009]. When the pendula are driven by an external force, we anticipate a novel *dynamic isolation* effect, where the temporal modulation effectively decouples the system from the external force. Most importantly, we demonstrate that a tunable non-trivial coupling Peierls phase between the pendula can be implemented.

The main results of this Chapter are published in Salerno and Carusotto [2014].

3.1 Temporal modulation of classical harmonic oscillators.

We consider a system of two identical coupled pendula, modelled as a pair of coupled harmonic oscillators of equal masses m . Within the small-oscillation regime, the displacements are much smaller than the length L of the pendula and therefore the equations of motion can be linearised. The spatial displacements of the pendula from the equilibrium position are indicated as $x_{1,2}$ respectively. The two pendula, taken separately and isolated, have the same natural oscillation frequency, equal to $\omega_0 = \sqrt{g/L}$. All possible friction mechanisms acting on the two pendula are

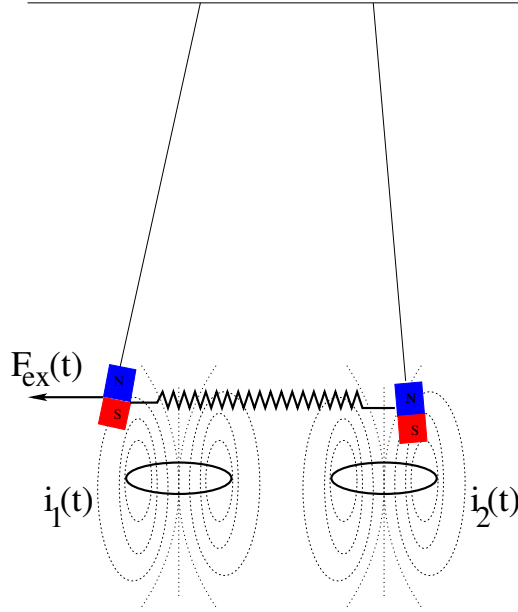


Figure 3.1: Sketch of the physical system described by Eqs. (3.1) and one of the possible realizations of the temporal modulation of the natural oscillation frequencies of the pendula. The two pendula are coupled through a spring and each contains a magnet that interacts with the magnetic field generated by a coil. The specific form of the modulation is controlled by the time-dependent current $i_{1,2}(t)$ flowing in the corresponding coil. The first pendulum may be externally driven by a time-dependent force $F_{\text{ex}}(t)$, for later purposes.

assumed to have the constant value ξ , that is equal for the two oscillators. The coupling between the pendula occurs via a spring of constant k and the restoring force of the spring is proportional to the displacements of the two pendula according to Hooke's law.

Newton's equations of motion are written as:

$$\begin{aligned}
 m \dot{x}_1 &= p_1 \\
 \dot{p}_1 &= -m\omega_1^2(t) x_1 + k(x_2 - x_1) - \xi \dot{x}_1 \\
 m \dot{x}_2 &= p_2 \\
 \dot{p}_2 &= -m\omega_2^2(t) x_2 + k(x_1 - x_2) - \xi \dot{x}_2.
 \end{aligned} \tag{3.1}$$

The key element is a time-periodic modulation of the system, which is included in Eq. (3.1) as a temporal modulation of the frequencies $\omega_{1,2}(t)$ around the natural frequency ω_0 . One of the possible concrete realizations of this model is sketched in Fig. 3.1. Each pendulum contains a magnet which feels the magnetic field generated by a coil located below its axis. In this way, the gravitational restoring force felt by each pendulum is supplemented by a contribution of magnetic origin, which can be controlled via the (time-dependent) current $i_{1,2}(t)$ flowing in the corresponding coil. Another possible realization could be to directly change the length L of the pendula, through an engine that rolls and unrolls the string.

However, regardless of the actual realization, we assume that the effective modulation of the natural oscillator frequencies has the form:

$$\omega_{1,2}^2(t) = \omega_0^2 [1 + v_{1,2}(t)]. \tag{3.2}$$

In order to simplify the forthcoming equations, we introduce the rescaled quantities:

$$V_{1,2}(t) = \frac{v_{1,2}(t) \omega_0}{2}, \quad \Omega = \frac{k}{m\omega_0}, \quad \gamma = \frac{\xi}{2m}.$$

We now want to show that in certain regimes, Newton's equations of motion (3.1) can be formally mapped onto the Heisenberg equation for a tight-binding Hamiltonian, where the bosonic annihilation and creation operators are replaced by C-numbers, and commutators with Poisson's

brackets. To this end, we consider the following transformation:

$$\alpha_i = \sqrt{\frac{m\omega_0}{2}}x_i + i\sqrt{\frac{1}{2m\omega_0}}p_i. \quad (3.3)$$

These classical complex variables represent the classical analogue of the annihilation operators of the quantum harmonic oscillator. It is also very easy to show that the square modulus $|\alpha_i|^2$ have a direct physical meaning, being proportional to the instantaneous oscillation energy of the i -th pendulum.

With the help of the transformation in Eq. (3.3), Newton's equations for the two pendula are then summarized in a pair of complex equations:

$$\begin{cases} \dot{\alpha}_1 = -i\omega_0 \alpha_1 - iV_1(t)(\alpha_1 + \alpha_1^*) - \gamma(\alpha_1 - \alpha_1^*) + i\frac{\Omega}{2}(\alpha_2 + \alpha_2^* - \alpha_1 - \alpha_1^*) \\ \dot{\alpha}_2 = -i\omega_0 \alpha_2 - iV_2(t)(\alpha_2 + \alpha_2^*) - \gamma(\alpha_2 - \alpha_2^*) + i\frac{\Omega}{2}(\alpha_1 + \alpha_1^* - \alpha_2 - \alpha_2^*) \end{cases} \quad (3.4)$$

for the $\alpha_{1,2}$ complex variables. Complex conjugate equations hold for the $\alpha_{1,2}^*$.

In the following we shall concentrate our attention on a sinusoidal form of the temporal modulations:

$$V_i(t) = (-1)^i V \sin(\omega t). \quad (3.5)$$

Such modulations are periodic with period $T = 2\pi/\omega$, and have an opposite sign for the two oscillators.

3.2 The rotating-wave approximation.

Analytical insight into the physics of the modulated system can be obtained within the so-called *rotating-wave approximation*, well-known in the context of quantum optics. Equations (3.4) can be simplified under the assumption that the natural frequencies ω_0 of the pendula are much larger than all other internal frequencies in the problem, that is:

$$\omega_0 \gg \max(\Omega, \gamma, \omega). \quad (3.6)$$

In this case, the fastest time dependence of α_i is proportional to $e^{-i\omega_0 t}$, while the one of their conjugate variables $\alpha_i^*(t)$ is proportional to $e^{i\omega_0 t}$. This is equivalent to saying that the α variables rotate at $\approx \omega_0$ and their conjugate variables α^* rotate at $\approx -\omega_0$. Then, by moving to a frame that is rotating at the frequency ω_0 , the α_i variables only has a (relatively) slow evolution, while their complex conjugate variables α_i^* will oscillate quickly around a frequency $\approx -2\omega_0$.

We will often refer to terms proportional to the the α_i variables as being *rotating-wave* terms, since they are the leading ones in this rotating frame. The α_i^* will be instead the *counter-rotating-wave* terms, because their frequency is negative in the frame rotating at ω_0 and therefore they appear to oscillate in the opposite direction to the reference frame. It is then immediate to see that in the limit $\omega_0 \rightarrow \infty$ the contribution of the α_i^* 's to the motion equation for α_i is negligible as the fast oscillations quickly average to zero.

As a result, the rotating-wave approximation is legitimately implemented by neglecting in the Eq. (3.4) for α_i the terms involving the counter-rotating-wave variables α_i^* and therefore by completely decoupling the counter-rotating-wave from the rotating-wave variables. Equations (3.4), within this approximation, are written as:

$$\begin{cases} \dot{\alpha}_1 = -i\omega_0 \alpha_1 - iV_1(t)\alpha_1 - \gamma\alpha_1 + i\frac{\Omega}{2}(\alpha_2 - \alpha_1) \\ \dot{\alpha}_2 = -i\omega_0 \alpha_2 - iV_2(t)\alpha_2 - \gamma\alpha_2 + i\frac{\Omega}{2}(\alpha_1 - \alpha_2). \end{cases} \quad (3.7)$$

3.2.1 Connection to the tight-binding model.

We now highlight the connection of the rotating-wave description of the coupled pendula in Eq. (3.7) to a tight-binding model of quantum physics. Neglecting the damping term, the resulting

Hamiltonian for the internal system dynamics:

$$\mathcal{H}(t) = \sum_{i=1}^2 \left(\omega_0 + V_i(t) + \frac{\Omega}{2} \right) \alpha_i^* \alpha_i - \sum_{i=1}^2 \left(\frac{\Omega}{2} \alpha_i^* \alpha_{3-i} + \frac{\Omega}{2} \alpha_{3-i}^* \alpha_i \right) \quad (3.8)$$

is then a classical counterpart of a bosonic tight-binding Hamiltonian, where the bosonic annihilation and destruction operators \hat{a}_i and \hat{a}_i^\dagger are replaced by the \mathbb{C} -numbers complex variables α_i and α_i^* . The first term in Eq. (3.8) accounts for the on-site energy, while the second one describes the hopping between the two sites. In terms of the α variables, Newton's equations of motion Eqs. (3.7) represent the Heisenberg equations of motion associated with the tight-binding Hamiltonian in Eq. (3.8).

In the Hamiltonian, the rotating-wave approximation consists of neglecting all non-energy-conserving terms proportional to $\alpha_i \alpha_j$ and $\alpha_i^* \alpha_j^*$ and only keep the energy-conserving ones $\alpha_i^* \alpha_j$.

We also notice that, if the anharmonicity of the pendula were taken into account beyond the linearized Eqs. (3.1), a new term would appear in Eq. (3.8). Such a term would be the on-site interaction term $U \alpha_i^* \alpha_i^* \alpha_i \alpha_i$, that is typical of the Bose-Hubbard model of condensed-matter physics.

3.3 Analytical equations of motion within the rotating-wave approximation.

We have set up the analogy between the coupled pendula in the rotating-wave regime and the tight-binding model. Now, we want to obtain some analytical insight into the dynamics of the system. To this end, we introduce the following transformation of the complex variables:

$$\boxed{\beta_i(t) = \alpha_i(t) e^{i \int_0^t V_i(t') dt'}} \quad (3.9)$$

This transformation defines a frame in which the pendula are not modulated and their oscillation energy is proportional to $|\beta_i(t)|^2$. In such a frame, the phase factor involving the modulation is exactly equal to 1 at the stroboscopic times $t_n = nT$, for the chosen sinusoidal form of the modulation. This means that the new variables are related to the original ones by a canonical transformation which is invariant under the time translation $t \rightarrow t + nT$. With the transformation in Eq. (3.9), the Hamiltonian Eq. (3.8) is written as:

$$\mathcal{H}'(t) = \sum_{i=1}^2 \left(\omega_0 + \frac{\Omega}{2} \right) \beta_i^* \beta_i - \sum_{i=1}^2 \left(\frac{\Omega}{2} \beta_i^* \beta_{3-i} e^{-i \int_0^t (V_{3-i}(t') - V_i(t')) dt'} + \text{c.c.} \right). \quad (3.10)$$

We notice that the temporal modulation enters directly in the Hamiltonian as a complex coupling-amplitude. The time-dependent problem can be solved by means of Floquet theory for periodic systems. The effective dynamics of the system can be obtained via an expansion in the modulation frequency, known as the Magnus expansion. We performed this expansion at first order following the approach, for example, given in Goldman et al. [2015b] or Bukov et al. [2015]. The effective Hamiltonian is:

$$\mathcal{H}^{\text{EFF}} = \frac{1}{T} \int_0^T \mathcal{H}'(t) dt,$$

which is valid in the limit of high modulation frequency $\omega_0 \gg w \gg \Omega$, where the higher order terms of the Magnus expansion are negligible. The effective equations are derived from this effective Hamiltonian as:

$$\dot{\beta}_i = \{\beta_i, \mathcal{H}^{\text{EFF}}\} = \frac{1}{T} \int_0^T \{\beta_i, \mathcal{H}'(t)\},$$

where the parenthesis $\{f, g\} = -i \sum_{j=1}^2 \left(\frac{\partial f}{\partial \beta_j} \frac{\partial g}{\partial \beta_j^*} - \frac{\partial g}{\partial \beta_j} \frac{\partial f}{\partial \beta_j^*} \right)$ is the canonical Poisson bracket. Therefore, from the equations of motion Eq. (3.7), substituting the transformed variables of Eq. (3.9) and integrating over a period of the temporal modulation, we get the following equations of motion:

$$\boxed{\begin{aligned} \dot{\beta}_1 &= -i \left(\omega_0 + \frac{\Omega}{2} \right) \beta_1 + i \frac{\Omega_{12}^{\text{eff}}}{2} \beta_2 \\ \dot{\beta}_2 &= -i \left(\omega_0 + \frac{\Omega}{2} \right) \beta_2 + i \frac{\Omega_{21}^{\text{eff}}}{2} \beta_1. \end{aligned}} \quad (3.11)$$

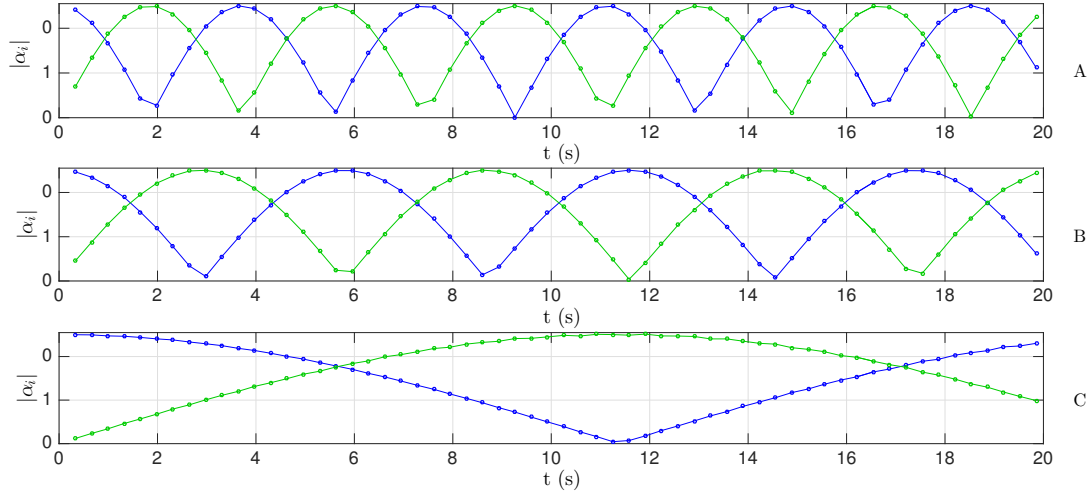


Figure 3.2: Results of a numerical integration of the equations of motion Eq. (3.4) with a Runge-Kutta algorithm. The blue (green) dots indicate the modulus $|\alpha_1|$ ($|\alpha_2|$) of the oscillation amplitude of the first (second) pendulum, normalized to the initial amplitude, while the lines are guides to the eyes. At the initial time $t = 0$, only the first oscillator is excited, while $\alpha_2(t = 0) = 0$. The evolution of the two pendula is followed with a stroboscopic sampling at the modulation frequency w of the full numerical solution. The three panels are obtained for three different values of the modulation amplitude, showing the renormalization of the effective coupling frequency. $I_0 = 0$ in **A**, $I_0 \approx 0.63$ in **B**, and $I_0 \approx 1.05$ in **C**. System parameters are: $\omega_0/\Omega \approx 147$, $w/\Omega \approx 11$, $\gamma/\Omega = 0$.

The effective couplings in Eqs. (3.11) are defined by:

$$\Omega_{ij}^{\text{eff}} \equiv \frac{\Omega}{T} \int_0^T dt e^{i \int_0^t [V_i(t') - V_j(t')] dt'} \quad (3.12)$$

and they are such that they are complex conjugate to each other, $\Omega_{12}^{\text{eff}} = \Omega_{21}^{\text{eff}*}$. For the specific modulation considered here, the effective coupling has the simple expression:

$$\Omega_{\text{eff}} \equiv \Omega_{12}^{\text{eff}} = \Omega e^{-2iI_0} \mathcal{J}_0(2I_0) \quad (3.13)$$

where we have used the Anger-Jacobi expansion to obtain the $\mathcal{J}_0(2I_0)$ zero-order Bessel function of argument $2I_0 = 2V/w$. The modulus $|\Omega_{\text{eff}}|$ will exhibit a series of zeros in correspondence to the zeros of the Bessel function \mathcal{J}_0 , which are indicative of a complete *dynamical decoupling* between the two pendula. Further evidence for this dynamical decoupling effect can be observed in Fig. 3.2. As we have just discussed, the dynamics of the system in Eq. (3.4), sampled at the stroboscopic times $t_n = nT$ is effectively described by a time-independent discrete evolution law. In order to prove that this is the case, we have numerically integrated Newton's equations of motion in their complete form given in Eq. (3.4), for the vanishing friction case $\gamma = 0$, with a standard fourth order Runge-Kutta algorithm. The evolution of the amplitudes $|\alpha_{1,2}|$, sampled at the frequency w of the temporal modulation, are reported in Fig. 3.2. Different panels correspond to the same modulation frequency w but different values of the amplitude V , representing different regimes.

In panel 3.2-A, there is no temporal modulation, so $V = 0$: the amplitudes of the two oscillators exhibit the usual beating effect, that is a periodic exchange of energy between the oscillators at the coupling frequency Ω . As a result of a non-zero temporal modulation $V_i(t)$, for increasing values of its amplitude V , the frequency of the beat is modified, as expected and anticipated in Eq. (3.13). In particular, for the parameters of panels 3.2-B and 3.2-C, the beat frequency is more and more reduced. For even larger amplitudes V , we observed a non-monotonic behaviour of the effective beat frequency. An analysis of the effective coupling based on numerical simulations of the equation of motion will be given in the remainder of the Chapter.

3.3.1 Monochromatic driving.

In order to perform a detailed study of the effect of the modulation and, at the same time, to propose a viable procedure to experimentally observe these phenomena, it is useful to consider the realistic case of dissipative pendula driven by an external force. We assume that such a driving force is monochromatic at frequency ω_{ex} :

$$F_{\text{ex}}(t) = 2f_{\text{ex}}\delta_{i,1} \cos(\omega_{\text{ex}}t),$$

where $\delta_{i,j}$ is the usual Kronecker delta, so that the external force acts only the first pendulum. The driven-dissipative form of the equations of motion (3.4) then is:

$$\dot{\alpha}_i = -i(\tilde{\omega}_0 - i\gamma)\alpha_i - iV_i(t)(\alpha_i + \alpha_i^*) + iF_{\text{ex}}(t) - i\left(\frac{\Omega}{2} + i\gamma\right)\alpha_i^* + i\frac{\Omega}{2}(\alpha_{3-i} + \alpha_{3-i}^*) \quad (3.14)$$

for $i = 1, 2$ and where we have defined the short-hand notation $\tilde{\omega}_0 = \omega_0 + \Omega/2$.

The same procedure as the one done in the previous subsection for Eq. (3.4) must be applied to Eq. (3.14) in order to obtain the effective dynamics within Floquet theory. We are interested in the steady-state regime, where the α_i variables oscillate at $\approx \omega_{\text{ex}}$. We assume this frequency is comparable with ω_0 , so that $|\omega_0 - \omega_{\text{ex}}| \ll w$. We use a slightly modified transformation of (3.9):

$$\beta_i(t) = \alpha_i(t) e^{i\int_0^t V_i(t') dt'} e^{i\omega_{\text{ex}}t} \quad (3.15)$$

that includes also the external driving frequency. Within the rotating-wave approximation, we obtain explicit expressions that are valid in the steady oscillation regime, where the β_i are not oscillating. By setting $\dot{\beta}_i = 0$, and solving the two-by-two system, analytical forms of the amplitudes of oscillation are found for the steady-state. These amplitudes are the ‘‘resonance curves’’ as function of ω_{ex} :

$$\begin{aligned} \beta_1(\omega_{\text{ex}}) &= \frac{2f_{\text{ex}}^{\text{eff}}(\tilde{\omega}_0 - i\gamma - \omega_{\text{ex}})}{4(\tilde{\omega}_0 - i\gamma - \omega_{\text{ex}})^2 - |\Omega_{\text{eff}}|^2} \\ \beta_2(\omega_{\text{ex}}) &= \frac{f_{\text{ex}}^{\text{eff}}\Omega_{\text{eff}}^*}{4(\tilde{\omega}_0 - i\gamma - \omega_{\text{ex}})^2 - |\Omega_{\text{eff}}|^2}. \end{aligned} \quad (3.16)$$

The effective coupling Ω_{eff} is exactly the same as in Eq. (3.13). We notice that also the external driving force gets renormalised:

$$f_{\text{ex}}^{\text{eff}} \equiv \frac{f_{\text{ex}}}{T} \int_0^T dt e^{i\int_0^t V_i(t') dt'}, \quad (3.17)$$

and that, with the specific modulation in Eq. (3.5), has the explicit form:

$$f_{\text{ex}}^{\text{eff}} = f_{\text{ex}} e^{-iI_0} \mathcal{J}_0(I_0), \quad (3.18)$$

having again used the Anger-Jacobi expansion for obtaining the Bessel function. More insights into the derivation of Eq. (3.16) can be found in Appendix B. According to the specific value of the argument $I_0 = V/w$ of the Bessel function, the effective driving force can be also equal to zero, meaning that a complete *dynamical isolation* from the external force can occur. We shall further explore this result in the numerical simulation of the system in the following.

3.3.2 First-order correction beyond the rotating-wave approximation.

The analytical results of the previous section were obtained within the rotating-wave approximation that is strictly valid only in the regime where $\omega_0 \rightarrow \infty$. For realistic oscillators, the validity of this approximation is good so long as the following inequality chain is satisfied:

$$\omega_0 \gg w \gg \Omega \gg \gamma. \quad (3.19)$$

The first inequality in Eq. (3.19) is the same as in Eq. (3.6). The second one justifies our calculating the effective dynamics after a time average over the period $T = 2\pi/w$ of the temporal modulation, by using the high-frequency expansion of Floquet theory, as in Holthaus [1992] or Bukov et al.

[2015]. The last inequality is essential for observing an effective coupling before the oscillations damp out. In addition to this, it is also important to satisfy the following chain of inequalities $w \gg |\omega_0 - \omega_{\text{ex}}| \approx \Omega$ so that we can have clear access to the spectroscopic features.

We now extend the validity of expressions in Eq. (3.16) by considering a first order correction to the rotating-wave approximation. We notice that, since α and α^* are coupled through Eq. (3.14) and its complex-conjugate equation, a rotating-wave contribution appears also from the counter-rotating-wave variable α^* . The full derivation of the first order correction is given in the Appendix C, and the result is the following frequency shift:

$$\Delta\omega_0 \equiv \tilde{\omega}_0 - \frac{V^2}{4\omega_0}, \quad (3.20)$$

which is more and more important for larger amplitude V of the temporal modulation. All other counter-rotating-wave contributions involving Ω and γ are negligible for the chosen parameters and were not included in Eq. (3.20). The shift is a classical analogue of the shift of nuclear magnetic resonance discovered by Bloch and Siegert [1940]. We obtain equations similar to Eq. (3.16) where the natural detuning frequency $\tilde{\omega}_0 - \omega_{\text{ex}}$ is shifted according to Eq. (3.20):

$$\Delta\omega \equiv \tilde{\omega}_0 - \omega_{\text{ex}} - \frac{V^2}{4\omega_0}. \quad (3.21)$$

Equations. (3.16), with the substitution $\tilde{\omega}_0 - \omega_{\text{ex}} \rightarrow \Delta\omega$, are the new resonance curves valid to the first order in the rotating-wave approximation:

$$\begin{aligned} \beta_1(\omega_{\text{ex}}) &= \frac{2 f_{\text{ex}}^{\text{eff}} (\Delta\omega - i\gamma)}{4(\Delta\omega - i\gamma)^2 - |\Omega_{\text{eff}}|^2} \\ \beta_2(\omega_{\text{ex}}) &= \frac{f_{\text{ex}}^{\text{eff}} \Omega_{\text{eff}}^*}{4(\Delta\omega - i\gamma)^2 - |\Omega_{\text{eff}}|^2}. \end{aligned} \quad (3.22)$$

By taking the ratio of these two resonance curves, we can also calculate the effective coupling Ω_{eff} as:

$$\Omega_{\text{eff}} = 2(\Delta\omega + i\gamma) \frac{\beta_2^*}{\beta_1}. \quad (3.23)$$

This formula will be used in the following to estimate, from the numerical simulations, the effective coupling as a complex quantity, allowing us to measure both its modulus and phase.

3.4 Results of the driven-dissipative numerical simulations.

We have numerically integrated Newton's equation of motion, in their driven-dissipative form given in Eq. (3.14), with a standard fourth order Runge-Kutta algorithm. For a given value of the external frequency ω_{ex} , these equations have been integrated until the steady-state regime at long times $t \ll \gamma$, where we observe regular periodic oscillations. For the stroboscopic sampling at times $t_n = nT$, the steady-state oscillations have the form $\alpha_i(t) \approx A_i(\omega_{\text{ex}}) e^{-i\omega_{\text{ex}}t}$. The complex amplitudes A_i are obtained via a Fourier transformation of the stroboscopically sampled numerical solutions. The moduli $|A_i|$, as a function of the frequency of the external force, give the response spectra shown in Fig. 3.3. The numerical results are shown with points and are compared with the theoretical predictions in Eq. (3.22), shown in solid lines, that includes the first-order correction to the rotating-wave approximation. Each panel corresponds to a different value of the modulation amplitude V and illustrates a different regime.

The case of no modulation is shown in panel 3.3-A: the spectra are characterized by a pair of peaks, of equal width γ , that correspond to the two eigenmodes of the system: the two pendula oscillating with the same (lower frequency peak) or opposite (higher frequency peak) phase. We notice that at all frequencies, the oscillation amplitudes of the two pendula remain comparable, signifying that both pendula are almost equally excited.

Panel 3.3-B shows a case where the coupling of the two pendula is dramatically suppressed: this effect is apparent in the figure as the two peaks merge into a single one and no significant excitation is transferred to the second pendulum, which remains basically at rest with a negligible

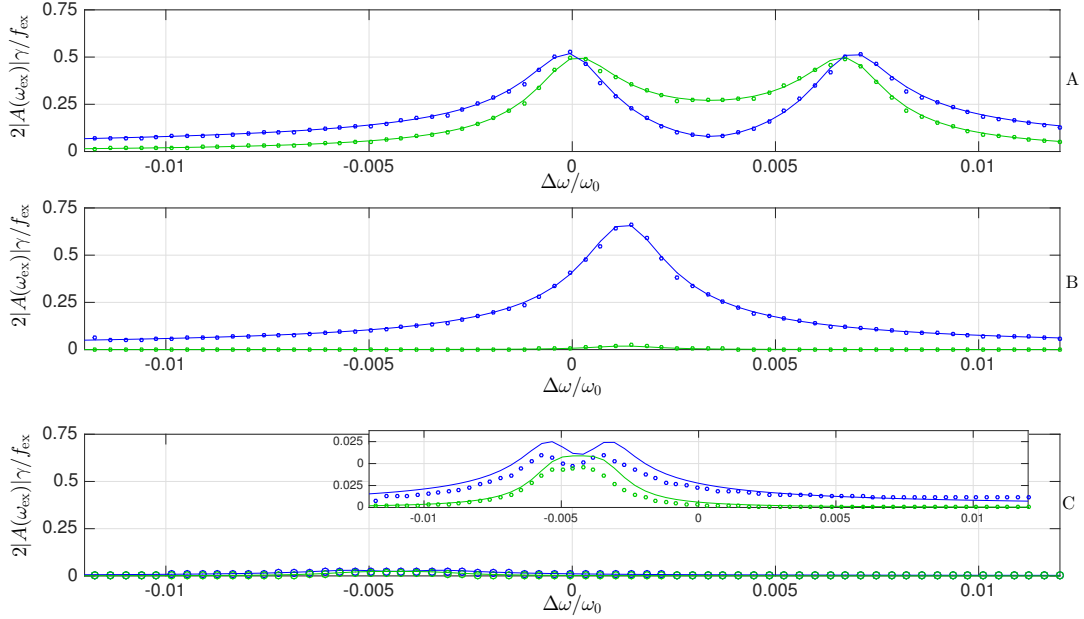


Figure 3.3: Response spectra $|A_i(\omega_{\text{ex}})|$ as a function of the frequency ω_{ex} of the external force. The stroboscopically sampled numerical results are shown for the first (second) pendulum as blue (green) dots, normalized to the peak amplitude $f_{\text{ex}}/(2\gamma)$ of a single isolated pendulum in the small γ limit. The solid lines show the analytical spectra based on the rotating-wave approximation of Eq. (3.22). The different panels corresponds to different values of the modulation amplitude, $I_0 = 0$ in **A**, $I_0 = 1.21$ in **B**, $I_0 = 2.31$ in **C**. The inset in panel-**C** shows an enlargement of the main plot. System parameters are: $\omega_0/\Omega \approx 147$, $w/\Omega \approx 11$, $\gamma/\Omega \approx 0.15$, $f_{\text{ex}}/\Omega \approx 6$.

oscillation amplitude. The first pendulum behaves as if it was isolated, except that its resonance frequency is shifted due to the counter-rotating-wave terms in Eq. (3.20). This behaviour is the driven-dissipative manifestation of the *dynamical decoupling* effect, already seen in the lowest panel of Fig. 3.2 for vanishing friction.

Panel 3.3-C shows the novel regime where the global excitation by the external force is suppressed, while some effective coupling of the two pendula is still present. The suppressed excitation is visible as a very small oscillation amplitude of both pendula, while the presence of a significant coupling is apparent in the inset where the response of the first pendulum is still showing a doublet. The absence of a significant excitation in the system is a *dynamical isolation* of the two pendula from the external driving. This effect is due to the vanishing of the effective driving force $f_{\text{ex}}^{\text{eff}}$, for a value of the amplitude of the temporal modulation V such that the Bessel function in Eq. (3.18) of argument $I_0 = V/w$, is close to a zero.

These different regimes are comprehensively illustrated in Fig. 3.4. For each of the response spectra, calculated for different values of the amplitude of the modulation V , we present only the resonant response at the peaks, that is the maximum oscillation amplitude $|A_i(\omega_{\text{ex}})|$ for all external drive frequencies ω_{ex} . This quantity has been normalised to the maximum of the oscillation amplitude for the two oscillators and is presented as a function of the modulation amplitude. The resonant response as calculated from the numerical simulations is presented in Fig. 3.4 with points of different colors for the two oscillators, while the solid lines are the analytical predictions of the rotating-wave approximation at first order given in Eq. (3.18). The agreement between numerical and analytical data is very good, in particular for what concerns the position of the dynamical isolation points for which $f_{\text{ex}}^{\text{eff}} = 0$ and both $\max(|A_{1,2}|) = 0$. Although not shown here, we have found that the agreement gets worse when the inequality chain of Eq. (3.19) is only marginally satisfied. The dynamical decoupling seen in Fig. 3.3-B corresponds in Fig. 3.4 to the minimum of $\max(|A_2|)$ that is visible around $I_0 \simeq 1.2$. The dynamical isolation seen in Fig. 3.3-C lies in the vicinity of the simultaneous minima of both $\max(|A_{1,2}|)$ that are visible around $I_0 \simeq 2.4$. In the figure, note the further dynamical decoupling point around $I_0 \simeq 2.7$.

We now present further insights into the coupling between the two pendula as resulting from the temporal modulation. By applying Eq. (3.23) to the numerical results, we extracted the effective

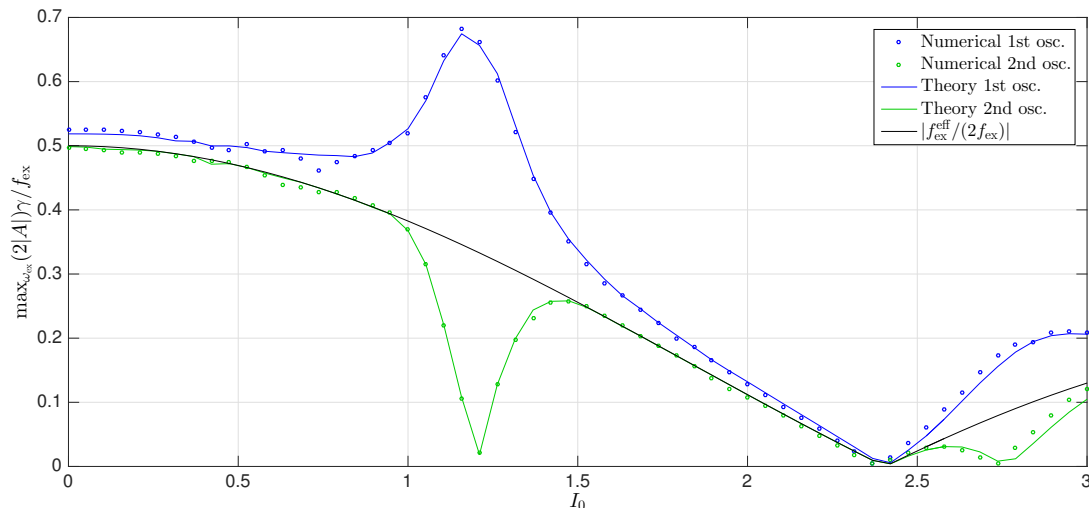


Figure 3.4: Blue (green) dots show the normalized maximum of the numerical amplitude of the oscillations for the first (second) pendula as a function of the modulation amplitude I_0 . The solid lines show the result of the analytical calculation based on the rotating-wave approximation. Blue (green) lines are the resonance peaks as in Eq. (3.22) for β_1 (β_2). Black line is the effective driving force in Eq. (3.18). System parameters as in Fig. 3.3.

coupling as a complex quantity. The modulus of Ω_{eff} is presented in Fig. 3.5, where the numerical points are compared with the analytical expression that was obtained in Eq. (3.13). The agreement appears again to be very good, in particular concerning the position of the dynamical decoupling points at which $\Omega_{\text{eff}} = 0$. The small discrepancies occur when both numerator and denominator of Eq. (3.23) go to zero and the procedure is more sensitive to numerical errors.

3.4.1 The coupling phase.

In this Chapter, we have seen that the temporal modulation of the bare frequency of two coupled harmonic oscillators is able to dynamically decouple them from each other or to dynamically isolate them both from an external driving force, depending on the magnitude of the temporal modulation.

The most crucial and probably the most important consequence of the temporal modulation is that the effective coupling develops a *non-trivial phase*, as shown in Fig. 3.6, where we present the argument of Ω_{eff} as obtained from Eq. (3.23) as a function of I_0 . The physical interpretation of this phenomena is the following. The two eigenmodes of the bare system, for $I_0 = 0$, correspond to in-phase and out-of-phase oscillations of the two pendula. The temporal modulation allows us to tune the relative phase of these oscillations to any value θ from 0 to 2π for the “in-phase” eigenmode, and to $\pi - \theta$ for the “out-of-phase” eigenmode. We also notice that the coupling phase displays π jumps whenever the effective coupling Ω_{eff} in Fig. (3.13) goes through a zero.

From the point of view of fundamental physics, such a non-trivial phase between the pendula is a classical analogue of the Peierls phase of a quantum tight-binding model, as introduced in the previous Chapters, and the complex hopping amplitude $J e^{i\phi_{ij}} \leftrightarrow \Omega_{ij}^{\text{eff}}$ is matched to the complex coupling between the pendula.

This stunning result opens the intriguing possibility of creating a scheme for generating an artificial gauge field in a purely classical system. In analogy to quantum-Hall systems, surprising phenomena are expected to appear in multi-dimensional lattices of many temporally modulated pendula, where their oscillation patterns show the behaviour of a topological insulator. However, the temporal modulation introduced in this Chapter does not formally break time reversal symmetry, as this symmetry is restored when a different time origin is considered in Eq. (3.5). For this purpose a different scheme is needed and it will be discussed in the next Chapter.

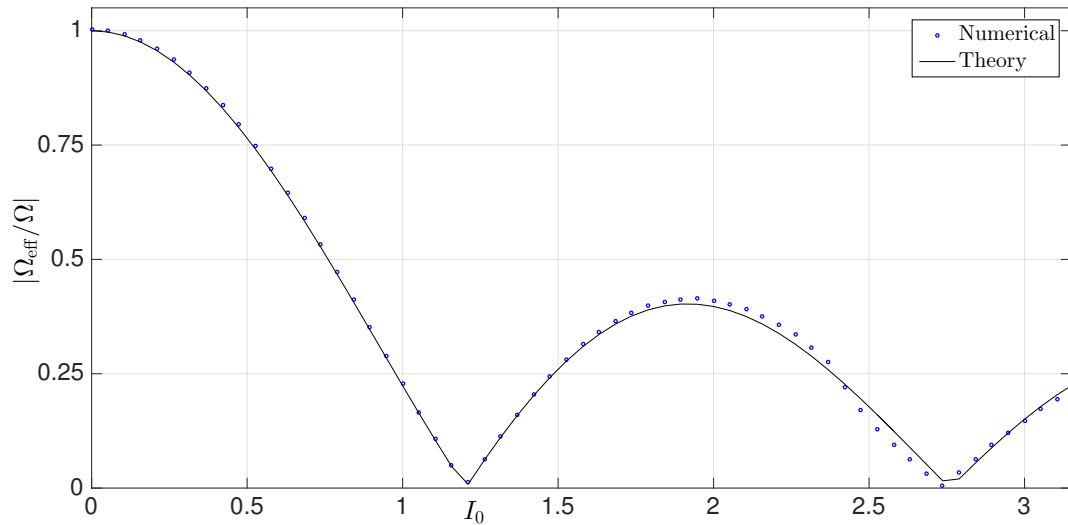


Figure 3.5: Modulus of the effective coupling frequency $|\Omega_{\text{eff}}|/\Omega$. Dots are the results of the numerical calculations, while the solid line is the analytical prediction of the rotating-wave approximation in Eq. (3.23). System parameters as in Fig. 3.3.

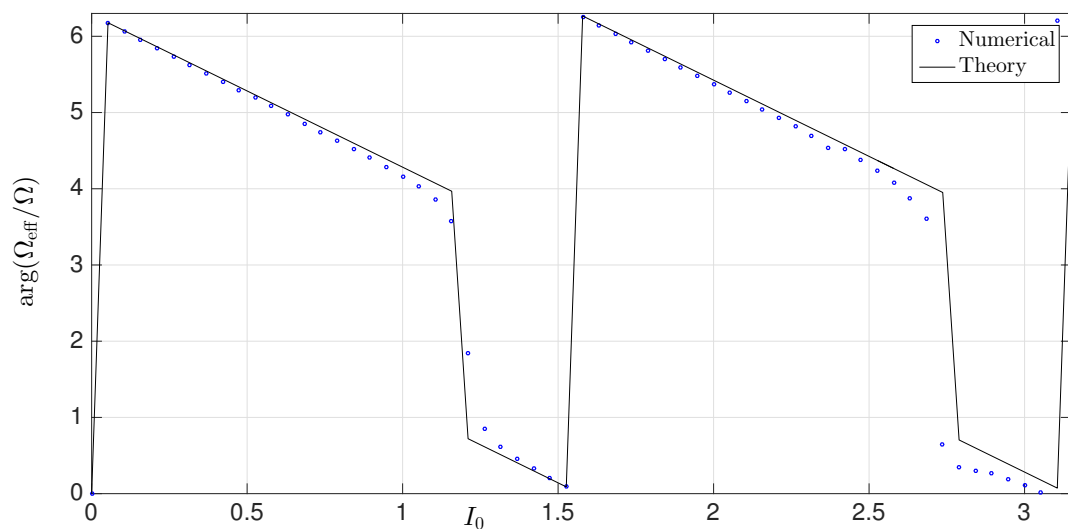


Figure 3.6: Phase $\arg(\Omega_{\text{eff}})$ modulo 2π of the effective coupling frequency. Dots are the results of the numerical calculations, while the solid line is the analytical prediction of the rotating-wave approximation in Eq. (3.23). System parameters as in Fig. 3.3.

Chapter 4

The Harper-Hofstadter model in a classical mechanical system.

Meet the topo-pendula (in theory).

In Chap. 3 we have proposed a viable scheme to realize a tunable non-trivial coupling phase in a system of two coupled classical harmonic oscillators. We have also seen that such a phase is the analogue of the Peierls phase of a quantum tight-binding model. This remarkable result opens up the possibility of simulating a strong artificial magnetic flux, of the order of the flux quanta, to realize the Harper-Hofstadter model in a purely classical system governed by Newton's equations.

The Harper-Hofstadter model is the archetypical lattice model of a quantum Hall system. As we have seen in Chap. 1, it has a rich fractal energy spectra known as the Hofstadter butterfly, studied by Hofstadter [1976] where the eigenstates associated to the energy bands are characterized by a non-trivial topological invariant, that is the Chern number. This invariant is also related to the quantisation of the conductance in the quantum Hall effect, as shown by Thouless et al. [1982].

In this Chapter we will generalize the scheme of frequency-modulated coupled classical harmonic oscillators of Chap. 3 to obtain non-trivial topological effects that are analogous to the integer quantum Hall effect. We will obtain, within the Floquet framework and by applying the rotating-wave approximation, effective equations of motion that obey the Harper-Hofstadter model. We will show that the hallmarks of this model, such as the topologically robust and chiral edge states, the self-similar energy spectra and the Chern invariants can be obtained in classical physics, and we explore a classical analogue of the Hofstadter butterfly and the quantum Hall effect.

The main results of this Chapter are published in Salerno et al. [2016].

4.1 The model.

We consider a square lattice of $N = N_x \times N_y$ sites, labelled by two indexes (i, j) . Each lattice site hosts a pendulum of mass $m_{i,j}$ and frequency $\tilde{\omega}_{i,j}$, whose oscillation plane is rigidly fixed along, for example, the unit-cell diagonal, as shown in Fig. 4.1. We indicate with $z_{i,j}$ the displacement of each pendulum from its equilibrium point along this fixed direction. As we did in the previous Chapter, we also assume that the natural frequencies of the pendula are periodically modulated in time around the mean value $\tilde{\omega}_{i,j} \equiv \langle \omega_{i,j}(t) \rangle$. All the pendula are coupled to their nearest neighbours by springs of rest length equal to the lattice spacing and of constant k_x and k_y along the two x and y directions respectively. The pendula belonging to the edges of the lattice are coupled to a fixed wall. Including loss mechanisms with a friction coefficient ξ , the linearised Newton's equations of

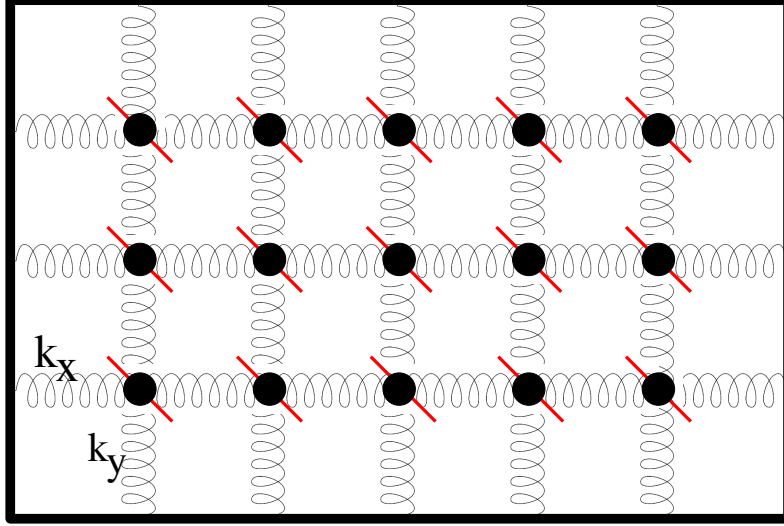


Figure 4.1: View from above of a square lattice of pendula constrained to oscillate along the plane indicated by the thick red lines. The coupling between neighbouring pendula is provided by elastic springs with spring constants k_x and k_y . Pendula on the edges are coupled to a rigid wall.

motion for the generic (i, j) -th pendulum, driven by an external force $\mathcal{F}_{i,j}^{\text{ex}}(t)$, read as:

$$\begin{aligned} m_{i,j} \dot{z}_{i,j} &= p_{i,j} \\ \dot{p}_{i,j} &= -m_{i,j} \omega_{i,j}^2(t) z_{i,j} + \sum_{\pm 1} k_x (z_{i\pm 1, j} - z_{i,j}) + \sum_{\pm 1} k_y (z_{i, j\pm 1} - z_{i,j}) - 2\xi \dot{z}_{i,j} - F_{i,j}^{\text{ex}}(t). \end{aligned} \quad (4.1)$$

We follow the same procedure as the previous Chapter and generalise the transformation in Eq. (3.3), to include the position-dependent frequency and mass, such that the square modulus $|\alpha_{i,j}|^2$ is still proportional to the oscillation energy of the specific (i, j) -th pendulum:

$$\alpha_{i,j} = \sqrt{\frac{m_{i,j} \tilde{\omega}_{i,j}}{2}} z_{i,j} + i \frac{p_{i,j}}{\sqrt{2m_{i,j} \tilde{\omega}_{i,j}}}. \quad (4.2)$$

We now assume for simplicity that the product $m_{i,j} \tilde{\omega}_{i,j} \equiv \mu$ is constant for every site (i, j) and we define the bare coupling frequencies as:

$$\Omega_x \equiv k_x / (2\mu), \quad \Omega_y \equiv k_y / (2\mu).$$

As before, we combine the second-order differential equations in Eq. (4.1) to get a set of N first-order differential equations for the complex variables $\alpha_{i,j}$:

$$\begin{aligned} \dot{\alpha}_{i,j} &= -i \left[\frac{\tilde{\omega}_{i,j}}{2} + \frac{\omega_{i,j}^2(t)}{2\tilde{\omega}_{i,j}} - i\gamma_{i,j} + 2\Omega_x + 2\Omega_y \right] \alpha_{i,j} - i \left[\frac{\tilde{\omega}_{i,j}}{2} - \frac{\omega_{i,j}^2(t)}{2\tilde{\omega}_{i,j}} + i\gamma_{i,j} + 2\Omega_x + 2\Omega_y \right] \alpha_{i,j}^* \\ &+ i \sum_{\pm 1} \Omega_x (\alpha_{i\pm 1, j} + \alpha_{i\pm 1, j}^*) + i \sum_{\pm 1} \Omega_y (\alpha_{i, j\pm 1} + \alpha_{i, j\pm 1}^*) + i f_{i,j}^{\text{ex}}(t), \end{aligned} \quad (4.3)$$

and a similar set of N equations for $\alpha_{i,j}^*$. The damping rate is $\gamma_{i,j} \equiv \xi/m_{i,j}$, while the external driving force is taken to be monochromatic at frequency ω_{ex} with amplitude proportional to $f_{i,j}$:

$$f_{i,j}^{\text{ex}}(t) \equiv \mathcal{F}_{i,j}^{\text{ex}}(t) / \sqrt{2\mu} = 2f_{i,j} \cos(\omega_{\text{ex}} t). \quad (4.4)$$

4.1.1 The temporal and spatial modulation.

Inspired by the realization of the Harper-Hofstadter model with ultra-cold atoms in optical lattices by [Aidelsburger et al. \[2013\]](#) and [Miyake et al. \[2013\]](#) and by related proposals in the

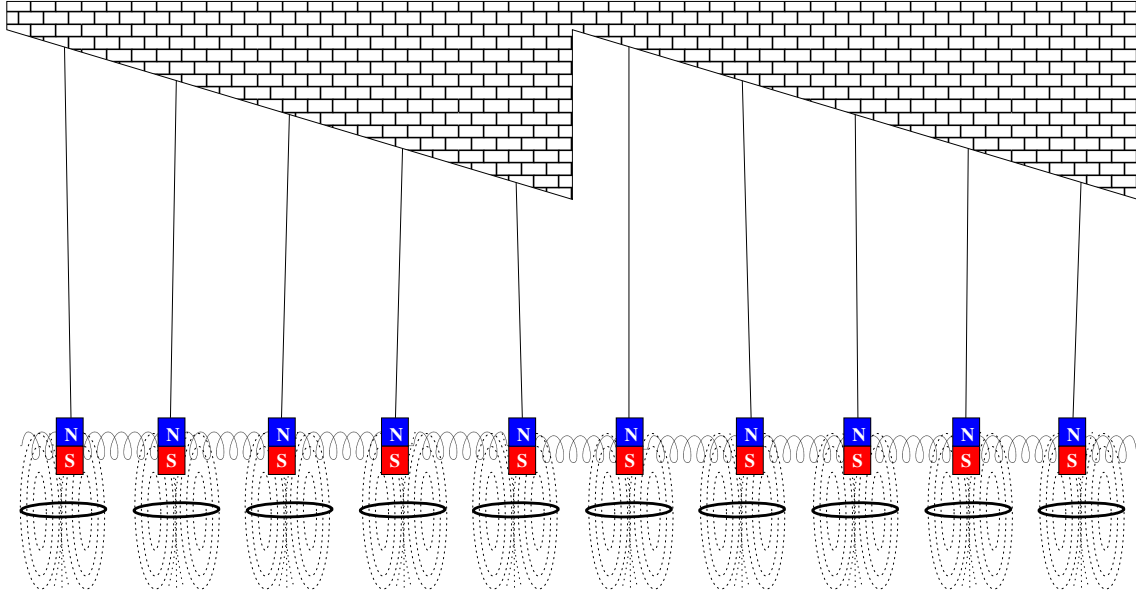


Figure 4.2: Section of the system along the x direction, sketching the spatial modulation of the natural frequencies of the pendula with period $s = 5$. The temporal modulation is implemented as in Chap. 3, by acting on the gravitational restoring force of each pendulum. A magnet is attached to the mass of the pendulum and interacts with the time-dependent magnetic field generated by an externally controlled current flowing in the coil below the axis of oscillation.

photonic context such as Fang et al. [2012] and Wang et al. [2015b], we take the natural frequency of the pendula, *i.e.* a part of the single-particle on-site energy in the tight-binding analogy, to be temporally and spatially modulated. In particular, we assume that the specific form of the frequency modulation is:

$$\omega_{i,j}^2(t) = \tilde{\omega}_{i,j}^2 \left(1 + 2 \frac{V_{i,j}(t)}{\tilde{\omega}_{i,j}} \right) \quad (4.5)$$

where $V_{i,j}(t)$ is the temporal modulation.

The spatial modulation is chosen to be:

$$\tilde{\omega}_{i,j} = \omega_0 - 2\Omega_x - 2\Omega_y + wS(i), \quad (4.6)$$

where

$$S(i) \equiv \text{mod}(i - 1, s) \quad (4.7)$$

is a saw-tooth function along the x -direction, of period s . We schematically show such a spatial modulation in Fig. 4.2, where the pendula are hung from a tilted roof such that their lengths satisfy Eq. (4.6). Of course, Fig. 4.2 is just a sketch, since for simplicity we have not taken into account in the drawing the non-linear dependence of the frequency from the length of the pendulum.

The spatial modulation in Eq. (4.6) strongly suppress the coupling of the pendula along the x direction, due to a “huge” mismatch of frequency between neighbouring pendula because $w \gg \Omega$. Such a hopping can be restored if a suitable temporal modulation is chosen. In fact, as shown by Goldman et al. [2015b], when the frequency of the modulation is exactly on resonance with the detuning of neighbouring sites, a uniform coupling is restored over the whole lattice. Given the specific sawtooth form of Eq. (4.7) chosen for $S(i)$, a bi-harmonic temporal modulation is needed:

$$V_{i,j}(t) = V [\cos(wt + \phi_{i,j}) + (s - 1) \cos(w(s - 1)t - \phi_{i,j})] \quad (4.8)$$

where the amplitude V is position independent. The first component at frequency w restores a uniform hopping between the pairs of pendula with natural frequency difference w , on the “small steps” of the spatial modulation. The second component at frequency $w(s - 1)$ addresses the hopping between pendula with a frequency difference $w(s - 1)$, on the “big steps” of $S(i)$.

We will show that the position-dependence of the phase $\phi_{i,j}$ offers us a way to control the coupling phase along x . In order to obtain the desired Harper-Hofstadter model, as was done in

Aidelsburger et al. [2013], a possible choice is:

$$\phi_{i,j} = 2\pi\theta(i+j). \quad (4.9)$$

We shall see in the remainder of the Chapter that such a phase is able to produce a uniform flux per plaquette.

To summarise, with the temporal modulation in Eq. (4.5) and the spatial modulation in Eq. (4.6), Newton's equations of motion in their form Eq. (4.3) have become:

$$\dot{\alpha}_{i,j} = -i[\omega_0 + wS(i) + V_{i,j}(t) - i\gamma_{i,j}] \alpha_{i,j} - i[V_{i,j}(t) - i\gamma_{i,j} + 2\Omega_x + 2\Omega_y] \alpha_{i,j}^* + i \sum_{\pm 1} \Omega_x (\alpha_{i\pm 1,j} + \alpha_{i\pm 1,j}^*) + i \sum_{\pm 1} \Omega_y (\alpha_{i,j\pm 1} + \alpha_{i,j\pm 1}^*) + i f_{i,j}^{\text{ex}}(t). \quad (4.10)$$

4.1.2 Analytical derivation of the Harper-Hofstadter effective equation of motion.

We will now show how Newton's equations of motion take the form of the Heisenberg equations of motion for the Harper-Hofstadter model. Performing the rotating-wave approximation to Eq. (4.10), we straightforwardly obtain:

$$\dot{\alpha}_{i,j} = -i[\omega_0 + wS(i) + V_{i,j}(t) - i\gamma_{i,j}] \alpha_{i,j} + i \sum_{\pm 1} [\Omega_x \alpha_{i\pm 1,j} + \Omega_y \alpha_{i,j\pm 1}] + i f_{i,j}^{\text{ex}}(t). \quad (4.11)$$

Throughout the Chapter we will focus on the case where a single (i_p, j_p) site is driven. We again assume the inequality chain as in Eq. (3.19):

$$\omega_0 \gg sw \gg \Omega_{x,y} \gg \gamma_{i,j}, \quad (4.12)$$

where this time the first inequality required for the rotating-wave approximation is more strict because it has to be valid for the fastest frequency of the temporal modulation in Eq. (4.8).

Following an analogous procedure to that in Chap. 3, we introduce the $\beta_{i,j}$ variables:

$$\beta_{i,j}(t) \equiv \alpha_{i,j}(t) e^{iwt(S(i)-S(i_p))} e^{i\omega_{\text{ex}}t} e^{i \int_0^t V_{i,j}(t') dt'} \quad (4.13)$$

and look for the steady-state solution. In the steady-state regime, the $\beta_{i,j}$ variables oscillate with the same frequency as the external driving force, which is tuned in the vicinity of the natural frequency of the driven pendulum (i_p, j_p) . We again obtain the effective equations of motion within the Floquet formalism of time periodic systems in the high-frequency limit, that is by time averaging Eq. (4.11) over the period $T = 2\pi/w$ of the temporal modulation. The full forms of these equations are given in Appendix D and are expressed as sums of Bessel functions. Here we present a simplified form of the effective equations, that was obtained by considering only the largest contribution in these sums:

$$\dot{\beta}_{i,j} = -i(\omega_0 + wS(i_p) - \omega_{\text{ex}}) \beta_{i,j} - \gamma_{i,j} \beta_{i,j} + i f_{i_p, j_p}^{\text{ex}} \mathcal{J}_0(V/w)^2 + i \sum_{\pm 1} \Omega_x e^{\mp i(\varphi_{i\pm 1, j} - \frac{\pi}{2})} \mathcal{J}_{\pm 1}(I_0) \mathcal{J}_0(I_0) \beta_{i\pm 1, j} + i \sum_{\pm 1} \Omega_y \mathcal{J}_0(I_0)^2 \beta_{i, j\pm 1} \quad (4.14)$$

where, with the definition of the modulation phase in Eq. (4.9), we have introduced the following quantities:

$$\varphi_{i\pm 1, j} \equiv -(2\pi\theta(i+j) \pm \pi\theta) \quad (4.15)$$

$$I_0 \equiv \frac{V}{w} \sqrt{2 - 2\cos(2\pi\theta)}. \quad (4.16)$$

As detailed in Appendix D, the condition of validity for Eq. (4.14) is that the next order of the Bessel functions can be neglected,

$$\mathcal{J}_{(s-1)}(I_0) \ll \mathcal{J}_1(I_0). \quad (4.17)$$

From this expression, it is apparent that a very large period of the spatial modulation s would be optimal, with a linear ramp in the bare frequencies of the harmonic oscillators in Eq. (4.6). While this configuration is possible for the ultracold atomic system of [Aidelsburger et al. \[2013\]](#) or [Miyake et al. \[2013\]](#), it is not possible for these classical harmonic oscillators as the condition $\omega_0 \gg sw$ for the rotating-wave approximation does not allow us to use an arbitrarily large value of s . We found that a good compromise can be found already for s as small as 5.

As in Chap. 3, we notice from Eq. (4.14) that the frequencies Ω_x and Ω_y are renormalised by the Bessel functions and also that the effective couplings along the two directions of the lattice can be very different from each other. Since the goal of this Chapter is to recover the usual Harper-Hofstadter model with equal hopping in the two directions, it is useful to start from suitably chosen $\Omega_{x,y}$ that will result in the same effective coupling J for the two directions. We assume that the bare couplings can be chosen accordingly to the following relations:

$$\Omega_x = \frac{J}{\mathcal{J}_0(I_0) \mathcal{J}_1(I_0)}, \quad \Omega_y = \frac{J}{\mathcal{J}_0(I_0)^2}. \quad (4.18)$$

One must of course be careful in tuning the amplitude of the modulation V , such that the frequencies in Eq. (4.18) satisfy the inequality of Eq. (4.12).

As with the hopping terms, so is the amplitude of the driving term in Eq. (4.14) renormalised by the Bessel functions. We choose the bare driving force on the pumped site as:

$$f_{i_p, j_p}^{\text{ex}} = 2f/\mathcal{J}_0(V/w)^2 \quad (4.19)$$

in order to keep the effective driving intensity f constant as we vary V or w .

With Eq. (4.14), without driving and dissipation, we have a classical version of the Heisenberg equations derived from the following Harper-Hofstadter Hamiltonian:

$$\hat{\mathcal{H}} = \sum_{i,j} \left[-\Delta\omega \hat{\beta}_{i,j}^\dagger \hat{\beta}_{i,j} - J \left(\hat{\beta}_{i,j}^\dagger \hat{\beta}_{i,j+1} + e^{i2\pi\theta(i+j)} e^{i(\pi\theta - \pi/2)} \hat{\beta}_{i,j}^\dagger \hat{\beta}_{i+1,j} + \text{h.c.} \right) \right] \quad (4.20)$$

where $\Delta\omega \equiv \omega_{\text{ex}} - \omega_0 - wS(i_p)$ is the energy at which the Harper-Hofstadter model is coherently probed. We see clearly that the non-trivial hopping phase in Eq.(4.20) is determined by the modulation phase in Eq. (4.9). The magnetic flux enclosed within a plaquette is calculated by summing the phases accumulated on each link when hopping around a plaquette of the lattice. With the definition in Eq. (4.9), the sum of the phases gained by the complex hopping elements in Eq. (4.14), is uniform for the whole lattice and equal to:

$$\sum_{\square} \phi = \frac{1}{2} (-\phi_{i+1,j} - \phi_{i,j} + \phi_{i,j+1} + \phi_{i+1,j+1}) = 2\pi\theta, \quad (4.21)$$

where \square indicates that the sum is done over a plaquette of the lattice. As a result, our model of frequency-modulated coupled oscillators is a classical simulator of the Harper-Hofstadter model, where the magnetic flux is freely controlled by the parameter θ .

This outcome inspires us to generate the Hofstadter butterfly by simply tuning the phase of all the temporal modulations of the pendula according to Eq. (4.9). At this stage, we notice that any other choice of the temporal modulation phase $\phi_{i,j}$ leading to the same flux per plaquette would have given an equivalent Harper-Hofstadter model, that only differs by a gauge transformation.

First-order correction beyond the rotating-wave approximation.

Before concluding this section, we want to include the first effect beyond the rotating-wave approximation in our analytical results. Analogously to what we have seen in the previous Chapter, the first order correction is a global Bloch-Siegert shift of the detuning frequency:

$$\Delta\omega \equiv \omega_{\text{ex}} - \omega_0 - wS(i_p) \rightarrow \omega_{\text{ex}} - \bar{\omega},$$

with:

$$\bar{\omega} = \omega_0 + wS(i_p) - \frac{V^2}{4\omega_0} (2 - 2s + s^2) - 2 \frac{(\Omega_x + \Omega_y)^2}{\omega_0}. \quad (4.22)$$

The derivation of such a shift is the same as the one for obtaining Eq. (3.20): more details are given in Appendix C.

4.2 Results of the numerical simulations.

We now present the numerical results of the integration of the equations of motion in their complete form given in Eq. (4.10). In order to assess the validity of the effective Harper-Hofstadter model obtained via the Floquet approach, we have quantitatively compared our numerical predictions to those from the effective equation of motion for the Harper-Hofstadter model in Eq. (4.14).

The set of N time-dependent equations (4.10) have been numerically integrated with a standard fourth-order Runge-Kutta. The total time of integration $t \gg 1/\min(\gamma_{i,j}) \equiv 1/\gamma$ is chosen large enough to ensure that the steady state has been reached. The matching with the Floquet picture was performed, as in Chap. 3, by a stroboscopic sampling of the numerical solution at integer times of the period of the modulation $t_n = nT$. At these times t_n and under the monochromatic drive in Eq. (4.4), the steady-state solution has the form:

$$\alpha_{i,j}(t_n) \approx A_{i,j}(\omega_{\text{ex}}) e^{-i\omega_{\text{ex}}t_n},$$

where $A_{i,j}$ are the oscillation amplitudes of such a steady state. To study the response of the system to a particular driving frequency, we will present the total intensity, which is obtained as the sum of the oscillation amplitudes $|A_{i,j}|^2$ of all the pendula:

$$I(\omega_{\text{ex}}) = \sum_{i,j} |A_{i,j}(\omega_{\text{ex}})|^2.$$

The total intensity is a function of the detuning $\Delta\omega = \omega_{\text{ex}} - \bar{\omega}$, which is the energy at which the Harper-Hofstadter model is coherently probed. In fact, depending on the value of such a detuning $\Delta\omega$ and the position (i_p, j_p) of the driven site, different behaviours are expected. For $\Delta\omega$ within a band of the bulk Harper-Hofstadter model and (i_p, j_p) located far from the edges, the bulk of the system is excited and so the response is dominated by delocalized band states. When $\Delta\omega$ belongs to a gap between two energy bands, the total oscillation is suppressed unless (i_p, j_p) is located close to an edge of the system, so that edge states can be excited. We shall now present a detailed study of these regimes.

4.2.1 The response spectrum.

In Fig. 4.3 we present the response spectra calculated by driving the central site of a lattice of 25×25 pendula with a flux per plaquette of $\theta = 1/4$ in units of the flux quantum. Losses are chosen to be $\gamma/J = 0.1$, which are large enough to ensure that the excitation damps out before reaching the edge of the system and therefore that the response spectra is mainly determined by the bulk properties. The blue circles show the response spectra of a system of bare frequency $\omega_0/J = 200$, temporal modulation frequency $w/J = 20$ and amplitude such that $I_0 = 0.5$ from Eq. (4.16). This corresponds to $V/J \approx 7.1$, $\Omega_x/J \approx 4.4$ and $\Omega_y/J \approx 1.1$. The orange triangles are instead calculated for $\omega_0/J = 2000$, $w/J = 50$, and again $I_0 = 0.5$, which corresponds to $V/J \approx 17.7$, and the same Ω_x and Ω_y as before. We compare these numerical spectra with the prediction of the Harper-Hofstadter model.

From the properties of the pristine Harper-Hofstadter model, reviewed in Chap. 1, a system with a flux of $\theta = p/q$ has exactly q bands, separated by gaps in which topologically protected edge states are found. The theoretical position of these bands, for $\theta = 1/4$, is highlighted by the green shaded area. Although only 3 areas are highlighted, we must remember that for even q , the two central bands touch at a finite number of points in momentum space, therefore in energy they appear as a single band. We see that the regions of highest intensity for both blue and orange curves agree with the positions of the theoretical bands of the model, signifying that the general bulk properties are well captured by our description. The broadening of the peaks with respect to these green areas is due to the losses, and it is typical of the driven-dissipative systems, as reviewed by Carusotto and Ciuti [2013].

To have a more quantitative comparison with the theoretical model, we also show the prediction of the driven-dissipative Harper-Hofstadter model studied in Umucalılar and Carusotto [2011] and Ozawa and Carusotto [2014]. This spectra is presented with the solid black line in Fig. 4.3 and its detailed structure is directly comparable with our numerical results. From the theoretical driven-dissipative spectra, we see four peaks corresponding to the four bands of the Harper-Hofstadter. We notice immediately that the two outer peaks of our numerical spectra presented with blue circles are more clearly shaped than the two central ones, which are indeed difficult to resolve.

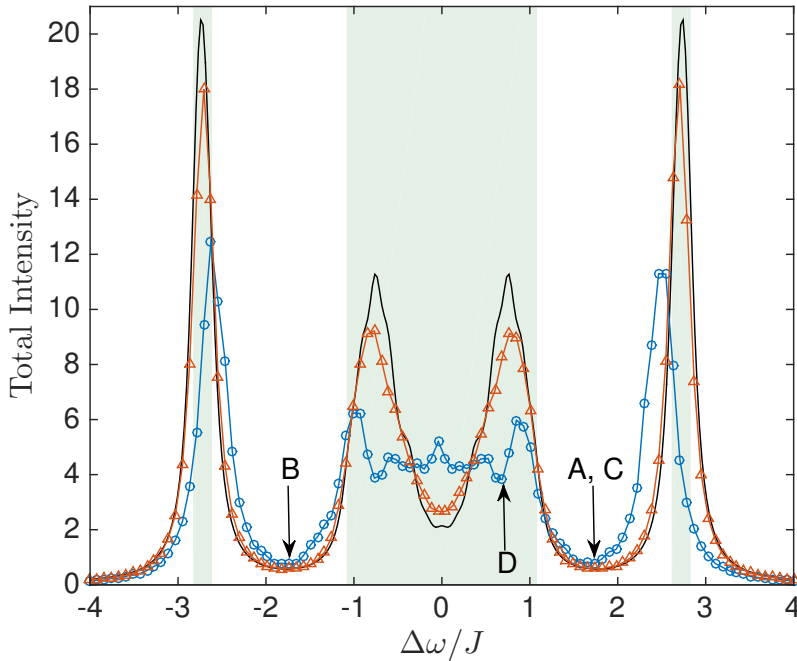


Figure 4.3: Response spectra of a 25×25 lattice with a flux per plaquette $\theta = 1/4$ and losses $\gamma/J = 0.1$ where the central lattice site is pumped. The blue circles and orange triangles correspond to the spectra calculated from the steady state of Eq. (4.10) as a function of the detuning from the external driving frequency $\Delta\omega = \omega_{\text{ex}} - \bar{\omega}$, including the shift in Eq. (4.22). Parameters are: $\omega_0/J = 200$, $w/J = 20$, $I_0 = 0.5$ for the blue circles, and $\omega_0/J = 2000$, $w/J = 50$, $I_0 = 0.5$ for the orange triangles. Black curve shows the spectra as obtained from the driven-dissipative Harper-Hofstadter model. Green areas show the position of the Harper-Hofstadter bands. Frequencies indicated by arrows are used in Fig. 4.4.

However, regardless of the detailed structure, the general form of the blue spectra is not dissimilar from this theoretical black spectra. The second numerical spectra, which is presented with orange triangles, instead agree very well, even in the finest detailed structure, with the spectra of the driven-dissipative Harper-Hofstadter model. This is because for the considered set of parameters, the inequality (4.12) is better satisfied, meaning that the system is well described by the equations obtained in the rotating-wave approximation. We do not show here, but we have checked that the deviation from the Harper-Hofstadter model would be much more dramatic for parameters that satisfy the inequality (4.12) even less than the parameters for the blue spectra: this is because, by reducing ω_0 , the rotating-wave approximation is no longer valid. We will investigate the contribution of the counter-rotating-wave terms in this break-down of the effective model in the next Chapter.

4.2.2 Topological edge states.

We now want to study the properties of the eigenmodes associated with the energy spectra of Fig. 4.3, to show that, as expected from the Harper-Hofstadter model, the states whose energy lies within the gaps are topologically protected and localized along the edge of the system.

To this end, in Fig. 4.4 we show, in colour scale, the steady state intensity distribution obtained by pumping one site in the middle of the bottom edge with different values of the detuning $\Delta\omega/J$ corresponding to the arrows in Fig. 4.3. System parameters are $\omega_0/J = 200$, $w/J = 20$ and $I_0 = 0.5$ as for the blue spectra of Fig. 4.3. Losses are $\gamma/J = 0.05$, and are smaller than the previous figure in order to allow the excitation amplitude to propagate over an adequate distance, before decaying. In fact, this distance is set by the ratio of the group velocity of the edge state over the loss rate, as is usual in driven-dissipative systems.

The intensity distributions shown in panels 4.4-A, 4.4-B and 4.4-C are obtained by driving the system in the band gap where the chiral edge-states are expected, that is, between two peaks

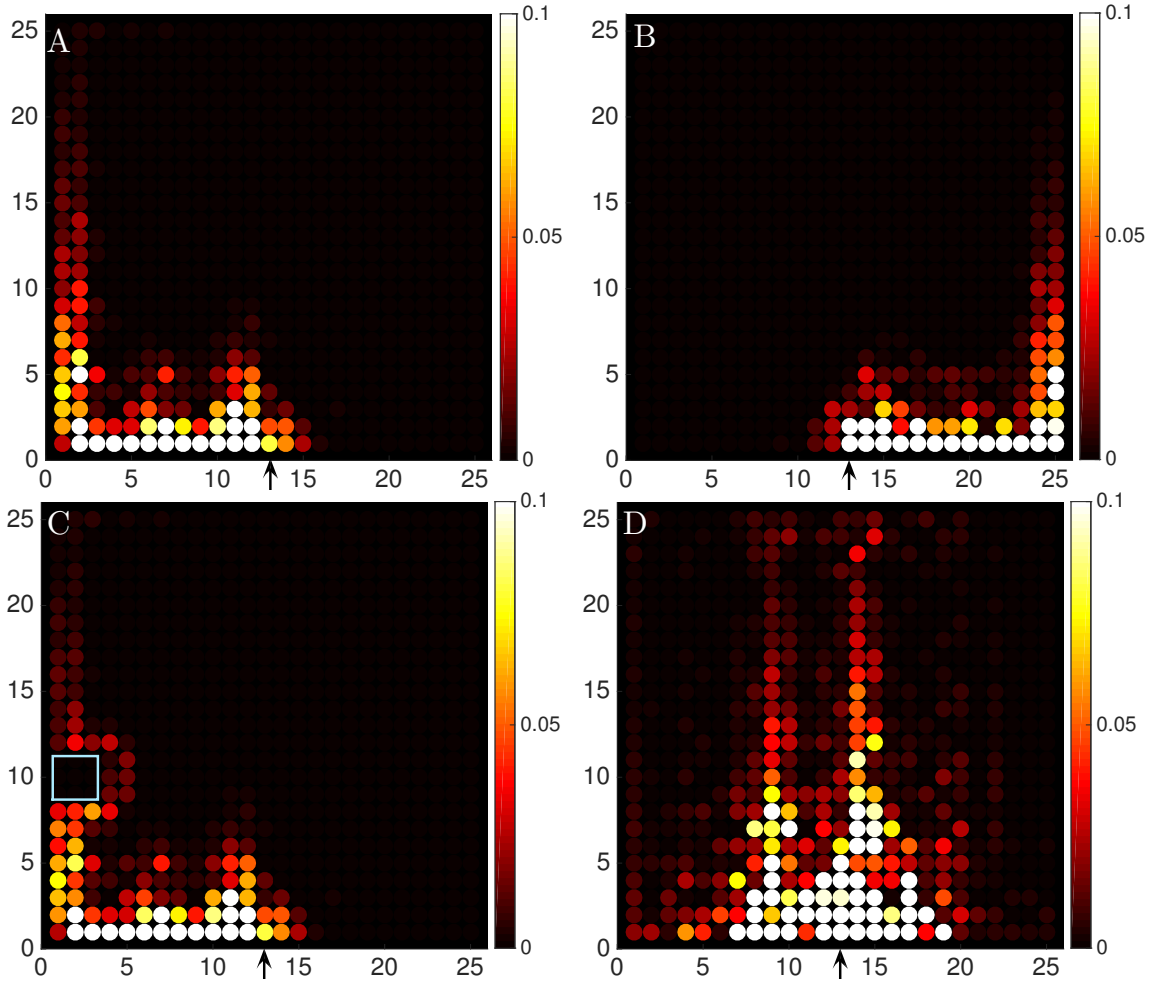


Figure 4.4: Spatial steady-state oscillation intensity distribution for a lattice of 25×25 pendula with $\theta = 1/4$, $\gamma/J = 0.05$, $I_0 = 0.5$, $w/J = 20$ and $\omega_0/J = 200$, obtained by pumping a single site on the lower edge for different values of the detuning of the pumping frequency $\Delta\omega/J$. Panel **A** and **C** are for $\Delta\omega/J = 1.7$ located in a gap and show the excitation of an edge state with clockwise chirality. In panel **C**, the blue square indicates the position of a defect composed of 3×3 missing pendula on the left edge. Panel **B** is for $\Delta\omega/J = -1.7$ located again in a gap and shows the excitation of an edge state with counter-clockwise chirality. Panel **D** is for $\Delta\omega/J = 0.7$ located in an energy band and shows the excitation of bulk states. The arrow indicates the position of the pumped site on the lower edge.

in the spectra of Fig. 4.3. We see the pendula with the biggest oscillation amplitudes are indeed localized on the edge of the system, apart from a small excitation that penetrates in the bulk close to the pendulum that is driven. Such excitation is exponentially decaying into the bulk, because no propagating states are available at that energy in the bulk of the lattice. As one can see by comparing panels 4.4-A and 4.4-B, the direction of unidirectional propagation changes when the sign of $\Delta\omega$ is changed, as expected from the Harper-Hofstadter model. Also the chirality of the edge states is very clear from the direction of the propagation compared to the position of the arrow in the panels, that indicates the pumped site. In Fig. 4.4-C, we illustrate the topological robustness of the edge state against a defect, modelled as 3×3 missing pendula, that is introduced on the left edge of the lattice. The edge state is found to propagate around the defect, without being scattered into the bulk, as expected.

Finally, panel 4.4-D shows the steady-state intensity distribution when the detuning corresponds to a Harper-Hofstadter band: in this case, the excitation penetrates deeply into the bulk and shows no preferred chirality.

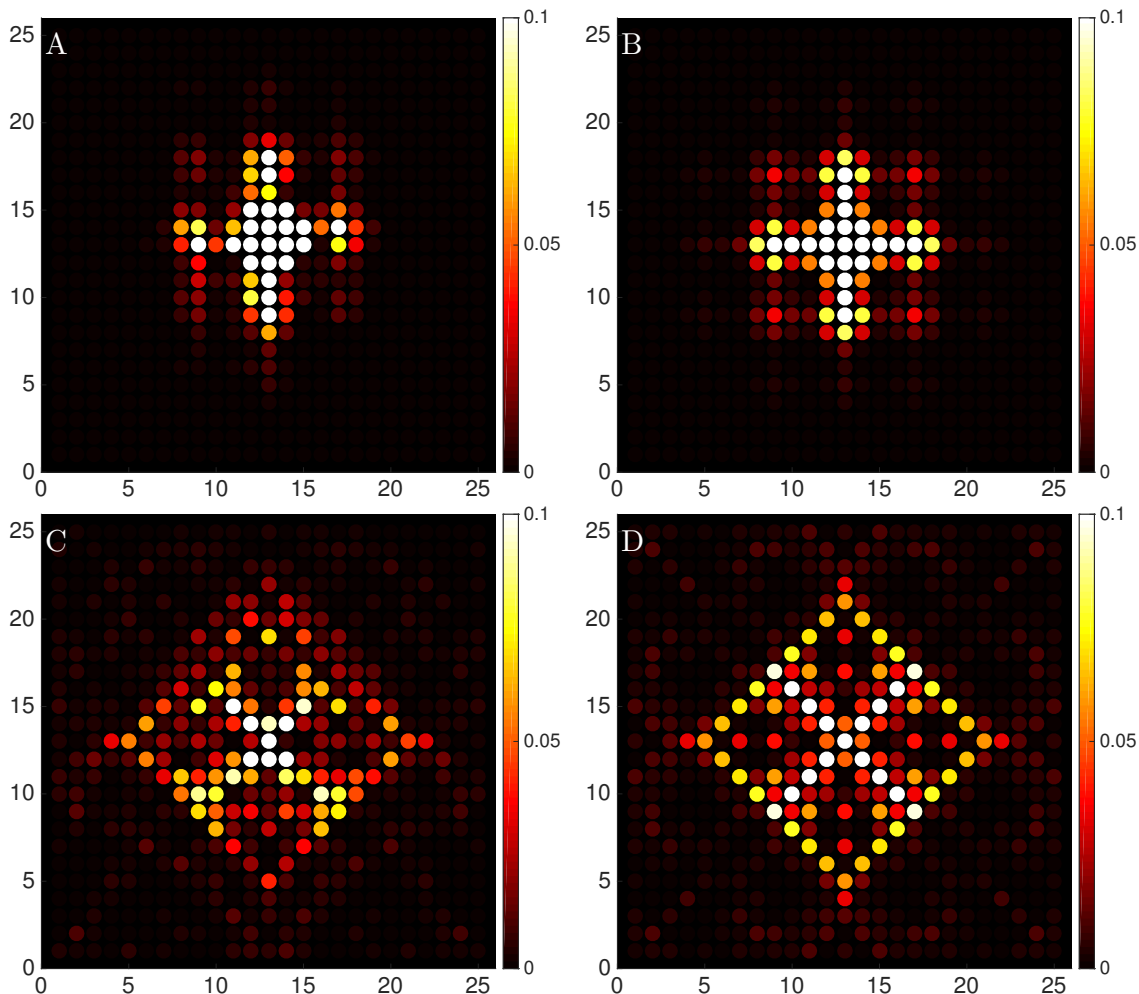


Figure 4.5: Spatial steady-state oscillation intensity pattern for a lattice of 25×25 pendula with $\gamma/J = 0.1$, $I_0 = 0.5$, $w/J = 50$ and $\omega_0/J = 2000$, obtained by pumping the central site. Panels **A** and **C** are obtained from full numerical integration of Newton's equation of motion, while panels **B** and **D** are obtained from a driven-dissipative Harper-Hofstadter model as in [Umucalilar and Carusotto \[2011\]](#) and [Ozawa and Carusotto \[2014\]](#), and are shown for comparison. The first row is for $\theta = 1/4$ and $\Delta\omega/J = 2.7$ corresponding to the center of the highest band. The second row is for $\theta = 1/9$ and $\Delta\omega/J = 0$ corresponding to the middle of the central band.

4.2.3 Bulk wave functions.

While the existence of the chiral edge states is one hallmark of a quantum Hall system, we now demonstrate that our scheme truly is a simulator of the Harper-Hofstadter model. We show now that the characteristic features of the driven-dissipative Harper-Hofstadter model can also be observed in the response of the bulk of the system, and not only from the existence of the edge states. In Fig. 4.5, we present the intensity distribution of the system when the central site of the lattice is driven with a detuning frequency resonant with an energy band. For the panels in the upper row, the magnetic flux is $\theta = 1/4$, while $\theta = 1/9$ for the panels in the lower row; losses are $\gamma/J = 0.1$ in all panels. Panels 4.5-A and 4.5-C show the distributions of the full numerical integration of Eq. (4.10) with $\omega_0/J = 2000$, $w/J = 50$, $I_0 = 0.5$ and can be compared with panels 4.5-B and 4.5-D that are obtained from the driven-dissipative Harper-Hofstadter model as in [Umucalilar and Carusotto \[2011\]](#) and [Ozawa and Carusotto \[2014\]](#). We notice that the two pattern distributions are in excellent qualitative agreement, in particular where the symmetry and the periodicity of the pattern is concerned. As anticipated around Fig. 4.3, when the natural frequency ω_0 is reduced away from the rotating-wave approximation limit, the spatially symmetric structure of the oscillation amplitude pattern is broken and the agreement with the driven-dissipative Harper-Hofstadter model is less good (not shown).

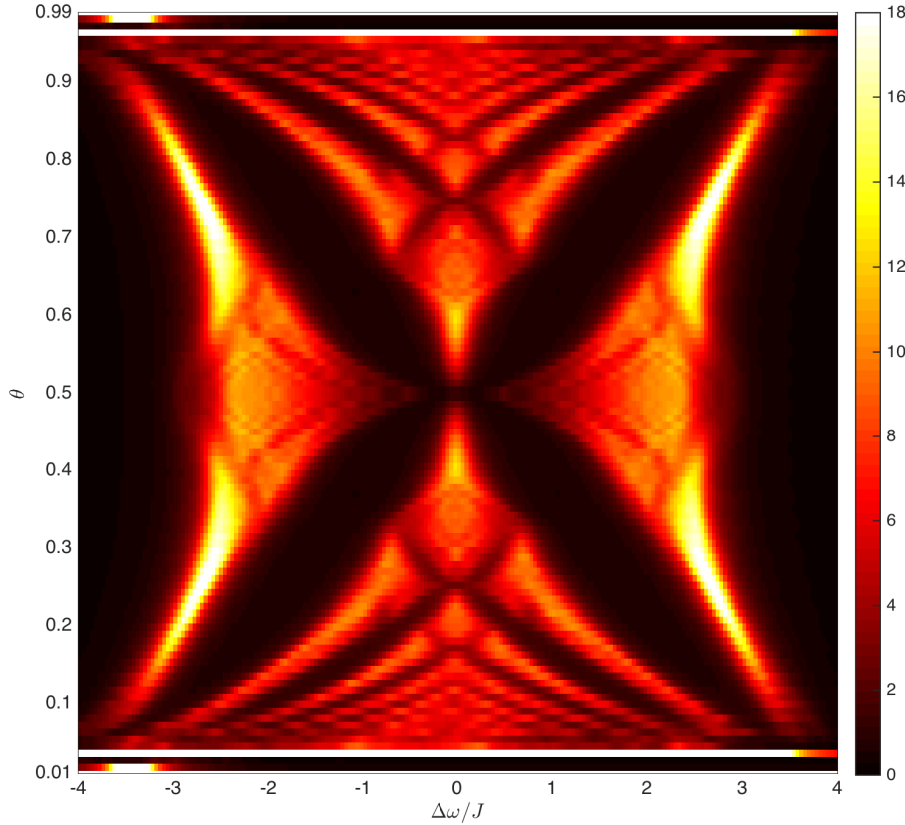


Figure 4.6: Total intensity response spectra as a function of flux per plaquette θ and frequency detuning $\Delta\omega/J$. The total intensity of the oscillation is depicted with the color scale, where lower intensities are in darker colors. Black regions indicating negligible intensities correspond to the energy gaps between energy bands. The peculiar structure of the Hofstadter butterfly pattern is clearly visible. System parameters are: $\omega_0/J = 2000$, $w/J = 50$, $\gamma/J = 0.1$, $I_0 = 0.5$, for a lattice of 25×25 sites where only the central one is pumped.

4.2.4 The Hofstadter butterfly.

The system of frequency-modulated coupled pendula that we have proposed in this Chapter allows us to change the magnetic flux θ per plaquette by simply adjusting the phase of the modulation of each pendula in Eq. (4.8). In this way, our scheme is sufficiently flexible to explore a wide portion of the flux-frequency plane and observe the Hofstadter butterfly. Collecting a large number of numerically calculated spectra of the total intensity for different values of θ in a single colour-plot, we obtain the pattern shown in Fig. 4.6. Although the presence of dissipation does not allow us to resolve details of the fractal structure that are smaller than the loss rate, the emerging picture shows a close resemblance to the butterfly of Fig. 1.2.

One remark on the numerical method used to calculate Fig. 4.6. In order to speed up the computational time, the equations of motion in Eq. (4.3) have been solved by expanding the solution in the Fourier basis, instead of solving the full differential equations until reaching the steady state. Solving the linear system for the Fourier components coupled by the time-dependent modulation is equivalent to, but much faster than, solving the full differential equations until reaching the steady state. More details on this decomposition method are found in Appendix E.

It is interesting to note that the agreement with the well-known Hofstadter butterfly gets worse in the top and bottom regions of the spectra and eventually breaks down. Those areas correspond to very low values of the magnetic flux θ for which the number of bands is large and the smoothing has most dramatic consequences. To understand the break-down from the butterfly structure, we checked the solutions with the full numerical Runge-Kutta integration method and we observed that in these regions the system is dynamically unstable. This means that a stationary steady state can not exist and therefore the Hofstadter butterfly pattern completely breaks down. These deviations stem from the strength of the counter-rotating-wave-terms as controlled by the amplitude of the

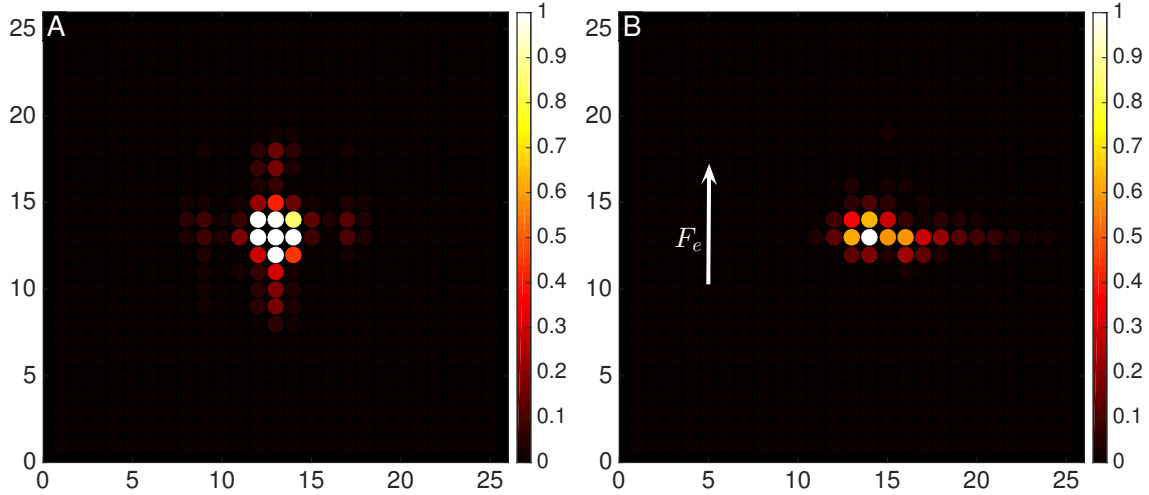


Figure 4.7: Spatial steady-state oscillation intensity distribution for a lattice of 25×25 pendula with $\theta = 1/4$, $\gamma/J = 0.1$, $I_0 = 0.5$, $w/J = 50$ and $\omega_0/J = 2000$, obtained by pumping the central site with a detuning corresponding to the middle of the lowest band $\Delta\omega/J = -2.7$. For panel **A** there is no external force $F_e/J = 0$, and the centre of the intensity distribution indeed remains at the centre of the system. For panel **B**, the force $F_e/J = 0.5$ is directed along the y -direction as indicated by the arrow and induces a sizeable rightward shift of the centre of the distribution towards the positive x direction as expected from the integer quantum Hall effect.

temporal modulation V . In our simulation, we take $I_0 = 0.5$ to be fixed which, from Eq. (4.16), results in an increase of V as the flux is decreased. Larger V implies a larger contribution from counter-rotating-wave terms, that results in the emergence of a parametric instability Arnold [1989]. We note that the spectra obtained from the Fourier decomposition method appear to be still stable despite the exponential growth of the Runge-Kutta solution because such a method begins from the ansatz of a steady-state solution and so cannot predict the instability. More insights into the instability will be given in the following Chapter.

4.2.5 The quantum Hall effect and the Chern number.

In the previous Sections, we have demonstrated that the system of frequency-modulated coupled harmonic oscillators can be a classical simulator of the Harper-Hofstadter model. As a final point, we now show that an analogue of the integer quantum Hall effect can be observed even in a classical mechanical context. We have seen in Chap. 1 that the main feature of the integer quantum Hall effect is that a current appears in the direction orthogonal to the applied electric field. The associated conductivity is an integer multiple of the conductance quantum e^2/h , and this integer is related to the Chern number of the populated bands. For the bosonic model considered here, these bands can be populated by a suitable excitation scheme.

In order to introduce an analogue of the electric field in our model, we need to generate a linear potential acting on the excitation field $\alpha_{i,j}$. Applying such a potential along the positive y -direction would correspond to a term of the form $-iF_e j \alpha_{i,j}$ in Eq. (4.3). Equivalently, and perhaps more straightforwardly, the analogue electric field could be introduced through an additional linear gradient of the bare oscillation frequency along the y -direction in Eq. (4.6), with $\tilde{\omega}_{i,j} \rightarrow \tilde{\omega}_{i,j} + F_e j$.

In Fig. 4.7-A we show the intensity distribution of a system of 25×25 pendula with $\theta = 1/4$ and $\gamma/J = 0.1$ in the absence of the external force and for a detuning $\Delta\omega/J = -2.7$ such that only the lowest band is excited with a resulting population that is approximately uniform. As discussed by Ozawa and Carusotto [2014], these conditions can be fulfilled provided the energy width of the band Δ_{width} is much smaller than the band gap Δ_{gap} and the loss rate falls in between these two energy scales. The intensity pattern is symmetric both in x and in y and is centred around the middle point. When a non-zero force $F_e/J = 0.5$ along the vertical direction is applied as in panel 4.7-B, the oscillation pattern clearly shifts to the right in the direction orthogonal to the applied force. This is a manifestation of the Lorentz force and a clear signature of a Hall-like effect.

| Band | | 1 st | 2 nd | 3 rd |
|------------------------|-------|-----------------|-----------------|-----------------|
| $\theta = \frac{1}{3}$ | C_e | -0.803 | | -0.873 |
| | C | -1 | +2 | -1 |
| $\theta = \frac{1}{4}$ | C_e | -0.972 | | |
| | C | -1 | +1 | +1 |
| $\theta = \frac{1}{5}$ | C_e | -0.878 | | |
| | C | -1 | -1 | +4 |
| $\theta = \frac{2}{5}$ | C_e | | | +1.725 |
| | C | +2 | -3 | +2 |

Table 4.1: Estimated value C_e of the Chern numbers as calculated from Eq. (4.23) for a system of 25×25 lattice sites with the parameters given in the main text. These are compared to the exact values C , for different bands and several values of the rational flux θ .

In order to assess the quantized nature of this Hall effect, we can quantify the lateral shift as:

$$\langle x \rangle \equiv \sum_{i,j} \frac{j |A_{i,j}|^2}{I(\omega_{ex})}$$

and compare it to the prediction for the integer quantum Hall effect in driven-dissipative systems of [Ozawa and Carusotto \[2014\]](#):

$$\langle x \rangle = -F_e \left(\frac{qC}{2\pi\gamma} + \eta \right). \quad (4.23)$$

The q in Eq. (4.23) is the denominator of the rational flux $\theta = p/q$, while C is the Chern number of the excited band, as defined in Eq. (1.29). The real number η quantifies the spurious contribution of the bandwidth, that is responsible for a non-uniform population of the band, as well of the other neighbouring bands.

In Table 4.1 we summarize the estimated Chern numbers C_e of different bands for four different θ as calculated from Eq. (4.23) for a system of 25×25 lattice sites, $\omega_0/J = 2000$, $w/J = 50$, $F_e/J = 0.07$ and $\Delta_{\text{width}} < \gamma < \Delta_{\text{gap}}$. The constant η , that does not depend on the losses γ , is eliminated by calculating the linear coefficient in the shift given in Eq. (4.23) for two values of $\gamma \in [\Delta_{\text{width}}, \Delta_{\text{gap}}]$. Choosing any value in this frequency range only affects the calculation of the Chern number to the least-significant digit. When the method is not applicable because $\Delta_{\text{width}} \gtrsim \Delta_{\text{gap}}$, the corresponding Chern number of these bands was not calculated. In all other cases, the agreement with the Chern number C of the Harper-Hofstadter model is good.


The topological invariant, together with the energy spectra and the chiral edge states, confirm that the system described in this Chapter, within the rotating wave approximation, is the classical mechanical analogue of the Harper-Hofstadter model. In the next chapter we shall discuss the relaxation of the rotating wave approximation and its role in the effective model.

Chapter 5

The Harper-Hofstadter model in a classical mechanical system: beyond the rotating-wave approximation.

If you raise a wall, think of what is left outside.

Italo Calvino – *Il barone rampante*.

 We have shown in Chap. 3 that Newton’s equations for a system of coupled classical harmonic oscillators are, in a convenient regime, analogous to the Heisenberg equations of motion obtained from a quantum tight-binding Hamiltonian. In Chapter 4 we have also proved that arrays of pendula, with a specific frequency-modulation scheme, obey the effective dynamics of the Harper-Hofstadter model.

The rotating-wave approximation plays a crucial role in the validity of this formal analogy. In fact, it allows us to neglect, at the level of the effective Hamiltonian, the terms that are “not commuting” with the number “operator” $\alpha^* \alpha$, and to keep only the ones that are conserving the oscillation energy $|\alpha|^2$ (*i.e.* the instantaneous energy rather than the total energy, which also contains the elastic energy of the springs). In such a way, the remaining terms are exactly the ones of a tight-binding Hamiltonian, when the quantum operators are replaced by C-numbers. In Chap. 4, we also mentioned that when the rotating-wave approximation is more and more relaxed, a break-down of the effective Harper-Hofstadter model may happen.

In this Chapter we want to deeply investigate the limitations of such a mapping as the role of the counter-rotating-wave terms is increased. To this end, we study the eigenvalues of the system without driving and dissipation, which give an energy spectrum that is not smeared out by the losses and to obtain a clear estimate of the gaps between energy bands. As a result, we observe a distortion of the Harper-Hofstadter bands, that is eventually accompanied by a band closing with the disappearance of topological edge states for increasing strength of the counter-rotating-wave terms in the equation of motion. Besides, we also notice that, for certain values of the parameters, complex energy modes in the energy spectrum may appear. Those complex modes signal the emergence of a dynamical instability, which was anticipated also in the previous Chapter when discussing the Hofstadter butterfly around Fig. 4.6. We study such an instability and relate it to the *parametric instability* of a classical system with time-dependent parameters, that is well-known from classical mechanics textbooks such as Arnold [1989].

The main results of this chapter are partially reported in Salerno et al. [2016].

5.1 A reformulation of the model.

In this section we want to derive the Floquet energy spectrum of the system of frequency-

modulated coupled pendula without driving and dissipation. We will not integrate the differential equation as we did in Chap. (4), but rather directly diagonalize the Floquet effective Hamiltonian. In this way, by making use of the theory of stability in classical mechanics, we can gain more analytical insights into the parametric instability and predict its emergence.

It is convenient to recast the N equations in Eq. (4.3), together with the corresponding N equations for $\vec{\alpha}^*$, in the matrix form:

$$\boxed{i \frac{\partial}{\partial t} \begin{pmatrix} \vec{\alpha} \\ \vec{\alpha}^* \end{pmatrix} = \mathcal{M}(t) \begin{pmatrix} \vec{\alpha} \\ \vec{\alpha}^* \end{pmatrix}}, \quad (5.1)$$

where $\vec{\alpha} = (\alpha_{1,1}, \alpha_{2,1} \dots \alpha_{N_x-1, N_y}, \alpha_{N_x, N_y})^\top$ is a column vector. The $2N \times 2N$ time-periodic matrix $\mathcal{M}(t)$ has the following block-structure:

$$\mathcal{M}(t) = \begin{pmatrix} A(t) & B(t) \\ -B(t) & -A(t) \end{pmatrix}. \quad (5.2)$$

The $A(t)$ and $B(t)$ are $N \times N$ real symmetric matrices, periodic with the modulation period $T = 2\pi/w$, and with the following structure:

$$A(t) = \begin{pmatrix} d_{1,1}^A(t) & -\Omega_x & 0 & \dots & 0 & -\Omega_y & 0 & \dots & \dots & 0 \\ -\Omega_x & d_{2,1}^A(t) & -\Omega_x & 0 & \dots & 0 & -\Omega_y & 0 & \dots & 0 \\ 0 \dots & \ddots & \ddots & \ddots & 0 & \dots & 0 & \ddots & \dots & 0 \\ 0 \dots & \ddots & 0 \dots & \ddots & \ddots & \ddots & 0 \dots & \ddots & \dots & 0 \\ 0 \dots & \ddots & 0 & \dots & 0 & \ddots & \ddots & \ddots & \dots & 0 \\ 0 \dots & 0 & -\Omega_y & 0 & \dots & 0 & -\Omega_x & d_{N_x-1, N_y}^A & -\Omega_x & \\ 0 \dots & \dots & 0 & -\Omega_y & 0 & \dots & 0 & -\Omega_x & d_{N_x, N_y}^A(t) & \end{pmatrix}, \quad (5.3)$$

where the diagonal elements are: $d_{i,j}^A(t) = \omega_0 + wS(i) + V_{i,j}(t)$ and i, j are the indexes along the lattice. The matrix $B(t)$ has the same structure as $A(t)$ if the diagonal elements are instead: $d_{i,j}^B(t) = V_{i,j}(t) + 2\Omega_x + 2\Omega_y$.

Due to the coupling between the variables $\vec{\alpha}$ and $\vec{\alpha}^*$, we notice that the matrix $\mathcal{M}(t)$ is not Hermitian with respect to the standard positive-definite inner product, but that:

$$\mathcal{M}(t)^\dagger = \sigma_z \mathcal{M}(t) \sigma_z \quad (5.4)$$

where $\sigma_z = \begin{pmatrix} \mathbb{1} & 0 \\ 0 & -\mathbb{1} \end{pmatrix}$ and $\mathbb{1}$ is the $N \times N$ identity matrix. From the specific structure of the matrix $\mathcal{M}(t)$ and the fact that $A(t)$ and $B(t)$ are real symmetric matrices, Eq. (5.4) is easily proved.

5.1.1 The mapping at a period.

The mapping at a period is defined as:

$$\mathcal{U} \begin{pmatrix} \vec{\alpha}(0) \\ \vec{\alpha}(0)^* \end{pmatrix} = \begin{pmatrix} \vec{\alpha}(T) \\ \vec{\alpha}(T)^* \end{pmatrix}. \quad (5.5)$$

This represents the evolution operator of the state $(\vec{\alpha}, \vec{\alpha}^*)^\top$ within one period of the modulation T . The time evolution can be expressed as the evolution with a time-independent matrix. In fact, according to the Floquet theory of time-periodic systems, see for instance Bukov et al. [2015], we have that the mapping is defined as the time-ordered exponential matrix of the stroboscopic Floquet matrix \mathcal{M}_F :

$$\boxed{\mathcal{U} = e^{-i\mathcal{M}_F T} \equiv \mathcal{T} e^{-i \int_0^T \mathcal{M}(t) dt}}. \quad (5.6)$$

Without loss of generality, we can focus on the properties of this effective time-independent stroboscopic Floquet matrix \mathcal{M}_F rather than the original $\mathcal{M}(t)$. Let's say that ϵ_n is then an eigenvalue of \mathcal{M}_F :

$$\mathcal{M}_F \begin{pmatrix} \vec{u}_n \\ \vec{v}_n \end{pmatrix} = \epsilon_n \begin{pmatrix} \vec{u}_n \\ \vec{v}_n \end{pmatrix}, \quad (5.7)$$

where \vec{u}_n and \vec{v}_n are column vectors of length N . The matrix \mathcal{M}_F has a block structure similar to the one of $\mathcal{M}(t)$ in Eq. (5.2). Using its explicit expression, provided that all blocks are real, it follows that:

$$\mathcal{M}_F \begin{pmatrix} \vec{v}_n^* \\ \vec{u}_n^* \end{pmatrix} = -\epsilon_n^* \begin{pmatrix} \vec{v}_n^* \\ \vec{u}_n^* \end{pmatrix}. \quad (5.8)$$

5.2 The instability.

The non-Hermiticity of $\mathcal{M}(t)$ with respect to the standard inner product, that is stated in Eq. (5.4), is crucial for the appearance of complex energy-modes and the emergence of an instability. In fact, if $\mathcal{M}(t)$ were a Hermitian matrix, then \mathcal{U} would be unitary and the eigenvalues of the stroboscopic Floquet matrix \mathcal{M}_F would always be real, as in Shirley [1965]. In our system, instead, the matrix $\mathcal{M}(t)$ describes, in terms of the complex variables in Eq. (4.2), the one-period evolution of the system which is symplectic in the original $x_{i,j}$ and $p_{i,j}$ variables. As a result, this matrix is not Hermitian with respect to the standard inner product, as shown in Eq. (5.4) which implies that, in general, the eigenvalues of the Floquet matrix \mathcal{M}_F can also be complex, so the system can be dynamically unstable.

It is known from classical mechanics textbooks as Arnold [1989], that if all the eigenvalues λ_n of the mapping at a period \mathcal{U} are distinct and lie on the unit circle in the complex plane, the system is strongly stable, as it was proved by Krein [1950]. Since the Floquet matrix is related to \mathcal{U} by Eq. (5.6), the stability of the system can be checked just by looking at the eigenvalues of \mathcal{M}_F . Notice that the condition on the eigenvalues of \mathcal{U} to lie on the unit circle implies that the Floquet spectra has to be real. In fact, if ϵ_n is an eigenvalue of the Floquet matrix \mathcal{M}_F with eigenvector $(\vec{u}_n, \vec{v}_n)^\top$, then the eigenvalues of \mathcal{U} from Eq. (5.6) are:

$$\mathcal{U} \begin{pmatrix} \vec{u}_n \\ \vec{v}_n \end{pmatrix} = e^{-i\mathcal{M}_F T} \begin{pmatrix} \vec{u}_n \\ \vec{v}_n \end{pmatrix} = e^{-i\epsilon_n T} \begin{pmatrix} \vec{u}_n \\ \vec{v}_n \end{pmatrix}, \quad (5.9)$$

therefore

$$\boxed{\lambda_n = e^{-i\epsilon_n T}}. \quad (5.10)$$

It is straightforward to check that if $\epsilon_n \in \mathbb{R}$, *i.e.* the Floquet energies are real, then $|\lambda_n| = 1$ is on the unit circle and the system is dynamically stable, as it is expected.

5.2.1 The Krein signature.

From Eq. (5.7) and Eq. (5.8), we see that the matrix $\mathcal{M}(t)$, hence also the matrix \mathcal{M}_F , has two set of N eigenvalues ϵ_n and $-\epsilon_n^*$, that are associated with different eigenvectors. Such eigenvectors can be distinguished according to their *Krein signature*, as shown by Krein [1950]. The Krein signature of a certain eigenvector $(\vec{u}_n, \vec{v}_n)^\top$, corresponding to a certain eigenvalue, is defined as the sign of the norm:

$$\boxed{\mathcal{K} \equiv \text{sign} \left[\begin{pmatrix} u_n^* & v_n^* \end{pmatrix} \sigma_z \begin{pmatrix} u_n \\ v_n \end{pmatrix} \right] = \text{sign} [|u_n|^2 - |v_n|^2]}. \quad (5.11)$$

Notice that this definition corresponds to the norm of a semi-definite inner product, that follows from the modified condition of Hermiticity of the matrix $\mathcal{M}(t)$ in Eq. (5.4).

By definition, the Krein signature in Eq. (5.11) is either $\pm 1, 0$. The arising of the dynamical instability is signalled by this signature. In fact, we show that all unstable eigenvalues of \mathcal{M}_F have $\mathcal{K} = 0$.

From Eq. (5.7) and Eq. (5.8), it is easy to prove that if the Krein signature for the eigenvector corresponding to the eigenvalue ϵ_n is $\mathcal{K} = +1$:

$$|\vec{u}_n|^2 - |\vec{v}_n|^2 > 0,$$

then the Krein signature corresponding to the eigenvalue $-\epsilon_n^*$ is $\mathcal{K} = -1$, since:

$$|\vec{v}_n|^2 - |\vec{u}_n|^2 < 0.$$

Conversely, if the former is negative, the latter is positive. Therefore, if all the Krein signature are non-zero, there are equal numbers of states with positive and negative \mathcal{K} .

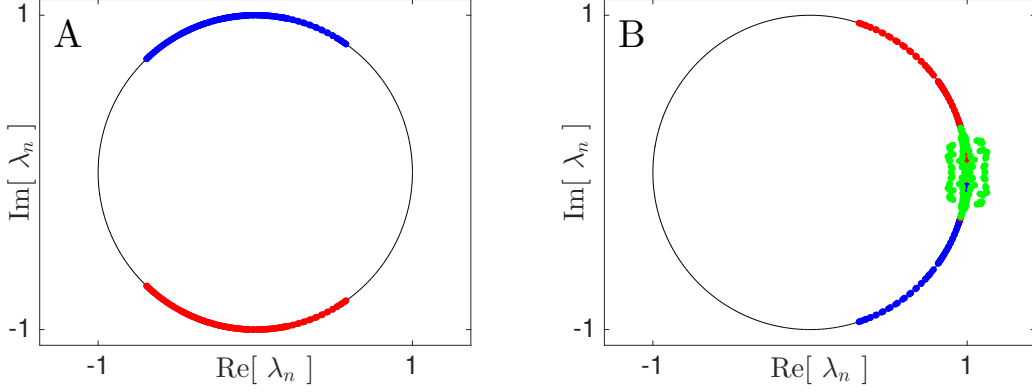


Figure 5.1: Representation on the unit circle of the eigenvalues of the matrix \mathcal{U} in the complex plane. Red points corresponds to eigenvalues with Krein signature $\mathcal{K} > 0$, points in blue are the eigenvalues with $\mathcal{K} < 0$ and green points are unstable eigenvalues with $\mathcal{K} = 0$. Panel **A** shows a stable configuration for $\omega_0/w = 5.4$, where all eigenvalues lies on the unit circles. Panel **B** shows the unstable configuration $\omega_0/w = 5.08$, where some eigenvalues are clearly not lying on the unit circle. Parameters are: $\theta = 1/5$, $s = 5$, $w/J = 50$, and periodic boundary conditions apply.

We now prove that the Krein signature of a certain eigenvector of the matrix \mathcal{M}_F is zero if the corresponding eigenvalue has a non-zero imaginary component.

We will use that the row vector $(\vec{u}_n^\dagger, -\vec{v}_n^\dagger)$ is a left eigenvector of \mathcal{M}_F with the eigenvalue ϵ_n^* . In fact:

$$\begin{aligned} (\vec{u}_n^\dagger \quad -\vec{v}_n^\dagger) \mathcal{M}_F &= \left[\mathcal{M}_F^\dagger \begin{pmatrix} \vec{u}_n \\ -\vec{v}_n \end{pmatrix} \right]^\dagger = \left[\mathcal{M}_F^\dagger \sigma_z \begin{pmatrix} \vec{u}_n \\ \vec{v}_n \end{pmatrix} \right]^\dagger = \left[\sigma_z \mathcal{M}_F \begin{pmatrix} \vec{u}_n \\ \vec{v}_n \end{pmatrix} \right]^\dagger \\ &= \left[\epsilon_n \begin{pmatrix} \vec{u}_n \\ -\vec{v}_n \end{pmatrix} \right]^\dagger = (\vec{u}_n^\dagger \quad -\vec{v}_n^\dagger) \epsilon_n^*. \end{aligned} \quad (5.12)$$

Therefore, we can write:

$$\begin{aligned} (\vec{u}_n^\dagger \quad -\vec{v}_n^\dagger) \left[\mathcal{M}_F \begin{pmatrix} \vec{u}_n \\ \vec{v}_n \end{pmatrix} \right] &= [(\vec{u}_n^\dagger \quad -\vec{v}_n^\dagger) \mathcal{M}_F] \begin{pmatrix} \vec{u}_n \\ \vec{v}_n \end{pmatrix} \\ (\vec{u}_n^\dagger \quad -\vec{v}_n^\dagger) \left[\epsilon_n \begin{pmatrix} \vec{u}_n \\ \vec{v}_n \end{pmatrix} \right] &= [(\vec{u}_n^\dagger \quad -\vec{v}_n^\dagger) \epsilon_n^*] \begin{pmatrix} \vec{u}_n \\ \vec{v}_n \end{pmatrix}. \end{aligned} \quad (5.13)$$

Multiplying out, we have:

$$\epsilon_n (|\vec{u}_n|^2 - |\vec{v}_n|^2) = \epsilon_n^* (|\vec{u}_n|^2 - |\vec{v}_n|^2). \quad (5.14)$$

If the imaginary part of ϵ_n is non-zero, $\epsilon_n \neq \epsilon_n^*$. Then, the previous equation is true only if:

$$|\vec{u}_n|^2 - |\vec{v}_n|^2 = 0. \quad (5.15)$$

Therefore, an unstable mode ϵ_n of the matrix \mathcal{M}_F corresponds to an eigenvector with zero Krein signature. This also holds for the eigenvalues λ_n of \mathcal{U} .

We now show a visual representation of emergence of the instability as the parameters of the system are changed. We have just proved that an unstable mode λ_n of the mapping \mathcal{U} has signature $\mathcal{K} = 0$, and we know that in this case $|\lambda_n| \neq 1$. Krein [1950] showed that an eigenvalue of \mathcal{U} can leave the unit circle only by colliding with another eigenvalue of opposite Krein signature, while two eigenvalues of the same Krein signature go through one another.

This is evident in Fig. 5.1, where we represent, on the unit circle in the complex plane, the eigenvalues of the matrix \mathcal{U} coloured according to their Krein signature. Eigenvalues with positive \mathcal{K} are shown in red, eigenvalues with negative \mathcal{K} are displayed in blue and unstable eigenvalues with zero Krein signature are displayed in green.

We have diagonalized the matrix \mathcal{U} obtained from Eq. (5.6) for two different values of the ratio ω_0/w . We recall that the eigenvalues of the Floquet matrix \mathcal{M}_F correspond to the oscillation

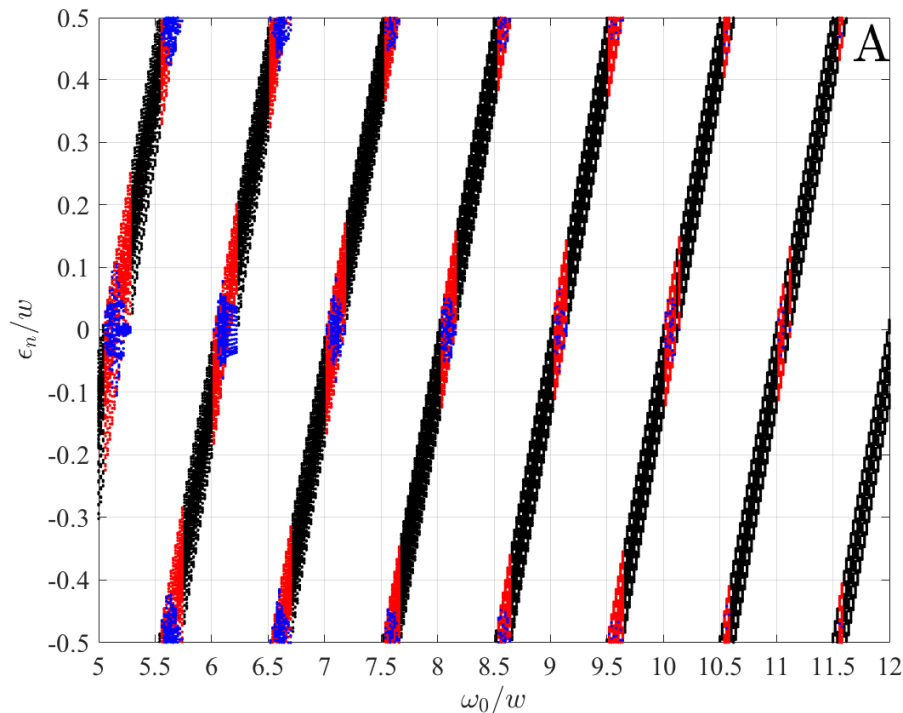


Figure 5.2: Floquet quasi-energies ϵ_n , modulo w , in units of w , associated with $\mathcal{K} \geq 0$, and $|\lambda_n| \geq 1$. The system has a magnetic flux $\theta = 1/5$, with periodic boundary conditions; driving and dissipation are not included. The energy spectra are presented as a function of ω_0/w , for a fixed value of the amplitude modulation $V/w \approx 0.4$. When all the eigenvalues at a particular frequency are stable, we denote them in black, otherwise we denote them either in red or blue. Red points are purely real modes, while blue points are the unstable modes, plotted according to the real part of their complex energy. Parameters are: $s = 5$, $w/J = 50$, $V/J = 20$, and periodic boundary conditions apply.

frequencies of the system, and therefore are in the vicinity of the natural bare frequency ω_0 . As a consequence, when the ratio ω_0/w is changed, the eigenvalues λ_n of \mathcal{U} rotate on the unit circle. A full rotation on the unit circle is performed when ω_0/w is increased by 1, because they are periodic with $w = 2\pi/T$, as: $e^{-i\epsilon_n(t+T)} = e^{-i\epsilon_n t}$.

In panel 5.1A, we show the case of $\omega_0/w = 5.4$. All eigenvalues λ_n have $\mathcal{K} \neq 0$ and, as expected, they lie on the unit circle in the complex plane. When the natural frequency of the pendula ω_0 is reduced, the eigenvalues with negative Krein signature rotate clock-wise, while the eigenvalues with positive Krein signature rotate counter-clock-wise. The two different sets collide when reaching the real axis on the complex plane, and an instability develops. In panel 5.1B where $\omega_0/w = 5.08$, we show that eigenvalues with zero Krein signature are not lying on the unit circle, while some of the positive \mathcal{K} eigenvalues have already collided with the negative ones and moved on.

5.2.2 The parametric instability.

We have just seen that, as a function of the ratio ω_0/w , the eigenvalues of the mapping \mathcal{U} rotate on the unit circle. The parametric instability arises every time the positive and negative Krein eigenvalues meet on the real axis of the complex-plane. This happens twice in a round-trip, at $\text{Re}[\lambda_n] = \pm 1$. The eigenvalues λ_n perform a full rotation on the unit circle when ω_0/w is increased by 1, therefore the instability occurs when:

$$\boxed{2\omega_0/w = m, \text{ with } m \in \mathbb{N}.} \quad (5.16)$$

This result is well-known in the classical mechanical context of the parametric resonance, see Arnold [1989]. However, the result in Eq. (5.16) is valid in the limit of small amplitude of the

modulation $V \rightarrow 0$, Arnold [1989]. In general, there is a region of parameters ω_0/w , around the values of Eq. (5.16) for which the system is parametrically unstable, and a large amplitude V increases this region.

In Fig. 5.2 the Floquet energy spectra ϵ_n of the system are shown as the bare frequency ω_0 is changed for a fixed value of w and of the amplitude modulation $V/w \approx 0.4$. With no loss of information, in the figure we have only presented the stable eigenvalues ϵ_n of the Floquet matrix \mathcal{M}_F that are associated with a positive Krein-signature and among the unstable eigenvalues, only the ones with $|e^{-i\epsilon_n T}| = |\lambda_n| \geq 1$. The eigenvalues are displayed modulo w in order to emphasise their linear dependence on the frequency ω_0 and their periodicity in w . When all the eigenvalues ϵ_n at a particular frequency are stable, we denote them in black, otherwise we denote them either in red or blue. The points in blue correspond to the modes which have become unstable, plotted here according to the real part of the energy. The points in red are eigenmodes with purely real energies. We refer to frequencies for which there are blue points as instability regions.

As anticipated above, we observe that the instability regions occur every integer and half-integer times of ω_0/w . In particular, it is evident that purely imaginary modes start to develop around $\epsilon_n/w = 0$ and $\epsilon_n/w = \pm 1/2$, which is $\text{Re}[\lambda_n] = 1$. We also notice that the extension of the blue unstable points (that have $\mathcal{K} = 0$) gets larger as the rotating-wave approximation is less valid in the small ω_0 limit. However, we find that the instabilities still persist for a very high ratio $\omega_0/w \approx 12$ in the conservative case considered here.

Theoretically, the parametric instability can be observed around the infinite collection of points in Eq. (5.16). In practice, it is usually observed only for small values of the m in Eq. (5.16), and the reasons are the followings. The region of instability gets thinner as the number m is increased, as is visible also in Fig. 5.2. Besides this, the instability itself is weaker for large m as shown in Arnold [1989], and we have also observed that the deviation from $|\lambda_n| = 1$ gets correspondingly weaker as m is increased. Once losses are included in the model, stability improves because there is a minimum value \bar{V} of the amplitude of the modulation in order for the parametric instability to appear. The value \bar{V} gets larger for larger m in Eq. (5.16). These arguments explain why in the large ω_0 calculations shown in the previous Chapter, instabilities were only observed at very high amplitude of the modulation V , on the order of $V/J \approx 100$.

5.3 The band-gap closing and the topological transition.

Finally, we show how the detailed structure of the Floquet quasi-energy spectra is affected by the counter-rotating-wave terms as the ratio ω_0/w is reduced.

We consider a system with magnetic flux $\theta = 1/q$ and apply periodic boundary conditions, so that the edge states do not appear in the energy spectra, allowing us for a clear estimate of the presence and the extension of the band-gaps. Periodic boundary conditions are easily applied when considering a finite system of $N_x \times N_y$ lattice site, with $N_x = N_y$ commensurate with the least common multiple of q and s . For simplicity, we have chosen $q = s = 5$, and $N_x = N_y = 15$.

The eigenvalues of \mathcal{M}_F are calculated as in the previous section and are exactly the ones already represented in Fig. 5.2. However, in order to allow us for an easy and direct comparison of the spectra at different ω_0/w , we have shifted each of them by the quantity $\bar{\omega}$ as defined in Eq. (4.22). The result of this procedure is plotted in Fig. 5.3.

For large values of $\omega_0/w \approx 20$ (not shown here), we have that the spectra consists of 5 bands in perfect agreement with the Harper-Hofstadter model. This is because the rotating-wave approximation is well satisfied and the effective dynamics is the one of the Harper-Hofstadter model.

When the ratio between ω_0/w is decreased, the band structure of the Floquet matrix remains qualitatively similar to the Harper-Hofstadter model, with only minor deviations due to the counter-rotating-wave terms, that mainly reduce the band-gaps. However, a remarkable result is that as ω_0/w is reduced further, the band-gaps eventually close. From Fig. 5.3 it is not clear whether small gaps open again after $\omega_0/w \approx 7$, due to the finite system size.

To understand the topological properties of the system beyond the rotating-wave approximation, we have also studied the eigenstate of \mathcal{M}_F with open boundary conditions, searching for the localized edge states. The resulting spectra is similar to the one in Fig. 5.3, except that modes corresponding to the edge states are visible between the gaps, therefore the identification of the gap is not as immediate as it was with the periodic-boundary conditions. By analysing the eigenstates, as soon as all the gaps are closed, around $\omega_0/w \approx 7$, we notice that none of the eigenstates of \mathcal{M}_F are localized along the edges any more.

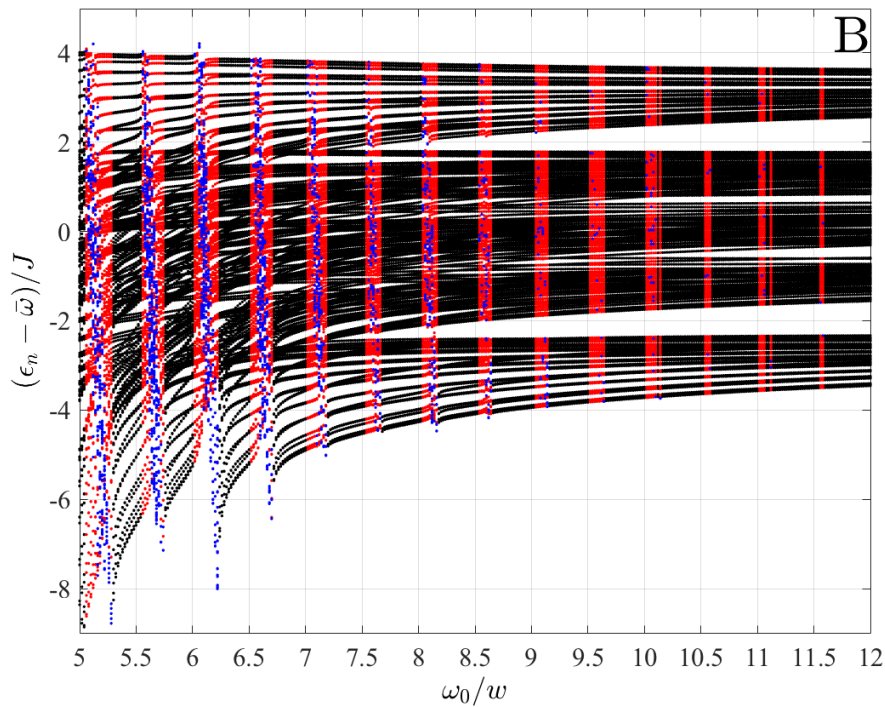


Figure 5.3: Floquet quasi-energies ϵ_n , modulo w , shifted by $\bar{\omega}$ as defined in Eq. (4.22), associated with either a positive Krein-signature \mathcal{K} or with $\mathcal{K} = 0$ and $|\lambda_n| \geq 1$. The system has a magnetic flux $\theta = 1/5$, with periodic boundary conditions; driving and dissipation are not included. The energy spectra are presented as a function of ω_0/w , for a fixed value of the amplitude modulation $V/w \approx 0.4$. When all the eigenvalues at a particular frequency are stable, we denote them in black, otherwise we denote them either in red or blue. Red points are purely real modes, while blue points are the unstable modes, plotted according to the real part of their complex energy. Parameters are: $\theta = 1/5$, $s = 5$, $w/J = 50$.

From this analysis, we conclude that the counter-rotating-wave terms have an important role in the break-down of the effective Harper-Hofstadter model. When the parameters are far from the rotating-wave approximation, the system does not present any of the clear evidences of non-trivial topology, as for example the localized edge states.

Chapter 6

The honeycomb lattice.

Graphene is much more than just a flat crystal. It possesses a number of unusual properties which are often unique or superior to those in other materials.

Konstantin S. Novoselov – *Nobel lecture.*

So far, we have considered the square lattice geometry for the implementation of an artificial gauge field by time-reversal symmetry breaking and the realization of the topological Harper-Hofstadter model in a classical mechanical system. However, as we have seen in Chap. 2, the generation of a non-trivial coupling phase is not the only signature of a magnetic field. We have anticipated that in the honeycomb lattice geometry of *graphene*, for example, inhomogeneous strain is responsible for the generation of an artificial pseudo-magnetic field.

Graphene is a material made out of carbon atoms arranged in an hexagonal structure. It was the first two-dimensional material to be identified, successfully isolated and characterized. It is mechanically a very strong, transparent, flexible conductor, and it immediately attracted the scientific community for these properties, which are very interesting for both fundamental studies and device applications. In fact, from the electronic point of view, it is a semi-metal with unusual linearly-dispersing electronic low-energy excitations that mimic the physics of quantum electrodynamics as these excitations can be described as massless, chiral, Dirac fermions.

It is exactly this linear Dirac dispersion that makes graphene such a peculiar material with so many extraordinary properties, as reviewed for example by [Castro Neto et al. \[2009\]](#), [Goerbig \[2011\]](#) and [Vozmediano et al. \[2010\]](#). Dirac fermions behave differently compared to ordinary electrons if subjected to magnetic fields or external electrostatic potentials, giving rise to interesting phenomena such as relativistic Landau levels or the paradox of Klein tunnelling. We shall also see how the effect of an elastic deformation of the honeycomb lattice structure, such as the one induced by a mechanical strain, can be described in terms of an artificial valley-dependent magnetic field acting on the electrons.

In this Chapter, we review those properties of particles moving in an honeycomb lattice that are the most relevant to the work carried out in the thesis.

6.1 Band structure of the honeycomb lattice.

The lattice structure of graphene is the honeycomb lattice, as is shown in the left part of Fig.6.1, in which the carbon atoms occupy the vertices of the hexagons. The honeycomb lattice is a Bravais lattice with two atoms per unit cell, labelled as A and B , which are at a distance a , that is the

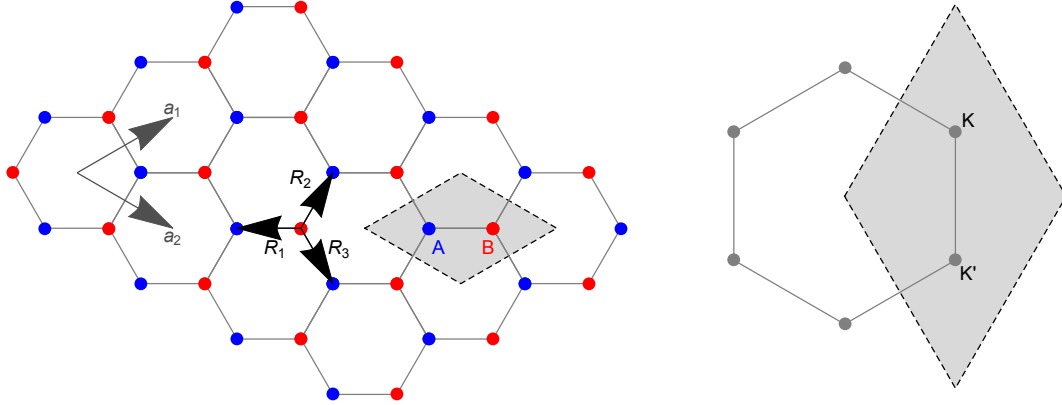


Figure 6.1: On the left, the honeycomb lattice in real space, composed of sites arranged on the vertices of the hexagons. The unit cell is highlighted in grey and contains the two crystallographic inequivalent points A and B . The two vectors, \vec{a}_1 and \vec{a}_2 , that generate the lattice from the unit cell are also indicated, together with the nearest-neighbour vectors \vec{R}_1 , \vec{R}_2 and \vec{R}_3 . The Brillouin zone is depicted on the right, and has the same hexagonal structure as the real-space lattice. The grey area, that represents the real-space unit cell transformed in quasi-momentum space, has two inequivalent points K and K' .

lattice spacing. The generators of the lattice, indicated in Fig.6.1, are:

$$\vec{a}_1 = \left(\frac{3}{2}a, \frac{\sqrt{3}}{2}a \right) \quad \vec{a}_2 = \left(\frac{3}{2}a, -\frac{\sqrt{3}}{2}a \right).$$

With these generators, the whole lattice can be explored by moving from one unit cell to the other by an integer times i, j of unit vectors.

It is also useful to define the vectors that connect nearest-neighbour sites as follows:

$$\vec{R}_1 = (-a, 0) \quad \vec{R}_2 = \left(\frac{1}{2}a, \frac{\sqrt{3}}{2}a \right) \quad \vec{R}_3 = \left(\frac{1}{2}a, -\frac{\sqrt{3}}{2}a \right).$$

The reciprocal lattice is shown in the right part of Fig.6.1. The first Brillouin zone can be taken in the form of a hexagon and is delimited by the points K and K' , which are located at:

$$\begin{aligned} K &= \left(\frac{2\pi}{3a}, \frac{2\pi}{3\sqrt{3}a} \right), \quad K = \left(-\frac{2\pi}{3a}, \frac{2\pi}{3\sqrt{3}a} \right), \quad K = \left(0, -\frac{4\pi}{3\sqrt{3}a} \right) \\ K' &= \left(-\frac{2\pi}{3a}, -\frac{2\pi}{3\sqrt{3}a} \right), \quad K' = \left(\frac{2\pi}{3a}, -\frac{2\pi}{3\sqrt{3}a} \right), \quad K' = \left(0, \frac{4\pi}{3\sqrt{3}a} \right). \end{aligned} \quad (6.1)$$

As for the real-space lattice, only two of these six points are independent and can be taken in the unit cell of the reciprocal lattice, as visible in the right part of Fig. 6.1, while the rest are all equivalent by symmetry.

To obtain the band structure of the honeycomb lattice, we consider the tight-binding Hamiltonian in real space, as in Wallace [1947]. We call respectively $\hat{a}(i, j)$ and $\hat{b}(i, j)$ the destruction operator of a particle on the lattice site A and B in the unit cell (i, j) . The coupling between nearest neighbour atoms along the direction of \vec{R}_l is indicated as t_l . The tight binding Hamiltonian is:

$$\begin{aligned} \hat{\mathcal{H}} = \sum_{i,j} \left[-t_1 \hat{a}^\dagger(i, j) \hat{b}(i, j) - t_2 \hat{a}^\dagger(i+1, j) \hat{b}(i, j) - t_3 \hat{a}^\dagger(i, j+1) \hat{b}(i, j) \right. \\ \left. - t_1 \hat{b}^\dagger(i, j) \hat{a}(i, j) - t_2 \hat{b}^\dagger(i-1, j) \hat{a}(i, j) - t_3 \hat{b}^\dagger(i, j-1) \hat{a}(i, j) \right], \end{aligned} \quad (6.2)$$

where we have introduced the labelling of the unit cells as shown in Fig. 6.2. We now move into

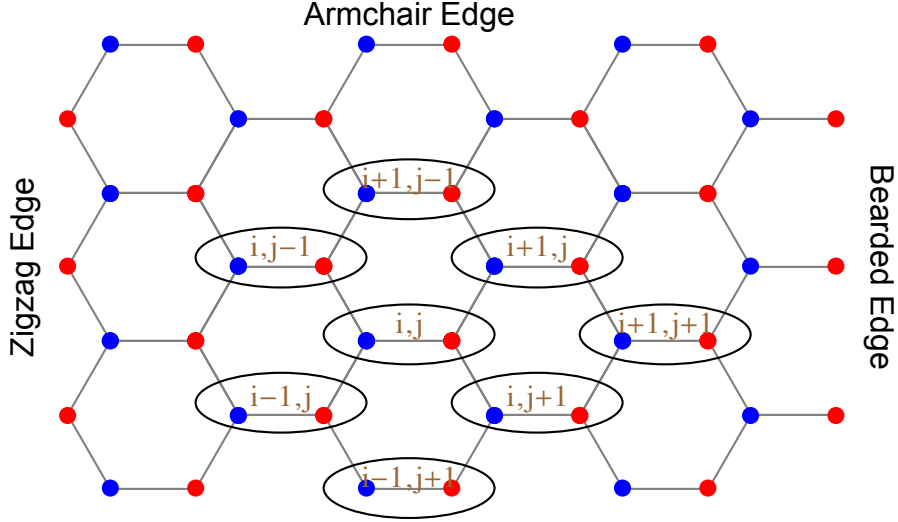


Figure 6.2: Edge terminations in the honeycomb lattice and labelling of the unit cells used in Eq. (6.2). Each unit cell is composed by two sites of type A and B , which are shown in blue and red respectively. The unit cells are also labelled with two indexes, i, j , which are incremented according to the vectors \vec{a}_1 and \vec{a}_2 .

quasi-momentum space, where we define operators as:

$$\hat{a}(i, j) = \frac{1}{V} \int_{k_x \in \text{BZ}} \int_{k_y \in \text{BZ}} \hat{a}_k e^{i(\vec{k} \cdot \vec{a}_1 + j\vec{k} \cdot \vec{a}_2)} dk_x dk_y$$

$$\hat{b}(i, j) = \frac{1}{V} \int_{k_x \in \text{BZ}} \int_{k_y \in \text{BZ}} \hat{b}_k e^{i(\vec{k} \cdot \vec{a}_1 + j\vec{k} \cdot \vec{a}_2)} e^{-i\vec{k} \cdot \vec{R}_1} dk_x dk_y,$$

where the integrals run over quasi-momenta in the Brillouin zone and V is the total area of the Brillouin zone. The extra term $e^{i\vec{k} \cdot \vec{R}_1}$ is for taking into account the inter unit-cell distance between A and B sites. Substituting everything into Eq. (6.2), we have $\hat{\mathcal{H}} = \frac{1}{V} \int_{k_x \in \text{BZ}} \int_{k_y \in \text{BZ}} \hat{\mathcal{H}}_k dk_x dk_y$, where:

$$\hat{\mathcal{H}}_k = -\hat{a}_k \hat{b}_k^\dagger e^{-i\vec{k} \cdot \vec{R}_1} (t_1 + t_2 e^{-i\vec{k} \cdot \vec{a}_1} + t_3 e^{-i\vec{k} \cdot \vec{a}_2}) - \hat{b}_k \hat{a}_k^\dagger e^{i\vec{k} \cdot \vec{R}_1} (t_1 + t_2 e^{i\vec{k} \cdot \vec{a}_1} + t_3 e^{i\vec{k} \cdot \vec{a}_2}). \quad (6.3)$$

The previous expression becomes:

$$\hat{\mathcal{H}}_k = (\hat{a}_k^\dagger, \hat{b}_k^\dagger) \begin{pmatrix} 0 & V^*(\vec{k}) \\ V(\vec{k}) & 0 \end{pmatrix} \begin{pmatrix} \hat{a}_k \\ \hat{b}_k \end{pmatrix} = (\hat{a}_k^\dagger, \hat{b}_k^\dagger) \hat{\mathcal{H}} \begin{pmatrix} \hat{a}_k \\ \hat{b}_k \end{pmatrix}, \quad (6.4)$$

where we have used a *pseudo-spin* matrix expression that describes the two sublattices of the honeycomb lattice. The off-diagonal element is:

$$V(\vec{k}) = -t_1 \exp(-ik_x a) - t_2 \exp\left(i \frac{k_x + k_y \sqrt{3}}{2} a\right) - t_3 \exp\left(i \frac{k_x - k_y \sqrt{3}}{2} a\right),$$

which has a straightforward expression in terms of the nearest neighbour vectors:

$$V(\vec{k}) = -t_1 e^{i\vec{k} \cdot \vec{R}_1} - t_2 e^{i\vec{k} \cdot \vec{R}_2} - t_3 e^{i\vec{k} \cdot \vec{R}_3}. \quad (6.5)$$

By diagonalizing the hamiltonian $\hat{\mathcal{H}}$ in Eq. (6.4), we obtain the energy structure of the honeycomb lattice as a function of the quasi-momentum k_x and k_y in the first Brillouin zone. This energy dispersion consists of two bands. In particular, for the case of homogeneous hopping $t_1 = t_2 = t_3 = t$ these two bands have the following analytical expression:

$$E = \pm t \sqrt{3 + 4 \cos\left(\frac{3k_x a}{2}\right) \cos\left(\frac{\sqrt{3}k_y a}{2}\right) + 2 \cos(\sqrt{3}k_y a)}. \quad (6.6)$$

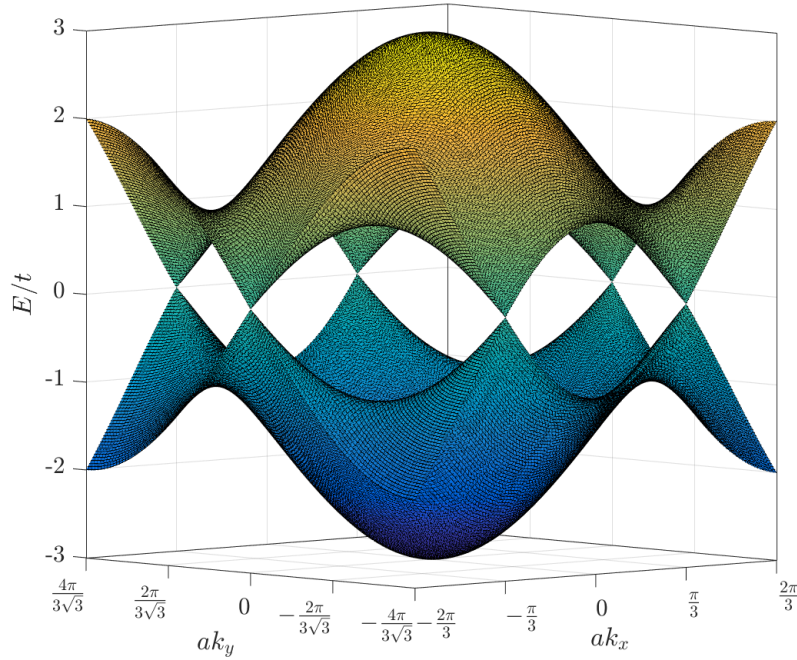


Figure 6.3: Energy bands of graphene, given in (6.6), as a function of quasi-momentum \vec{k} in the first Brillouin zone.

The energy bands are shown in Fig. 6.3, for quasi-momenta belonging to the first Brillouin zone, for values of $k_x \in [-2\pi/(3a), 2\pi/(3a)]$ and $k_y \in [-4\pi/(3\sqrt{3}a), 4\pi/(3\sqrt{3}a)]$, such that the Brillouin zone has the form of a hexagon, as shown in Fig. 6.1. From Fig. 6.3 we notice that the two bands touch each other at $E = 0$ in six points; these are called Dirac points. We also notice that these Dirac points correspond to the K and K' points, which are the corners of the hexagonal Brillouin zone.

6.1.1 Expansion around the K point: Dirac-like Hamiltonian.

We now want to give more insights into the energy dispersion at the Dirac points. This dispersion can be obtained by expanding the full band structure in Eq. (6.6), close to the desired vector in Eq. (6.1), as $\vec{k} = \vec{K} + \vec{q}$, with $|\vec{q}| \ll 1/a$. An equivalent, but more interesting way, is to expand directly the $\hat{\mathcal{H}}$ in Eq. (6.4): this procedure will also allow us to clearly see that the tight-binding Hamiltonian can be put in the form of a Dirac-like Hamiltonian, as done by [Di Vincenzo and Mele \[1984\]](#).

From Eq. (6.5) for $t_1 = t_2 = t_3 = t$, we have at the first order of the expansion around the K point the following off-diagonal element: $V(\vec{k}) \rightarrow V(\vec{K} + \vec{q}) \approx -i3at/2(q_x + iq_y)$. Therefore, the Hamiltonian can be written as:

$$\hat{\mathcal{H}} = \begin{pmatrix} 0 & V^*(\vec{k}) \\ V(\vec{k}) & 0 \end{pmatrix} \approx \begin{pmatrix} 0 & i\hbar v_D(q_x - iq_y) \\ -i\hbar v_D(q_x + iq_y) & 0 \end{pmatrix}, \quad (6.7)$$

having introduced the quantity:

$$v_D = \frac{3at}{2\hbar}. \quad (6.8)$$

In order to show the equivalence with the Dirac-like Hamiltonian, there is one caveat: the extra imaginary factors must be reabsorbed into a new definition of the spinor wave functions around the Dirac point, such that:

$$\Phi = \begin{pmatrix} \psi_A \\ \psi_B \end{pmatrix} \rightarrow \Psi = \begin{pmatrix} -i\psi_A \\ \psi_B \end{pmatrix}. \quad (6.9)$$

In this way, the Hamiltonian in Eq. (6.7) is transformed to a new Hamiltonian $\hat{\mathcal{H}}_D$, such that Ψ is an eigenvector of eigenvalue E , that are the same as in Eq. (6.6) close to the Dirac points. In the end we have that the $\hat{\mathcal{H}}_D$ can be put in the following form, using the usual 2×2 Pauli matrices in the column vector form $\vec{\sigma} \equiv (\sigma_x, \sigma_y)^\top$:

$$\boxed{\hat{\mathcal{H}}_D = -\hbar v_D \vec{\sigma} \cdot \vec{q}}. \quad (6.10)$$

Equation (6.10) tells us that the electrons in graphene can be described by an equation that is formally equivalent to the massless Dirac equation. The sublattice pseudo-spin is represented by the Pauli matrices $\vec{\sigma}$, where “spin up” corresponds to the component on one sublattice and “spin down” to that on the other one. The energy dispersion of such a Hamiltonian is linear in \vec{q} , resulting in an isotropic cone-like shape whose slope is constant and equal to the Dirac velocity v_D . For their shape, the low-energy bands expanded around the Dirac points are also called “Dirac cones”.

6.2 Gauge field in honeycomb lattices.

In this section we shall now see how an artificial gauge field can be generated in honeycomb geometries by means of a deformation of the lattice, for example, such as the one generated by a mechanical stretch of a graphene flake [Vozmediano et al. \[2010\]](#). In fact, [Kane and Mele \[1997\]](#) and then [Suzuura and Ando \[2002\]](#) realized that the effects of a size or a shape deformation in carbon nanotubes are the same as the ones of an effective vector potential acting on the pristine system. This idea was soon extended to two-dimensional graphene, as done by [Morozov et al. \[2006\]](#), [Guinea et al. \[2010a\]](#), [de Juan et al. \[2012\]](#), where the possibility of strain engineering were also explored, as in [Pereira and Castro Neto \[2009\]](#), [Guinea et al. \[2010b\]](#).

As a first step, we consider a *homogeneous strain*, that is a constant and spatially-independent hopping with different values along the three directions of the lattice:

$$t_1 \neq t_2 \neq t_3.$$

As done in the previous section, we expand the Hamiltonian in Eq. (6.4) around the K ($\xi = 1$) or K' ($\xi = -1$) point by setting $\vec{k} = (q_x, q_y - \xi 4\pi/(3\sqrt{3}a))$, where $|\vec{q}| \ll 1/a$ and the valley index $\xi = \pm 1$ labels the K, K' -points. At first order in q , we get that the off-diagonal term in the Hamiltonian is:

$$\begin{aligned} V \left(\vec{q} - \xi \vec{y} \frac{4\pi}{3\sqrt{3}a} \right) &\approx -q_x \left(\frac{\sqrt{3}a}{4} \xi (t_2 - t_3) - \frac{ia}{4} (4t_1 + t_2 + t_3) \right) - \\ &q_y \left(\frac{3a}{4} \xi (t_2 + t_3) - i \frac{\sqrt{3}a}{4} (t_2 - t_3) \right) - \\ &\frac{1}{2} (2t_1 - t_2 - t_3) - i \frac{\sqrt{3}}{2} \xi (t_2 - t_3). \end{aligned} \quad (6.11)$$

With a simple manipulation, we can re-write Eq. (6.11) in the form:

$$V(\vec{q}) \approx -iv_D^x (\hbar q_x + e\mathcal{A}_x) + v_D^y (\hbar q_y + e\mathcal{A}_y), \quad (6.12)$$

where the Dirac velocity is generally no longer isotropic,

$$\begin{aligned} v_D^x &= \frac{a}{4\hbar} (4t_1 + t_2 + t_3) + i \frac{\sqrt{3}a}{4\hbar} \xi (t_2 - t_3) \\ v_D^y &= \frac{3a}{4\hbar} (t_2 + t_3) - i \frac{\sqrt{3}a}{4\hbar} \xi (t_2 - t_3), \end{aligned} \quad (6.13)$$

and an artificial magnetic vector potential appears with components $\mathcal{A}_{x,y}$ such that:

$$\begin{aligned} v_D^x e\mathcal{A}_x &= \frac{\sqrt{3}}{2} \xi (t_2 - t_3) \\ v_D^y e\mathcal{A}_y &= \frac{1}{2} \xi (2t_1 - t_2 - t_3). \end{aligned} \quad (6.14)$$

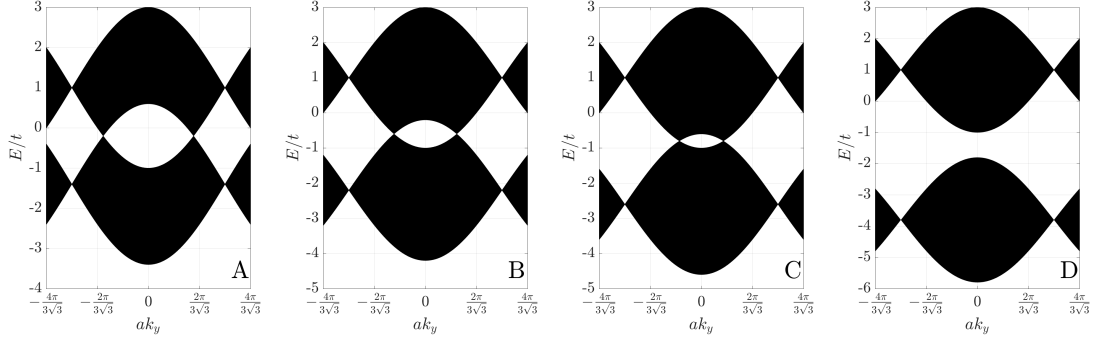


Figure 6.4: Energy bands for different values of the ratio t_1/t . From left to right: $t_1/t = 1.2, 1.6, 1.8, 2.4$. Notice how the Dirac points move in k_y , because of an effective vector potential \mathcal{A}_y .

Since the sign of $\vec{\mathcal{A}}$ depends on the particular valley index ξ , hence around which Dirac point is the expansion calculated, this potential is called a *pseudo-vector potential*.

In the $t_1 = t_2 = t_3$ case of a pristine honeycomb lattice, it is easy to check that the artificial vector potential is zero and the Dirac velocities $v_D^{x,y}$ in both the x, y directions are equal to each other and to Eq. (6.8).

For generic, but still spatially-uniform hoppings, $t_1 \neq t_2 \neq t_3$, the band dispersion as seen in Fig. 6.3 is distorted. Provided that the hopping imbalance is not too strong, the Dirac cones are still present, but their position in quasi-momentum space is shifted by an amount that is proportional to the vector potential $\vec{\mathcal{A}}$. At the same time, the different values of the Dirac velocities in the x, y directions $v_D^x \neq v_D^y$ and the appearance of an imaginary part in these signal that neither the group velocity nor the pseudo-spin are parallel to the wavevector \vec{q} any more. This imaginary part can be understood as off-diagonal components in the Dirac velocity recast in a tensorial form, as shown in de Juan et al. [2012].

6.2.1 Motion of Dirac points for a homogeneous uni-axial strain.

We now discuss in more quantitative detail the motion of the Dirac points under a homogeneous strain. As we have introduced, the Dirac points are special points at which the two energy bands touch each other with a linear dispersion. In order to precisely evaluate these points, one has to solve $\det(\hat{\mathcal{H}}) = 0$, which gets to:

$$t_1^2 + t_2^2 + t_3^2 + 2t_1t_3 \cos\left(\frac{3ak_x}{2} - \frac{\sqrt{3}ak_y}{2}\right) + 2t_2t_3 \cos(\sqrt{3}ak_y) + 2t_1t_2 \cos\left(\frac{3ak_x}{2} + \frac{\sqrt{3}ak_y}{2}\right) = 0. \quad (6.15)$$

This equation is satisfied for the pristine lattice $t_1 = t_2 = t_3$ for each of the six K, K' points given in Eq. (6.1).

We now consider the case in which the hopping along two of the three lattice directions are equal $t_2 = t_3 = t$, and we let the hopping in the remaining direction be different but constant over the lattice, $t_1 \neq t$. From the results of the previous section, we know that this particular type of homogeneous uni-axial strain introduces a vector potential that, according to Eq. (6.14), is purely oriented along the y -direction:

$$e\mathcal{A}_x = 0, \quad e\mathcal{A}_y = \frac{\xi}{v_D^y} (t_1 - t). \quad (6.16)$$

We can simplify Eq. (6.15) using that $k_x = \{0, \pm 2\pi/(3a)\}$ must be on the vertical edges of the Brillouin zone, since there is no vector potential along x . Therefore, for $k_x = \pm 2\pi/(3a)$, we have:

$$t_1 \pm 2t \cos\left(\frac{\sqrt{3}k_y a}{2}\right) = 0$$

which has the solution in the first Brillouin zone:

$$k_y = \pm \frac{2}{a\sqrt{3}} \arccos\left(\frac{t_1}{2t}\right). \quad (6.17)$$

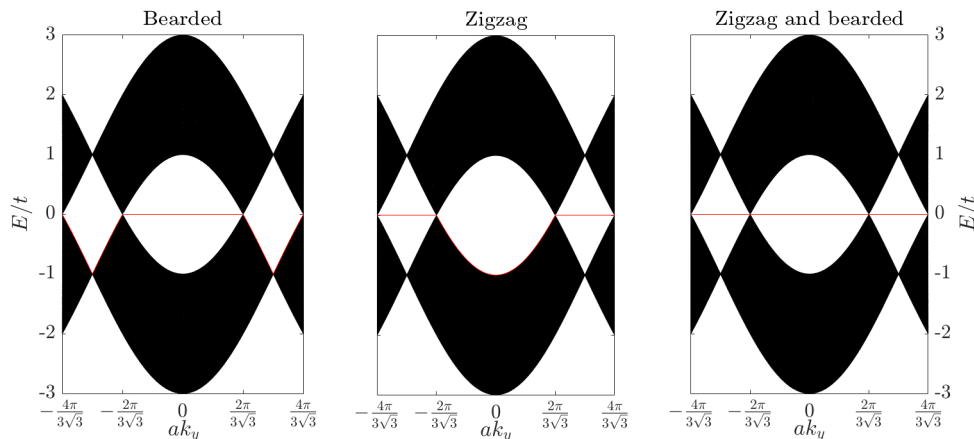


Figure 6.5: Energy spectrum of a semi-infinite ribbon of pristine graphene for three combinations of terminations along the open direction: bearded-bearded, zigzag-zigzag and zigzag-bearded.

This result means that if $t_1 = t$, the Dirac point is exactly in the K -point $k_y = 2\pi/(3\sqrt{3}a)$, otherwise, it is shifted, as also seen in [Pereira et al. \[2009\]](#).

The motion of the Dirac point is shown in Fig. 6.4, where the energy bands are plotted for increasing values of the ratio t_1/t . It is clear how the point where the bands touch, which are by definition the Dirac points, move away from the K , K' points, which are the corners of the hexagonal Brillouin zone. For a particular value of the hopping $t_1 = 2t$, the two Dirac points annihilate into a single one, and then further increase of the $t_1/t > 2$ ratio, results in a gapped band dispersion. This result is consistent with Eq. (6.17), because $t_1 = 2t$ is exactly the maximum value of t_1 for which k_y is real, hence a Dirac cone exists.

Homogeneous uni-axial strain is therefore capable of driving a transition, from a gapless semi-metallic phase to a gapped insulating one, after the critical point $t_1 = 2t$; such a transition is called a *Lifshitz transition*. This is also a topological transition, because the two Dirac points can be associated with opposite topological Berry phases which cancel out when the Dirac point merge.

6.3 The edge states.

Another important aspect of the honeycomb lattice is the presence of zero-energy *edge states* depending on the termination of the lattice. When considering a finite ribbon of graphene, there are three different types of edges according to how the stripe is terminated, as is shown in Fig. 6.2. These terminations are called armchair, zigzag and bearded, and have different behaviours. Some of them possess localized zero-energy edge states, which appear flat in the energy spectrum and which are separated from the rest of the band, as shown by [Kohmoto and Hasegawa \[2007\]](#). In particular, the zigzag and bearded edges support these zero edge states, while the armchair is known to exhibit edge states only for the non uniform case $t_1 \neq t_2, t_3$.

Examples of the spectra obtained for a semi-infinite ribbon with different types of edge terminations are shown in Fig. 6.5, in the homogeneous case $t_1 = t_2 = t_3 = t$, for a finite number $N = 200$ lattice sites along the x -direction and for periodic boundary conditions along the y -direction. We notice that the energy spectra appear similar to those shown in Fig. 6.4 apart from the presence of flat zero energy modes, highlighted by red lines, that are located in different parts of the Brillouin zone according to the particular edge termination. As the orientation shown in Fig. 6.2 fixes the armchair edge along the x -axis, we will not discuss this case, but only the the zigzag and bearded edges. The first panel on the left of Fig. 6.5 shows the energy spectrum as obtained for a ribbon that terminates on both ends with a bearded edge. The edge state for this termination is found between $k_y \in \left[-\frac{2\pi}{3\sqrt{3}a}, \frac{2\pi}{3\sqrt{3}a}\right]$. In the central panel we show the energy spectrum as obtained for a ribbon that terminates on both ends with a zigzag edge, which extends from $k_y \in \left[-\frac{4\pi}{3\sqrt{3}a}, -\frac{2\pi}{3\sqrt{3}a}\right]$ and $k_y \in \left[\frac{2\pi}{3\sqrt{3}a}, \frac{4\pi}{3\sqrt{3}a}\right]$. In the third panel the ribbon terminates with bearded on one side and zigzag on the other, and we see that the edge state that covers all k_y 's in the Brillouin zone is actually the combination of the two edge states on the two different terminations. Details on the

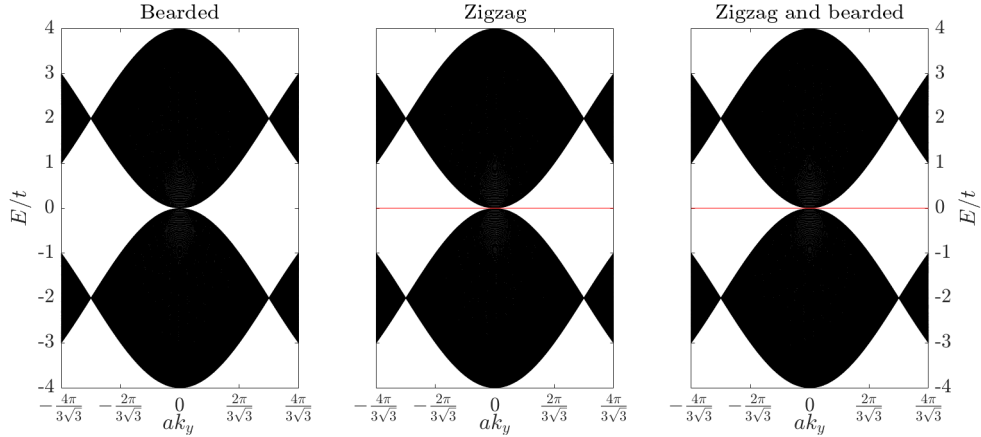


Figure 6.6: Energy spectrum of inhomogeneous graphene for $t_2 = t_3 = t$ and $t_1 = 2t$, for three combinations of terminations: bearded-bearded, zigzag-zigzag and zigzag-bearded.

numerical derivation of these spectra are given in Appendix F.

An interesting feature about edge states is their different behaviour in the presence of a vector potential. As we saw in the previous section, a vector potential is mimicked with an anisotropic choice of the three hoppings, for example a uni-axial deformation $t_2 = t_3 = t$ but $t_1 \neq t$. The effect of this being to shift the Dirac points away from the highly symmetric K, K' points towards each other. The bearded edge state disappears for all k_y when the ratio $t_1/t \rightarrow 2$ tends to the critical value of the Lifshitz transition introduced above, while conversely, the zigzag edge state extends more and more for all k_y . Results for the special limiting case $t_1 = 2t$ are shown in Fig. 6.6 for the same type of edges already discussed in Fig. 6.5. Not shown in the figure is the appearance of an edge state for the armchair termination, as discussed instead by Kohmoto and Hasegawa [2007].

The existence of zero-energy edge states can be predicted theoretically, as shown in Ryu and Hatsugai [2002] and Delplace et al. [2011], based on the bulk-edge correspondence between a non-trivial Zak phase – which is a Berry phase across a one-dimensional Brillouin zone – and the existence of a localized state at the boundary of the ribbon.

6.4 The next-nearest-neighbour coupling.

So far we have considered a tight-binding model of the honeycomb lattice with only nearest-neighbour hoppings. However, for realistic systems, it may be important to go beyond this approximation. In real graphene, for example, electrons hop to next-nearest-neighbour (NNN) sites with an amplitude t' that has been estimated as being on the order of five percent of the nearest-neighbour hopping t Castro Neto et al. [2009]. Before moving on, we generalize the results of the previous sections to the case of non-zero NNN hoppings.

The momentum-space Hamiltonian corresponding to Eq. (6.4) in presence of NNN hopping is:

$$\hat{\mathcal{H}}_{\text{NNN}} = \begin{pmatrix} V'(\vec{k}) & V^*(\vec{k}) \\ V(\vec{k}) & V'(\vec{k}) \end{pmatrix} = \hat{\mathcal{H}} + \hat{\mathcal{H}}', \quad (6.18)$$

where the anti-diagonal matrix $\hat{\mathcal{H}}$ gives the contribution only from nearest-neighbour hoppings as before, and the diagonal matrix $\hat{\mathcal{H}}'$ describes the NNN hoppings. Following the same strategy as before, we define the NNN lattice vectors to be:

$$\vec{D}_1 = (0, \sqrt{3}a), \quad \vec{D}_2 = \left(\frac{3}{2}a, \frac{\sqrt{3}}{2}a\right), \quad \vec{D}_3 = \left(\frac{3}{2}a, -\frac{\sqrt{3}}{2}a\right).$$

Then we have:

$$V'(\vec{k}) = -2t' \left(\cos(\vec{k} \cdot \vec{D}_1) + \cos(\vec{k} \cdot \vec{D}_2) + \cos(\vec{k} \cdot \vec{D}_3) \right). \quad (6.19)$$

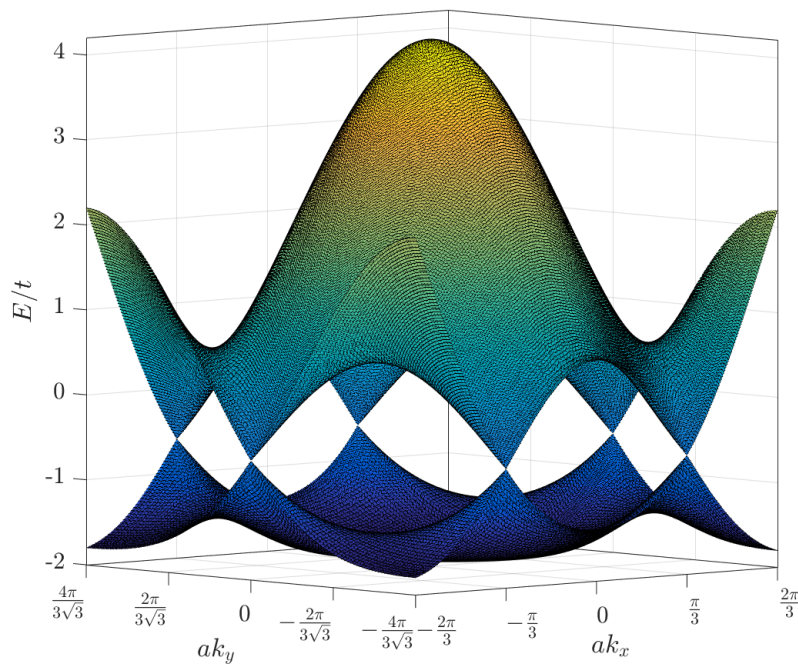


Figure 6.7: Energy bands of graphene, given in (6.20), as a function of \vec{k} in the first Brillouin zone. The NNN coupling strength is $t'/t = 0.2$ which, compared to the estimates of NNN coupling in real graphene, has been exaggerated for clarity.

The energies are now:

$$E = \pm t \sqrt{3 + 4 \cos\left(\frac{3k_x a}{2}\right) \cos\left(\frac{\sqrt{3}k_y a}{2}\right) + 2 \cos(\sqrt{3}k_y a)} - t' 4 \cos\left(\frac{3k_x a}{2}\right) \cos\left(\frac{\sqrt{3}k_y a}{2}\right) + 2 \cos(\sqrt{3}k_y a). \quad (6.20)$$

Figure 6.7 shows the plot of the two energy bands as calculated from Eq. (6.20). We notice that the principal effect of the NNN coupling is to break the symmetry between the upper and lower band. However, the physics around the Dirac points, and their positions are affected by the NNN coupling only to higher orders than the ones considered so far in this Chapter. This is because the Dirac points are robust against any perturbation that does not break the inversion symmetry between the two sublattices Kane and Mele [2005a]. Inversion symmetry breaking would correspond to a σ_z term in the Hamiltonian Eq. (6.10), while the NNN term in Eq. (6.18) is proportional to the identity and it only shifts the energy.

6.5 Artificial graphene.

Artificial graphene is a name given to a wide range of two-dimensional systems that mimic the properties of real natural graphene. Such systems can have the advantage that physical parameters are much easier to control and manipulate, even going beyond what is possible for natural graphene and suggesting new directions in which to push experimental investigations in materials science Polini et al. [2013].

These systems are realized using particles other than electrons, moving in a honeycomb structure. Examples of artificial graphene are: light inside a photonic lattice composed of arrays of waveguides as in Rechtsman et al. [2013c]; microwaves in a photonic lattice composed of dielectric resonators as in Bellec et al. [2013a]; polaritons in a lattice of coupled micropillars etched in a planar semiconductor microcavity as in Jacqmin et al. [2014]; ultracold atoms in optical lattices

as in [Tarruell et al. \[2012\]](#); or mechanical phonons of a system of masses and springs, as proposed by [Wang et al. \[2015c\]](#), [Kariyado and Hatsugai \[2015\]](#), or realized by [Wang et al. \[2015a\]](#), [Nash et al. \[2015\]](#).

Some of the greatest advantages of such artificial graphene systems are that the tunnelling of particles between different lattice sites can be controlled in an independent and flexible way, and that the honeycomb lattice can be shaped in any form and with any type of terminations. This allowed physicists to observe, for the first time, phenomena that were only predicted by theoretical calculations for the honeycomb lattice, but never observed in real graphene because they were impossible to realize. For example, a linear and homogeneous uni-axial strain is troublesome to achieve with real graphene, but very easily implemented in these artificial systems, resulting in a clear verification of the Dirac point motion, as in [Soltan-Panahi et al. \[2011\]](#), [Rechtsman et al. \[2013a\]](#) and [Bellec et al. \[2013b\]](#). Another example is the observation of the localized edge states, in particular the one associated with the bearded edge which is unstable in real graphene, as done in [Plotnik et al. \[2014\]](#), [Bellec et al. \[2014\]](#) and [Milićević et al. \[2015\]](#). Furthermore, with these artificial realizations, it is possible to tailor or enhance physical quantities that we cannot control in natural graphene, such as the next-nearest-neighbour or spin-orbit coupling, as done in [Jacqmin et al. \[2014\]](#), and to design new types of Hamiltonians, as in [Rechtsman et al. \[2013b\]](#), [Jotzu et al. \[2014\]](#).

Artificial magnetic field and pseudo-Landau levels in a strained honeycomb lattice.

The eye does not see things, but images of things that mean other things.

Italo Calvino – *Le città invisibili*.

In the previous Chapter, we have reviewed some of the general properties of honeycomb lattices. We have seen that the low-energy modes near the Dirac points are described by an equation that is formally equivalent to the massless Dirac equation, and in particular that an homogeneous strain can be described in terms of an artificial valley-dependent magnetic vector potential. As a consequence, a suitably spatially-dependent strain can generate an artificial constant magnetic field, such that the low-energy modes are quantized Landau levels. Due to the underlying Dirac dispersion of the honeycomb band structure, the spacing between Landau levels will not be uniform, as for a massive particle in free space with a real magnetic field, but will rather follow a square-root law, starting from zero energy for both positive and negative energies.

The idea of a strain-induced artificial magnetic field was studied in real graphene, as done by [Pereira and Castro Neto \[2009\]](#), [Pereira et al. \[2009\]](#), [Guinea et al. \[2010a\]](#) and [Guinea et al. \[2010b\]](#), where the strain is physically applied through mechanical forces acting on the sample. The atoms forming the lattice are physically pushed closer together or pulled further apart in a spatially-dependent way, resulting in a modulation of both the sample geometry and the hopping amplitudes, see [Castro Neto et al. \[2009\]](#). Typical geometries used in experiments involve graphene nanobubbles [Levy et al. \[2010\]](#) or trigonal deformations of the honeycomb lattice [Guinea et al. \[2010b\]](#), which reflect the symmetry of the lattice, and are straightforwardly applicable to a real sample of graphene. In the photonics community, such trigonal deformations were first implemented in the artificial graphene of coupled waveguides by [Rechtsman et al. \[2013c\]](#). Given the propagating nature of this optical set-up, evidence of the Landau levels could only be obtained in an indirect way from the localized edge modes, which reside in the energy-gaps between the Landau levels, while it was not possible to obtain detailed information on the microscopic structure of the Landau levels themselves.

In this chapter, we propose an alternative photonic set-up consisting of an array of cavities with a honeycomb geometry, as inspired by the experiments of [Jacqmin et al. \[2014\]](#) and [Bellec et al. \[2013a\]](#). In contrast to the propagating waveguide set-up of [Rechtsman et al. \[2013c\]](#), the cavity arrays are intrinsically driven-dissipative systems, which will allow us to use spectroscopic techniques to characterize their eigenstates. As we have studied also for the pendula, the different eigenmodes of a driven-dissipative system naturally appear as peaks in the transmission/absorption spectra under a coherent incident field. When the pump frequency is set on resonance with a given mode

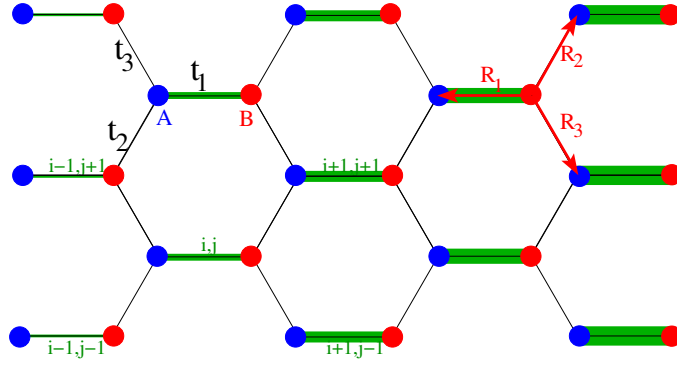


Figure 7.1: The *strained* honeycomb lattice, with N_x unit cells along the x -armchair direction and N_y along the y -bearded direction (in the figure $N_x = N_y = 5$). The unit cell is labelled with two indices (i, j) . The strain is introduced as a spatially-dependent hopping t_1^i and schematically represented by the thickness of the green line connecting the A and B sites in the unit cell along the \vec{R}_1 direction. The thicker the green line, the stronger the coupling.

spectrally isolated from its neighbours, the intensity profiles in both real and momentum space faithfully reproduce the mode wave function. We will apply this general spectroscopic technique to the case of a uni-axially strained honeycomb lattice and investigate the Landau levels appearing in the presence of a strain-induced artificial magnetic field.

The main results of this Chapter are published in Salerno et al. [2015].

7.1 The strained honeycomb lattice.

We consider an infinite ribbon along the y -direction that is of finite size L_x along the x -direction, with N_x unit cells oriented as in Fig. 7.1, terminated on both ends with bearded edges. We assume a uni-axial strain, $t_2 = t_3 = t \neq t_1$, but this time we introduce a spatial dependence of the hopping elements $t_1^{(i,j)}$ on the site indices (i, j) along the horizontal direction. Specifically, we assume that the hopping $t_1^{(i,j)}$ is positive and has the following spatial dependence:

$$\boxed{t_1^{(i,j)} \equiv t_1(x_i) = t \left(1 + \frac{x_i}{3a} \tau \right)}. \quad (7.1)$$

The positive dimensionless parameter τ quantifies the intensity of the spatially-inhomogeneous strain and the positions $x_i \in (-L_x/2, L_x/2)$. In this way, the hopping linearly increase by $\tau/2$ when passing from a unit cell i to the adjacent one $i + 1$. We set the hopping in the middle of the ribbon to be $t_1(0) = t$. Physically, the hopping should all have the same sign at all positions along x , therefore we require the condition $t_1(-L_x/2) \geq 0$ at one edge, which imposes an upper bound on the strain,

$$\frac{\tau L_x}{6a} < 1. \quad (7.2)$$

This condition automatically implies that $t_1(L_x/2) \leq 2t$ at the other edge, which guarantees – within a local band picture – that no local Lifshitz transition to a gapped state takes place in the considered ribbon.

The vector potential, as defined from Eq. (6.14) in the Landau gauge with the specific form of the strain in Eq. (7.1), is now spatially dependent. The artificial magnetic field \vec{B} , that is naturally defined as the curl of \vec{A} :

$$\boxed{e\vec{B} = \xi \frac{2\hbar}{9a^2} \tau \vec{z}}, \quad (7.3)$$

is oriented along the direction perpendicular to the lattice. Inserting the values of the electron charge and the lattice spacing of real graphene, the field in Eq. (7.3) would correspond to a magnetic field $|B| \approx 2\tau 10^3$ T. It is important to notice that this strain-induced artificial gauge field does not break time-reversal symmetry, therefore the magnetic field \vec{B} has opposite signs in the two

$\xi = \pm 1$ valleys. In this sense, the strained-induced field is not a “true” magnetic field, but rather a *pseudo-magnetic field*. The magnetic length that is associated to this pseudo-magnetic field is:

$$l_B \equiv \sqrt{\hbar/|eB|} = 3a/\sqrt{2\tau}. \quad (7.4)$$

Generally, there is also a small spatial dependence of the Dirac velocity, as we see from Eq. (6.13) and discussed by de Juan et al. [2012]. With the specific form of the strain in Eq. (7.1), the two components of the Dirac velocity in Eq. (6.13) become:

$$\begin{cases} v_D^x = v_D + \tau\hat{x}/3\hbar \\ v_D^y = v_D. \end{cases} \quad (7.5)$$

where at the lowest order in q and x , we have expressed the spatial dependence of the hopping amplitudes in terms of a position operator \hat{x} . If the modulation of the hopping along the x direction is small compared to the hoppings in the other two directions, we can neglect the spatial variation of the Dirac velocity, as we do initially below. In more quantitative terms, the variation of v_D^x on a magnetic length l_B remains small compared to v_D as long as the strain is weak $\sqrt{\tau} \ll 1$.

7.1.1 Analytical derivation of the Landau levels in a uni-axially strained honeycomb lattice.

We shall now derive how the strain-induced pseudo-magnetic field rearranges the continuous conical dispersion around the Dirac points into a series of discrete Landau levels. The procedure to diagonalize the Hamiltonian is closely analogous to the usual one for charged massive particles in a uniform magnetic field in free space, as done by Castro Neto et al. [2009] or Goerbig [2011]. The off-diagonal matrix element in Eq. (6.11):

$$\hat{V} = -i\hbar\hat{q}_x v_D + \xi\hbar\hat{q}_y v_D + t\tau\hat{x}/3a, \quad (7.6)$$

becomes itself an operator that acts on the spatial wave function. Using the standard canonical relation $[\hat{x}, \hat{q}_x] = i$, it is straightforward to show that the following commutation relation holds:

$$[\hat{V}^\dagger, \hat{V}] = t^2\tau.$$

We can therefore introduce a creation operator $\hat{a}^\dagger \equiv \hat{V}/(t\sqrt{\tau})$ which satisfies the usual commutation rules $[\hat{a}, \hat{a}^\dagger] = 1$ of a quantum harmonic oscillator and recast Eq. (7.6) into the form of the creation operator of a shifted harmonic oscillator:

$$\hat{V} = \hbar\omega \left(\sqrt{\frac{m\omega}{2\hbar}} (\hat{x} - x_0) - i\sqrt{\frac{1}{2m\hbar\omega}} \hbar\hat{q}_x \right) = \hbar\omega\hat{a}^\dagger, \quad (7.7)$$

where we have defined the mass:

$$m \equiv t\sqrt{\tau}/(2v_D^2).$$

The oscillation center is shifted in the x direction by the q_y -dependent distance:

$$x_0 \equiv -\frac{3\xi\hbar v_D a}{t\tau} \hat{q}_y = -\xi l_B^2 \hat{q}_y, \quad (7.8)$$

and the oscillator frequency is:

$$\hbar\omega \equiv \sqrt{\frac{2\hbar v_D t\tau}{3a}} = t\sqrt{\tau}. \quad (7.9)$$

In this way, we recover the cyclotron frequency of a massless Dirac particle in a real magnetic field Goerbig [2011]

$$\omega = v_D \sqrt{2|eB|/\hbar}. \quad (7.10)$$

To obtain the eigenfunctions $\phi_{A,B}(x, y)$, we now re-write the Hamiltonian around the Dirac points, with the help of Eq. (7.7), as:

$$\hat{\mathcal{H}} \begin{pmatrix} \phi_A \\ \phi_B \end{pmatrix} = \hbar\omega \begin{pmatrix} 0 & \hat{a} \\ \hat{a}^\dagger & 0 \end{pmatrix} \begin{pmatrix} \phi_A \\ \phi_B \end{pmatrix} = \mathcal{E} \begin{pmatrix} \phi_A \\ \phi_B \end{pmatrix}. \quad (7.11)$$

Separating the equations, we have:

$$(\hbar\omega)^2 \hat{a} \hat{a}^\dagger \phi_A = \mathcal{E}^2 \phi_A \quad (7.12)$$

$$(\hbar\omega)^2 \hat{a}^\dagger \hat{a} \phi_B = \mathcal{E}^2 \phi_B. \quad (7.13)$$

From Eq.(7.13), we immediately see that ϕ_B is an eigenvector of the number operator: $\hat{a}^\dagger \hat{a} |N\rangle = N |N\rangle$ with an non-negative integer eigenvalue $N \geq 0$. Therefore, ϕ_B is a 1D harmonic oscillator eigenfunction $|N\rangle$ with frequency ω , centred at the q_y -dependent position (7.8). Most remarkably, for each ϕ_B with a given $N \neq 0$, two independent eigenstates exist with opposite energies $\mathcal{E} = \pm \hbar\omega\sqrt{N}$. Obtaining the corresponding ϕ_A requires a bit more care: from Eq. (7.11), for $N = 0$ one finds a single eigenstate with $\phi_A = 0$, while for $N > 0$:

$$\phi_A = \frac{\hbar\omega}{\mathcal{E}} \hat{a} |N\rangle = \frac{\hbar\omega}{\pm \hbar\omega\sqrt{N}} \sqrt{N} |N-1\rangle = \pm |N-1\rangle. \quad (7.14)$$

To summarize, both the positive and negative energy states can be organized in a single sequence labelled by an integer $-\infty < n < \infty$ with energies following the square-root law of relativistic Landau levels with a cyclotron frequency ω ,

$$\mathcal{E}_n = \pm \hbar\omega \sqrt{|n|} = \pm t \sqrt{\tau |n|}. \quad (7.15)$$

For each eigenstate, the total wave function in the position representation is:

$$\psi_{\pm|n|}(x, y) = e^{iq_y y} \begin{pmatrix} \phi_A(x) \\ \phi_B(x) \end{pmatrix} = e^{iq_y y} \begin{pmatrix} \pm \langle x ||n-1\rangle \\ \langle x ||n\rangle \end{pmatrix} \quad (7.16)$$

where $|N\rangle$ can be explicitly written in the position representation as a Hermite polynomial of degree $N \geq 0$,

$$\langle x | N \rangle \propto e^{-(x-x_0)^2/(2l_B^2)} \text{H}_N \left(\frac{x-x_0}{l_B} \right) \quad (7.17)$$

and we have implicitly assumed that $|-1\rangle = 0$. This full wavefunction $\psi(x, y)$ is therefore a spinor with a Landau level wave function in each component: for $|n| > 0$, the relative sign of the two components ϕ_A and ϕ_B is opposite for opposite eigenstates at $\pm n$. For $n = 0$ the two sublattices are decoupled, because from Eq. (7.16) we see that the Landau level wave function associated with $n = 0$ is completely localized on the B sublattice:

$$\psi_0(x, y) \propto e^{iq_y y} \begin{pmatrix} 0 \\ e^{-(x-x_0)^2/(2l_B^2)} \end{pmatrix}.$$

We also notice that there is no dependence on the valley index ξ in the spinor of Eq. (7.16), meaning that the wave function in the strained lattice is the same for the two Dirac valleys. This is an important difference to the case of a non-strained system in a real external magnetic field, where the wave function is valley-dependent and the role of the A and B sublattices is inverted when passing from $\xi = 1$ to $\xi = -1$, as reviewed for example by [Goerbig \[2011\]](#).

All the discussion so far neglects the dependence of the Dirac velocity on the hopping amplitudes in Eq. (6.13). The first correction to the relativistic Landau levels in Eq. (7.15) comes from the spatial dependence of the Dirac velocity in Eq. (7.5). Substituting the value $v_D^x \simeq v_D + t\tau x_0/3\hbar$ evaluated at the oscillation center x_0 into (7.6), one obtains an expression of the Landau levels that includes the first order correction,

$$\mathcal{E}_n = \pm t \sqrt{\tau |n|} \sqrt{1 - \xi q_y a}. \quad (7.18)$$

This correction shifts each level around the K, K' points with a square-root dependence on q_y : the fact that the resulting levels are no longer flat is a key difference with respect to the standard Landau levels in the presence of a real magnetic field, where the Dirac velocity remains independent of position. Further corrections coming from second- and higher-order terms in the expansion (6.11) of $V(\vec{q})$ in powers of q are beyond the scope of the present thesis.

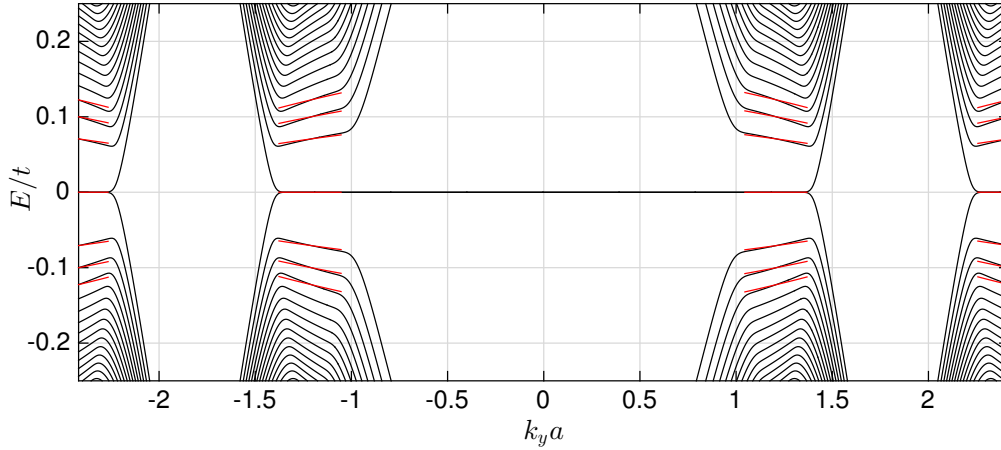


Figure 7.2: The structure of levels around zero energy as a function of k_y , in units of the bare hopping t . This is numerically calculated from exact diagonalization of the tight-binding Hamiltonian for a ribbon of $N_x = 601$ unit cells along x with a strain of $\tau = 0.005$, and periodic boundary conditions along the y -direction. Relativistic Landau levels appear around the Dirac points K and K' for $k_y a \simeq \pm 1.21$ and ± 2.42 . Red lines indicates the analytical prediction for the lowest Landau levels including the first order correction to the Dirac velocity according to Eq. (7.18).

7.1.2 Comparison with numerical results from exact diagonalization.

The analytical results of the previous section were based on several approximations, in particular the very notion of an artificial vector potential $\vec{\mathcal{A}}$ relied on a local band structure for each value of the hopping $t_l^{(i,j)}$. In order to verify the quantitative accuracy of this approach, we have numerically diagonalized the full tight-binding Hamiltonian and compared the outcome with the aforementioned analytical results.

In Fig. 7.2 we show the low-energy dispersion around the Dirac points of a large system of $N_x = 601$ unit cells along x , with a relatively small strain parameter of $\tau = 0.005$, and periodic boundary conditions along y . The energy levels at zero energy are doubly degenerate, consisting of the $n = 0$ Landau level and of the localized edge state associated with the left bearded edges (that terminate with A sites). Around the Dirac points, we highlight the formation of quantized Landau levels. Their energies are in good agreement with the analytical prediction of Eq. (7.18), which are plotted in red and include the corrections due to the spatial dependence of the Dirac velocity. The slight discrepancies that are visible to a careful eye can be explained by the approximations in our analytical calculations, *e.g.* the neglecting of higher-order terms in the expansion of Eq. (6.11). The finite extension in k_y of the Landau level structure around the Dirac points, roughly indicated in Fig. 7.2 by the extension of the red lines, is limited by the Landau level touching the physical boundary of the system at $x = \pm L_x/2$, as can be seen from Eq. (7.8). In the spectra, this is apparent as a sudden increase of the level energy.

The agreement between the analytical model and the full numerics gets better for smaller values of the strain parameter τ : in this regime, the magnetic length extends for a larger number of sites (proportional to $1/\sqrt{\tau}$) and the \vec{k} -space wave function consequently gets more localized in the vicinity of the Dirac point. This makes the continuum approximation underlying the analytical model more and more accurate. At the same time, the value of the vector potential $\vec{\mathcal{A}}$ within the real-space wave function decreases as $\sqrt{\tau}$, thus reducing the importance of the corrections to the isotropic conical Dirac dispersion. Of course, this accuracy comes at the price of a reduced energy spacing of the Landau levels, which are themselves proportional to $\sqrt{\tau}$.

The spatial structure of the wave functions is studied in Fig. 7.3, where the square modulus of the numerical eigenfunctions obtained from the exact diagonalization is plotted for two Landau levels with $n = 1$ and $n = 2$. The contributions from the A and B sublattices are separated and represented in blue and red respectively, for easier identification. Dots correspond to the numerical eigenfunctions and lines to the analytical wave functions as calculated in Eq. (7.17) with $ak_y = 4\pi/(3\sqrt{3})$ around the K' point. As predicted by the analytical model, exactly at the

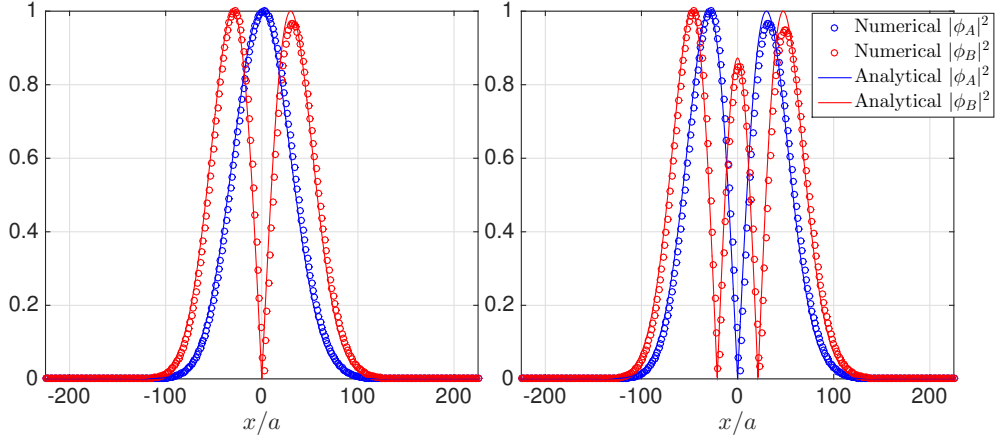


Figure 7.3: Square modulus of the wave function of Landau levels around the K' point as numerically obtained from exact diagonalization of the tight-binding Hamiltonian. The wave function has been separated for the two sublattices $|\phi_A|^2$ (blue) and $|\phi_B|^2$ (red). Left panel: $n = 1$, right panel: $n = 2$. Dots correspond to the numerical eigenfunction, lines to the analytical wave function in Eq. (7.17).

K, K' points the wave function is symmetrically centred in the ribbon while we find, as k_y moves away from the Dirac point, that its center x_0 is shifted according to Eq. (7.8) (not shown here). The left panel shows the states for $n = 1$: according to Eq. (7.16), the total wave function is $\psi_{n=1} \propto (|0\rangle, |1\rangle)$. On A sites, the wave function is a Gaussian times the zero-th order Hermite polynomial, so the overall profile is Gaussian, as visible from the blue curve. On B sites, instead, the wave function is proportional to a first-order Hermite polynomial, and the Gaussian profile has one node as visible from the red curve. In the right panel of Fig. 7.3, which shows the $n = 2$ Landau level, there is one node in the A -site wave function as expected, and two nodes in the B -site state. The slight asymmetry around the centre depends on the sign of the hopping gradient.

7.2 Steady state in a coherently driven-dissipative lattice.

We now describe our proposal to probe the Landau spectra by studying the steady state of a driven-dissipative system, such as a photonic lattice made of a coupled cavity array as in [Jacqmin et al. \[2014\]](#) or microwave resonators of [Bellec et al. \[2013a,b, 2014\]](#). In both cases, the nearest-neighbour hopping is due to the spatial overlap between modes localized on adjacent sites, so the required spatial dependence of the hopping Eq. (7.1) can be tailored by a careful design of the distance between neighbouring sites. Note that obtaining a gradient of t_1 along the x direction does not involve distorting the lattice, nor the geometry of the edge terminations, but only varying the distance between some of the neighbouring sites along x .

We consider a large but finite honeycomb lattice, with the same orientation as the one that was sketched in Fig. 7.1. We assume that photons are lost uniformly from all sites at the rate γ and the coherent pump is spatially localized in the central part of the lattice. This set-up is beneficial to focus on the bulk properties of the lattice and to suppress spurious effects due to reflections from the lattice edges. We coherently pump the system with a monochromatic field at frequency ω_0 . The pump has a spatial amplitude $f_{i,j}$ so that, in the steady state, the time-dependent fields over A or B sites at position (i, j) are:

$$a_{i,j}(T) = a_{i,j} e^{-i\omega_0 T} \quad b_{i,j}(T) = b_{i,j} e^{-i\omega_0 T}. \quad (7.19)$$

with the time-independent amplitudes $a_{i,j}$ and $b_{i,j}$ satisfying a linear system of Heisenberg equations:

$$\begin{aligned} \hbar(\omega_0 + i\gamma) a_{i,j} + t_1^i b_{i,j} + t b_{i-1,j-1} + t b_{i-1,j+1} &= f_{i,j} \\ \hbar(\omega_0 + i\gamma) b_{i,j} + t_1^i a_{i,j} + t a_{i+1,j+1} + t a_{i+1,j-1} &= f_{i,j} \end{aligned} \quad (7.20)$$

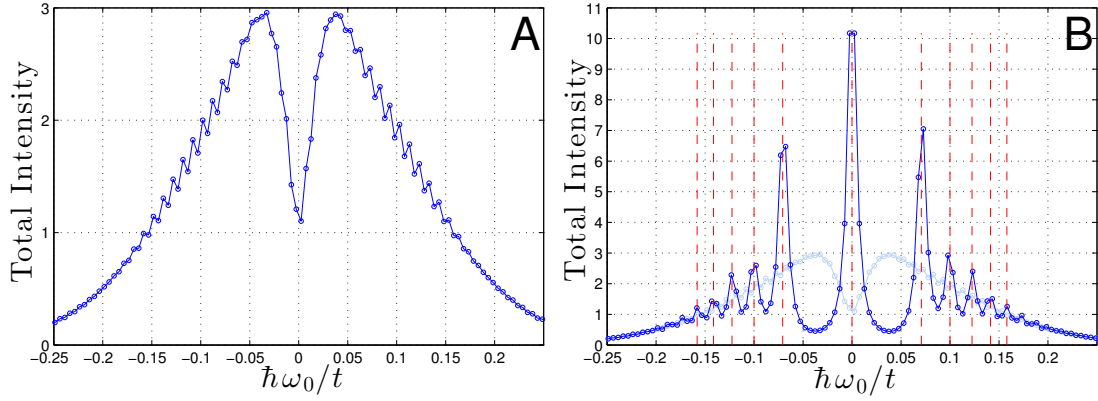


Figure 7.4: Dots show numerically calculated spectra of the total field intensity in Eq. (7.22) as a function of the pumping frequency ω_0 for two values of the strain parameter, in arbitrary units. The loss rate is $\hbar\gamma/t = 0.005$, and we take $N = 601$ and $\sigma_x/a = \sigma_y/a = 10$ for all panels. Panel **A** is for $\tau = 0$ (no strain), while panel **B** is for $\tau = 0.005$ (strained) in dark blue and $\tau = 0$ (unstrained) in light blue for easier comparison. The solid lines are a guide to the eye and the red dashed lines indicate the analytical energies of the first six Landau levels as predicted by Eq. (7.15).

for the indexing given in Fig. 7.1.

As we want to probe Landau levels arising from the pseudo-magnetic field, it is important to separate the contribution of the two inequivalent points K and K' . To this end, we adopt the same technique proposed by Ozawa and Carusotto [2014] and we assume the coherent driving to have a Gaussian spatial profile of width $\sigma_{x,y}$ in the two x, y directions, and to have an in-plane wave vector in the vicinity of, e.g., the K' Dirac point:

$$f_{i,j} = f_0 \exp\left(-\frac{x_{i,j}^2}{2\sigma_x^2}\right) \exp\left(-\frac{y_{i,j}^2}{2\sigma_y^2}\right) e^{i\vec{K}' \cdot \vec{R}_{i,j}} \quad (7.21)$$

where $\vec{R}_{i,j}$ is the position vector of the appropriate site of the hexagonal lattice and the origin is assumed to be located in the middle of the central unit cell. Provided the spatial extensions $\sigma_{x,y} \gg a$, the coherent pump selectively addresses a small region in \vec{k} -space in the vicinity of the desired K' Dirac point and efficiently excludes the other Dirac point.

In Fig. 7.4 we show examples of spectra of the total intensity summed over all lattice sites

$$I_T = \sum_{i,j} (|a_{i,j}|^2 + |b_{i,j}|^2) \quad (7.22)$$

as a function of the pump frequency ω_0 .

Fig. 7.4-A shows the spectra of the unstrained case $\tau = 0$. In this case, we know that the eigenstates of the honeycomb lattice form a continuum with a conical Dirac dispersion $\omega \simeq v_D |q|$ in the vicinity of the K, K' points, so the spectrum is a featureless continuum, with only a peculiar dip in the center due to the Dirac cone. The small oscillations in the spectra are due to finite size effects stemming from a small but non-zero reflection at the edges and these disappear if larger systems are considered. When a small strain $\tau = 0.005$ is introduced, pronounced peaks emerge in the spectra shown in Fig. 7.4-B, corresponding to the Landau levels. We compare the numerical spectra with the analytical energies of Landau levels, as given by Eq. (7.15), and plotted with dashed vertical red lines. We see that the position of the peaks in Fig. 7.4 is in good agreement with the analytical values.

As usual, for a pump frequency close to resonance with a peak, the field intensity profile follows the wave function of the corresponding mode: the two cases of unstrained and strained honeycomb lattices will be separately discussed in the next sections.

7.2.1 The perfect honeycomb lattice.

Figure 7.5 shows the field amplitude $|a_{i,j}|^2$ and $|b_{i,j}|^2$ for the unstrained case, on the A and B sites in the steady state for two different pumping frequencies ω_0 and for two different spatial

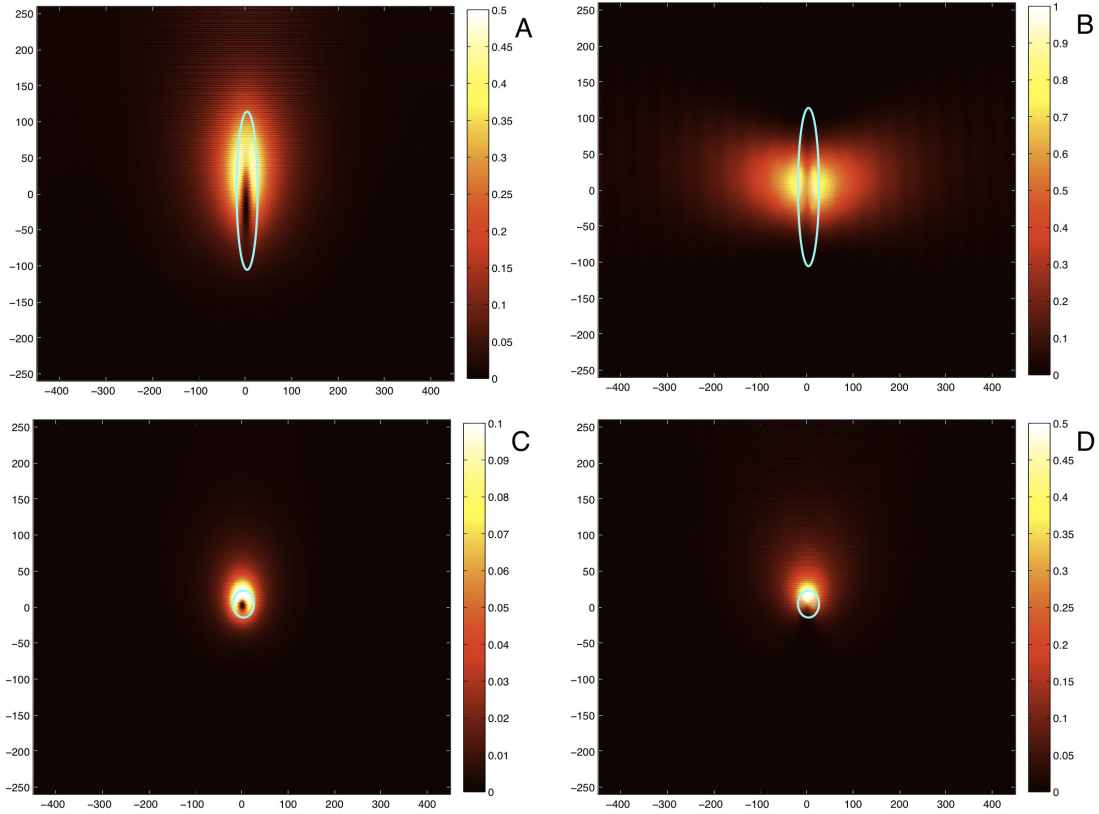


Figure 7.5: Field intensity distribution as numerically calculated from Eq. (7.20) for different pumping frequencies ω_0 . $N = 601$, $\hbar\gamma/t = 0.005$, $\tau = 0$ and $\sigma_x/a = 10$ for all panels. Panels **A** and **B** are for $\sigma_y/a = 50$, while panels **C** and **D** are for $\sigma_y/a = 10$. The pumping area spot is highlighted by the cyan circle. Panels **A** and **C** are for $\hbar\omega_0/t = 0$, corresponding to the Dirac point, while panels **B** and **D** are for a positive detuning $\hbar\omega_0/t = 0.1$.

extents of the pump along y . The first row is obtained for $\sigma_x/a = 10$ and $\sigma_y/a = 50$, at $\omega_0 = 0$ for Fig. 7.5-A and at $\omega_0 > 0$ for Fig. 7.5-B. The second row is obtained for $\sigma_x/a = \sigma_y/a = 10$, at the same two pumping frequencies.

The intensity patterns display an interesting structure that can be qualitatively understood as follows. The pump excites waves that expand radially in all directions with the Dirac velocity for a distance of the order of v_D/γ , the so-called conical diffraction, see Peleg et al. [2007]. The angular dependence around the pump spot is determined by the matching of the phase profile of the pump with the relative phase of the A and B sites at different wave vectors in the vicinity of the Dirac point. As can be seen in Fig. 7.5-A and Fig. 7.5-C for $\omega_0 = 0$, constructive interference reinforces the intensity in the positive- y direction, while destructive interference reduces the intensity in the negative- y direction.

At finite frequency $\omega_0 \neq 0$, another mechanism contributes to the determination of the pattern: as one can see in Fig. 7.5-B, the intensity is now concentrated laterally in the positive and negative x direction and there is almost no intensity in the positive- y direction. This fact can be explained in terms of the momentum distribution of the incident field, which does not overlap with the resonant Dirac wave at a finite wave vector $k_y \simeq \omega_0/v_D \gg 1/\sigma_y$ in the positive- y direction. As expected, this feature no longer occurs for a smaller σ_y for which $k_y \simeq \omega_0/v_D < 1/\sigma_y$ and a good overlap is again possible also in the positive- y direction. As a result, the angular distribution is in this case again maximal in the positive- y direction, see Fig. 7.5-D.

7.2.2 The strained honeycomb lattice.

The spatial structure of Landau levels in a strained honeycomb lattice are illustrated in Fig. 7.6. We considered a relatively weak strain of $\tau = 0.005$ and show the steady-states intensity patterns for different pumping frequencies ω_0 . Fig. 7.60-4 are for frequencies of the first five Landau

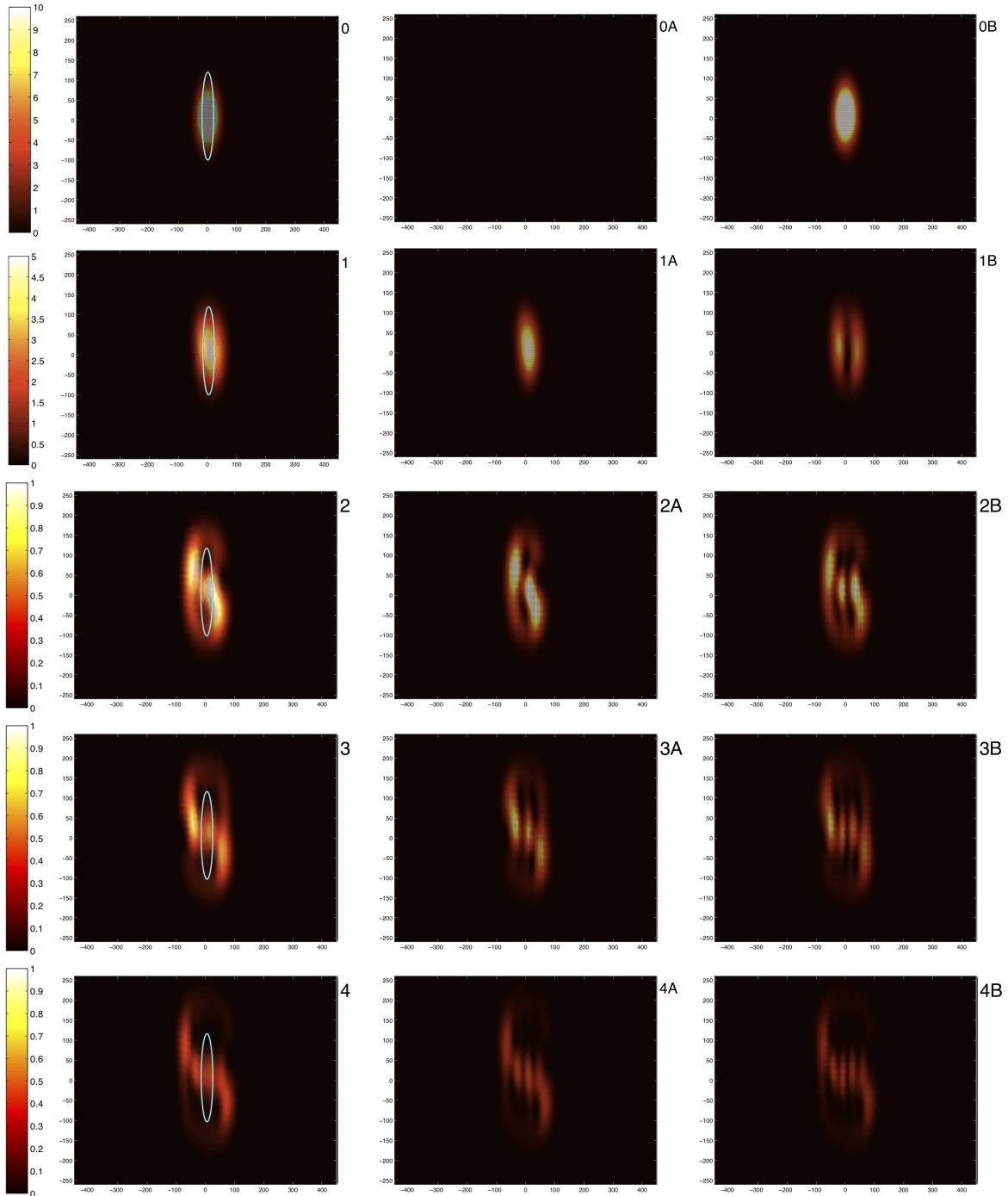


Figure 7.6: Numerically calculated steady-state intensity distribution for different pump frequencies ω_0 on resonance with the different Landau levels at the K' point. We have chosen $N = 601$, $\hbar\gamma/t = 0.005$, $\tau = 0.005$, $\sigma_x/a = 10$ and $\sigma_y/a = 50$ for all panels. Panels **0-4** show the total intensity for frequencies $\omega_0 = 0, \omega, \omega\sqrt{2}, \omega\sqrt{3}, \omega\sqrt{4}$ corresponding to the first five Landau levels. The pumped region is highlighted by the cyan circle. While the left panels show the complete intensity distribution, the central **0A-4A** and right **0B-4B** panels isolate the intensity distribution on A and B sites.

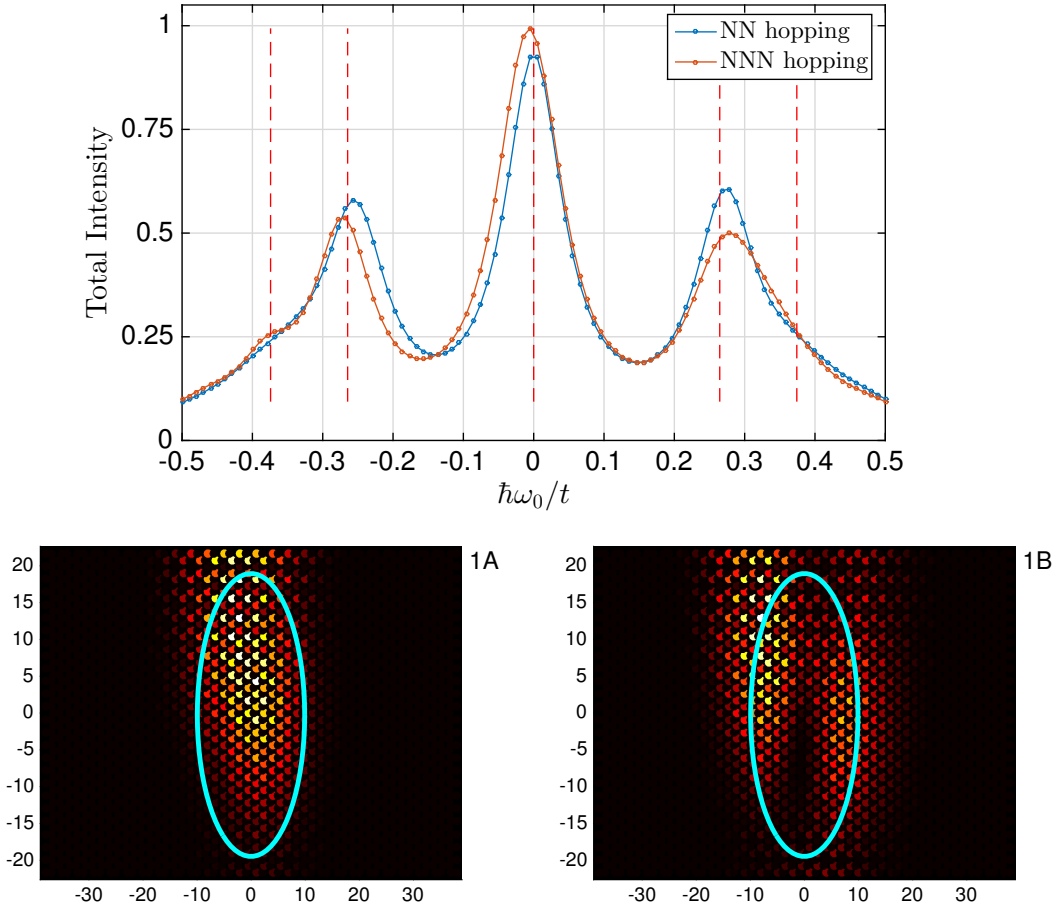


Figure 7.7: Numerical calculations using realistic parameters of state-of-the-art experimental setups, namely $N_x = N_y = 51$, $\hbar\gamma/t = 0.05$, $\tau = 0.07$, $\sigma_x/a = 5$ and $\sigma_y/a = 10$. Upper panel: spectra of the total field intensity as a function of the pumping frequency ω_0 . The blue curve is the spectra obtained with only nearest-neighbour hopping, the orange curve includes contributions also from the position dependent next-nearest-neighbour (NNN) hopping, with $t' = 0.08t$. Solid lines are a guide to the eye and red dashed lines are the analytical energies of the first three Landau levels as predicted by Eq. (7.15). Lower panels: steady-state intensity distributions on the A (panel 1A) and B (panel 1B) sites for a pump frequency ω_0 tuned on resonance with the $n = 1$ Landau level at the K' point, in the presence of NNN hopping processes with a realistic amplitude $t' = 0.08t$.

levels $n = 0 \dots 4$, according to Eq. (7.15). Parameters for all panels were chosen to give the best representation of the Landau level wave functions with a realistic form of the pump. In particular, a relatively wide pump spot along y was needed so that the range of excited momenta $q_y \simeq 1/\sigma_y$ is sufficiently small such that the jitter of the guiding center x_0 is smaller than the magnetic length l_B . This helps to avoid blurring of the Landau level intensity pattern.

To better understand the mode structure, the separated field intensity distributions on respectively the A and the B sites are shown in the panels labelled with **A** or **B**: as expected, the qualitative structure of the intensity profile follows the shape of the eigenstates shown in Fig. 7.3. In particular, the numbers of nodes and the width of the field amplitudes coincide with what is expected from the analytical wave functions Eq. (7.16).

The particular spiral-like shape is due to the interference between the resonant Landau level and its neighbours, that are non-resonantly excited. More details on this effect are given in Appendix G.

7.3 Experimental remarks.

From the experimental point of view, the requirements to clearly observe the patterns discussed in the previous section are a relatively small value of the loss rate and a relatively large size of the lattice. Firstly, stronger loss rates may hinder a clear identification of the Landau level peaks in the spectra of Fig. 7.4 and are responsible for strong mixing of neighbouring eigenstates in the spatial pattern of Fig. 7.6. Secondly, in smaller lattices spurious reflections at the lattice edges may occur as well as significant distortions of the mode wave functions. While propagation towards the lattice edges can be a problem for propagating Dirac waves in perfect honeycomb lattices, this issue is much less severe in the presence of strain as the Landau levels are spatially localized. As a result, finite size effects are negligible as soon as the size of the lattice is larger than the magnetic length l_B .

In particular, we note that two consecutive Landau levels can be resolved if the separation between them is larger than the linewidth, namely $\hbar\gamma < \mathcal{E}_n - \mathcal{E}_{n-1}$. This means that the n -th gap is resolved if:

$$\frac{\hbar\gamma}{t} < (\sqrt{n} - \sqrt{n-1}) \frac{\sqrt{\tau}}{2}. \quad (7.23)$$

In order for the Landau wave function not to be distorted by the edges of the lattices, we need the magnetic length to be much smaller than the size of the system. The total length of the lattice in Fig. 7.1 is $L_x = (3N_x - 1)a/2$. The condition $l_B \ll L_x/2$, then, implies that:

$$\tau > \left(\frac{6\sqrt{2}}{3N_x - 1} \right)^2. \quad (7.24)$$

In order for the key features of Landau level wave function not to be blurred, such as the number of nodes or the width of the wave function, one also needs that the position x_0 of the guiding center jitters by less than a magnetic length under the uncertainty of $q_y \simeq 1/L_y$: remarkably, this imposes a condition $l_B \ll L_y$ analogous to Eq. (7.24). Finally, we need to keep in mind the condition already given in Eq. (7.2), which set an upper bound on the strain τ in order to have a physical $t_1 \geq 0$ hopping at all points of the lattice:

$$\tau < \frac{12}{3N_x - 1}. \quad (7.25)$$

For the sake of concreteness, we can discuss these criteria having in mind a realistic experiment using photonic Jacqmin et al. [2014] or microwave Bellec et al. [2013a,b, 2014] technology: state-of-the-art samples are in both cases restricted to relatively small lattices, with a few tens of sites in each direction. From Eq. (7.25), this imposes an upper bound to the strain $\tau < 0.08$.

For a realistic loss rate $\hbar\gamma/t \approx 0.05$ of current experiments, a value $\tau \approx 0.07$ of the strain should however allow us to resolve the first two gaps between Landau levels. This is illustrated in the upper panel of Fig. 7.7, where we show the total intensity spectra as a function of the pump frequency: peaks corresponding to the lowest Landau levels are clearly visible with an excellent agreement with the analytical prediction of Eq. (7.15). We also show that the spectra are only slightly affected when a position-dependent NNN hopping is included with a realistic amplitude $t' = 0.08t$.

In the lower panels of Fig. 7.7 we show the intensity distribution for a pump on resonance with the peak corresponding to the $n = 1$ Landau level. Independently of the presence of a NNN hopping, the peculiar nodal profile of the mode is clearly visible as a central black stripe in the B sites intensity pattern shown in panel **B**. The horizontal dark fringes that are visible in the upper and lower part of the image are, instead, a spurious effect due to reflections on the edges of the lattice.

Chapter 8

Spin-orbit coupling in a honeycomb lattice.

Spin-orbit coupling is the interaction between the spin of a particle and its own motion. Perhaps the most famous example of the effects of such a coupling is the energy shift of the levels of an atomic electron stemming from the interaction between the spin of the electron and the magnetic field generated by the orbit of the electron around the nucleus. Spin-orbit coupling is also naturally present in solid materials due to the crystalline structure, but in some cases, however, this effect is weak and not always of easy manipulation and control.

As we have discussed so far, an enormous advantage of artificial materials is the possibility to tune and design the system Hamiltonian. Different ways to implement a synthetic spin-orbit coupling are reviewed for ultracold atomic gases with dressed states by Galitski and Spielman [2013], Li et al. [2015], or for optical photons using the polarization degree of freedom, by Cardano and Marrucci [2015]. In particular, Sala et al. [2015] implemented a spin-orbit coupling for a polariton, *i.e.* a quasi-particle arising from the interaction of a photon and an exciton in a semiconductor micropillar, which has the same polarization properties as the photon. The polaritons in different micropillars are coupled with different tunnelling amplitudes according to whether their *pseudo-spin* polarization state is parallel or orthogonal to the link direction, as shown by de Vasconcellos et al. [2011], due to a polarization splitting of the bonding (longitudinal) or anti-bonding (transverse) states.

In this chapter we take inspiration from the work of Sala et al. [2015] and apply the concept of polarization splitting within classical mechanics to realize a system with spin-orbit coupling. We start by showing that a *pre-tensioned* spring induces a splitting between the longitudinal and transverse degrees of freedom of a mechanical system of two coupled pendula. As the motion along the longitudinal (L) and transverse (T) directions acts as a pseudo-spin, we will then review how, for an extended system, such an L-T splitting can be described as a spin-orbit coupling.

We have also experimentally realized a mechanical benzene molecule that implements this spin-orbit coupling, and studied the eigenmodes of the system. The experiment is the result of a collaboration with Prof. Nicola Pugno, Alice Berardo, Ludovic Taxis and Giuseppe Vettori from the Department of Civil, Environmental and Mechanical Engineering of the University of Trento.

8.1 L-T splitting in classical mechanics.

We start by considering a spring of rest length ℓ_0 and spring constant k , which is pre-elongated to a length ℓ and kept in equilibrium by some other external force, as shown in the left part of Fig. 8.1. This could be, for example, the situation of two pendula whose hanging points are at a distance that is larger than ℓ_0 . In the equilibrium configuration, the gravitational restoring force of the pendulum balances exactly the restoring force of the spring, whose length will be $\ell > \ell_0$, as schematically shown in the right part of Fig. 8.1. When a further elongation that changes the

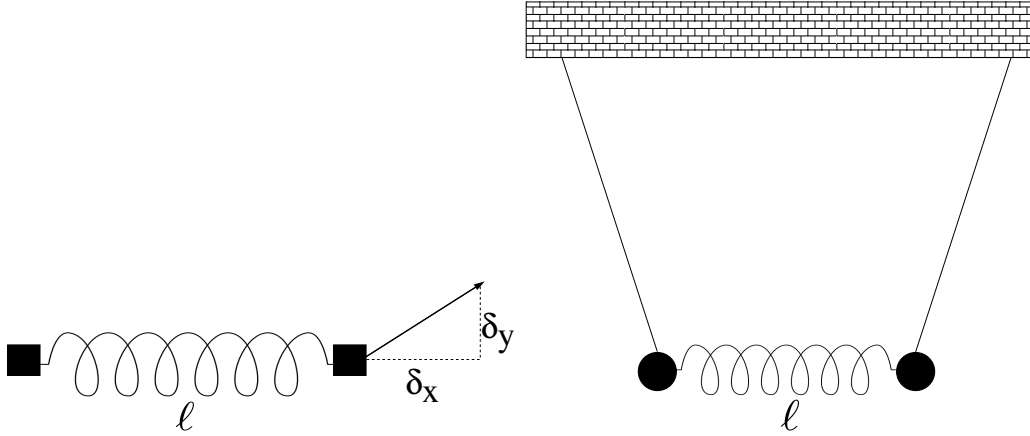


Figure 8.1: On the left, we show an isolated pre-tensioned spring stretched to a length ℓ by some external force and subjected to a further elongation that changes its length by δ_x and δ_y along the two directions. On the right, sketch of one of the possible situations that could produce the desired stretch of the spring.

length by δ_x and δ_y along the two directions is applied to spring, the elastic energy stored in it is:

$$U = \frac{1}{2}k \left(\sqrt{(\delta_x + \ell)^2 + \delta_y^2} - \ell_0 \right)^2, \quad (8.1)$$

having assumed a linear spring, *i.e.* that the applied elongation is not causing any an-harmonic behaviour. From this expression, we can see that the small oscillations in the x - and y -directions around the equilibrium position are characterized by two different quantities:

$$\left. \frac{\partial^2 U}{\partial \delta_x^2} \right|_{\delta_x=0, \delta_y=0} = k \equiv k_L, \quad \left. \frac{\partial^2 U}{\partial \delta_y^2} \right|_{\delta_x=0, \delta_y=0} = k \left(1 - \frac{\ell_0}{\ell} \right) \equiv k_T \quad (8.2)$$

while $\left. \frac{\partial^2 U}{\partial \delta_x \partial \delta_y} \right|_{\delta_x=0, \delta_y=0} = 0$ because of reflection symmetry. Equation (8.2) defines the couplings respectively in the longitudinal and transverse directions, defined with respect to the axis of the spring. If the initial length of the spring $\ell = \ell_0$ is exactly equal to the rest length, from Eq. (8.2) we get that the restoring force of the spring in the transverse direction is zero, since $k_T = 0$. We have therefore that the motion along the two directions is completely decoupled, and that the restoring force of the spring is mainly in the longitudinal direction and proportional to k_L . However, when $\ell \neq \ell_0$, the motion along the longitudinal direction responds with a different spring constant than the motion along the perpendicular direction, according to Eq. (8.2). The strength of this *L-T splitting* depends on the ration ℓ_0/ℓ and it is stronger for more pre-elongated springs. The longitudinal and transverse motions are considered as different pseudo-spins of an oscillator, and the L-T splitting couples these two pseudo-spins, giving rise to the spin-orbit coupling in classical mechanics, as we shall see in detail in the next section.

8.2 Modes of honeycomb lattices with L-T splitting.

We now derive the eigenmodes of an extended system of pendula connected by equally pre-tensioned springs arranged in an honeycomb lattice. Similar theoretical ideas are proposed in the paper by [Kariyado and Hatsugai \[2015\]](#). We assume that the masses are all equal to m and that the springs are identical and their spring constant is k . According to the amount ℓ of elongation in the equilibrium configuration, we have from Eq. (8.2) that the frequencies of the motion along the longitudinal and transverse directions are:

$$\Omega_L \equiv \sqrt{\frac{k_L}{m}}, \quad \Omega_T \equiv \sqrt{\frac{k_T}{m}}. \quad (8.3)$$

From the expressions of these two frequencies, we can directly separate the equation of motion for the system of pendula along the L-T directions. For this purpose, it is useful to identify the

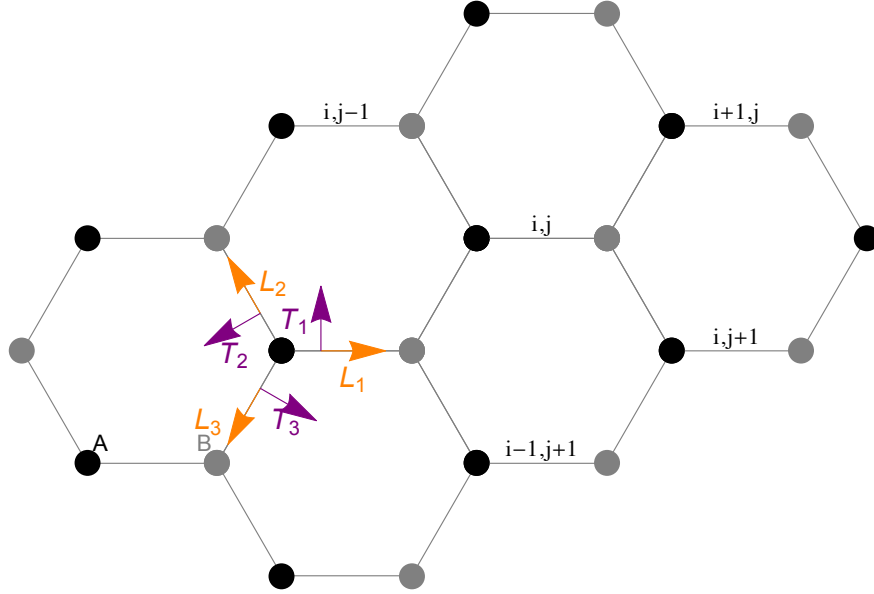


Figure 8.2: Representation of the longitudinal and transverse unit vectors. We also show the indexing of the unit cells, as was also introduced in Chap. 6.

following unit vectors, which are drawn with coloured arrows in Fig. 8.2:

$$\begin{aligned} \hat{L}_1 &= (1, 0), & \hat{L}_2 &= \left(-\frac{1}{2}, \frac{\sqrt{3}}{2}\right), & \hat{L}_3 &= \left(-\frac{1}{2}, -\frac{\sqrt{3}}{2}\right), \\ \hat{T}_1 &= (0, 1), & \hat{T}_2 &= \left(-\frac{\sqrt{3}}{2}, -\frac{1}{2}\right), & \hat{T}_3 &= \left(-\frac{\sqrt{3}}{2}, \frac{1}{2}\right). \end{aligned} \quad (8.4)$$

Each pendulum occupies the vertex of a hexagon and it is free to oscillate with a frequency ω_0 . We use the labelling shown in Fig. 8.2, that is the same as in Chap. 6. We indicate with $\vec{a}_{i,j} = (a_{i,j}^x, a_{i,j}^y)$ the position of the mass located on an A -site in the unit cell i, j . For masses in the sublattice A , Newton's equations of motion are the following:

$$\begin{aligned} \ddot{\vec{a}}_{i,j} &= -\omega_0^2 \vec{a}_{i,j} \\ &+ \Omega_L^2 \left\{ \left[(\vec{b}_{i,j} - \vec{a}_{i,j}) \cdot \hat{L}_1 \right] \hat{L}_1 + \left[(\vec{b}_{i,j-1} - \vec{a}_{i,j}) \cdot \hat{L}_2 \right] \hat{L}_2 + \left[(\vec{b}_{i-1,j} - \vec{a}_{i,j}) \cdot \hat{L}_3 \right] \hat{L}_3 \right\} \\ &+ \Omega_T^2 \left\{ \left[(\vec{b}_{i,j} - \vec{a}_{i,j}) \cdot \hat{T}_1 \right] \hat{T}_1 + \left[(\vec{b}_{i,j-1} - \vec{a}_{i,j}) \cdot \hat{T}_2 \right] \hat{T}_2 + \left[(\vec{b}_{i-1,j} - \vec{a}_{i,j}) \cdot \hat{T}_3 \right] \hat{T}_3 \right\}, \end{aligned} \quad (8.5)$$

while, for the B -sublattice, symmetry along the three directions imposes that:

$$\begin{aligned} \ddot{\vec{b}}_{i,j} &= -\omega_0^2 \vec{b}_{i,j} \\ &+ \Omega_L^2 \left\{ \left[(\vec{a}_{i,j} - \vec{b}_{i,j}) \cdot (-\hat{L}_1) \right] (-\hat{L}_1) + \left[(\vec{a}_{i,j+1} - \vec{b}_{i,j}) \cdot (-\hat{L}_2) \right] (-\hat{L}_2) \right. \\ &\quad \left. + \left[(\vec{a}_{i+1,j} - \vec{b}_{i,j}) \cdot (-\hat{L}_3) \right] (-\hat{L}_3) \right\} \\ &+ \Omega_T^2 \left\{ \left[(\vec{a}_{i,j} - \vec{b}_{i,j}) \cdot (-\hat{T}_1) \right] (-\hat{T}_1) + \left[(\vec{a}_{i,j+1} - \vec{b}_{i,j}) \cdot (-\hat{T}_2) \right] (-\hat{T}_2) \right. \\ &\quad \left. + \left[(\vec{a}_{i+1,j} - \vec{b}_{i,j}) \cdot (-\hat{T}_3) \right] (-\hat{T}_3) \right\}. \end{aligned} \quad (8.6)$$

For obtaining the dispersive normal modes, as we did in Chap. 6, we write our variables as:

$$\begin{aligned} \vec{a}_{i,j} &= \frac{1}{V} \int_{k_x \in BZ} \int_{k_y \in BZ} \begin{pmatrix} a_x^k \\ a_y^k \end{pmatrix} e^{i(\vec{k} \cdot \vec{a}_1 + j\vec{k} \cdot \vec{a}_2)} e^{i\Omega t} dk_x dk_y \\ \vec{b}_{i,j} &= \frac{1}{V} \int_{k_x \in BZ} \int_{k_y \in BZ} \begin{pmatrix} b_x^k \\ b_y^k \end{pmatrix} e^{i(\vec{k} \cdot \vec{a}_1 + j\vec{k} \cdot \vec{a}_2)} e^{-i\vec{k} \cdot \vec{R}_1} e^{i\Omega t} dk_x dk_y. \end{aligned} \quad (8.7)$$

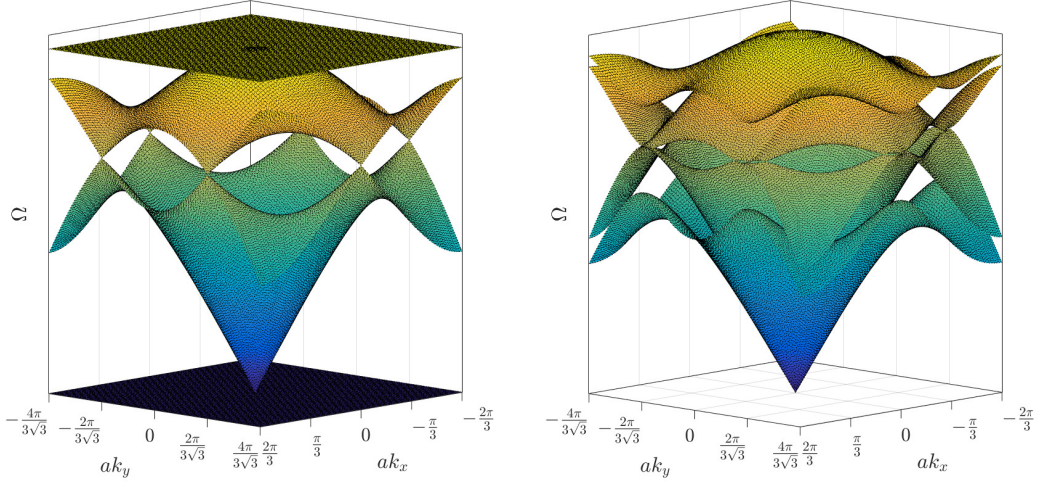


Figure 8.3: Frequency dispersion bands of phonons in a honeycomb lattice in the presence of a spin-orbit interaction induced by the L-T splitting, obtained as $\Omega = \sqrt{-\varepsilon}$, where ε are the eigenvalues of the matrix in Eq. (8.8), for $\omega_0 = 0$. On the left, $\Omega_T^2/\Omega_L^2 = 0$ and we see that two of the four bands are dispersion-less. On the right $\Omega_T^2/\Omega_L^2 = 0.5$ and all four bands are dispersive.

In this way, we can write the dynamical matrix $-\Omega^2\Psi_{xy} = D\Psi_{xy}$ in the following basis:

$$\Psi_{xy} = \begin{pmatrix} a_x^k \\ a_y^k \\ b_x^k \\ b_y^k \end{pmatrix},$$

by projecting each of the equations in Eq. (8.5) and Eq. (8.6) along the x - and y - direction. The resulting dynamical matrix is:

$$D = \begin{pmatrix} d_0 & 0 & F_L^*(k) & W^*(k) \\ 0 & d_0 & W^*(k) & F_T^*(k) \\ F_L(k) & W(k) & d_0 & 0 \\ W(k) & F_T(k) & 0 & d_0 \end{pmatrix}, \quad (8.8)$$

where for short-hand notation we have introduced the following quantities:

$$\begin{aligned} d_0 &= -\frac{3}{2}(\Omega_L^2 + \Omega_T^2) - \omega_0^2, & F_L(k) &= \Omega_L^2 e^{i\vec{k}\cdot\vec{R}_1} + \frac{3\Omega_T^2 + \Omega_L^2}{4} (e^{i\vec{k}\cdot\vec{R}_2} + e^{i\vec{k}\cdot\vec{R}_3}), \\ W(k) &= \frac{\sqrt{3}}{4}(\Omega_L^2 - \Omega_T^2) (e^{i\vec{k}\cdot\vec{R}_2} - e^{i\vec{k}\cdot\vec{R}_3}), & F_T(k) &= \Omega_T^2 e^{i\vec{k}\cdot\vec{R}_1} + \frac{3\Omega_L^2 + \Omega_T^2}{4} (e^{i\vec{k}\cdot\vec{R}_2} + e^{i\vec{k}\cdot\vec{R}_3}). \end{aligned} \quad (8.9)$$

The eigenvalues ε of the dynamical matrix in Eq. (8.8) are the energy bands of the honeycomb lattice in the presence of spin-orbit coupling, as found for example by [Wu and Das Sarma \[2008\]](#), [Jacqmin et al. \[2014\]](#), and are related to the frequencies of the eigenmodes of the system as: $\Omega = \sqrt{-\varepsilon}$.

In Fig. 8.3 we show the eigenfrequencies Ω of the phonons of the honeycomb lattice for two cases. On the left, we have considered the case of $\Omega_T = 0$, which happens when $\ell = \ell_0$ in Eq. (8.2). We see that there are two flat non-dispersive modes, corresponding to the transverse modes, and another two dispersive longitudinal modes. This is the same regime as in [Jacqmin et al. \[2014\]](#), that lead to the direct observation of a flatband for a polariton system. On the right part of Fig. 8.3, we show the eigenfrequencies in presence of a spin-orbit coupling $\Omega_T^2/\Omega_L^2 = 0.5$. In this case we see that all modes are dispersive. In the limiting case (not shown) of $\Omega_T^2/\Omega_L^2 = 1$, the four modes becomes two, with a two-fold degeneracy. From the standard theory of harmonic crystals [Aschroft and Mermin \[1976\]](#), we can identify these four modes to be the ‘‘acoustical’’ and ‘‘optical’’ modes of the phonons in the honeycomb lattice.

8.2.1 The circular polarization basis.

More insight into the nature of the spin-orbit coupling can be obtained in the basis of *circular polarization* $+/-$, rather than in the basis of coordinates x/y , as done in [Sala et al. \[2015\]](#). To move into the new basis, we implement the following unitary transformation:

$$M = \frac{1}{\sqrt{2}} \begin{pmatrix} 1 & i & 0 & 0 \\ 1 & -i & 0 & 0 \\ 0 & 0 & 1 & i \\ 0 & 0 & 1 & -i \end{pmatrix}. \quad (8.10)$$

This transformation, acting on the vector Ψ_{xy} , gives a new vector:

$$M\Psi_{xy} = \Phi \equiv \frac{1}{\sqrt{2}} \begin{pmatrix} a_x^k + ia_y^k \\ a_x^k - ia_y^k \\ b_x^k + ib_y^k \\ b_x^k - ib_y^k \end{pmatrix} = \begin{pmatrix} a_+ \\ a_- \\ b_+ \\ b_- \end{pmatrix}, \quad (8.11)$$

where for short-hand notation we have called $a_{\pm} \equiv (a_x^k \pm ia_y^k)/\sqrt{2}$, and similarly for b_{\pm} .

The dynamical matrix in Eq. (8.8) becomes:

$$\tilde{D} \equiv MDM^\dagger = \begin{pmatrix} \tilde{d}_0 & 0 & JV^*(k) & \Delta V_1^*(k) \\ 0 & \tilde{d}_0 & \Delta V_2^*(k) & JV^*(k) \\ JV(k) & \Delta V_1(k) & \tilde{d}_0 & 0 \\ \Delta V_2(k) & JV(k) & 0 & \tilde{d}_0 \end{pmatrix}, \quad (8.12)$$

where we have introduced:

$$J = \frac{\Omega_L^2 + \Omega_T^2}{2}, \quad \Delta = \frac{\Omega_L^2 - \Omega_T^2}{2}, \quad (8.13)$$

and

$$\begin{aligned} \tilde{d}_0 &= -\frac{3}{2}J - \omega_0^2, & V_1(k) &= e^{i\vec{k}\cdot\vec{R}_1} + e^{i\vec{k}\cdot\vec{R}_2} e^{-i2\pi/3} + e^{i\vec{k}\cdot\vec{R}_3} e^{i2\pi/3}, \\ V(k) &= e^{i\vec{k}\cdot\vec{R}_1} + e^{i\vec{k}\cdot\vec{R}_2} + e^{i\vec{k}\cdot\vec{R}_3}, & V_2(k) &= e^{i\vec{k}\cdot\vec{R}_1} + e^{i\vec{k}\cdot\vec{R}_2} e^{i2\pi/3} + e^{i\vec{k}\cdot\vec{R}_3} e^{-i2\pi/3}. \end{aligned} \quad (8.14)$$

The matrix in Eq. (8.12) can be put in terms of a Hamiltonian with a spin operator acting on the pseudo-spin of the sublattice and another spin operator acting on the polarization degree of freedom. We now introduce these two operators. The first one acting on the sublattice degree of freedom is:

$$\Sigma_{\pm} = \frac{\Sigma_x \pm i\Sigma_y}{2} \equiv \sigma_{\pm} \otimes \mathbb{1}_2, \quad (8.15)$$

while the second one, that acts instead on the polarization degree of freedom, is:

$$S_{\pm} = \frac{S_x \pm iS_y}{2} \equiv \mathbb{1}_2 \otimes \sigma_{\pm}, \quad (8.16)$$

where $\mathbb{1}_n$ is the n -by- n identity matrix and σ_{\pm} are defined as usual $\sigma_{\pm} = \sigma_x \pm i\sigma_y$ from the 2-by-2 Pauli matrices. The two operators in Eq. (8.15) and Eq. (8.16) commute with each other. The explicit matrix-expression of the operators Σ_{\pm} and S_{\pm} is the following:

$$\begin{aligned} \Sigma_+ &= \begin{pmatrix} 0 & 0 & 1 & 0 \\ 0 & 0 & 0 & 1 \\ 0 & 0 & 0 & 0 \\ 0 & 0 & 0 & 0 \end{pmatrix}, & \Sigma_- &= \begin{pmatrix} 0 & 0 & 0 & 0 \\ 0 & 0 & 0 & 0 \\ 1 & 0 & 0 & 0 \\ 0 & 1 & 0 & 0 \end{pmatrix}, \\ S_+ &= \begin{pmatrix} 0 & 1 & 0 & 0 \\ 0 & 0 & 0 & 0 \\ 0 & 0 & 0 & 1 \\ 0 & 0 & 0 & 0 \end{pmatrix}, & S_- &= \begin{pmatrix} 0 & 0 & 0 & 0 \\ 1 & 0 & 0 & 0 \\ 0 & 0 & 0 & 0 \\ 0 & 0 & 1 & 0 \end{pmatrix}. \end{aligned} \quad (8.17)$$

The action of those operators is better understood in the following basis:

$$|A+\rangle = \begin{pmatrix} 1 \\ 0 \\ 0 \\ 0 \end{pmatrix}, \quad |A-\rangle = \begin{pmatrix} 0 \\ 1 \\ 0 \\ 0 \end{pmatrix}, \quad |B+\rangle = \begin{pmatrix} 0 \\ 0 \\ 1 \\ 0 \end{pmatrix}, \quad |B-\rangle = \begin{pmatrix} 0 \\ 0 \\ 0 \\ 1 \end{pmatrix}, \quad (8.18)$$

where A, B stand for the sublattice degrees of freedom and $+, -$ for the polarization degrees of freedom. We have that:

$$\begin{aligned} \Sigma_+ S_+ |B-\rangle &= |A+\rangle, & \Sigma_+ S_- |B+\rangle &= |A-\rangle, \\ \Sigma_- S_+ |A-\rangle &= |B+\rangle, & \Sigma_- S_- |A+\rangle &= |B-\rangle, \end{aligned} \quad (8.19)$$

since Σ_+ is the sublattice pseudo-spin raising operator and S_+ is the polarization pseudo-spin raising operator. It is worth mentioning at this point that the rotation operator for the polarization in the $+/-$ basis reads as:

$$R_\theta = \begin{pmatrix} e^{i\theta} & 0 & 0 & 0 \\ 0 & e^{-i\theta} & 0 & 0 \\ 0 & 0 & e^{i\theta} & 0 \\ 0 & 0 & 0 & e^{-i\theta} \end{pmatrix}, \quad (8.20)$$

such that S_\pm operators transform under this rotation as spin-1 and not as spin-1/2, [Carusotto and Ciuti \[2013\]](#).

We can now expand the matrix in Eq. (8.12) around the K points $\vec{k} \rightarrow (q_x, q_y - 4\pi/(3\sqrt{3}a))$, for $|\vec{q}| \ll 1/a$ at the first order, as was done in Chap. 6. With the definition of the pseudo-spin operators and with the gauge transformation already used in Chap. 6 for Eq. (6.10), we have:

$$\begin{aligned} \tilde{D} &= \left(-\frac{3}{2}J - \omega_0^2 \right) \mathbb{1}_4 + \frac{3a}{2}J [\Sigma_+(q_x - iq_y) + \Sigma_-(q_x + iq_y)] + \\ &3\Delta i (\Sigma_- S_+ - \Sigma_+ S_-) + \frac{3a\Delta}{2} [\Sigma_- S_- (q_x - iq_y) + \Sigma_+ S_+ (q_x + iq_y)]. \end{aligned} \quad (8.21)$$

Introducing as usual the $\Sigma_{x,y}$ and $S_{x,y}$ operators from the Σ_\pm and S_\pm , the dynamical matrix D has the following form:

$$\begin{aligned} \tilde{D} &= \left(-\frac{3}{2}J - \omega_0^2 \right) \mathbb{1}_4 + \frac{3a}{2}J (\Sigma_x q_x + \Sigma_y q_y) - \\ &\frac{3\Delta}{2} (\Sigma_x S_y - \Sigma_y S_x) + \frac{3a\Delta}{4} [S_x (\Sigma_x q_x - \Sigma_y q_y) - S_y (\Sigma_y q_x + \Sigma_x q_y)]. \end{aligned} \quad (8.22)$$

From this expression, it is more evident how the terms in Δ describe the spin-orbit coupling. In particular, the case $\Delta = 0$ means that the $\Omega_L^2 = \Omega_T^2$ and the system consist of two ‘‘copies’’ of graphene along the longitudinal and transverse directions. In fact, for $\Delta = 0$ we recover the same expression as in Eq. (6.10), except that now Σ_x, Σ_y are 4×4 matrices. In addition, for the maximum value $\Delta = \Omega_L^2/2$, *i.e.* $\Omega_T^2 = 0$, we have the two non-dispersive band modes, as seen in left part of Fig. 8.3. Such spin-orbit term was originally found in [Sala et al. \[2015\]](#), [Nalitov et al. \[2015a\]](#) and [Nalitov et al. \[2015b\]](#) for the L-T splitting of polaritons in coupled micropillars.

8.3 A mechanical model of the benzene molecule with L-T splitting.

As a first step towards the implementation of spin-orbit coupling in classical systems on honeycomb lattices, we considered a mechanical analogue of a benzene molecule in the presence of spin-orbit coupling. The system is composed of six pendula of mass m , each occupying the vertex of an hexagon and free to oscillate at a bare frequency ω_0 . Coupling between neighbouring pendula at a distance a is provided by springs of constant k and rest length $\ell_0 < a$, such that in the equilibrium configuration the springs are pre-tensioned, as defined in the previous sections. A sketch of the system, as seen from above, is shown in Fig. 8.4, where also the unit longitudinal and transverse vectors are indicated. The different notation with respect to Fig. 8.2 serves only to

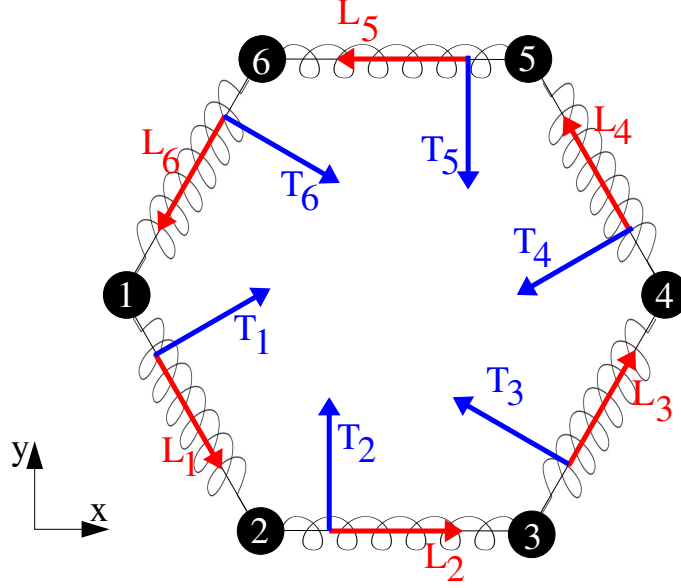


Figure 8.4: Mechanical analogue of the benzene molecule with spin-orbit coupling. The six pendula, as seen from above, are coupled with pre-tensioned springs, whose rest-length is smaller than the side of the hexagon. The red arrows indicate the longitudinal vectors, while the blue arrows indicate the transverse ones, useful for the analytical derivation of the eigenmodes from the equation of motion in Eq. (8.23).

simplify Newton's equations of motion, which now are, in fact, written in the following compact form:

$$\begin{aligned} \ddot{\vec{\psi}}_i = & -\omega_0^2 \vec{\psi}_i + \Omega_L^2 \left[(\vec{\psi}_{i+1} - \vec{\psi}_i) \cdot \hat{L}_i \right] \hat{L}_i + \Omega_L^2 \left[(\vec{\psi}_{i-1} - \vec{\psi}_i) \cdot \hat{L}_{i-1} \right] \hat{L}_{i-1} \\ & + \Omega_T^2 \left[(\vec{\psi}_{i+1} - \vec{\psi}_i) \cdot \hat{T}_i \right] \hat{T}_i + \Omega_T^2 \left[(\vec{\psi}_{i-1} - \vec{\psi}_i) \cdot \hat{T}_{i-1} \right] \hat{T}_{i-1}, \end{aligned} \quad (8.23)$$

for $i = 1, 6$, where the displacement of the i -th pendulum is a two component vector written in the $x - y$ basis $\vec{\psi}_i = (\psi_i^x, \psi_i^y)$ and periodic boundary conditions are intended in the form $i + 1 \rightarrow 1$ for $i = 6$ and $i - 1 \rightarrow 6$ for $i = 1$. We have also used that the longitudinal vectors are:

$$\hat{L}_1 = \left(\frac{1}{2}, -\frac{\sqrt{3}}{2} \right), \quad \hat{L}_2 = (1, 0), \quad \hat{L}_3 = \left(\frac{1}{2}, \frac{\sqrt{3}}{2} \right), \quad \hat{L}_4 = -\hat{L}_1, \quad \hat{L}_5 = -\hat{L}_2, \quad \hat{L}_6 = -\hat{L}_3, \quad (8.24)$$

and the transverse vectors are:

$$\hat{T}_1 = \left(\frac{\sqrt{3}}{2}, -\frac{1}{2} \right), \quad \hat{T}_2 = (0, 1), \quad \hat{T}_3 = \left(-\frac{\sqrt{3}}{2}, \frac{1}{2} \right), \quad \hat{T}_4 = -\hat{T}_1, \quad \hat{T}_5 = -\hat{T}_2, \quad \hat{T}_6 = -\hat{T}_3, \quad (8.25)$$

We solve the eigenvalue problem, searching for a solution of the type $\vec{\psi}_i(t) = \vec{\psi}_i e^{i\Omega t}$. As we did before, we project each of the equations in Eq. (8.23) along the x - and y - direction, in order to write the system in Eq. (8.23) within a matrix formalism in the x, y basis as: $-\Omega^2 \Psi = D\Psi$.

By diagonalizing the 12×12 matrix D we get the frequencies of the eigenmodes:

$$\left\{ \begin{array}{ll} \Omega_1 = \omega_0 & \text{2-fold degenerate} \\ \Omega_2 = \sqrt{\omega_0^2 + \Omega_L^2} & \\ \Omega_3 = \sqrt{\omega_0^2 + \Omega_T^2} & \\ \Omega_4 = \sqrt{\omega_0^2 + 3\Omega_L^2} & \\ \Omega_5 = \sqrt{\omega_0^2 + 3\Omega_T^2} & \\ \Omega_6 = \sqrt{\omega_0^2 + \frac{3}{2}(\Omega_L^2 + \Omega_T^2)} & \text{2-fold degenerate} \\ \Omega_7 = \frac{1}{2} \sqrt{4\omega_0^2 + 5\Omega_L^2 + 5\Omega_T^2 + \sqrt{25\Omega_L^4 - 14\Omega_L^2\Omega_T^2 + 25\Omega_T^4}} & \text{2-fold degenerate} \\ \Omega_8 = \frac{1}{2} \sqrt{4\omega_0^2 + 5\Omega_L^2 + 5\Omega_T^2 - \sqrt{25\Omega_L^4 - 14\Omega_L^2\Omega_T^2 + 25\Omega_T^4}} & \text{2-fold degenerate} \end{array} \right. \quad (8.26)$$

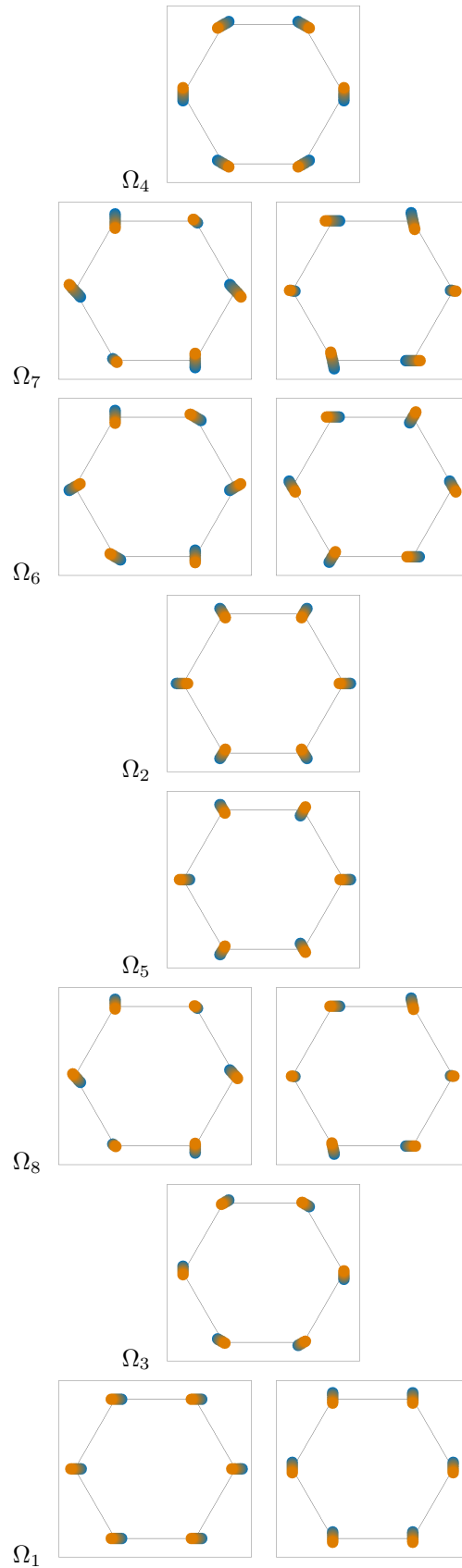


Figure 8.5: Spatial eigenmodes of the mechanical benzene molecule for $\omega_0 = 8.8$ rad/s, $\Omega_L = 7.44$ rad/s and $\Omega_T = 3.52$ rad/s. The motion of the six pendula, within half a period of oscillation, is spatially represented around the equilibrium positions. The colour gradient is indicative of time. The different eigenmodes are ordered according to their increasing frequency of oscillation.

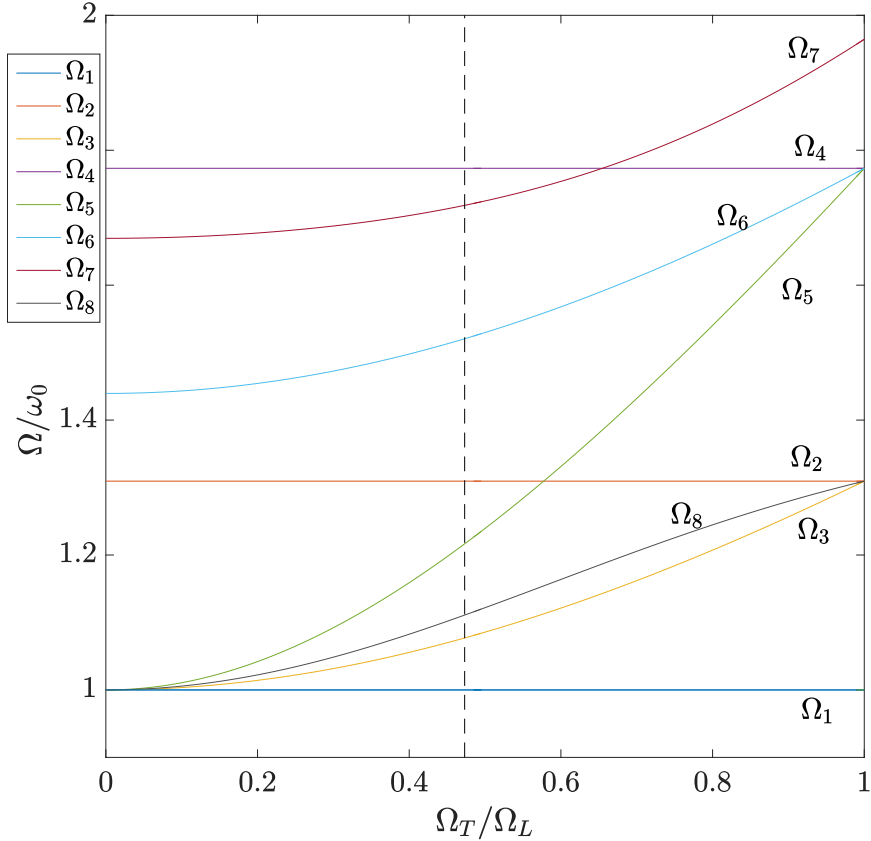


Figure 8.6: Frequency of the eigenmodes of the mechanical benzene molecule as a function of the ratio Ω_T/Ω_L , for fixed $\Omega_L = 7.44\text{rad/s}$ and $\omega_0 = 8.8\text{rad/s}$. The vertical dashed black line indicates the ratio of Ω_T/Ω_L that was used to order the eigenmodes in Fig. 8.5. The same ratio resulted in the experimental data of the next section.

In the general case of $\Omega_T \neq \Omega_L$, the twelve eigenmodes are grouped into a set of eight different values.

In Fig. 8.5 we show the resulting motion of the six pendula for each of the twelve eigenmodes of the mechanical benzene molecule. These modes are the eigenvectors of the matrix D associated to the eigenfrequencies in Eq. (8.26), for $\omega_0 = 8.8\text{ rad/s}$, $\Omega_L = 7.44\text{ rad/s}$ and $\Omega_T = 3.52\text{ rad/s}$; these are the experimental parameters presented in the next section. The motion of the pendula is represented within half a period of oscillation around the equilibrium positions, and the colour gradient is indicative of time. The twelve eigenmodes are grouped and ordered according to their increasing oscillation frequency.

In Fig. 8.6 we show the frequency of the eigenmodes of the mechanical benzene molecule as a function of the ratio Ω_T/Ω_L , for fixed $\Omega_L = 7.44\text{rad/s}$ and $\omega_0 = 8.8\text{rad/s}$. We see that if $\Omega_T = \Omega_L$, the number of different eigenfrequencies is four, and they can be labelled according to the orbital angular momentum, as discussed in Sala et al. [2015]. However, for the general case $\Omega_T \neq \Omega_L$, we notice that the eigenfrequencies split and cross each other as the ratio Ω_T/Ω_L is varied. The vertical dashed black line in Fig. 8.6 indicates the particular value of the ratio Ω_T/Ω_L that was used to sort the eigenmodes in Fig. 8.5. The same ratio resulted in the experimental data of the next section.

8.3.1 Experimental data.

In collaboration with Prof. Nicola Pugno, Alice Berardo, Ludovic Taxis and Giuseppe Vettori, we realized an experiment to prove that the pre-tensioned springs induce a spin-orbit coupling, by checking the frequencies of the eigenmodes of the mechanical benzene as derived in Eq. (8.26).

In Fig. 8.7 we show a picture of the experimental setup. Each pendulum is realized as a sphere of mass $(0.596 \pm 0.001)\text{ Kg}$ and radius $R = (2.7 \pm 0.05)\text{ cm}$ attached to a string of length

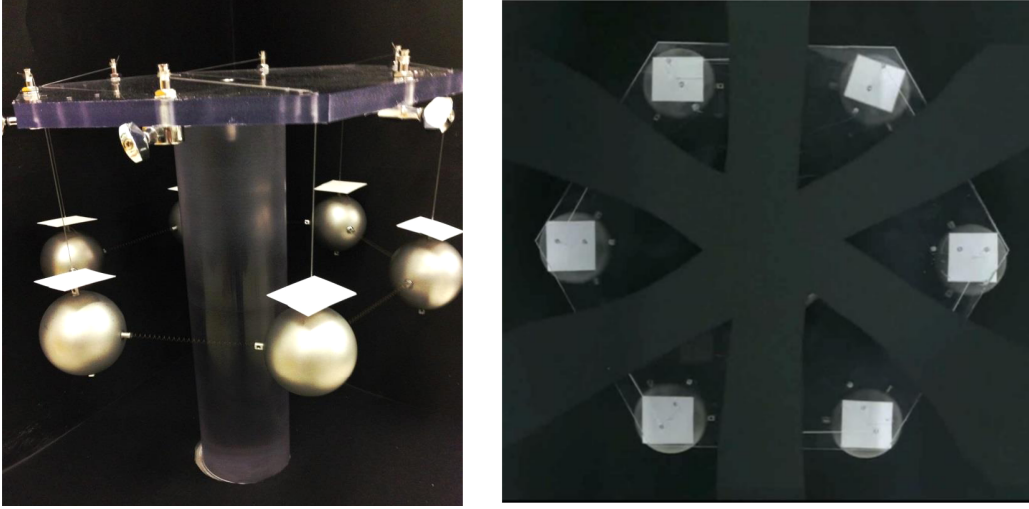


Figure 8.7: On the left, picture of the setup used for the experiment. On the right, snapshot of the video used for measuring the displacements of the pendula through the position of the white squares.

$l = (10.0 \pm 0.1)$ cm, hanging from a transparent plastic roof. The natural frequency of the pendula is:

$$\omega_0 = \sqrt{\frac{g}{l + R}} = (8.79 \pm 0.04) \text{ rad/s}, \quad (8.27)$$

where the error is calculated according to the error analysis, see [Taylor \[1997\]](#).

The pendula are coupled through springs of elastic constant $k = (33 \pm 3)$ N/m and $\ell_0 = (74.5 \pm 0.5)$ mm. In the equilibrium configuration, the elongation of the springs is $\ell = (96.0 \pm 0.5)$ mm. The values of the elastic constants of the springs were extracted from Hooke's law: by measuring the elongations of a spring when subjected to known forces, the slope of the resulting line is the elastic constant of the spring.

From the results in Eq. (8.2), we expect that the longitudinal and transverse frequencies are:

$$\Omega_L = \sqrt{\frac{k}{m}} = (7.44 \pm 0.34) \text{ rad/s}, \quad \Omega_T = \sqrt{\frac{k}{m} \left(1 - \frac{\ell_0}{\ell}\right)} = (3.52 \pm 0.17) \text{ rad/s}. \quad (8.28)$$

Initially, one of the pendula is displaced from its equilibrium position in a random direction and let free to oscillate. The initial condition is such that the subsequent motion of the pendula is a superposition of all eigenmodes of the system. This motion is recorded with a standard video-camera positioned above the system in order to extract the $x_i(t)$ and $y_i(t)$ displacement of each mass from their equilibrium position. The motion of the pendula is sampled at a frequency $\nu_s = 25$ Hz, for a total time of $T = 92$ s. The video is analysed to extract the location of the center of a white square of paper that is rigidly attached to the string of the pendulum itself. These white squares allow us to numerically identify more easily the position of the pendulum, especially on a black background, as is shown in the right panel of Fig. 8.7. We then calculate the displacements of the pendula from their equilibrium positions. In Fig. 8.8 we show the motion of the six pendula as extracted from the video analysis.

The data on the displacements $x_i(t)$ and $y_i(t)$ of the pendula from their equilibrium positions are then further analysed. A fast Fourier transform on each set of data is performed, to obtain the Fourier amplitudes $|F_{x_i}(\Omega)|$ and $|F_{y_i}(\Omega)|$. The frequency axis is defined as usual $\Omega \in [-\pi\nu_s, \pi\nu_s]$, with a step of $\Delta\Omega = 2\pi/T$.

In Fig. 8.9 dots show the total intensity of the Fourier spectra, $\sum_{i=1}^6 (|F_{x_i}(\Omega)| + |F_{y_i}(\Omega)|)$, for the region of interest. The theoretical eigenmodes, calculated from Eq. (8.26) with the experimental values given in Eq. (8.27) and Eq. (8.28), are shown in Fig. 8.9 with dashed black vertical lines. We see a qualitative overall agreement between the experiment and the theoretical predictions, especially regarding the number of peaks and the position of some of the eigenmodes. The small discrepancy for the two eigenmodes around 9.5 rad/s is still within the experimental error, that is indicated with the light blue area. There is however a sizeable deviation of the two peaks around

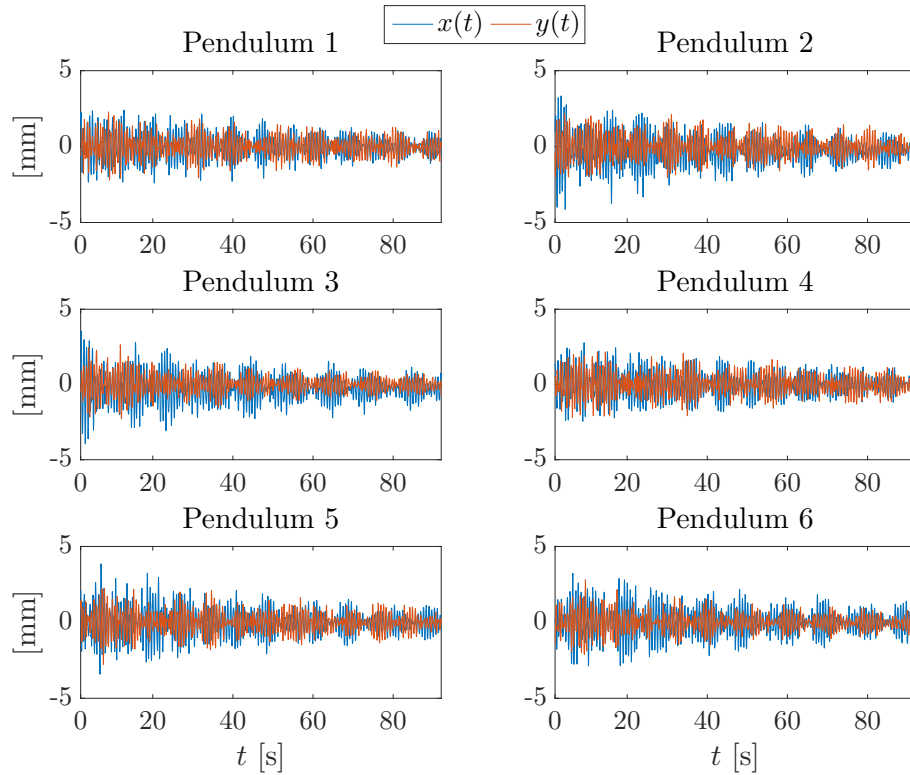


Figure 8.8: Experimental displacements $x_i(t)$ and $y_i(t)$ of the six pendula from their equilibrium positions as extracted from the video analysis.

10.4 and 12 rad/s. Further checks are needed for understanding this phenomena, but one of the explanation could be the following. These frequencies correspond to eigenmodes with a radial symmetry of oscillation, which stress all the six springs at the same time. The springs are already elongated due to pre-tensioning, and a further elongation stretches them into a non-linear regime, which is beyond our analysis.

Nevertheless, it is remarkable how a simple system, such the one that we presented in this section, is able to show the effect of a spin-orbit coupling arising from the L-T splitting of the mechanical modes.

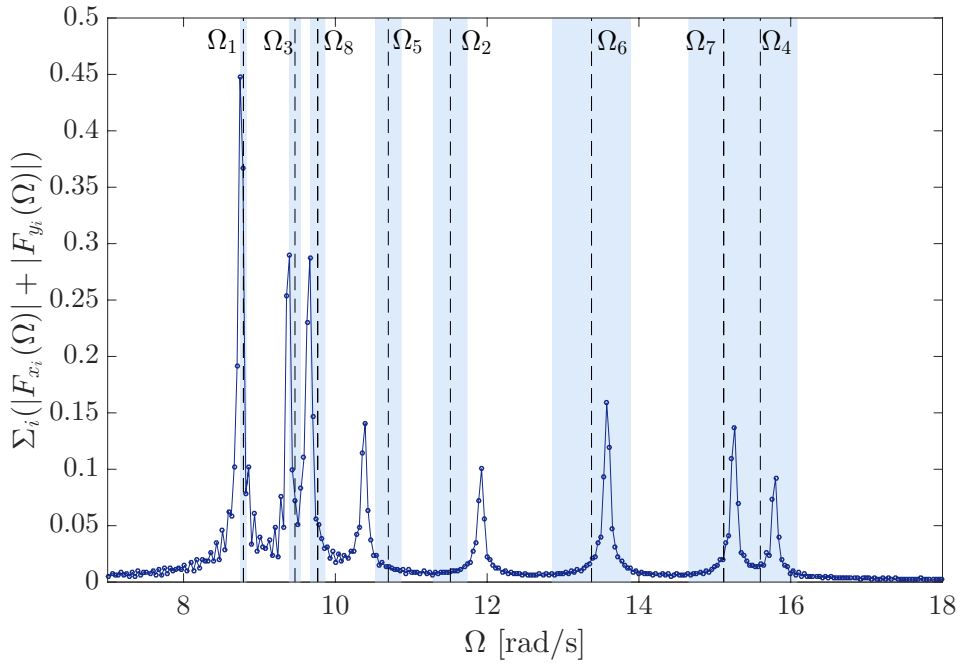


Figure 8.9: Experimental spectra in the region of interest. Dots show the total intensity of the Fourier spectra, $\sum_{i=1}^6 (|F_{x_i}(\Omega)| + |F_{y_i}(\Omega)|)$, while the solid line is a guide to the eye. The black dashed lines corresponds to the theoretical values of the eigenfrequencies as analytically calculated in Eq. (8.26) together with the experimental error as calculated from error propagation analysis Taylor [1997], represented as a light blue area. The eigenfrequencies ordered as in Eq. (8.26) are also indicated. We see a qualitative overall agreement within the experimental error, and a discrepancy on only two of the eigenmodes.

Conclusions and outlooks.

I call my world Flatland, not because that is what we call it, but rather to make its nature clearer to you, my happy readers, who are privileged to live in Space.

Edwin Abbott Abbot – *Flatland: a romance of many dimensions.*

This thesis was dedicated to the study of the properties of classical mechanical and photonic systems in the presence of artificial gauge fields.

In the first part, we have started by considering a pair of coupled classical harmonic oscillators governed by Newton's equations of motion. We have shown that, in the rotating wave approximation, the dynamics of the system can be described by equations that have the same form as Heisenberg's equations of motion written for a quantum tight-binding Hamiltonian. We have also seen that, when the natural frequencies of such oscillators are suitably modulated in time, surprising phenomena happen, such as dynamical decoupling and isolation and in particular the appearance of a tunable non-trivial Peierls coupling phase. We have then extended this idea by theoretically designing a scheme to realize a Floquet topological insulator for a two-dimensional lattice of frequency-modulated pendula. We have implemented a flexible and externally tunable artificial magnetic field through a fast and well-chosen temporal-modulation of the natural frequencies of each pendulum. Since such modulation breaks time-reversal symmetry, the system can be described as a classical analogue of the Harper-Hofstadter model. In fact, through spectroscopic analysis of the collective oscillations of the pendula, we have demonstrated that the energy dispersion of the proposed scheme has the self-similar structure of the Hofstadter butterfly, as well as the topological properties of an integer quantum Hall system. We have also given examples of the existence of one-way propagating topological edge-states in the gaps between the bands and we have pointed out that the topological Chern number associated with the energy bands can be estimated from the shift of the oscillation amplitudes. Additionally, we have explored regimes where the quantum analogy with the classical oscillators gets weaker yet the topological effects remain, until the system becomes topologically trivial. It is interesting to note that our results are valid for coupled harmonic oscillators of any physical nature with a natural frequency that is temporally modulated.

An exciting outlook for such classical mechanical periodically-driven systems would be, for example, the creation of topologically protected Floquet edge modes between bands with zero Chern number as proposed in other Floquet systems by [Rudner et al. \[2013\]](#). In addition, when the anharmonicity of the pendula is taken into account beyond the linearised equations of motion, one could study the interplay of topology with nonlinearity. This nonlinearity is analogous to an on-site interaction in the quantum tight-binding Hamiltonian and may lead to a variety of new and unexpected effects. Furthermore, we believe that another important future direction would be the exploration of unique topological models in classical systems, even beyond the quantum Hall analogy. Another very interesting point that could be investigated is the role of the counter rotating wave terms in topological systems and its interplay with the parametric instability. In our

model, the increasing of the counter rotating wave terms led to the destruction of the topological effects, but one could, for instance, design different schemes in which the role of these terms is opposite and enhances the topological order.

In the second part of this thesis, we have focussed on the honeycomb geometry and the implementation of a strain-induced artificial gauge field. We have envisaged the strain in a driven-dissipative photonic system of an array of cavities to be implemented as an inhomogeneous spatial modulation of the tight-binding coupling between neighbouring sites. The great advantage of such photonic driven-dissipative systems is that they allow for the use of spectroscopic techniques to characterize the eigenmodes that are resonant with the coherent driving field. In this way, we have shown that the spectroscopic intensity profiles, in both real and momentum space, faithfully reproduce the mode wave function associated with the relativistic Landau levels. We have also briefly discussed the experimental feasibility of our proposal, using realistic parameters from available experiments such as a photonic lattice made of a coupled cavity arrays or microwave resonators.

A very natural outlook in this case is the practical realisation of the strained scheme with the proposed systems, that would allow for a direct observation of the Landau wave functions at a macroscopic scale. Further studies in this direction are already in progress. Besides, with these photonic systems, it is typically easy to perform transmission and absorption measurement under a coherent incident field. In this way, one could study wave-propagation physics in distorted honeycomb lattices, in particular by sending photons across a region where either an artificial magnetic vector potential or magnetic field are present and analyse the transmission through a “magnetic barrier”.

The last chapter was dedicated to spin-orbit coupling in a classical mechanical system with a honeycomb geometry. We have theoretically studied this system and we have also shown the preliminary results of an experiment concerning a mechanical benzene molecule composed of pendula coupled with pre-tensioned springs. Further investigations on this experiment are currently under development, together with new perspectives for considering an extended lattice and including the effect of nonlinearities beyond the harmonic approximation of the pendula. Moreover, the simulation of an artificial magnetic field for this simple mechanical system is very easy to realise experimentally. By mounting the system on a rotating table, we could investigate the interplay of an artificial gauge field with the spin-orbit coupling induced by the pre-tensioned springs.

To conclude, artificial gauge fields can be a very important ingredient for the study of fascinating properties of both classical and quantum systems. The recent developments in this direction have already opened up many new opportunities for both theory and experiment, and bring the promise of many other avenues of research to be explored in the future.

Appendices

Appendix A

Solution of the Harper Equation.

In this appendix we derive the Hofstadter energy spectrum Eq. (1.17) by solving the Harper equation Eq. (1.15), following the derivation from Marder [2010].

We write Harper's equation in the form:

$$\begin{pmatrix} g(j+1) \\ g(j) \end{pmatrix} = \begin{pmatrix} \varepsilon - 2 \cos(2\pi j\theta - \kappa) & -1 \\ 1 & 0 \end{pmatrix} \begin{pmatrix} g(j) \\ g(j-1) \end{pmatrix} = \mathcal{A}(j) \begin{pmatrix} g(j) \\ g(j-1) \end{pmatrix}. \quad (\text{A.1})$$

The “transfer matrix” structure is evident, as the vector $(g(j+1), g(j))^\top$ is obtained from the vector $(g(j), g(j-1))^\top$ through the matrix $\mathcal{A}(j)$. We can write also the vector $(g(j), g(j-1))^\top$ by applying the transfer matrix $\mathcal{A}(j-1)$ to the vector $(g(j-1), g(j-2))^\top$. Iterating this process j times, we have:

$$\begin{pmatrix} g(j+1) \\ g(j) \end{pmatrix} = \mathcal{A}(j)\mathcal{A}(j-1) \begin{pmatrix} g(j-1) \\ g(j-2) \end{pmatrix} = \dots = \prod_{m=1}^j \mathcal{A}(m) \begin{pmatrix} g(1) \\ g(0) \end{pmatrix}. \quad (\text{A.2})$$

From Bloch's theorem, we can also write $g(j+q) = e^{ikq} g(j)$, thus only q of this wavefunctions are independent. We have:

$$\begin{pmatrix} g(q+1) \\ g(q) \end{pmatrix} = e^{ikq} \begin{pmatrix} g(1) \\ g(0) \end{pmatrix}. \quad (\text{A.3})$$

From Eq. (A.2), we define the product of q of transfer matrices as:

$$Q(\varepsilon, \kappa) = \prod_{j=1}^q \mathcal{A}(j) = \prod_{j=1}^q \begin{pmatrix} \varepsilon - 2 \cos(2\pi j\theta - \kappa) & -1 \\ 1 & 0 \end{pmatrix}, \quad (\text{A.4})$$

and write, for $j = q$:

$$\begin{pmatrix} g(q+1) \\ g(q) \end{pmatrix} = Q(\varepsilon, \kappa) \begin{pmatrix} g(1) \\ g(0) \end{pmatrix}. \quad (\text{A.5})$$

Equations (A.3) and (A.5) implies that:

$$\text{Det} [Q(\varepsilon, \kappa) - e^{ikq}] = 0. \quad (\text{A.6})$$

The matrix $Q(\varepsilon, \kappa)$ is a product of q matrices of determinat 1, so it has determinant 1 itself. From Eq. (A.6) we have that:

$$\text{Det}[Q(\varepsilon, \kappa)] + e^{2ikq} - \text{Tr}[Q(\varepsilon, \kappa)] e^{ikq} = 0, \quad (\text{A.7})$$

therefore:

$$\boxed{\text{Tr}[Q(\varepsilon, \kappa)] = 2 \cos(qk)}. \quad (\text{A.8})$$

This is already an important property of the trace of the matrix product, that gives the allowed eigenvalues ε at a specific κ and k . By varying both κ and k one gets the allowed energy bands in

momentum space. However, we now want to obtain a relation that will allow us to get the whole spectrum regardless of the value of κ or k . We start by noticing that Eq. (A.8) is valid for any given value of κ , also for $\text{Tr}[Q(\varepsilon, \kappa + 2\pi/q)] = 2 \cos(qk)$, then

$$\text{Tr}[Q(\varepsilon, \kappa)] = \text{Tr}[Q(\varepsilon, \kappa + 2\pi/q)].$$

Besides, $Q(\varepsilon, \kappa + 2\pi/q)$ is built from a product of matrices \mathcal{A} exactly as $Q(\varepsilon, \kappa)$, only in a different order. Thus, the trace of Q can be written as a Fourier series:

$$\text{Tr}[Q(\varepsilon, \kappa)] = \sum_{m=-\infty}^{\infty} F_m(\varepsilon) e^{iq\kappa m}, \quad (\text{A.9})$$

but we immediately see from Eq. (A.4) that the highest Fourier component that can appear in Q is $e^{iq\kappa}$. Taking only $m = -1, 0, 1$ in the sum:

$$\text{Tr}[Q(\varepsilon, \kappa)] = F_0(\varepsilon) + F_1(\varepsilon) e^{iq\kappa} + F_{-1}^*(\varepsilon) e^{-iq\kappa}.$$

We select in Eq. (A.4) the corresponding Fourier components. For F_1 it is easy to check that:

$$F_1(\varepsilon) = \prod_{m=1}^q (-e^{-i2\pi\theta m}) = (-1)^q e^{-i\pi\theta q(q+1)}. \quad (\text{A.10})$$

The constant value F_0 is found from a value κ_0 such that the F_1 and F_1^* terms vanish, *i.e.* $F_0 = \text{Tr}[Q(\varepsilon, \kappa_0)]$. Putting Eq. (A.10) into the Fourier expansion, we find that the sum of terms depending upon κ is:

$$(-1)^q 2 \cos[\pi\theta(q^2 + q) - q\kappa] = (-1)^q 2 \cos[\pi p(q+1) - q\kappa],$$

since $\theta = p/q$. The cosine then vanishes by choosing $\kappa_0 = \pi/2q$. The trace of Q can be written as:

$$\text{Tr}[Q(\varepsilon, \kappa)] = \text{Tr}[Q(\varepsilon, \pi/2q)] + 2 \cos[\pi\theta(q^2 + q) + \pi q - q\kappa] \leq 2, \quad (\text{A.11})$$

where the last inequality stands from Eq. (A.8). Because k and κ can be freely varied, Eq. (A.11) means that $\text{Tr}[Q(\varepsilon, \pi/2q)] \leq 2 + 2 \cos(f(\kappa))$ and that therefore ε is an allowed eigenvalue if it satisfies:

$$\boxed{|\text{Tr}[Q(\varepsilon, \pi/2q)]| \leq 4.} \quad (\text{A.12})$$

The solution of the Harper equation was found in this form by Hofstadter, and the set of allowed energies form the Hofstadter butterfly.

Appendix B

Derivation of the effective dynamics: two sites.

In this appendix, we give the complete and detailed derivation of the effective dynamics and the resonance curves in Eq. (3.16) of Chap. 3.

We start from Eq. (3.14), that within the rotating-wave approximation reads as:

$$\dot{\alpha}_i = -i(\tilde{\omega}_0 + V_i(t) - i\gamma)\alpha_i + iF_{\text{ex}}(t) + i\frac{\Omega}{2}\alpha_{3-i}. \quad (\text{B.1})$$

According to the transformation in Eq. (3.15), we substitute

$$\alpha_i(t) = \beta_i(t) e^{-i\int_0^t V_i(t') dt'} e^{-i\omega_{\text{ex}}t}$$

into the previous equation and get:

$$\begin{aligned} \dot{\beta}_i - i(V_i(t) + \omega_{\text{ex}})\beta_i = \\ -i(\tilde{\omega}_0 + V_i(t) - i\gamma)\beta_i + i f_{\text{ex}}(1 + e^{i2\omega_{\text{ex}}}) e^{i\int_0^t V_i(t') dt'} + i\frac{\Omega}{2}\beta_{3-i} e^{-i\int_0^t (V_{3-i}(t') - V_i(t')) dt'}. \end{aligned} \quad (\text{B.2})$$

Neglecting the term in $e^{i2\omega_{\text{ex}}}$ because we are in the rotating-wave approximation, we now can apply the Magnus expansion to the first order, *i.e.* apply the time-average to Eq. (B.2):

$$0 = \frac{1}{T} \int_0^T \left[-\dot{\beta}_i - i(\tilde{\omega}_0 - \omega_{\text{ex}} - i\gamma)\beta_i + i f_{\text{ex}} e^{i\int_0^t V_i(t') dt'} + i\frac{\Omega}{2}\beta_{3-i} e^{-i\int_0^t (V_{3-i}(t') - V_i(t')) dt'} \right] dt. \quad (\text{B.3})$$

The coupling term in Eq. (B.3), for $i = 1$ is:

$$\Omega_{21}^{\text{eff}} = \frac{\Omega}{T} \int_0^T e^{i2I_0} e^{-i2I_0 \cos(\omega t)} dt. \quad (\text{B.4})$$

We apply now the Anger-Jacobi expansion of the exponential of a cosine in terms of a sum of Bessel functions:

$$e^{ix \cos(y)} = \sum_{m=-\infty}^{\infty} i^m \mathcal{J}_m(x) e^{imy} \quad (\text{B.5})$$

and get:

$$\Omega_{21}^{\text{eff}} = \sum_{m=-\infty}^{\infty} \frac{\Omega}{T} e^{i(2I_0 + m\pi/2)} \mathcal{J}_m(2I_0) \int_0^T e^{im\omega t} dt. \quad (\text{B.6})$$

In order for the integral to be non-zero, since the time-average is over $T = 2\pi/\omega$, it has to be $m = 0$. Therefore:

$$\Omega_{21}^{\text{eff}} = \Omega e^{i2I_0} \mathcal{J}_0(2I_0), \quad (\text{B.7})$$

which gives exactly the $\Omega_{12}^{\text{eff}} = \Omega_{21}^{\text{eff}*}$ as in Eq. (3.13).

Similarly for the effective external driving force:

$$f_{\text{ex}}^{\text{eff}} = \frac{f_{\text{ex}}}{T} \int_0^T e^{-iI_0} e^{iI_0 \cos(\omega t)} dt = f_{\text{ex}} e^{-I_0} \mathcal{J}_0(I_0), \quad (\text{B.8})$$

that is Eq. (3.18).

With the effective force and effective coupling, Eq. (B.3) for $i = 1, 2$ become:

$$\begin{aligned} 0 &= -i(\tilde{\omega}_0 - \omega_{\text{ex}} - i\gamma)\beta_1 + i f_{\text{ex}}^{\text{eff}} + i \frac{\Omega_{\text{eff}}^*}{2} \beta_2, \\ 0 &= -i(\tilde{\omega}_0 - \omega_{\text{ex}} - i\gamma)\beta_2 + i \frac{\Omega_{\text{eff}}}{2} \beta_1, \end{aligned} \quad (\text{B.9})$$

having put $\dot{\beta}_i = 0$ because we are interested in the steady-state where the variables do not oscillate. This set of equations is easily solvable for β_1, β_2 , giving the response spectra in Eq. (3.16).

Appendix C

Derivation of the Bloch-Siegert shift.

In this appendix we present the full derivation of the Bloch-Siegert shift that comes from a first-order correction to the rotating-wave approximation of the equation of motion.

For sake of simplicity, we only consider an isolated pendulum and write the corresponding equations of motion:

$$\begin{aligned}\dot{\alpha} &= -i(\tilde{\omega}_0 - i\gamma)\alpha - iV(t)(\alpha + \alpha^*) - i\left(\frac{\Omega}{2} + i\gamma\right)\alpha^*, \\ \dot{\alpha}^* &= i(\tilde{\omega}_0 + i\gamma)\alpha^* + iV(t)(\alpha^* + \alpha) + i\left(\frac{\Omega}{2} - i\gamma\right)\alpha.\end{aligned}\tag{C.1}$$

Since the Eqs. (C.1) couple the α and α^* variables, a rotating-wave contribution appears also from the counter-rotating-wave variable α^* . In order to calculate this contribution, we allow the variables in the rotating frame to have a small correction that oscillates with an opposite frequency. For example, the α^* variables in a frame that rotates at $\approx -\omega_0$ will be written as:

$$\alpha^*(t) = \alpha^* + \delta\alpha^* e^{-i2\omega_0 t}.\tag{C.2}$$

We substitute the previous expression in the second equation of Eq. (C.1), separating the contribution of the rotating-wave terms from the one that oscillates at $\approx -2\omega_0$. We have:

$$\dot{\alpha}^* - i(\tilde{\omega}_0 + i\gamma + V(t))\alpha^* = i2\omega_0\delta\alpha^* e^{-i2\omega_0 t} + i\left(V(t) + \frac{\Omega}{2} - i\gamma\right)\alpha e^{-i2\omega_0 t}.\tag{C.3}$$

The first term on the right-hand side is equal to zero, since it corresponds to Eq. (C.1) to the leading order in the rotating-wave approximation. The second term gives:

$$\delta\alpha^* \simeq -\frac{V(t) + \frac{\Omega}{2} - i\gamma}{2\omega_0}\alpha.\tag{C.4}$$

Putting Eq. (C.4) back into Eq. (C.2), and transforming back to the frame that rotates as $\approx \omega_0$, we have:

$$\alpha^*(t) e^{i2\omega_0 t} \approx \alpha^* e^{i2\omega_0 t} - \frac{V(t) + \frac{\Omega}{2} - i\gamma}{2\omega_0}\alpha.\tag{C.5}$$

This expression contains the explicit contribution to the rotating-wave-terms, that can be finally substituted in the first equation in Eq. (C.1), obtaining:

$$\dot{\alpha} = -i(\tilde{\omega}_0 - i\gamma + V(t))\alpha - i\left(V(t) + \frac{\Omega}{2} + i\gamma\right)\left(\frac{V(t) + \Omega/2 - i\gamma}{2\omega_0}\right)\alpha.\tag{C.6}$$

where the counter-rotating-wave terms α^* were neglected, because the leading order was already included through the rotating-wave part in Eq. (C.5).

Equation (C.6) is the first-order correction to the rotating-wave approximation of Eq. (3.7), with driving and dissipation. By using the transformation in Eq. (3.15), we average over the period $T = 2\pi/w$ of the temporal modulation, obtaining the classical analogue of the Bloch-Siegert shift:

$$\Delta_{\text{shift}} \equiv -\frac{1}{2\omega_0} \frac{1}{T} \int_0^T \left[\left(V(t) + \frac{\Omega}{2} \right)^2 + \gamma^2 \right]. \quad (\text{C.7})$$

This shift summarizes the principal effect of the counter-rotating-wave terms beyond the rotating-wave approximation, and it is more and more important for larger amplitude V of the temporal modulation.

For the specific form of the temporal modulation that was used in the Chap. 3, $V(t) = V \sin(\omega t)$:

$$\Delta_{\text{shift}} = -\frac{V^2}{4\omega_0} - \frac{\Omega^2}{8\omega_0} - \frac{\gamma^2}{2\omega_0}. \quad (\text{C.8})$$

For the bi-harmonic modulation of Chap. 4, $V_{i,j}(t) = V(\cos(\omega t + \phi_{i,j}) + (s-1)\cos((s-1)\omega t - \phi_{i,j}))$, and the specific form of the coupling along x and y , we have:

$$\Delta_{\text{shift}} = -\frac{V^2}{4\omega_0}(2 - 2s + s^2) - 2\frac{(\Omega_x + \Omega_y)^2}{\omega_0} - \frac{\gamma^2}{2\omega_0}. \quad (\text{C.9})$$

Appendix D

Derivation of the effective dynamics: the lattice.

In this appendix, we give insight into the effective Harper-Hofstadter equation of motion in Eq. (4.14) of Chap. 4. The derivation of the effective dynamics follows the one in Appendix B. Upon the unitary transformation to the β_{ij} variables in Eq. (4.13), after substitution into Eq. (4.11), the equations of motion are:

$$\begin{aligned}
 \dot{\beta}_{i,j} - i\omega_{\text{ex}} + iwS(i_p)\beta_{i,j} &= -i[\omega_0 - i\gamma_{i,j}]\beta_{i,j} \\
 i\Omega_x\beta_{i+1,j} e^{-iw[S(i+1)-S(i)]t} e^{-i\int_0^T [V_{i+1,j}(t')-V_{i,j}(t')]dt'} \\
 + i\Omega_x\beta_{i-1,j} e^{-iw[S(i-1)-S(i)]t} e^{-i\int_0^T [V_{i-1,j}(t')-V_{i,j}(t')]dt'} \\
 + i\Omega_y\beta_{i,j+1} e^{-i\int_0^T [V_{i,j+1}(t')-V_{i,j}(t')]dt'} + i\Omega_y\beta_{i,j-1} e^{-i\int_0^T [V_{i,j-1}(t')-V_{i,j}(t')]dt'} \\
 + i\int_{i,j}^{\text{ex}} e^{-iw[S(i)-S(i_p)]t} e^{i\int_0^T V_{i,j}(t')dt'}.
 \end{aligned} \tag{D.1}$$

We first focus on the coupling along y . We have:

$$\begin{aligned}
 T_y = i\Omega_y \left[\beta_{i,j+1} e^{-i\frac{V}{w}(A^+ \cos(wt) + B^+ \sin(wt) + B^+ \sin((s-1)wt) - A^+ \cos((s-1)wt))} + \right. \\
 \left. \beta_{i,j-1} e^{-i\frac{V}{w}(A^- \cos(wt) + B^- \sin(wt) + B^- \sin((s-1)wt) - A^- \cos((s-1)wt))} \right],
 \end{aligned} \tag{D.2}$$

having used the explicit form of the temporal modulation $V_{i,j} = V[\cos(wt + \phi_{i,j}) + (s-1)\cos((s-1)wt - \phi_{i,j})]$ and where we have defined:

$$A^\pm \equiv \sin(\phi_{i,j\pm 1}) - \sin(\phi_{i,j}), \quad B^\pm \equiv \cos(\phi_{i,j\pm 1}) - \cos(\phi_{i,j}). \tag{D.3}$$

The exponential part in Eq. (D.2) can be also written as:

$$A^\pm \cos(wt) \pm B^\pm \sin(wt) = \sqrt{A^{\pm 2} + B^{\pm 2}} \cos\left(wt \mp \arctan\left(\frac{B^\pm}{A^\pm}\right)\right). \tag{D.4}$$

Calling $C^\pm \equiv \sqrt{A^{\pm 2} + B^{\pm 2}}$ and $\varphi^\pm \equiv \arctan(B^\pm/A^\pm)$, we have:

$$\begin{aligned}
 T_y = \\
 i\Omega_y \left[\beta_{i,j+1} e^{-i\frac{V C^+}{w}(\cos(wt - \varphi_{i,j}^+) - \cos((s-1)wt + \varphi_{i,j}^+))} + \beta_{i,j-1} e^{-i\frac{V C^-}{w}(\cos(wt - \varphi_{i,j}^-) - \cos((s-1)wt + \varphi_{i,j}^-))} \right].
 \end{aligned} \tag{D.5}$$

Substituting the form of the modulation phase $\phi_{i,j} = 2\pi\theta(i+j)$ in the expressions for C^\pm and $\varphi_{i,j}^\pm$, we have:

$$C \equiv C^\pm = \sqrt{2 - 2\cos(2\pi\theta)}, \quad \varphi_{i,j}^\pm = -(2\pi\theta(i+j) \pm \pi\theta). \tag{D.6}$$

We now use the Anger-Jacobi expansion Eq. (B.5), and average over one period T of the temporal modulation to obtain:

$$\begin{aligned} \langle T_y \rangle_T = \frac{i\Omega_y}{T} \int_0^T \left[\beta_{i,j+1} \sum_{p,r=-\infty}^{\infty} \mathcal{J}_p \left(\frac{VC}{w} \right) \mathcal{J}_r \left(\frac{VC}{w} \right) e^{iwt(r+p(s-1))} e^{i(p-r)\varphi_{i,j}^+} e^{i\pi/2(p+r)} \right. \\ \left. \beta_{i,j-1} \sum_{p,r=-\infty}^{\infty} \mathcal{J}_p \left(\frac{VC}{w} \right) \mathcal{J}_r \left(\frac{VC}{w} \right) e^{iwt(r+p(s-1))} e^{i(p-r)\varphi_{i,j}^-} e^{i\pi/2(p+r)} \right] dt. \end{aligned} \quad (\text{D.7})$$

The integral is non-null if the exponential $e^{iwt(r+p(s-1))} = 1$, that is for $r = -p(s-1)$. The expression for the effective coupling along y is then:

$$\Omega_y^{\text{EFF}} \equiv \Omega_y \sum_{p=-\infty}^{\infty} \mathcal{J}_{-(s-1)p}(I_0) \mathcal{J}_p(I_0) e^{ips\varphi_{i,j}^{\pm}} e^{i(sp-2p)\pi/2}, \quad (\text{D.8})$$

where we have used the definition of $I_0 = VC/w$.

We now proceed to the effective coupling along the x direction:

$$\begin{aligned} T_x = i\Omega_x \left[\beta_{i+1,j} e^{-i\frac{V}{w}(\tilde{A}^+ \cos(wt) + \tilde{B}^+ \sin(wt) + \tilde{B}^+ \sin((s-1)wt) - \tilde{A}^+ \cos((s-1)wt))} \right. \\ \left. \beta_{i-1,j} e^{-i\frac{V}{w}(\tilde{A}^- \cos(wt) + \tilde{B}^- \sin(wt) + \tilde{B}^- \sin((s-1)wt) - \tilde{A}^- \cos((s-1)wt))} \right]. \end{aligned} \quad (\text{D.9})$$

where we have defined

$$\tilde{A}^{\pm} \equiv \sin(\phi_{i\pm 1,j}) - \sin(\phi_{i,j}), \quad \tilde{B}^{\pm} \equiv \cos(\phi_{i\pm 1,j}) - \cos(\phi_{i,j}). \quad (\text{D.10})$$

As before, the exponential part in Eq. (D.9) can be also written as:

$$\tilde{A}^{\pm} \cos(wt) \pm \tilde{B}^{\pm} \sin(wt) = C \cos(wt \mp \varphi_{i,j}^{\pm}), \quad (\text{D.11})$$

where C and $\varphi_{i,j}^{\pm}$ are the same as in Eq. (D.6).

We now use the Anger-Jacobi expansion and average over one period of the modulation to obtain:

$$\begin{aligned} \langle T_x \rangle_T = \\ \frac{i\Omega_x}{T} \int_0^T \left[\beta_{i+1,j} \sum_{p,r=-\infty}^{\infty} \mathcal{J}_p \left(\frac{VC}{w} \right) \mathcal{J}_r \left(\frac{VC}{w} \right) e^{iwt(r+p(s-1)-[S(i+1)-S(i)])} e^{i(p-r)\varphi_{i,j}^+} e^{i\pi/2(p+r)} + \right. \\ \left. \beta_{i-1,j} \sum_{p,r=-\infty}^{\infty} \mathcal{J}_p \left(\frac{VC}{w} \right) \mathcal{J}_r \left(\frac{VC}{w} \right) e^{iwt(r+p(s-1)-[S(i-1)-S(i)])} e^{i(p-r)\varphi_{i,j}^-} e^{i\pi/2(p+r)} \right] dt. \end{aligned} \quad (\text{D.12})$$

This coupling depends on the position along the static spatial modulation $S(i)$. We first focus on the couplings between pendula that have a natural-frequency difference of $S(i\pm 1) - S(i) = \pm 1$, where the \pm indicates that the hopping is calculated going towards the left (+1) or towards the right (-1). We have that in this case the integral in Eq. (D.12) is non-null if the exponential $e^{iwt(r+p(s-1)-[S(i\pm 1)-S(i)])} = 1$, that is for $r = -p(s-1) \mp 1$. The expression for the effective coupling along x is then:

$$\Omega_x^{\text{EFF}(\pm w)} \equiv \Omega_x \sum_{p=-\infty}^{\infty} \mathcal{J}_{\pm 1-(s-1)p}(I_0) \mathcal{J}_p(I_0) e^{-i\varphi_{i,j}^{\pm}(\pm 1-p-(s-1)p)} e^{i(\pm 1-(s-1)p+p)\pi/2}. \quad (\text{D.13})$$

This equation describes the hopping along the small steps of the static spatial modulation.

The coupling between pendula that have a natural-frequency difference of $S(i\pm 1) - S(i) = \mp(s-1)$ is obtained for $r = -p(s-1) \mp (s-1)$ in the sum, and it is equal to:

$$\begin{aligned} \Omega_x^{\text{EFF}(\mp w(s-1))} \equiv \\ \Omega_x \sum_{p=-\infty}^{\infty} \mathcal{J}_{(s-1)(\mp 1-p)}(I_0) \mathcal{J}_p(I_0) e^{-i\varphi_{i,j}^{\pm}(\mp(s-1)-p-(s-1)p)} e^{i(\mp(s-1)+p-(s-1)p)\pi/2}. \end{aligned} \quad (\text{D.14})$$

where this time \mp indicates the hopping calculated going towards the left (-1) or towards the right ($+1$). This is because the frequency-difference along the “big step” of the static modulation has an opposite sign to the ones along the “small steps”.

Finally, the effective driving force:

$$f_{i_p, j_p}^{\text{EFF}} \equiv f_{i_p, j_p}^{\text{ex}} \sum_{p'=-\infty}^{\infty} \mathcal{J}_{-(s-1)p'} \left(\frac{V}{w} \right) \mathcal{J}_{p'} \left(\frac{V}{w} \right) e^{-i(p'+(s-1)p')\phi_{i,j}}. \quad (\text{D.15})$$

The following effective equations of motion are found:

$$\dot{\beta}_{i,j} = -i\Delta\omega\beta_{i,j} - \gamma_{i,j}\beta_{i,j} + if_{i_p, j_p}^{\text{EFF}} + i \sum_{\pm 1} \Omega_x^{\text{EFF}} \beta_{i\pm 1, j} + i \sum_{\pm 1} \Omega_y^{\text{EFF}} \beta_{i, j\pm 1}. \quad (\text{D.16})$$

We now assume that $\mathcal{J}_0(I_0) \gtrsim \mathcal{J}_1(I_0) \gg \mathcal{J}_p(I_0)$, with $p \geq 2$ and take only the largest term in the sums. In Eq. (D.8), (D.13), and (D.15) we have that $p = p' = 0$, while in Eq. (D.14) we must take $p = \mp 1$. Remarkably, in this approximation, the hopping along x is uniform and does not depend on the position along the static-spatial modulation, thus allowing for clear definitions of Ω_x^{EFF} , Ω_y^{EFF} and $f_{i_p, j_p}^{\text{EFF}}$:

$$\begin{aligned} \Omega_x^{\text{EFF}} &= \Omega_x \mathcal{J}_{\pm 1}(I_0) \mathcal{J}_0(I_0) e^{\mp i(2\pi\theta(i+j)\pm\pi\theta-\pi/2)}, \\ \Omega_y^{\text{EFF}} &= \Omega_y \mathcal{J}_0(I_0)^2, \\ f_{i_p, j_p}^{\text{EFF}} &= f_{i_p, j_p}^{\text{ex}} \mathcal{J}_0(V/w)^2. \end{aligned} \quad (\text{D.17})$$

By combining Eq. (D.17) with the effective equations of motion in Eq. (D.16) to lowest order in I_0 and V , we obtain exactly the equations in Eq. (4.14). From Eq. (D.8), (D.13) and (D.14) we notice that the second largest term in the sums is proportional to $\mathcal{J}_{(s-1)}(I_0)$, that is very small if $I_0 \ll 1$ or when considering a large period of the static modulation $s \gg 2$. We found that an optimal combination of these two requirements that fulfils the inequality Eq. (4.12) with the renormalisation of Eq. (4.18) is to have $I_0 = 0.5$ with $s = 5$.

Appendix E

Fourier decomposition of the equations of motion.

We now comment on the Fourier decomposition that was used as an alternative method to the full-time integration with Runge-Kutta for solving the set of differential equations in Eq. (4.3) to produce the butterfly spectra in Fig. 4.6.

From the properties of periodically driven systems [Goldman and Dalibard \[2014\]](#), [Goldman et al. \[2015b\]](#), we know that, during a Floquet evolution between two stroboscopic times $t_n = nT$, the system exhibits micro-motion, with a period set by the frequency of the temporal modulation w . We are interested in the steady state, therefore, we search for a solution of Eq. (4.3) that oscillates at the frequency of the external driving ω_{ex} . To this end, we expand the $\alpha_{i,j}(t)$ in a Fourier series, using both ω_{ex} and w as harmonics:

$$\alpha_{i,j}(t) = \sum_{m=-\infty}^{\infty} \sum_{n=-\infty}^{\infty} \alpha_{i,j}^{(m,n)} e^{imwt} e^{in\omega_{\text{ex}}t}, \quad (\text{E.1})$$

where $\alpha_{i,j}^{(m,n)}$ are the time-independent Fourier amplitudes, assuming that all the time-dependencies are in the exponential term, having care in writing the conjugate variables as:

$$\alpha_{i,j}^*(t) = \sum_{m=-\infty}^{\infty} \sum_{n=-\infty}^{\infty} \alpha_{i,j}^{(-m,-n)} e^{imwt} e^{in\omega_{\text{ex}}t},$$

since the sum runs over symmetric indexes around 0. The sum over m is truncated to a finite number M , that is large enough to ensure a convergent solution. The sum over n takes only two values ± 1 , since we have assumed that the external driving force is a cosine with a defined frequency ω_{ex} . By substituting Eq. (E.1) in Eq. (4.3) and isolating the component proportional to $e^{imwt} e^{in\omega_{\text{ex}}t}$, we have a set of linear algebraic equations that can be inverted to find the coefficients $\alpha_{i,j}^{(m,n)}$.

In order to simulate the real experimental situation, we performed all the calculations using the full numerical integral of Eq. (4.3), except for the Hofstadter butterfly, where the full numerical integration would have been computationally demanding.

We have verified the good agreement between the two methods finding a mean error that is less than 1%. We note that the two methods are in fact equivalent when the system is dynamically stable. However, when there is an instability, the system does not reach the steady state. This is clearly seen in the full numerical integration method, where the solution shows the typical exponential growth of an unstable system. In the Fourier method the steady state is imposed by the decomposition Eq. (E.1) itself and so the emergence of an instability can not be predicted, as discussed in the main text.

Appendix F

Calculation of edge states of the honeycomb lattice.

In this appendix we show how to obtain the energy dispersion of a ribbon of a honeycomb lattice, that differs from the one of an infinite lattice for the presence of zero-energy modes, which depend on the various type of terminations. For simplicity, we consider a semi-infinite ribbon, of N unit cells along the x direction and infinite along the y direction, oriented as shown in Fig. F.1. The zigzag and the bearded termination can appear in the two edges on the left or on the right, depending if the first or the last lattice site is a site of type A or B . Since we have edges along the y -direction, we can apply periodic boundary conditions along y and keep the explicit dependence on the i index along the x -direction:

$$\begin{aligned} a(i, j) &= a_i e^{ij\vec{k}\cdot\vec{A}_y}, \\ b(i, j) &= b_i e^{ij\vec{k}\cdot\vec{A}_y}, \end{aligned} \quad (\text{F.1})$$

where $\vec{A}_y = (0, \sqrt{3}a/2)$ and $\vec{A}_x = (3a/2, 0)$ are the vectors giving the indexing shown in Fig. F.1.

Substituting these conditions into Eq. (6.2), with the notation in Fig.F.1, we get the following equations:

$$\begin{aligned} Ea(i) &= -t_1 b(i) - t b(i-1) 2 \cos\left(\frac{\sqrt{3}a}{2} k_y\right), \\ Eb(i) &= -t_1 a(i) - t a(i+1) 2 \cos\left(\frac{\sqrt{3}a}{2} k_y\right), \end{aligned} \quad (\text{F.2})$$

having assumed that $t_2 = t_3 = t$. For each lattice point A, B in all of the unit cells, we have a set of equations, that can be recast as a matrix:

$$\begin{pmatrix} \dots & \dots & \dots & \dots & \dots & \dots \\ \dots & 2t \cos\left(\frac{\sqrt{3}a}{2} k_y\right) & E & t_1 & 0 & \dots \\ \dots & 0 & t_1 & E & 2t \cos\left(\frac{\sqrt{3}a}{2} k_y\right) & \dots \\ \dots & \dots & \dots & \dots & \dots & \dots \end{pmatrix} \begin{pmatrix} \dots \\ b(i-1) \\ a(i) \\ b(i) \\ a(i+1) \\ \dots \end{pmatrix}, \quad (\text{F.3})$$

where the vector on the right contains all the fields on the lattice sites and it is ordered according to the same indexing as in Fig. F.1. The energy dispersion obtained by diagonalizing the matrix in Eq. (F.3) were shown in Fig. 6.5.

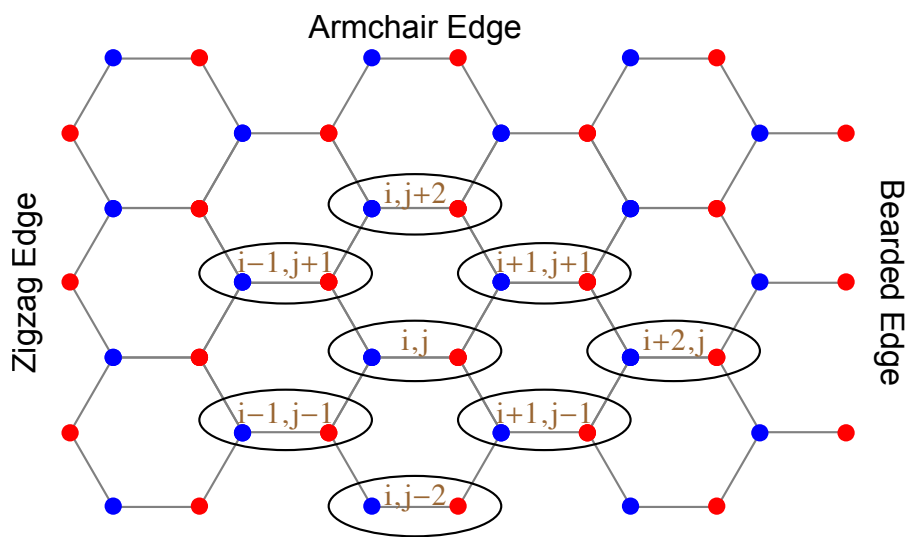


Figure F.1: Edge terminations in the honeycomb lattice. Each unit cell is composed by two sites of type A and B , which are shown in blue and red respectively. The unit cells are also labelled with two indexes, i, j , which are incremented according to the vectors $\vec{A}_y = (0, \sqrt{3}a/2)$ and $\vec{A}_x = (3a/2, 0)$. This labelling is more convenient for the calculation of the edge states compared to the one introduced in Fig. 6.2

Appendix G

Overlap between Landau levels due to a coherent external pump.

In this Appendix we comment on the particular spiral-like shape that was observed in Fig. 7.6. We want to show that when the dissipative system is pumped resonantly at the frequency of a Landau level, the interference between this resonant level and its neighbours, that are non-resonantly excited through a finite loss γ , has the spiral-shape of Fig. 7.6.

To do so, we consider the following wave function pump, that for simplicity is a delta in x and a Gaussian of width σ_y in y :

$$|P\rangle = \delta(x) e^{-\frac{y^2}{2\sigma_y^2}}. \quad (\text{G.1})$$

We recall that the Landau wave functions are:

$$|n, q_y\rangle = e^{iq_y y} e^{-\frac{(x-x_0)^2}{2l_B^2}} \text{H}_n\left(\frac{x-x_0}{l_B}\right), \quad (\text{G.2})$$

with $x_0 = l_B^2 q_y$ and $l_B = 3a/\sqrt{2\tau}$.

The wave function that is excited will be:

$$\psi = \sum_n \int dq_y \frac{|n, q_y\rangle \langle n, q_y | P \rangle}{\omega_p - \omega_n - i\gamma}, \quad (\text{G.3})$$

where ω_p is the frequency of the pump and the ω_n is the frequency of the n -th Landau level. We calculate separately:

$$\begin{aligned} \langle n, q_y | P \rangle &= \int_{-\infty}^{\infty} \delta(x) e^{-\frac{y^2}{2\sigma_y^2}} e^{iq_y y} e^{-\frac{(x-x_0)^2}{2l_B^2}} \text{H}_n\left(\frac{x-x_0}{l_B}\right) dx dq_y \\ &= e^{-\frac{x_0^2}{2l_B^2}} \text{H}_n\left(\frac{-x_0}{l_B}\right) e^{-\frac{q_y^2 \sigma_y^2}{2}} \sqrt{2\pi} \sigma_y. \end{aligned} \quad (\text{G.4})$$

Using the expressions in Eq. (G.1), Eq. (G.2) and Eq. (G.4), and assuming that we are resonantly pumping the $n = \tilde{n}$ level with $\omega_p = \omega_{\tilde{n}}$, and mix with only the $n = \tilde{n} + 1$, we have:

$$\begin{aligned} \psi &= \int dq_y \sqrt{2\pi} \sigma_y e^{-\frac{x_0^2}{2l_B^2}} e^{-\frac{q_y^2 \sigma_y^2}{2}} e^{iq_y y} e^{-\frac{(x-x_0)^2}{2l_B^2}} \\ &\quad \left[\frac{\text{H}_{\tilde{n}}\left(\frac{x-x_0}{l_B}\right) \text{H}_{\tilde{n}}\left(\frac{-x_0}{l_B}\right)}{\omega_{\tilde{n}} - \omega_{\tilde{n}} - i\gamma} + \frac{\text{H}_{\tilde{n}+1}\left(\frac{x-x_0}{l_B}\right) \text{H}_{\tilde{n}+1}\left(\frac{-x_0}{l_B}\right)}{\omega_{\tilde{n}} - \omega_{\tilde{n}+1} - i\gamma} \right]. \end{aligned} \quad (\text{G.5})$$

In Fig. G.1 we show the wave functions profile that is effectively excited by the pump, as obtained by numerically calculating the integral in Eq. (G.5) for similar values of the system

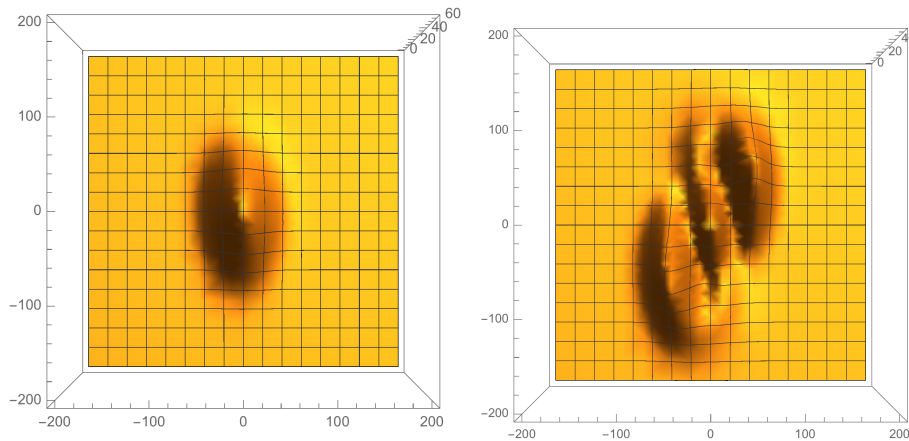


Figure G.1: Effectively excited wave functions, as obtained by the overlap between the resonant level that is selected by the pump, and the non-resonant level excited due a finite loss. Left panel shows $\tilde{n} = 0$, while right panel is for $\tilde{n} = 1$. System parameters are the same as in Fig. 7.6.

parameter as in Fig. 7.6. The figure on the left is obtained by pumping $\tilde{n} = 0$, and mixing with the $n = 1$ level. As we see, and expect from Fig. 7.6-1, the effective profile is Gaussian, not reflecting any spiral-like shape. Conversely, on the right side, $\tilde{n} = 1$ and we show a mixing with the $n = 2$ level. In this case the spiral-like shape is evident, as it was in Fig. 7.6-2. Of course, by decreasing the loss rate, in the limit of $\hbar\gamma/t \rightarrow 0$, the resonant mode is more and more dominant while the non-resonant contribution is suppressed and the spiral behaviour disappears.

Bibliography

- J. R. Abo-Shaeer, C. Raman, J. M. Vogels, and W. Ketterle. [Observation of vortex lattices in Bose-Einstein condensates](#). *Science*, **292**:476, 2001. (cited on p. [19](#))
- Y. Aharonov and D. Bohm. [Significance of electromagnetic potentials in the quantum theory](#). *Phys. Rev.*, 115:485, 1959. (cited on pp. [7](#) and [12](#))
- M. Aidelsburger, S. Nascimbène M. Atala, S. Trotzky, Y.-A. Chen, and I. Bloch. [Experimental realization of strong effective magnetic fields in an optical lattice](#). *Phys. Rev. Lett.*, **107**:255301, 2011. (cited on p. [21](#))
- M. Aidelsburger, M. Atala, M. Lohse, J. T. Barreiro, B. Paredes, and I. Bloch. [Realization of the Hofstadter Hamiltonian with ultracold atoms in optical lattices](#). *Phys. Rev. Lett.*, **111**:185301, 2013. (cited on pp. [22](#), [36](#), [38](#), and [39](#))
- V. V. Albert, L. I. Glazman, and L. Jiang. [Topological properties of linear circuit lattices](#). *Phys. Rev. Lett.*, **114**:173902, 2015. (cited on p. [24](#))
- V. I. Arnold. *Mathematical methods of classical mechanics*. Springer-Verlag (New York), 1989. (cited on pp. [45](#), [47](#), [49](#), [51](#), and [52](#))
- N. W. Ashcroft and N. D. Mermin. *Solid state physics*. Saunders College Publishing, 1976. (cited on pp. [6](#) and [80](#))
- J. E. Avron. *Multiscale Methods in Quantum Mechanics. Chapter 2: Colored Hofstadter butterflies*. Birkhäuser Boston, 2003. (cited on p. [14](#))
- M. Bellec, U. Kuhl, G. Montambaux, and F. Mortessagne. [Tight-binding couplings in microwave artificial graphene](#). *Phys. Rev. B*, **88**:115437, 2013a. (cited on pp. [63](#), [65](#), [70](#), and [75](#))
- M. Bellec, U. Kuhl, G. Montambaux, and F. Mortessagne. [Topological transition of Dirac points in a microwave experiment](#). *Phys. Rev. Lett.*, **110**:033902, 2013b. (cited on pp. [64](#), [70](#), and [75](#))
- M. Bellec, U. Kuhl, G. Montambaux, and F. Mortessagne. [Manipulation of edge states in microwave artificial graphene](#). *New J. Phys.*, **16**:113023, 2014. (cited on pp. [64](#), [70](#), and [75](#))
- B. A. Bernevig. *Topological insulators and topological superconductors*. Princeton university press, 2013. (cited on pp. [13](#) and [15](#))
- M. V. Berry. [Quantal phase factors accompanying adiabatic changes](#). *Proc. R. Soc. A*, **392**:45, 1984. (cited on p. [11](#))
- F. Bloch and A. Siegert. [Magnetic resonance for nonrotating fields](#). *Phys. Rev.*, **57**:522, 1940. (cited on p. [31](#))
- I. Bloch, J. Dalibard, and W. Zwerger. [Many-body physics with ultracold gases](#). *Rev. Mod. Phys.*, **80**:885, 2008. (cited on p. [18](#))

- M. Bukov, L. D'Alessio, and A. Polkovnikov. [Universal high-frequency behavior of periodically driven systems: from dynamical stabilization to Floquet engineering](#). *Advances in Physics*, **64**:139, 2015. (cited on pp. 21, 28, 30, and 48)
- M. E. Cage, R. F. Dziuba, and B. F. Field. [A test of the quantum Hall effect as a resistance standard](#). *IEEE Trans. Instrum. Meas.*, **IM-34**:301, 1985. (cited on p. 12)
- F. Cardano and L. Marrucci. [Spin-orbit photonics](#). *Nat. Phot.*, **9**:776, 2015. (cited on p. 77)
- I. Carusotto and C. Ciuti. [Quantum fluids of light](#). *Rev. Mod. Phys.*, **85**:229, 2013. (cited on pp. 17, 18, 40, and 82)
- A. H. Castro Neto, F. Guinea, N. M. R. Peres, K. S. Novoselov, and A. K. Geim. [The electronic properties of graphene](#). *Rev. Mod. Phys.*, **81**:109, 2009. (cited on pp. 55, 62, 65, and 67)
- M.-C. Chang and Q. Niu. [Berry phase, hyperorbits, and the Hofstadter spectrum: Semiclassical dynamics in magnetic Bloch bands](#). *Phys. Rev. B*, **53**:7010, 1996. (cited on p. 13)
- N. R. Cooper. [Rapidly rotating atomic gases](#). *Adv. Phys.*, **57**:539, 2008. (cited on p. 20)
- C. E. Creffield and F. Sols. [Comment on “Creating artificial magnetic fields for cold atoms by photon-assisted tunneling” by Kolovsky A. R.](#) *Europhys. Lett.*, **101**:40001, 2013. (cited on p. 21)
- J. Dalibard. [Introduction to the physics of artificial gauge fields](#). *arXiv:1504.05520*, 2015. (cited on pp. 7 and 19)
- J. Dalibard, F. Gerbier, G. Juzeliūnas, and P. Öhberg. [Colloquium: Artificial gauge potentials for neutral atoms](#). *Rev. Mod. Phys.*, **83**:1523, 2011. (cited on p. 18)
- F. de Juan, M. Sturla, and M. A. H. Vozmediano. [Space dependent Fermi velocity in strained graphene](#). *Phys. Rev. Lett.*, **108**:227205, 2012. (cited on pp. 59, 60, and 67)
- S. M. de Vasconcellos, A. Calvar, A. Dousse, J. Suffczyński, N. Dupuis, A. Lemaître, I. Sagnes, J. Bloch, P. Voisin, and P. Senellart. [Spatial, spectral, and polarization properties of coupled micropillar cavities](#). *Appl. Phys. Lett.*, **99**:101103, 2011. (cited on p. 77)
- C. R. Dean, L. Wang, P. Maher, C. Forsythe, F. Ghahari, Y. Gao, J. Katoch, M. Ishigami, P. Moon, M. Koshino, T. Taniguchi, K. Watanabe, K. L. Shepard, J. Hone, and P. Kim. [Hofstadter’s butterfly and the fractal quantum Hall effect in moiré superlattices](#). *Nature*, **497**:598, 2013. (cited on p. 17)
- P. Delplace, D. Ullmo, and G. Montambaux. [Zak phase and the existence of edge states in graphene](#). *Phys. Rev. B*, **84**:195452, 2011. (cited on p. 62)
- D. P. Di Vincenzo and E. J. Mele. [Self-consistent effective-mass theory for intralayer screening in graphite intercalation compounds](#). *Phys. Rev. B*, **29**:1685, 1984. (cited on p. 58)
- A. Eckardt and M. Holthaus. [AC-induced superfluidity](#). *Europhys. Lett.*, **80**:50004, 2007. (cited on p. 21)
- A. Eckardt, C. Weiss, and M. Holthaus. [Superfluid-insulator transition in a periodically driven optical lattice](#). *Phys. Rev. Lett.*, **95**:260404, 2005. (cited on p. 21)
- A. Eckardt, M. Holthaus, H. Lignier, A. Zenesini, D. Ciampini, O. Morsch, and E. Arimondo. [Exploring dynamic localization with a Bose-Einstein condensate](#). *Phys. Rev. A*, **79**:013611, 2009. (cited on p. 21)
- K. Fang, Z. Yu, and S. Fan. [Realizing effective magnetic field for photons by controlling the phase of dynamic modulation](#). *Nat. Phot.*, **6**:782, 2012. (cited on pp. 22 and 37)
- R. P. Feynman. [Simulating physics with computers](#). *Int. Jour. Theor. Phys.*, **21**:467, 1982. (cited on p. 17)
- T. Fukui, Y. Hatsugai, and H. Suzuki. [Chern numbers in discretized Brillouin zone: efficient method of computing \(spin\) Hall conductances](#). *J. Phys. Soc. Jpn.*, **74**:1674, 2005. (cited on p. 15)

- V. Galitski and I. B. Spielman. [Spin-orbit coupling in quantum gases](#). *Nature*, **494**:49, 2013. (cited on p. 77)
- I. M. Georgescu, S. Ashhab, and F. Nori. [Quantum simulation](#). *Rev. Mod. Phys.*, **86**:153, 2014. (cited on p. 17)
- M. O. Goerbig. [Electronic properties of graphene in a strong magnetic field](#). *Rev. Mod. Phys.*, **83**:1193, 2011. (cited on pp. 55, 67, and 68)
- N. Goldman and J. Dalibard. [Periodically driven quantum systems: effective Hamiltonians and engineered gauge fields](#). *Phys. Rev. X*, **4**:031027, 2014. (cited on p. 103)
- N. Goldman, G. Juzeliunas, P. Ohberg, and I. B. Spielman. [Light-induced gauge fields for ultracold atoms](#). *Rep. Prog. Phys.*, **77**:126401, 2014. (cited on p. 18)
- N. Goldman, N. R. Cooper, and J. Dalibard. [Preparing and probing Chern bands with cold atoms](#). *arXiv:1507.07805*, 2015a. (cited on p. 18)
- N. Goldman, J. Dalibard, M. Alidelsburger, and N. R. Cooper. [Periodically driven quantum matter: the case of resonant modulations](#). *Phys. Rev. A*, **91**:033632, 2015b. (cited on pp. 22, 28, 37, and 103)
- M. Grifoni and P. Hänggi. [Driven quantum tunneling](#). *Phys. Rep.*, **304**:229, 1998. (cited on p. 25)
- F. Großmann, T. Dittrich, P. Jung, and P. Hänggi. [Coherent destruction of tunneling](#). *Phys. Rev. Lett.*, **67**:516, 1991. (cited on p. 25)
- F. Guinea, A. K. Geim, M. I. Katsnelson, and K. S. Novoselov. [Generating quantizing pseudomagnetic fields by bending graphene ribbons](#). *Phys. Rev. B*, **81**:035408, 2010a. (cited on pp. 59 and 65)
- F. Guinea, M. I. Katsnelson, and A. K. Geim. [Energy gaps and a zero-field quantum Hall effect in graphene by strain engineering](#). *Nat. Phys.*, **6**:30, 2010b. (cited on pp. 59 and 65)
- M. Hafezi, E. A. Demler, M. D. Lukin, and J. M. Taylor. [Robust optical delay lines with topological protection](#). *Nat. Phys.*, **7**:907, 2011. (cited on p. 23)
- M. Hafezi, S. Mittal, J. Fan, A. Migdall, and J. M. Taylor. [Imaging topological edge states in silicon photonics](#). *Nat. Phot.*, **7**:1001, 2013. (cited on p. 23)
- D. M. Haldane and S. Raghu. [Possible realization of directional optical waveguides in photonic crystals with broken time-reversal symmetry](#). *Phys. Rev. Lett.*, **100**:013904, 2008. (cited on p. 19)
- F. D. M. Haldane. [Model for a quantum Hall effect without Landau levels: condensed-matter realization of the “parity anomaly”](#). *Phys. Rev. Lett.*, **61**:18, 1988. (cited on p. 21)
- P. G. Harper. [Single band motion of conduction electrons in a uniform magnetic field](#). *Proc. Phys. Soc.*, A **68**:874, 1955. (cited on pp. 5 and 8)
- M. Z. Hasan and C. L. Kane. [Colloquium: Topological insulators](#). *Rev. Mod. Phys.*, **82**:3045, 2010. (cited on p. 17)
- P. Hauke, O. Tieleman, A. Celi, C. Ölschlänger, J. Simonet, J. Struck, M. Weinberg, P. Windpassinger, K. Sengstock, M. Lewenstein, and A. Eckardt. [Non-abelian gauge fields and topological insulators in shaken optical lattices](#). *Phys. Rev. Lett.*, **109**:145301, 2012. (cited on p. 21)
- D. R. Hofstadter. [Energy levels and wave functions of Bloch electrons in rational and irrational magnetic fields](#). *Phys. Rev. B*, **14**:2239, 1976. (cited on pp. 5, 9, 10, and 35)
- M. Holthaus. [Collapse of minibands in far-infrared irradiated superlattices](#). *Phys. Rev. Lett.*, **69**:351, 1992. (cited on p. 30)
- T. Jacqmin, I. Carusotto, I. Sagnes, M. Abbarchi, D. D. Solnyshkov, G. Malpuech, E. Galopin, A. Lemaître, J. Bloch, and A. Amo. [Direct observation of Dirac cones and a flatband in a honeycomb lattice for polaritons](#). *Phys. Rev. Lett.*, **112**:116402, 2014. (cited on pp. 63, 64, 65, 70, 75, and 80)

- D. Jaksch and P. Zoller. **Creation of effective magnetic fields in optical lattices: the Hofstadter butterfly for cold neutral atoms.** *New J. Phys.*, **5**:56, 2003. (cited on p. 20)
- G. Jotzu, M. Messer, R. Desbuquois, M. Lebrat, T. Uehlinger, D. Greif, and T. Esslinger. **Experimental realization of the topological Haldane model with ultracold fermions.** *Nature*, **515**:237, 2014. (cited on pp. 21, 22, and 64)
- C. L. Kane and T. C. Lubensky. **Topological boundary modes in isostatic lattices.** *Nat. Phys.*, **10**:39, 2014. (cited on p. 19)
- C. L. Kane and E. J. Mele. **Size, shape, and low energy electronic structure of carbon nanotubes.** *Phys. Rev. Lett.*, **78**:1932, 1997. (cited on pp. 20 and 59)
- C. L. Kane and E. J. Mele. **Quantum spin Hall effect in graphene.** *Phys. Rev. Lett.*, **95**:226801, 2005a. (cited on pp. 18 and 63)
- C. L. Kane and E. J. Mele. **\mathbb{Z}_2 topological order and the quantum spin Hall effect.** *Phys. Rev. Lett.*, **95**:146802, 2005b. (cited on p. 18)
- T. Kariyado and Y. Hatsugai. **Manipulation of Dirac Cones in Mechanical Graphene.** *Scient. Reports*, **5**:18107, 2015. (cited on pp. 20, 64, and 78)
- Y. Kayanuma and K. Saito. **Coherent destruction of tunneling, dynamic localization, and the Landau-Zener formula.** *Phys. Rev. A*, **77**:010101, 2008. (cited on p. 25)
- M. Kohmoto and Y. Hasegawa. **Zero modes and edge states of the honeycomb lattice.** *Phys. Rev. B*, **76**:205402, 2007. (cited on pp. 61 and 62)
- A. R. Kolovsky. **Creating artificial magnetic fields for cold atoms by photon-assisted tunneling.** *EPL*, **93**:20003, 2011. (cited on p. 21)
- M. G. Krein. **Generalization of some investigations of Liapunov on linear differential equations with periodic coefficients.** *Dokl. Akad. Nauk SSSR*, **73**:445, 1950. (cited on pp. 49 and 50)
- R. B. Laughlin. **Quantized Hall conductivity in two dimensions.** *Phys. Rev. B*, **23**:5632(R), 1981. (cited on p. 13)
- N. Levy, S. A. Burke, K. L. Meaker, M. Panlasigui, A. Zettl, F. Guinea, A. H. Castro Neto, and M. F. Crommie. **Strain-induced pseudo-magnetic fields greater than 300 Tesla in graphene Nanobubbles.** *Science*, **329**:544, 2010. (cited on p. 65)
- Y. Li, G. I. Martone, and S. Stringari. **Bose-Einstein condensation with spin-orbit coupling.** *Annual Rev. of Cold Atoms and Molecules, World Scientific*, **3**:201, 2015. (cited on p. 77)
- H. Lignier, C. Sias, D. Ciampini, Y. Singh, A. Zenesini, O. Morsch, and E. Arimondo. **Dynamical control of matter-wave tunneling in periodic potentials.** *Phys. Rev. Lett.*, **99**:220403, 2007. (cited on p. 25)
- L. Lu, J. D. Joannopoulos, and M. Soljačić. **Topological photonics.** *Nat. Phot.*, **8**:821, 2014. (cited on p. 17)
- K. W. Madison, F. Chevy, W. Wohlleben, and J. Dalibard. **Vortex Formation in a Stirred Bose-Einstein Condensate.** *Phys. Rev. Lett.*, **84**:806, 2000. (cited on p. 19)
- M. Mancini, G. Pagano, G. Cappellini, L. Livi, M. Rider, J. Catani, C. Sias, P. Zoller, M. Inguscio, M. Dalmonte, and L. Fallani. **Observation of chiral edge states with neutral fermions in synthetic Hall ribbons.** *Science*, **349**:1510, 2015. (cited on p. 21)
- M. P. Marder. *Condensed matter physics.* John Wiley & Sons, Inc., (Hoboken, New Jersey), 2010. (cited on pp. 6 and 93)
- M. Milićević, T. Ozawa, P. Andreakou, I. Carusotto, T. Jacqmin, E. Galopin, A. Lemaître, L. Le Gratiet, I. Sagnes, J. Bloch, and A. Amo. **Edge states in polariton honeycomb lattices.** *2d Mat.*, **3**:034012, 2015. (cited on p. 64)

- S. Mittal, J. Fan, S. Faez, A. Migdall, J. M. Taylor, and M. Hafezi. **Topologically robust transport of photons in a synthetic gauge field.** *Phys. Rev. Lett.*, **113**:087403, 2014. (cited on p. 23)
- H. Miyake, G. A. Siviloglou, C. J. Kennedy, W. C. Burton, and W. Ketterle. **Realizing the Harper Hamiltonian with laser-assisted tunneling in optical lattices.** *Phys. Rev. Lett.*, **111**:185302, 2013. (cited on pp. 22, 36, and 39)
- S. V. Morozov, K. S. Novoselov, M. I. Katsnelson, F. Schedin, L. A. Ponomarenko, D. Jiang, and A. K. Geim. **Strong suppression of weak localization in graphene.** *Phys. Rev. Lett.*, **97**:016801, 2006. (cited on p. 59)
- D. Nakamura, Y. H. Matsuda, and S. Takeyama. **Precision of an Ultra-high Magnetic Field Generated by the Electro-magnetic Flux Compression.** *J. Low Temp. Phys.*, **170**:457, 2012. (cited on p. 17)
- A. V. Nalitov, G. Malpuech, H. Terças, and D. D. Solnyshkov. **Spin-orbit coupling and the optical spin Hall effect in photonic graphene.** *Phys. Rev. Lett.*, **114**:026803, 2015a. (cited on p. 82)
- A. V. Nalitov, D. D. Solnyshkov, and G. Malpuech. **Polariton \mathbb{Z} topological insulator.** *Phys. Rev. Lett.*, **114**:116401, 2015b. (cited on p. 82)
- L. M. Nash, D. Kleckner, A. Read, V. Vitelli, A. M. Turner, and W. T. M. Irvine. **Topological mechanics of gyroscopic metamaterials.** *Proc. Natl. Acad. Sci. USA*, **112**:14495, 2015. (cited on pp. 19 and 64)
- Nature Physics Insight. **Quantum Simulation.** *Nat. Phys.*, **8**(4), 2012. (cited on p. 17)
- J. Ningyuan, C. Owens, A. Sommer, D. Schuster, and J. Simon. **Time- and site-resolved dynamics in a topological circuit.** *Phys. Rev. X*, **5**:021031, 2015. (cited on p. 23)
- Q. Niu, D. J. Thouless, and Y.-S. Wu. **Quantized Hall conductance as a topological invariant.** *Phys. Rev. B*, **31**:3372, 1985. (cited on p. 13)
- T. Ozawa and I. Carusotto. **Anomalous and quantum Hall effects in lossy photonic lattice.** *Phys. Rev. Lett.*, **112**:133902, 2014. (cited on pp. 40, 43, 45, 46, and 71)
- T. Ozawa, H. M. Price, N. Goldman, O. Zilberberg, and I. Carusotto. **Synthetic dimensions in integrated photonics: From optical isolation to 4D quantum Hall physics.** *arXiv:1510.03910*, 2015. (cited on p. 21)
- J. Paulose, B. G. Chen, and V. Vitelli. **Topological modes bound to dislocations in mechanical metamaterials.** *Nat. Phys.*, **11**:153, 2015. (cited on p. 19)
- O. Peleg, G. Bartal, B. Freedman, O. Manela, M. Segev, and D. N. Christodoulides. **Conical diffraction and gap solitons in honeycomb photonic Lattices.** *Phys. Rev. Lett.*, **98**:103901, 2007. (cited on p. 72)
- V. M. Pereira and A. H. Castro Neto. **Strain engineering of graphene's electronic structure.** *Phys. Rev. Lett.*, **103**:046801, 2009. (cited on pp. 59 and 65)
- V. M. Pereira, A. A. Castro Neto, and N. M. R. Peres. **Tight-binding approach to uniaxial strain in graphene.** *Phys. Rev. B*, **80**:045401, 2009. (cited on pp. 61 and 65)
- L. P. Pitaevskii and S. Stringari. *Bose-Einstein Condensation and Superfluidity.* Oxford Science Publications, 2016. (cited on p. 18)
- Y. Plotnik, M. C. Rechtsman, D. Song, M. Heinrich, J. M. Zeuner, S. Nolte, Y. Lumer, N. Malkova, J. Xu, A. Szameit, Z. Chen, and M. Segev. **Observation of unconventional edge states in photonic graphene.** *Nature materials*, **13**:57, 2014. (cited on p. 64)
- M. Polini, F. Guinea, M. Lewenstein, H. C. Manoharan, and V. Pellegrini. **Artificial honeycomb lattices for electrons, atoms and photons.** *Nat. Nanotech.*, **8**:625, 2013. (cited on p. 63)

- L. A. Ponomarenko, R. V. Gorbachev, G. L. Yu, D. C. Elias, R. Jalil, A. A. Patel, A. Mishchenko, A. S. Mayorov, C. R. Woods, J.R. Wallbank, M. Mucha-Kruczynski, B. A. Piot, M. Potemski, I. V. Grigorieva, K. S. Novoselov, F. Guinea, V. I. Fal'ko, and A. K. Geim. [Cloning of Dirac fermions in graphene superlattices](#). *Nature*, **497**(7451):594, 2013. (cited on p. 17)
- H. M. Price, T. Ozawa, and I. Carusotto. [Quantum mechanics with a momentum-space artificial magnetic field](#). *Phys. Rev. Lett.*, **113**:190403, 2014. (cited on p. 11)
- H. M. Price, O. Zilberberg, T. Ozawa, I. Carusotto, and N. Goldman. [On the measurement of Chern numbers through center-of-mass responses](#). *arXiv:1602.01696 [cond-mat.quant-gas]*, 2016. (cited on p. 13)
- X.-L. Qi and S. C. Zhang. [Topological insulators and superconductors](#). *Rev. Mod. Phys.*, **83**:1057, 2011. (cited on p. 17)
- S. Raghu and D. M. Haldane. [Analog of quantum-Hall-effect edge states in photonic crystals](#). *Phys. Rev. A*, **78**:033834, 2008. (cited on pp. 18 and 19)
- M. C. Rechtsman, Y. Plotnik, J. M. Zeuner, D. Song, Z. Chen, A. Szameit, and M. Segev. [Topological Creation and Destruction of Edge States in Photonic Graphene](#). *Phys. Rev. Lett.*, **111**:103901, 2013a. (cited on p. 64)
- M. C. Rechtsman, J. M. Zeuner, Y. Plotnik, Y. Lumer, D. Podolsky, F. Dreisow, S. Nolte, M. Segev, and A. Szameit. [Photonic Floquet topological insulators](#). *Nature*, **496**:196, 2013b. (cited on pp. 22, 23, and 64)
- M. C. Rechtsman, J. M. Zeuner, A. Tünnermann, S. Nolte, M. Segev, and A. Szameit. [Strain-induced pseudomagnetic field and photonic Landau levels in dielectric structures](#). *Nat. Phot.*, **7**:153, 2013c. (cited on pp. 20, 63, and 65)
- M. S. Rudner, N. H. Lindner, E. Berg, and M. Levin. [Anomalous edge states and the bulk-edge correspondence for periodically driven two-dimensional systems](#). *Phys. Rev. X*, **3**:031005, 2013. (cited on p. 89)
- S. Ryu and Y. Hatsugai. [Topological origin of zero-energy edge states in particle-hole symmetric system](#). *Phys. Rev. Lett.*, **89**:077002, 2002. (cited on p. 62)
- K. Sacha, K. Targońska, and J. Zakrzewski. [Frustration and time-reversal symmetry breaking for Fermi and Bose-Fermi systems](#). *Phys. Rev. A*, **85**:053613, 2012. (cited on p. 21)
- J. J. Sakurai. *Modern quantum mechanics*. Addison-Wesley Publishing Company, 1994. (cited on p. 7)
- V. G. Sala, D. D. Solnyshkov, I. Carusotto, T. Jacqmin, A. Lemaître, H. Terças, A. Nal'itov, M. Abbarchi, E. Galopin, I. Sagnes, J. Bloch, G. Malpuech, and A. Amo. [Spin-orbit coupling for photons and polaritons in microstructures](#). *Phys. Rev. X*, **5**:011034, 2015. (cited on pp. 77, 81, 82, and 85)
- G. Salerno and I. Carusotto. [Dynamical decoupling and dynamical isolation in temporally modulated coupled pendulums](#). *EPL*, **106**:24002, 2014. (cited on pp. 3, 22, and 25)
- G. Salerno, T. Ozawa, H. M. Price, and I. Carusotto. [How to directly observe Landau levels in driven-dissipative strained honeycomb lattices](#). *2d Mat.*, **2**:034015, 2015. (cited on pp. 3, 20, and 66)
- G. Salerno, T. Ozawa, H. M. Price, and I. Carusotto. [Floquet topological system based on frequency-modulated classical coupled harmonic oscillators](#). *Phys. Rev. B*, **93**:085105, 2016. (cited on pp. 3, 22, 35, and 47)
- A. P. Schnyder, S. Ryu, A. Furusaki, and A. W. W. Ludwig. [Classification of topological insulators and superconductors in three spatial dimensions](#). *Phys. Rev. B*, **78**:195125, 2008. (cited on p. 18)
- J. F. Sherson, C. Weitenberg, M. Endres, M. Cheneau, I. Bloch, and S. Kuhr. [Single-atom-resolved fluorescence imaging of an atomic Mott insulator](#). *Nature*, **467**:68, 2010. (cited on p. 18)

- J. H. Shirley. [Solution of the Schrödinger equation with a Hamiltonian periodic in time.](#) *Phys. Rev.*, **138**:B979, 1965. (cited on pp. 21 and 49)
- P. Soltan-Panahi, J. Struck, P. Hauke, A. Bick, W. Plenkers, G. Meineke, C. Becker, P. Windpassinger, M. Lewenstein, and K. Sengstock. [Multi-component quantum gases in spin-dependent hexagonal lattices.](#) *Nature Physics*, **7**:434, 2011. (cited on p. 64)
- J. Struck, C. Ölschläger, M. Weinberg, P. Hauke, J. Simonet, A. Eckardt, M. Lewenstein, K. Sengstock, and P. Windpassinger. [Tunable gauge potential for neutral and spinless particles in driven optical lattices.](#) *Phys. Rev. Lett.*, **108**:225304, 2012. (cited on pp. 21 and 22)
- J. Struck, M. Weinberg, C. Ölschläger, P. Windpassinger, J. Simonet, K. Sengstock, R. Höppner nad P. Hauke, A. Eckardt, M. Lewenstein, and L. Mathey. [Engineering Ising-XY spin-models in a triangular lattice using tunable artificial gauge fields.](#) *Nat. Phys.*, **9**:738, 2013. (cited on p. 21)
- P. Strěda. [Quantised Hall effect in a two-dimensional periodic potential.](#) *J. Phys. C: Solid State Phys.*, **15**:L1299, 1982. (cited on p. 13)
- K. Stuhl, H. I. Lu, L. M. Ayccock, D. Genkina, and I. B. Spielman. [Visualizing edge states with an atomic Bose gas in the quantum Hall regime.](#) *Science*, 349:1450, 2015. (cited on p. 21)
- R. Süsstrunk and S. Huber. [Observation of phononic helical edge states in a mechanical topological insulator.](#) *Science*, **349**:47, 2015. (cited on p. 24)
- H. Suzuura and T. Ando. [Phonons and electron-phonon scattering in carbon nanotubes.](#) *Phys. Rev. B*, **65**:235412, 2002. (cited on p. 59)
- L. Tarruell, D. Greif, T. Uehlinger, G. Jotzu, and T. Esslinger. [Creating, moving and merging Dirac points with a Fermi gas in a tunable honeycomb lattice.](#) *Nature*, **483**:302, 2012. (cited on p. 64)
- J. R. Taylor. *An Introduction to Error Analysis.* University Science Books, 1997. (cited on pp. 86 and 88)
- D. J. Thouless, M. Kohmoto, M. P. Nightingale, and M. den Nijs. [Quantized Hall conductance in a two-dimensional periodic potential.](#) *Phys. Rev. Lett.*, **49**:405, 1982. (cited on pp. 13, 17, and 35)
- B. Tian, M. Endres, and D. Pekke. [Landau Levels in Strained Optical Lattices.](#) *Phys. Rev. Lett.*, **115**:236803, 2015. (cited on p. 20)
- O. Umucalılar and I. Carusotto. [Artificial gauge field for photons in coupled cavity arrays.](#) *Phys. Rev. A*, **84**:043804, 2011. (cited on pp. 23, 40, and 43)
- L. von Klitzing, G. Dorda, and M. Pepper. [New method for high-accuracy determination of the fine-structure constant based on quantized Hall resistance.](#) *Phys. Rev. Lett.*, **45**:494, 1980. (cited on p. 12)
- M. A. H. Vozmediano, M. I. Katsnelson, and F. Guinea. [Gauge fields in graphene.](#) *Phys. Rep.*, **496**:109, 2010. (cited on pp. 55 and 59)
- P. R. Wallace. [The band theory of graphite.](#) *Phys. Rev.*, **71**:622, 1947. (cited on p. 56)
- P. Wang, L. Lu, and K. Bertoldi. [Topological phononic crystals with one-way elastic edge waves.](#) *Phys. Rev. Lett.*, **115**:104302, 2015a. (cited on pp. 19 and 64)
- Y.-P. Wang, W. Wang, Z.-Y. Xue, W.-L. Yang, Y. Hu, , and Y. Wu. [Realizing and characterizing chiral photon flow in a circuit quantum electrodynamics necklace.](#) *Scient. Rep.*, **5**:8352, 2015b. (cited on p. 37)
- Y.-T. Wang, P.-G. Luan, and S. Zhang. [Coriolis force induced topological order for classical mechanical vibrations.](#) *New J. Phys.*, **17**:073031, 2015c. (cited on pp. 20 and 64)
- Z. Wang, Y. Chong, J. D. Joannopoulos, and M. Soljačić. [Observation of unidirectional backscattering-immune topological electromagnetic states.](#) *Nature*, **461**:772, 2009. (cited on p. 19)

- G. H. Wannier. **Dynamics of Band Electrons in Electric and Magnetic Fields.** *Rev. Mod. Phys.*, **34**:645, 1962. (cited on p. 8)
- C. Wu and S. Das Sarma. **$p_{x,y}$ -orbital counterpart of graphene: cold atoms in the honeycomb optical lattice.** *Phys. Rev. B*, **77**:235107, 2008. (cited on p. 80)
- D. Xiao, M.-C. Chang, and Q. Niu. **Berry phase effects on electronic properties.** *Rev. Mod. Phys.*, **82**:1959, 2010. (cited on pp. 11 and 13)
- G. L. Yu, R. V. Gorbachev, J. S. Tu, A. V. Kretinin, Y. Cao, R. Jalil, F. Withers, L. A. Ponomarenko, B. A. Piot, M. Potemski, D. C. Elias, X. Chen, K. Watanabe, T. Taniguchi, I. V. Grigorieva, K. S. Novoselov, V. I. Fal'ko, A. K. Geim, and A. Mishchenko. **Hierarchy of Hofstadter states and replica quantum Hall ferromagnetism in graphene superlattices.** *Nat. Phys.*, **10**:525, 2014. (cited on p. 17)
- J. Zak. **Magnetic translation group.** *Phys. Rev.*, **134**:A1602, 1964a. (cited on p. 6)
- J. Zak. **Magnetic translation group. II. Irreducible representations.** *Phys. Rev.*, **134**:A1607, 1964b. (cited on p. 6)
- A. Zenesini, H. Lignier, D. Ciampini, O. Morsch, and E. Arimondo. **Coherent control of dressed matter waves.** *Phys. Rev. Lett.*, **102**:100403, 2009. (cited on p. 25)